

DEVELOPMENT, CHARACTERIZATION, AND APPLICATIONS OF SELF-ASSEMBLING,
PHOTOCROSSLINKABLE COLLAGEN-BASED HYDROGELS

By

IAN DANIEL GAUDET

A Dissertation submitted to the

Graduate School-New Brunswick

Rutgers, The State University of New Jersey and

The Graduate School of Biomedical Sciences

University of Medicine and Dentistry of New Jersey

in partial fulfillment of the requirements

for the degree of

Doctor of Philosophy

Graduate Program in Biomedical Engineering

written under the direction of

David Ira Shreiber

and approved by

New Brunswick, New Jersey

[January, 2013]

Abstract of the Dissertation

Development, Characterization, and Applications of Self-Assembling, Photocrosslinkable
Collagen-based Hydrogels

By Ian D. Gaudet

Dissertation Director:

David I. Shreiber

Development of functional soft-tissue engineered constructs for use in regenerative medicine is currently limited by homogeneity within scaffolds that fails to recapitulate the complex architecture that supports normal function in healthy tissues. Additionally, recent breakthroughs in our understanding the biomechanical cell-matrix interface have provided insight into the role of substrate compliance during development and in the pathophysiological environment. This thesis is the result of investigation into using type-I collagen as a base material for creating dynamic, self-assembling, mechanically and biochemically tunable 3D hydrogel scaffolds into which instructive cellular cues can be imparted anisotropically via the directed application of light.

This overarching goal was approached by (1) evaluating extant methods for photonicallly manipulating type I collagen mechanical properties, which led us to the conclusion that published methods were inadequate for our purposes. Following this realization, we (2) developed a novel process for derivatizing free amines on collagen amino acid residues

to reactive methacrylamide moieties, allowing robust spatiotemporal control of mechanical properties through photocrosslinking with long-wave UV light and the water-soluble photoinitiator Irgacure 2959. Thorough characterization of this material, collagen methacrylamide (CMA), provided the basis for multiple applications in the field of soft tissue engineering. Additionally, (3) CMA was used in conjunction with synthetic photopolymers in an effort to create a hybrid natural/synthetic hydrogel material. CMA was also (4) employed as a dynamic hydrogel scaffold which we showed could be used to culture a number of neurogenic stem and progenitor cell types with a focus on using photomodulation to impart instructive heterogeneity to the mechanical and biochemical microenvironment. Finally, (5) we used a computational modeling approach to explain interesting yet poorly understood material phenomena exhibited by CMA observed during characterization. Using sequence and structure based models of an optimized triple helical segment of type-I collagen, we obtained valuable insight into the role of amino acid electrostatic interactions in CMA thermodynamic behavior as well as in the context of understanding the biophysical mechanisms of native type I collagen self-assembly and stability.

Dedication

For Winnie, George, and Marian. I wish you could be here now.

Acknowledgements

I would like to thank the many people that helped make this thesis possible. Foremost among them, my advisor and mentor, Dr. David Shreiber, who gave me the freedom to explore my own ideas, no matter how bad some of them were. Your guidance has greatly improved how I think critically about all things, bioengineering and otherwise. I would also like to thank the other members of my committee, Dr. Bonnie Firestein, Dr. Jason Burdick, and Dr. Prabhas Moghe. Your respective expertise and guidance in neurobiology, chemical engineering, and biomaterial interfaces was a huge help towards integrating an amazing number of scientific disciplines into this project. Additionally, your group members were instrumental in providing support with conducting experiments. In particular, I would like to thank Kathryn Drzewiecki, Dr. Joshua Katz, Kristina Hernandez, and Aaron Carlson for your collaborative efforts. I also owe Dr. Shirley Masand more gratitude than I can ever show; her enthusiasm, tireless effort, and genuine compassion have been a source of inspiration to me, our lab group, and the Biomedical Engineering department at large. I would also like to thank the BME staff, particularly Larry Stromberg and Julia Colvin, for all of your help in navigating the RU bureaucracy. Finally, I would like to thank my family, including my parents, my parents-in-law, and my fiancée. You have given me so much support along this long and sometimes rocky road, and you believed in me even when I didn't. I would not have accomplished this without everything you did for me.

List of Figures

Figure 1-1: Type I Collagen Network. Scale Bar = 10 μ m.....	1
Figure 2-2: Structure of FMN.....	10
Figure 2-2: Schiff Base Formation.....	12
Figure 2-3: Spectral Responsivity of PDA10A Photodetector.....	13
Figure 2-4: Frequency sweep of storage modulus of collagen crosslinked by FMN using different light sources.....	16
Figure 2-5: Frequency sweep of storage modulus of collagen crosslinked with FMN in the liquid phase prior to gelation.....	17
Figure 2-6: Frequency sweep of storage and loss moduli of liquid phase collagen crosslinked with FMN using longwave UV light.....	18
Figure 2-7: Frequency sweep of collagen gels photocrosslinked with FMN compared to 0.1mM Genipin crosslinking.....	19
Figure 2-8: Fibrin 10mg/mL Rheometry: Effect of FMN X-linking and Exogenous Calcium.....	20
Figure 2-9: Modulation of light intensity using opacity filters.....	21
Figure 2-10 Cytotoxicity of FMN on NIH3T3.....	22
Figure 2-11: FMN Cytotoxicity on Encapsulated 3T3 Fibroblasts.....	22
Figure 2-12: Cytotoxicity of Encapsulated 3T3 Fibroblasts in collagen crosslinked by 0.1mM FMN.....	23
Figure 2-13: LAA effect on post-photocrosslinking viability.....	24
Figure 2-14: AAS effect on post-photocrosslinking viability.....	25
Figure 2-15: GSH effect on post-photocrosslinking viability.....	25
Figure 2-16: Effect of AAS + GSH on post-photocrosslinking viability.....	26
Figure 2-17: DRG encapsulated in collagen gels +/- FMN photocrosslinking.....	27
Figure 2-18: Effect of 3T3 Concentration in FMN Photocrosslinked Fibrin gels.....	28
Figure 2-19: Effect of time of medium addition on post-crosslink viability	28
Figure 3-1: EDC.....	38
Figure 3-2: Sulfo-NHS.....	38
Figure 3-3: Schematic of EDC/NHS crosslinking reaction.....	39
Figure 3-4: UV Rheometry Schematic and Photo of parallel plates with UV light 'On'	46

Figure 3-5: NMR of Native Collagen, CMA with MAA:ε-Amine ratios in Deuterated DMSO	53
Figure 3-6: NMR spectra of native collagen, native collagen + 100μl free MAA, CMA without and with sulfo-NHS.....	54
Figure 3-7: NMR spectrum of optimized CMA protocol showing derivatized methacrylate peaks at 5.3-6.1.....	55
Figure 3-8: TNBSA Assay Data.....	57
Figure 3-9: Summary of CMA vs. Collagen Storage and Loss Moduli.....	58
Figure 3-10: Mechanical Tunability of CMA Gels via Differential Light Exposure Periods and Dynamic Temporal Control using Multiple Light Exposures	59
Figure 3-11: CD Spectra of CMA & Native Collagen in 0.02 M Acetic Acid.....	60
Figure 3-12: CD Spectra of CMA and Native Collagen in Phosphate Buffered Saline and 0.02M Acetic Acid	61
Figure 3-13: CD Melting Curve of CMA and Native Collagen in Phosphate Buffered Saline and 0.02M Acetic Acid.....	62
Figure 3-14: CD Spectra of CMA and Native Collagen in Phosphate Buffered Saline and 0.02M Acetic Acid.....	63
Figure 3-15: CD Melting Curve of CMA and Native Collagen in Phosphate Buffered Saline and 0.02M Acetic Acid.....	64
Figure 3-16: DLS Summary Plot of Intensity Peak Size of CMA and NC in PBS.....	66
Figure 3-17: DLS Intensity and Volume Peaks for Native Collagen and CMA in PBS	66
Figure 3-18: DLS Mean Intensity Peak Size (nm) for Native Collagen and CMA in PBS.....	67
Figure 3-19: DLS Intensity and Volume Peaks for Native Collagen and CMA in Acetic Acid.....	69
Figure 3-20: Mean Monodisperse Volume Peak Size (nm) for Native Collagen and CMA in 0.02 M Acetic Acid.....	70
Figure 3-21: SEM of CMA, CMA Photocrosslinked, and Native Collagen with Histogram of Fibril Diameter.....	71
Figure 3-22: Rheological Collagenase Degradation Rate; BCA Assay Quantification of Collagenase-Liberated Protein.....	72
Figure 3-23: Real-time G': Effect of PBS Salt Concentration on Native Collagen and CMA Fibrillogenesis Kinetics.....	73
Figure 3-24: Dry Weight of Native Collagen, CMA, and Photocrosslinked CMA Gels.....	74
Figure 3-25: Zero shear viscosity of 4.4 mg/mL Native Collagen and CMA at 4°C from Moore fit.....	75

Figure 3-26: Cold melt and reassembly curves of Native Collagen and CMA.....	77
Figure 3-27: Cold Melt Rheology of CMA with Photocrosslinking.....	78
Figure 3A-1: G': CMA +/- Photocrosslinking via SR-2000.....	90
Figure 3A-2: Native Collagen: Rheometer Comparison.....	91
Figure 3A-3: G': CMA +/- Photocrosslinking via Gemini II.....	92
Figure 3A-4: G': Effect of CMA Concentration +/- Photocrosslinking.....	93
Figure 3A-5: G': Effect of UV Exposure time on Photocrosslinking.....	94
Figure 3A-6: G': Optimized CMA +/- Photocrosslinking.....	95
Figure 3A-7: G': Kinexus Validation - CMA +/- Photocrosslinking.....	96
Figure 3A-8: G': Native Collagen +/- Photocrosslinking Conditions.....	97
Figure 3A-9: G': Effect of Shear during CMA Reconstitution +/- Photocrosslinking	98
Figure 3A-10: G': Native Collagen QC Lot 141 vs. 159.....	99
Figure 3A-11: G': CMA Synthesis QC: NC Lot 159.....	100
Figure 3A-12: Kinexus rSpace Software Output Chart of QC Validation of a New Native Collagen Batch..	101
Figure 3A-13: Real-time G': Effect of Light Intensity Modulation.....	102
Figure 3A-14: Real-time G': Effect of Photoinitiator Concentration.....	103
Figure 3A-15: Effect of I2959 Concentration on Photocrosslinked CMA Equilibrium G'.....	103
Figure 3A-16: Complete CMA G' and G'' Curves and Magnification of UV exposure period.....	104
Figure 3A-17: Real-time G' of CMA at 2.5, 3.0 and 3.5 mg/mL.....	105
Figure 4-4: Poly-(Ethylene Glycol) Diacrylate (PEGDA).....	106
Figure 4-5: Schematic of CMA gels crosslinked with PEG linkers with 1, 2, and 4 functional groups.....	108
Figure 4-6: CMAX2 Derivatization Schematic.....	113
Figure 4-7: ¹ H NMR spectrum of PEGDA.....	114
Figure 4-8: Effect of 0.1% (v/v) PEG258DA on Storage Modulus of Native Collagen and CMA Hydrogels.....	116
Figure 4-9: Effect of CMA Concentration Photocrosslinked with 0.1% PEG258DA on Gel Stiffness.....	117

Figure 4-10: G' and G'' Characterization of 3.0 mg/mL CMA Photo \pm 0.1% (v/v) 258 Da PEGDA.....	118
Figure 4-11: Summary of G' at 1 rad/s of CMA \pm photocrosslinking with Acrylated PEG Variants.....	119
Figure 4-12: CMA G' with crosslinking \pm 2000 Da PEG Variants.....	120
Figure 4-13: Acrylate-PEG-SCM.....	120
Figure 4-14: Thiol-PEG-COOH.....	121
Figure 4-15: Storage Modulus of Collagen-PEG-Thiol Photocrosslinked \pm PEG258DA.....	121
Figure 4-16: Cytotoxicity of Diacrylated and Monoacrylated PEG Variants of Different Molecular Weight.....	122
Figure 4-17: Live/Dead Staining of PEG Variant Exposure.....	123
Figure 4-18: MTS cytotoxicity screen of PEG macromers.....	124
Figure 4-19: PEG Molecular Weight Effect on Cytotoxicity.....	125
Figure 4-20: Live/Dead Staining of NIH-3T3 Fibroblasts on Native Collagen, CMA XL, CMA + 0.1% PEG258DA, TCP, TCP + 0.1% PEG258DA.....	126
Figure 4-21: MTS Assay Data: Dose Response Cytotoxicity of CMA Photocrosslinked with Various Concentrations of PEG258DA.....	127
Figure 4-22: Storage Modulus of CMAX2 (Batch 1) with Photocrosslinking \pm 0.1% PEG2KDA.....	128
Figure 4-23: Storage Modulus of CMAX2 (Batch 2) with Photocrosslinking \pm PEG2KDA.....	129
Figure 4-24: Modulus of CMAX2 (Batch 3) with Photocrosslinking \pm PEG2KDA.....	129
Figure 4-25: Storage Moduli \pm Photocrosslinking of CMAX2 from 2 Different Native Collagen Lots.....	130
Figure 4-26: Storage Moduli of CMAX2 Photocrosslinked \pm 0.1% and 1% (w/v) PEG2KDA.....	131
Figure 4-27: NMR of CMA, Further Derivatized to CMAX2.....	131
Figure 5-28: hMSC in 3D Gels 48 H after Photocrosslinking with 2 minutes UV and 0.025% in Mat-Tek D.....ishes.....	152
Figure 5-29: MTS Assay: hMSC in Native Collagen and CMA 48 H after Photocrosslinking.....	153
Figure 5-30: Cytocompatibility of hMSC encapsulated in native collagen or photocrosslinked CMA.....	154
Figure 5-31: Quantification of hMSC viability at 24 and 72 hours after encapsulation and/or photocrosslinking.....	155

Figure 5-32: hMSC after 7 days in GM and NIM on TCP.....	157
Figure 5-33: hMSC after 7 days in GM and NIM in Native Collage.....	158
Figure 5-34: hMSC after 7 days in GM and NIM in CMA.....	159
Figure 5-35: β 3-Tubulin Staining of hMSC in Growth Medium in Different Culture Conditions compared to Primary Neurons and Astrocytes.....	160
Figure 5-36: GFAP Staining of hMSC in Growth Medium Different Culture Conditions compared to Primary Neurons and Astrocytes.....	161
Figure 5-37: Live/Dead staining of hMSC in 3D CMA Gels.....	162
Figure 5-38: Annular-contracted hMSC-encapsulated photopatterned CMA disk.....	163
Figure 5-39: hMSC in a 3D CMA Gel 5 72 H after Photocrosslinking Circular Pattern in Center of Gel.....	164
Figure 5-40: Image-based Adhesion Assay. hMSC on Various Substrates for 90 Minute.....	165
Figure 5-41: MTS Adhesion Assay. hMSC on Various Substrates for 0, 30, 60, & 90 Minutes.....	166
Figure 5-42: Adhesion of SMC on Varying Ratios of CMA and Native Collagen.....	167
Figure 5-43: Pre-differentiated iPS-NSC in photocrosslinked CMA.....	169
Figure 5-44: Differentiating iPS-NSC in CMA gels 72 H after encapsulation.....	171
Figure 5-45: Montaged images of iPS-NSC in 1/2 Photocrosslinked CMA Photografted Peptide Gels.....	172
Figure 5-46: IHC staining of iPS-NSC after 5 Days in culture in CMA Gels.....	174
Figure 5-47: Tuj1 and GFAP staining of pre-differentiated iPS-NSC in CMA hydrogels.....	175
Figure 5-48: MAP2 expression in Pre-differentiated iPS-NSC in CMA \pm Photocrosslinking.....	176
Figure 5-49: SYN expression in Pre-differentiated iPS-NSC in CMA \pm Photocrosslinking.....	177
Figure 5-50: VGLUT expression in Pre-differentiated iPS-NSC in CMA \pm Photocrosslinking.....	178
Figure 5-51: Nestin and DAPI IHC of Differentiated iPS-NSC after 7 Days in Culture.....	180
Figure 5-52: Tuj1 , MAP2 and DAPI IHC of Differentiated iPS-NSC after 7 Days in Culture.....	181
Figure 5-53: Tuj1, VGLUT and DAPI IHC of Differentiated iPS-NSC after 7 Days in Culture.....	182
Figure 5-54: Tuj1, SYN and DAPI IHC of Differentiated iPS-NSC after 7 Days in Culture.....	183
Figure 5-55: Tuj1, GFAP and DAPI IHC of Differentiated iPS-NSC after 7 Days in Culture.....	184
Figure 5-56: iPS-NSC near Contracted Gel Edge.....	185

Figure 5-57: Montaged Images of CMA gels 1/2 Photocrosslinked with Methacrylated Peptide.....	187
Figure 5-58: DRG stained with NF-M in CMA.....	188
Figure 5-59: Quantification of neurite outgrowth from DRG in CMA Photocrosslinked \pm Methacrylated Peptide.....	189
Figure 5-60: MTS Assay Results, Cytotoxic Effects of Me-mPEG-PP on iPS-NSC.....	192
Figure 5-61: Live/Dead Stain of SKP-SC 72 H after Encapsulation in CMA.....	193
Figure 5-62: SKP-SC Cultured in 2D on CMA	194
Figure 5-63: Quantification of SKP-SC Number on CMA Substrates after 5 Days in Culture.....	195
Figure 5-64: Quantification of SKP-SC Process Morphology on CMA Hydrogels.....	196
Figure 5-65: Immunostained Differentiating aSCP on CMA Gels	197
Figure 5-66: 2D Culture of SKP-SC on TCP and CMA.....	200
Figure 5-67: 2D Culture of aSCP on TCP and CMA.....	201
Figure 5-68: Neurite Outgrowth from CMA-encapsulated DRG.....	202
Figure 5-69: Neurofilament-200 and DAPI Images of DRG Cultures.....	202
Figure 5-70: Live/Dead Staining of Dissociated, Differentiating aSCP in 3D CMA gels.....	204
Figure 5-71: Photopatterning CMA with Various Acrylated/Methacrylated Fluorophores.....	207
Figure 5-72: Penetration of UV light into CMA Vs Gel Height.....	208
Figure 5A-1: I2959 Toxicity in NIH-3T3 24 H after Photoinitiation.....	221
Figure 5A-2: I2959 Toxicity in hESC 24 H after Photoinitiation with UV.....	223
Figure 5A-3: I2959 Cytotoxicity in hMSC 24 H after Photoinitiation with UV.....	224
Figure 5A-4: I2959 Cytotoxicity in Sparsely Seeded hMSC 24 H after Photoinitiation with UV Light.....	225
Figure 5A-5: I2959 Cytotoxicity in DRG Embedded in CMA Gels and exposed to UV photoinitiation.....	226
Figure 5A-6: Live/Dead Staining 48 H after I2959 Photocrosslinking of L2.3 Glial Progenitor Neurospheres in 3D Gels.....	227
Figure 5A-7: MTS Viability Assay: High Cell Density L2.3 Glial Progenitor Neurospheres 72 H after UV-Irgacure 2959 Crosslinking \pm PEG2KDA.....	228
Figure 5A-8: Live/Dead Staining 48 H after I2959 Photocrosslinking of L2.3 Glial Progenitor Neurospheres in 3D Gels.....	229

Figure 5A-9: MTS Viability Assay: Low Cell Density L2.3 Glial Progenitor Neurospheres 72 H after UV-Irgacure 2959 Crosslinking \pm PEG2KDA.....	229
Figure 5A-10: I2959 Toxicity in hESC-derived NSC (RG8) 24 H after Photoinitiation with UV.....	231
Figure 5A-11: MTS Viability Assay: I2959 Cytotoxicity in hESC-derived NSC on TCP 24H after UV Exposure.....	231
Figure 5A-12: Live/Dead Staining 48 H after UV-I2959 Photocrosslinking RG8 NSC in 3D CMA Gels.....	232
Figure 5A-13: MTS Viability Assay: I2959 Cytotoxicity in hESC-derived NSC in CMA Gels 48 H after UV-I2959 Photocrosslinking.....	233
Figure 5A-14: Live/Dead Staining 24 H after UV-I2959 Photocrosslinking single cell CTX-8 in 3D CMA Gels.....	234
Figure 5A-15: Live/Dead Staining 24 H after UV-I2959 Photocrosslinking neurosphere CTX-8 in 3D CMA Gels.....	235
Figure 5A-16: hMSC in 3D CMA Gels 48 H after Photocrosslinking with UV-I2959.....	236
Figure 5A-17: MTS Viability Assay: hMSC in 3D CMA Gels 48 H after Photocrosslinking with UV-I2959.....	237
Figure 5A-18: hMSC in Native Collagen Gels 48 H after Photocrosslinking with UV-I2959.....	238
Figure 5A-19: MTS Viability Assay. hMSC in Native Collagen 48 H after Photocrosslinking with UV-I2959.....	239
Figure 5B-1: Proliferating iPS-NSC in CMA (A) and Photocrosslinked CMA after 24 H.....	240
Figure 5B-2: 7 day-differentiated iPS-NSC in native collagen, CMA, and photocrosslinked CMA after 7 days in culture.....	241
Figure 5B-3: 7 day-differentiated iPS-NSC in CMA after 1, 3, and 7 days.....	242
Figure 5B-4: iPS-NSC in CMA and Photocrosslinked CMA with 0, 1, 5 and 10 ug/mL Laminin.....	243
Figure 5B-5: CMA with encapsulated pre-differentiated iPS-NSC after 72 H in NDM and NDM + Y-27632.....	244
Figure 5B-6: Real-time UV rheology of CMA Control, CMA with 1% DMSO, and CMA with 0.1mg/mL Methacrylated-G6- Peptide and 1% DMSO.....	246
Figure 5B-7: Effect of DMSO Concentration on Gelation Time of CMA.....	247
Figure 5B-8: UV photocrosslinking of CMA with and without 1e7 cells/mL with Me-G6-Peptide and 2% DMSO.....	248
Figure 5B-9: Pre-differentiated iPS-NSC in CMA and CMA + 10% DMSO.....	249

Figure 6-73: Charge-charge Energy in 153-residue Trimers, Windowed from Full-length $\alpha 1$ and $\alpha 2$ Chains.....	257
Figure 6-74: Energy Gap between Full Length Collagen AAB Heterotrimer and AAB with 25% Total Lysines Mutated to Leucines.....	258
Figure 6-75: Schematic of 153 Residue AAA and AAB Trimers, Wild-type vs. 100% Lysine/Leucine Substitution Mutant.....	259
Figure 6-76: RMSD of Backbone Atoms during Molecular Dynamics Simulation.....	260
Figure 6-77: Average Backbone Hydrogen Bond Occupancy % During 50 ns Post-Equilibration Period.....	261
Figure 6-78: Distribution Plot of Hydrogen Bond Occupancy % within Each Trimer, Weak Criteria Set.....	262
Figure 6-79: Total Number of Hydrogen Bonds within Occupancy % Clusters. Criteria: 3.5 Å & 40° Bond Angle.....	263
Figure 6-80: Clustered Backbone Hydrogen Bond Occupancy, 3.5 Å & 40° Bond Angle.....	264
Figure 6-81: Comparison of Salt Bridge Length within 153 Residue AAA Trimers.....	265
Figure 6-82: Comparison of Salt Bridge Length within 153 Residue AAB Trimers.....	266
Figure 6-83: AAB trimer segment containing wild-type lysine.....	267
Figure 6-84: AAB trimer segment containing methacrylamide substitution.....	268
Figure 6-85: Heat Map of Backbone Hydrogen Bond Occupancy in AAB Trimers.....	268

List of Tables

Table 3-1: Comparison of Native Collagen and CMA Properties with Various Characterization Methods.....	79
Table 5-1: Primary Antibodies used in Immunohistochemistry.....	146
Table 5-2: Summary of Irgacure 2959 Photoinitiation Cytocompatibility.....	151

Table of Contents

Abstract of Dissertation.....	ii
Dedication.....	iv
Acknowledgements.....	v
List of Figures.....	vi
Chapter 1: Background.....	1
1.1 Collagen Hydrogels.....	1
1.2 Synthetic Hydrogels.....	3
1.3 Hydrogels as Scaffolds for CNS Regeneration.....	4
Chapter 2: Prelude: Collagen Photocrosslinking Approaches from Literature.....	9
2.1 Introduction.....	9
2.2 Flavin Mononucleotide Mediated Photocrosslinking.....	10
2.3 Methods.....	10
2.3.1 Collagen Stock Solution.....	10
2.3.2 <i>Collagen Gels</i>	11
2.3.3 <i>Photocrosslinking</i>	11
2.3.4 <i>Light Intensity Measurement</i>	12
2.3.5 <i>Rotational Rheometry</i>	13
2.3.6 <i>Cell Culture</i>	14
2.3.7 <i>Cytotoxicity Testing</i>	14
2.3.8 <i>Live/Dead Assay</i>	15
2.3.9 <i>Antioxidants</i>	15
2.4 Results.....	16
2.4.1 <i>Rheometry</i>	16
2.4.2 <i>Light intensity Modulation via Masking</i>	20

2.4.3	<i>Cytotoxicity</i>	21
2.4.5	<i>Fibrin Photocrosslinking with Encapsulated Cells</i>	27
2.5	Discussion: FMN Photocrosslinking.....	29
2.6	Methacrylate Derivatized Collagen.....	31
2.7	Methods.....	33
2.7.1	<i>Methacrylate Derivatization</i>	33
2.7.2	Photoinitiation.....	33
2.8	Results.....	34
2.9	Discussion: Methacrylic Anhydride Derivatization.....	35
2.10	Conclusion.....	36
Chapter 3: Collagen Methacrylamide Derivatization via EDC/Sulfo-NHS and Methacrylic Acid		
.....		38
3.1	Introduction: EDC Crosslinking as a Functionalization Modality.....	38
3.2	Derivatization of Collagen to CMA via EDC and methacrylic acid.....	40
3.3	Methods.....	41
3.3.1	<i>CMA Derivatization Optimization</i>	41
3.3.2	<i>Proton NMR</i>	42
3.3.3	<i>TNBSA Assay</i>	42
3.3.4	<i>Optimized CMA Synthesis Protocol</i>	43
3.3.5	<i>Rheometry</i>	44
3.3.6	<i>Circular Dichroism Spectroscopy</i>	46
3.3.7	<i>Dynamic Light Scattering</i>	47
3.3.8	<i>Scanning Electron Microscopy</i>	48
3.3.9	<i>Degradation via Collagenase</i>	49
3.3.10	<i>BCA Total Protein Assay</i>	49
3.3.11	<i>Gel Mass Analysis</i>	50

3.3.12	<i>Cold Melt Rheometry</i>	50
3.3.13	<i>Viscometry</i>	51
3.4	Results.....	51
3.4.1	<i>CMA Optimization</i>	51
3.4.2	<i>Proton NMR</i>	51
3.4.3	<i>TNBSA Assay for Amine Quantification</i>	55
3.4.4	<i>Rheometry</i>	57
3.4.5	<i>CD Spectroscopy</i>	59
3.4.6	<i>DLS</i>	65
3.4.7	<i>SEM</i>	70
3.4.8	<i>Collagenase Degradation</i>	71
3.4.9	<i>Gravimetric Analysis of Gel Mass</i>	73
3.4.10	<i>Viscometry</i>	74
3.4.11	<i>Cold Melt Rheology</i>	76
3.5	Discussion.....	80
3.6	Conclusions.....	87
3A	Appendix: Optimization of CMA Photocrosslinking and Rheological Testing.....	89
	Chapter 4: CMA PEG hybrids and CMAX2	106
4.1	Introduction: Hybrid Hydrogels.....	106
4.2	Methods.....	109
4.2.1	<i>PEGDA Synthesis</i>	109
4.2.2	<i>PEG/CMA Hybrid Rheology</i>	109
4.2.3	<i>PEG CMA Cytotoxicity</i>	110
4.2.4	<i>MTS Assay</i>	110
4.2.5	<i>Collagen-PEG-Acrylate and Collagen-PEG-Thiol</i>	111

4.2.6	<i>CMAX2 Synthesis</i>	111
4.2.7	<i>CMAX2 Characterization</i>	114
4.3	Results.....	114
4.3.1	<i>NMR: PEGDA Synthesis</i>	114
4.3.2	<i>PEG Solubility</i>	114
4.3.3	<i>CMA-PEG Hybrid Gel Rheometry</i>	115
4.3.4	<i>CPA and CPT Functionalization</i>	120
4.3.5	<i>PEG Cytotoxicity</i>	121
4.3.6	<i>CMAX2 Characterization</i>	127
4.4	Discussion.....	132
4.5	Conclusion.....	136
	Chapter 5: In Situ Photomodulation of Hydrogels for Cellular Instruction	138
5.1	Introduction: CNS Tissue Scaffold Engineering.....	138
5.2	Methods.....	141
5.2.1	<i>Cell Culture</i>	141
5.2.2	<i>Immunohistochemistry</i>	146
5.2.3	<i>Irgacure 2959</i>	147
5.2.4	<i>Photoinitiator Cytotoxicity Screening</i>	148
5.2.5	<i>3D Cell-containing Gel Photocrosslinking</i>	148
5.2.6	<i>Adhesion Assay</i>	149
5.2.7	<i>Photopatterning</i>	149
5.2.8	<i>Photolabile Peptides Crosslinking</i>	149
5.3	Results.....	150
5.3.1	<i>hMSC Culture in 3D Photocrosslinked Hydrogels</i>	150
5.3.2	<i>hMSC Neuronal Induction</i>	155

5.3.3	<i>Patterned Contraction</i>	163
5.3.4	<i>hMSC Adhesion Assay</i>	164
5.3.5	<i>iPS-NSC Culture in 3D CMA Photocrosslinked Gels</i>	167
5.3.6	<i>iPS-NSC Culture on 2D Peptide-Photocrosslinked CMA Gels</i>	179
5.3.7	<i>DRG Outgrowth in 3D CMA Gels Photocrosslinked with Methacrylated Laminin Peptide</i>	188
5.3.8	<i>Cellular Response to CMA Photografting with PSA-mimetic Peptide</i>	190
5.3.9	<i>Visualization of Photopatterning</i>	204
5.4	Discussion.....	208
5.5	Conclusion.....	219
5A	Appendix: Stem Cell Cytotoxicity Screening of I2959 Photoinitiation.....	220
5B	Appendix: Optimization of Photocrosslinking Differentiated iPS-NSC in CMA.....	239
	Chapter 6: Computer Modeling of CMA Molecular Structure	250
6.1	Introduction: Collagen Structure Characterization and Modeling.....	250
6.1	Methods.....	253
6.2.1	<i>Sequence-based Model</i>	253
6.2.2	<i>Structure-based Model</i>	254
6.3	Results.....	255
6.3.1	<i>Sequence-based Charge-Charge Energy Characterization</i>	255
6.3.2	<i>Structure-based Molecular Dynamics Modeling</i>	259
6.4	Discussion.....	269
6.5	Conclusion.....	273
7.	Concluding Discussion and Future Directions	274
	Bibliography	280
	Curriculum Vitae	291

1. Chapter 1: Background

1.1 Collagen Hydrogels

Hydrogels are attractive materials for use as tissue engineering scaffolds due to their potential to be injected into a defect or wound, then polymerized to provide a stable matrix for cellular growth, remodeling and regeneration into functional tissues [1]. Acid-soluble type I collagen, when pH neutralized, self assembles into a network of fibrils (Figure 1-1) to form a natural hydrogel, and has been

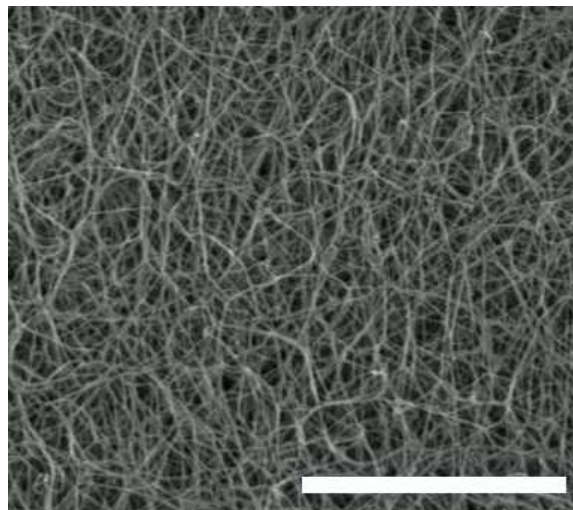


Figure 1-86: Type I Collagen Network. Scale Bar = 10 μ m

used extensively in medical devices and pharmaceuticals due to its availability, cytocompatibility, and inherent functional binding sites [2]. Type I collagen is the most abundant protein in mammals, comprising 30% of all protein in humans, and is the most common of the 28 known isoforms of collagen [3]. In vivo, type I collagen serves primarily as a structural protein and is found in skin, bone, tendon, ligament, corneal and connective tissue. The hierarchical structure of collagen, formed from tropocollagen monomers into micrometer-scale fibers, is the foundation behind the mechanical strength of collagen found in almost all load-bearing tissues [4]. The basis of this structure is the triple helix of collagen, which has been extensively studied during the last half century. The triple-helical tropocollagen molecule is made up of 3 left-handed helical α -chains, which vary in composition depending on the specific type of collagen. Each α -chain is defined by its characteristic Gly-X-Y sequence, where every third amino acid is glycine. Various other amino acids make up the other two, but the most common are the imino

acids proline and hydroxyproline [5], which are believed to assist in stabilizing the backbone of the triple helix. In type I collagen, the tropocollagen molecule comprises two identical $\alpha 1$ chains and one $\alpha 2$ chain, with the formation of fibrils driven by an entropic process in which solvent molecules are removed from the protein surface [6]. Fibrils are initially stabilized via hydrogen bonds and interchain charge pairs [7], with further stabilization imparted in vivo via covalent crosslinking, mainly through the actions of the enzymes such as lysyl oxidase [8]. This self assembly of fibrils and concomitant secondary stabilization are what gives type I collagen its mechanical strength. Younger collagens, such as that derived from bovine calf skin, have significantly less covalent crosslinks, are thus mechanically weaker and more soluble, which has led to their purification and use in the laboratory as hydrogels [9]. However, relative to many native tissues, collagen hydrogels typically have poor mechanical strength and the mechanical properties are not easily controlled, except through changing the macromer concentration or chemical crosslinking [10,11]. Furthermore, cellular adhesion to collagen matrices is highly variable and cell type-specific, and has profound implications on cell migration, proliferation, and other phenotypic behaviors [12]. These qualities limit or prevent the use of collagen in many applications. As such, many approaches have been developed to augment the natural properties of collagen.

However, these previous attempts at modifying collagen's material properties have presented significant challenges. Although chemical crosslinking using glutaraldehyde provides significant increases in mechanical strength, it is highly cytotoxic [13]. More cytocompatible crosslinking compounds, such as genipin, allow crosslinking in the presence of cells, although the degree of crosslinking is limited and localization of crosslinking is difficult due to diffusion of chemical agents through the hydrogel [14]. Enzymes, such as transglutaminases, are non-cytotoxic but are prohibitively expensive and are also subject to uncontrolled diffusion [15]. Other

approaches, such as exposure to UV light are either cytotoxic, in the case of UVC, or minimally effective and slow, as with UVA exposure [16]. Collagen has been reportedly directly crosslinked using UV light with riboflavin as a photosensitizing agent, although numerous tests in our lab have shown that this method does not significantly change the mechanical properties, and is quite cytotoxic as well [17]. More recently, there have been attempts made to modify collagen with photoactive groups to allow light, in conjunction with a photoinitiator, to produce significant changes spatially and in a cytocompatible manner. However, these approaches appear to have the common problem that the reaction conditions under which the collagen is modified are too harsh to preserve the complex tertiary structure, the result of which is that the collagen becomes partially denatured and is no longer able to spontaneously self-assemble [18-20].

1.2 Synthetic Hydrogels

Over the last two decades, synthetic polymer hydrogels have become increasingly popular as tissue engineering scaffolds due to the high degree of control afforded by direct control of the macromer composition [21]. One such material, polyethylene glycol (PEG), has been used in medical implants and pharmaceuticals in a number of formulations for decades. In 1995 West and Hubbell modified PEG by adding reactive acrylate groups to the end of the PEG macromer to form PEG diacrylate, which was then photopolymerized and used to form synthetic hydrogel matrices in which encapsulated cells could be grown [22].

More recently, photopolymerizable PEG-based materials have been produced for use as highly tunable tissue scaffolds and drug delivery systems [23,24]. The mechanical properties of PEG hydrogels can be precisely controlled by altering the polymer chain length and degree of branching [25]. While PEG is well tolerated by both encapsulated cells and host tissues, it is also

inherently non-adhesive and non-degradable. This prevents cells from either infiltrating the scaffold or remodeling it unless it is modified to include biodegradable moieties [26].

Hybrid materials, which contain a mixture of biomaterials and synthetic components, are also becoming popular as tissue engineering matrices due to the combination of their respective advantages. Several groups have successfully used combinations of natural and synthetic materials to optimize and tailor the properties of tissue engineering scaffolds to the particular application [27-29]. However, simply combining biomaterials with synthetics has limitations, due to the drawbacks of having both materials everywhere within the scaffold. In the case of PEG, this could prevent cell attachment. Other approaches using hybrid materials involve using collagen as a base material, and admixing additional natural or synthetic components such as hyaluronic acid and polyethylene oxide to form interpenetrating networks. A major drawback to this system is again there is little control over where materials interact, and it may be hard to determine with which material cells might interface due to the presence of two independent matrices [30-32]. A scaffold comprised of a single natural material with localized tunable control of its mechanical properties could be useful from a tissue engineering viewpoint in that the bioactivity would be consistent throughout the scaffold with variable stiffness imparted in a physiologically relevant manner. Furthermore, living tissues are highly variable in their localized properties, with different mechanical and biochemical properties within different parts of the tissue. To truly regenerate tissues with any real similarity to the original structure and functionality, an efficient scaffold will need the ability to be tailored with a heterogeneous structure.

1.3 Hydrogels as Scaffolds for CNS Regeneration

Mechanically tunable hydrogels have the potential to be used in a broad range of applications where heterogeneous control of the material properties is desired. One possible clinical application is in central nervous system (CNS) injury. The native tissue in the CNS has mechanical properties similar to those of collagen gels, and neural tissue behavior has been shown to be highly responsive to changes in stiffness [33]. Moreover, CNS injuries can result in lesion cavities with non-uniform geometries that are not amenable to solid scaffold implantation without the risk of additional damage to the injury site [34]. One major advantage of collagen is its ability to self-assemble, which allows the material to be injected into a defect of almost any geometry with minimal disruption of nearby healthy tissue, and then polymerize into a solid to provide a stable matrix. Photocrosslinking could then be accurately introduced into any spatial pattern where light application is accessible. As the photocrosslinking process can be cytocompatible, cells in the liquid scaffold can be injected into a defect, followed by scaffold modulation *in situ* to create an optimal environment for tissue regeneration that is customizable to an individual patient. Hydrogel scaffolds can also allow for controlled release of therapeutic agents such as growth factors, enzymes, and anti-inflammatory agents [35-38]. Here, the release rate of the therapeutic can be controlled locally by increasing the crosslinking density and hence the degradation rate of the scaffold. Local gradients of neurotrophic agents encapsulated within the matrix could provide another method for guiding cellular behavior. It is well known that chemotactic gradients present during neurogenesis contribute to proper axonal targeting; this phenomenon has also been recreated in the adult rat brain facilitating properly targeted axonal outgrowth [39]. The defined, anisotropic presentation of cues, such as adhesive ligands or matrix stiffness, can also provide critical directional information to regenerating neural tissue to potentially accelerate functional recovery. Neural recognition molecules, such as L1, Neural Cell Adhesion Molecule (NCAM), poly-sialic acid (PSA), and Tenascin-R, have been implicated in the

recruitment and/or repulsion of neuronal cell migration and may provide attractive options for photopatterning of neuroactive molecules [40,41]. In another instance, using a microfluidic-based assay, our laboratory has demonstrated that the growth of regenerating neurites from dorsal root ganglia is directed and enhanced down gradients of compliance. However, the scope and profile of these gradients were limited by the tolerable concentrations of the soluble crosslinker used, and by dimensional constraints associated with maintaining laminar flow regimes in microfluidic networks. Moreover, guidance of cell types other than neurons, such as astrocytes, has been shown to cause a secondary alignment of neurons [42]. Taking advantage of this may allow reorganization of the glial scar present in many CNS injuries, and could allow modulation of neurite ingrowth through the injury site in a long term manner.

Another potential use for tunable hydrogels is toward directing stem cell differentiation. The microenvironment surrounding a stem cell, including the mechanical and biochemical properties of the extracellular matrix, has been shown to have a profound effect on the proliferation rate of stem cells as well as differentiation fate [43]. More recently, human mesenchymal stem cells (hMSC) have been shown to not only differentiate into functional neuronal lineages [44], but also that the mechanical properties of the matrix were directly and solely responsible for the resultant differentiation fate [45]. Engler *et al* demonstrated that hMSC differentiation on 2D substrates was determined by substrate stiffness. Substrate stiffness of 0.1-1kPa, 8-17kPa, or 25-40kPa resulted in neurogenic, myogenic, or osteogenic lineages, respectively [46]. It was also shown recently that the combination of substrate stiffness and the presentation of adhesive ligands may act synergistically to drive hMSC differentiation. Rowlands *et al* showed, for instance, that hMSC differentiation could be pushed towards an osteogenic lineage via a stiff (80kPa) substrate coated with type-I collagen, but that type IV collagen on the same substrate resulted in differentiation into a myogenic lineage [47].

A spatially tunable hydrogel with the ability to control local properties within a 3D scaffold could potentially allow directed differentiation of stem cells seeded therein into a heterogeneous population, facilitating formation of complex tissues. Such constructs would have far reaching implications for clinical regeneration of damaged tissue, creation of 3D *in vitro* models of multicellular pathologies, and study of development in advanced geometries that more accurately mimic realistic geometries. Several groups have recently used collagen gels as matrices for stem and neural precursor cell-based therapies in CNS injury models[48,49]. While their results show that collagen gels are suitable for supporting both stem cell proliferation and differentiation into neural tissues, thus far these materials lack the ability to produce localized, controlled heterogeneity, which may be necessary to completely regenerate damaged tissues and restore function to pre-injury levels.

This dissertation discusses our examination of existing approaches for using light-based crosslinking to modify type I fibrillar collagen scaffolds as well as a novel process for creating a derivatized collagen-based material that allows robust, dynamic control of material properties. First, in Chapter 1, I describe our attempts to exploit existing approaches from the literature to modulate the stiffness collagen scaffolds, specifically photocrosslinking native collagen directly with visible light and flavin mononucleotide and generating methacrylated collagen via derivatization with methacrylic anhydride, as well as the problems associated with these approaches. Extensive experimentation with these methods led to determination that existing methods were not adequate for our desired applications, and motivated development of a simple yet efficacious method for generating photosensitive collagen methacrylamide. Optimization of this novel synthesis method as well as a thorough characterization of the resultant material using a variety of experimental modalities is presented in Chapter 2. Chapter 3 investigates the use of photosensitive synthetic polymers in conjunction with our collagen

based material and discusses the salient mechanical and biological advantages and disadvantages discovered thereupon. Chapter 4, I describe our screening of a variety of stem cell types for biocompatibility with the photocrosslinking process, which indicated a number of limitations for certain applications. Extended studies with the more robust cells detail specific applications and the constraints which arose from their implementation. In Chapter 5, I review our efforts aimed at using *in silico* molecular models of native collagen and collagen methacrylamide to help understand some of the unexpected material properties observed during characterization and experimentation with collagen methacrylamide, and how these properties might present opportunities for new applications of the material. Finally, in Chapter 6, I summarize our findings and conclusions and place our results in context with other photoactive materials, particularly the previous attempts at photocrosslinking type I collagen. I also discuss future directions for the research and material from both basic science and translation research perspectives.

2. Chapter 2: Prelude: Collagen Photocrosslinking Approaches from Literature

2.1 Introduction

Initial studies attempted to employ published methods of photocrosslinking collagen to create photonicallly induced stiffness gradients that could be used to guide neurite outgrowth, with potential applications in augmenting regeneration in the injured nervous system. Previous work showed that stiffness gradients can be used to control cellular behavior [50,51]. In our laboratory, Sundararaghavan et al., created durotactic gradients using microfluidic devices and showed that sensory neurite outgrowth from embryonic chicken dorsal root ganglia (DRG) was modulated to preferentially grow along a 1-dimensional gradient of decreasing stiffness in a 3-dimensional gel [52]. While this finding was exciting from a mechanistic viewpoint of innate neural regeneration and the implications for exploiting this phenomenon as a tool to regenerate nervous tissue injury, the system was not easily adaptable for clinical use given the constraints of creating these gradients in a microfluidic device. To exploit this phenomenon with a more translatable platform, we hypothesized that using light and a photoinitiator to catalyze crosslinking of collagen gels would allow formation of gradients in a more non-invasive way. Several promising approaches were found in the literature that were or could be employed light induced crosslinking of Type-I collagen. In particular, two approaches were chosen based on their published findings: (1) Using riboflavin to directly photocrosslink collagen [17], and (2) modifying collagen by derivatizing it with reactive acrylate or methacrylate groups and using a photoinitiator to catalyze photocrosslinking [20,18]. These published methods indicated that light could be used to modulate the mechanical properties of type-I collagen, and that control of the incident light exposure could be used to impart variable stiffness to the resulting scaffold.

2.2 Flavin Mononucleotide Mediated Photocrosslinking

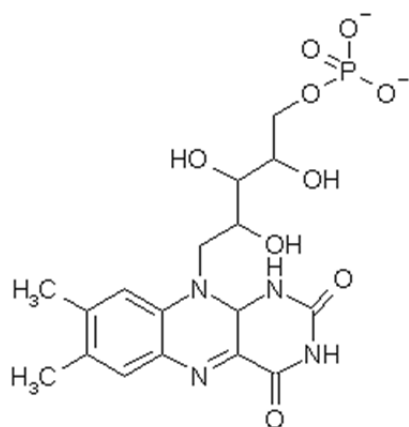


Figure 2-87: Structure of FMN

Flavin-mononucleotide (FMN, Figure 2-1) is a naturally occurring biomolecule involved in cellular metabolism via the electron transport chain [53]. FMN is also found in plants as a blue light-absorbing chromophore involved in the photosynthesis pathway [54]. FMN has also been used as a photoinitiator for the photocrosslinking of collagen gels and films [55,56].

Based on the results from Ibusuki et al., we attempted to use FMN to crosslink type-I bovine collagen using visible light. Using rotational rheometry, we characterized the mechanical properties of collagen hydrogels photocrosslinked with a range of FMN concentrations, light exposure times, and light intensity. We also examined the effect on cells encapsulated within gels to determine if the photocrosslinking process was compatible. Cytotoxicity was determined using live/dead staining and MTS assays. Finally, we looked at whether cytotoxicity could be mitigated using antioxidants.

2.3 Methods

2.3.1 *Collagen Stock Solution*

Acid soluble Bovine type I collagen from calf skin (Elastin Products Company, Owensville, MO) was dissolved in 0.02M acetic acid overnight at concentrations from 2-5mg/mL for stock solutions. Briefly, weighed masses of lyophilized collagen were mixed with the appropriate

volume of acetic acid in a 50mL conical tube and rotated at a moderate pace at 4°C. Solutions were then degassed under vacuum to remove air bubbles and finally stored at 4°C until further use.

2.3.2 *Collagen Gels*

For FMN crosslinking studies, collagen stock solution was brought to physiological pH and osmolality on ice in 1 mL batches. Typically, 677 μ L stock solution (3mg/mL) was added to a precursor solution composed of 20 μ L 50X HEPES, 140 μ L 0.1N NaOH, 100 μ L 10X MEM, 52 μ L 1X PBS or M199, 10 μ L L-Glutamine, and 1 μ L Penicillin/Streptomycin. For conditions where FMN was added to the precursor solution, FMN (Riboflavin 5' monophosphate sodium, Sigma) was dissolved in the 10X MEM solution prior to mixing. Initially, aliquots of 800 μ L were then dispensed into annular PDMS molds with an inner diameter of 25mm that were contact-sealed onto the inner surface of 35mm polystyrene Petri dishes. The method was later changed to form gels on 2" x2" glass slides with the PDMS ring contact molded on the surface of the glass to simplify transferring the gel to the rheometer. Molded solutions were then placed into a humidified incubator at 37°C and allowed to gel. Culture medium or 1x PBS was then added on top of the gels to maintain hydration, and the gels were returned to the incubator for at least an hour

2.3.3 *Photocrosslinking*

FMN forms free radicals following absorption of long-wave ultraviolet (UVA) and blue light, with radical generation reportedly dependent on light wavelength [57]. In the presence of oxygen, reactive oxygen species (ROS) are formed, which are believed to catalyze the formation of crosslinks between amino acid side chains on adjacent collagen molecules through the formation of covalent bonds such as the Schiff base [56,58,59] (see Figure 2-2). The final

concentrations of FMN ranged from 0.1-1mM, and light exposure times varied from 0-600s. Visible light irradiation of collagen solutions and gels to initiate photocrosslinking was performed

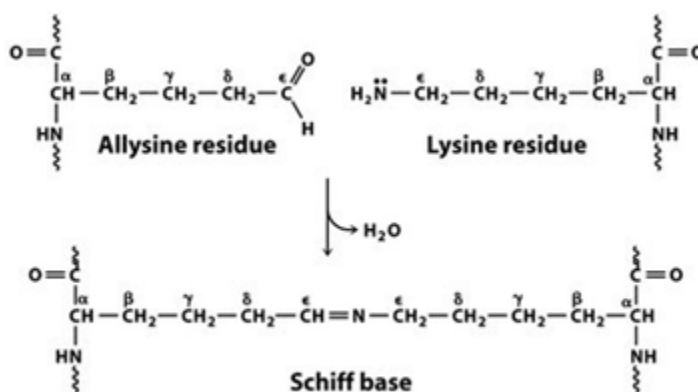


Figure 2-2: Schiff Base Formation

with a Nikon Intensilight with the

iris shutter set at 1/8 and with an

EXFO Mercury Bulb connected to a fiber optic light guide with a rectangular light diffuser. Irradiance of white light was ~ 0.5 and $5\text{mW}/\text{cm}^2$ with the Intensilight and the EXFO source, respectively. UVA light was provided by a UVL-21 (Industrial UV Products, Upland, CA), with irradiance measured at $4\text{-}8\text{mW}/\text{cm}^2$. Light sources were positioned above samples at a distance of 1cm or directly underneath samples with the polystyrene dish between the sample and the light source. Printed masks were used to modulate the incident light intensity. Adobe Photoshop was used to create variable transparency masks with 0-100% opacity, which were used to control bulk crosslinking as well as to impart gradient exposure and, theoretically, gradient crosslinking. Masks were printed on overhead projector transparencies using a 600dpi laser printer.

2.3.4 Light Intensity Measurement

Light source irradiance was measured using a PDA10A silicon photodetector (Thorlabs, Newton NJ) connected in parallel across a 1 k Ω resistor to a multimeter. Current from light converted through the silicon detector element was read as a voltage on the multimeter, which was then used to calculate the power of the incident light according to the equation:

$$\text{Power} = \text{Voltage} / (\text{Resistance} * F)$$

where F is an empirically derived spectral responsivity that depends on the wavelength of the incident light, provided with the photodetector as a plot of F vs λ (Figure 2-3).

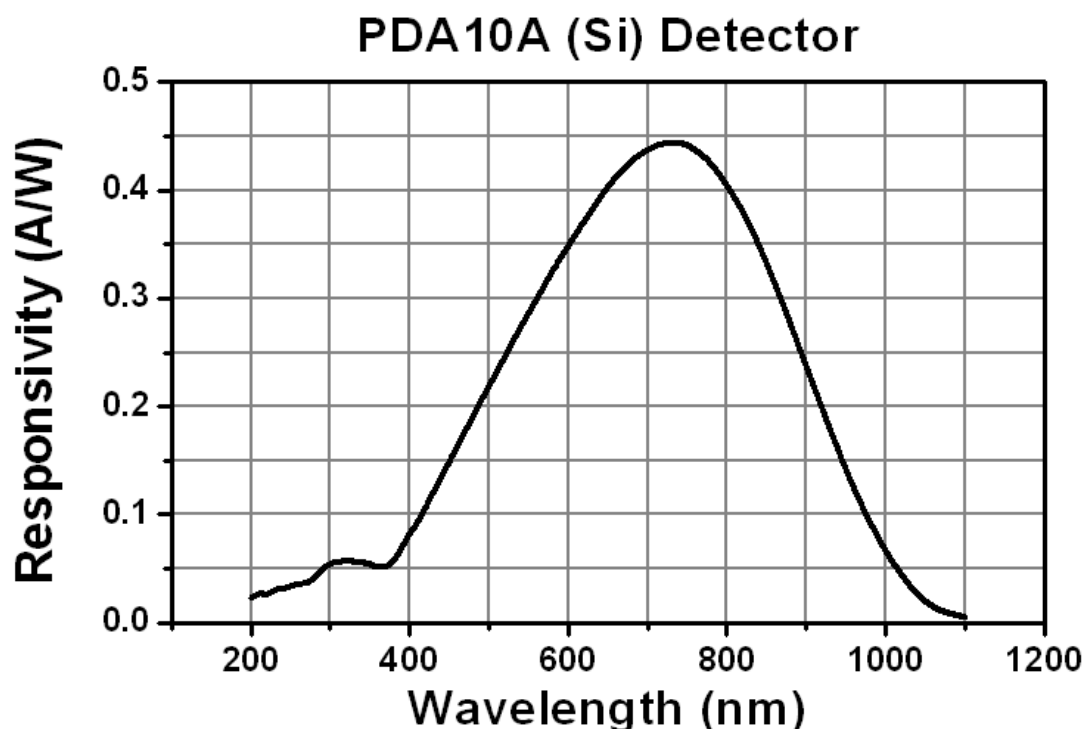


Figure 2-3: Spectral Responsivity of PDA10A Photodetector. Source: http://www.thorlabs.com/images/TabImages/PDA10A_response_large.gif

The irradiance was calculated by dividing the power by the area of the silicon element, 0.8mm^2 in this case, to give irradiance in units of W/cm^2 . Irradiance was measured in each experiment to ensure light intensity remained consistent.

2.3.5 Rotational Rheometry

Gels were gently transferred onto on the lower parallel plate of a Rheometrics SR-2000 rotational rheometer. A 20mm upper parallel plate was lowered until the gel was sandwiched between the plates at a gap of $750\text{-}800\mu\text{m}$. Excess water was removed, and gels were

equilibrated to 37°C using a Peltier plate connected to a circulating water/ethylene glycol bath. Following temperature equilibration, gels were oscillated at 1% strain in an increasing frequency sweep mode from 0.08Hz-10rad/s, and the storage and loss moduli were recorded.

2.3.6 Cell Culture

Mouse NIH-3T3 fibroblasts were grown on tissue culture treated polystyrene flasks in humidified 37°C incubators containing 5% CO₂. Culture medium was complete medium (DMEM, 10% FBS, 2mM L-glutamine, 1X P/S), sterile filtered. Cells were routinely passaged using 0.25% Trypsin with EDTA when cultures reached 90% confluence. Following detachment with trypsin, cells were washed with complete medium to inhibit trypsin, centrifuged for 2 minutes at 2000RPM, and resuspended in media for either re-plating or use in experiments.

Chicken dorsal root ganglia (DRG) were harvested from embryonic day 8 chicks. Briefly, chick embryos were decapitated, skin and internal organs removed using #5 fine tip forceps, and limbs were bluntly dissected away from the spinal cord to reveal rows of DRG, which were then transferred via the PNS-side tail to a dish containing HBSS on ice. DRG were cultured intact in collagen gels, with a growth medium comprising complete medium plus 50ng/mL NGF.

2.3.7 Cytotoxicity Testing

To test the cytotoxicity of FMN-derived radicals directly on cells, cells were plated on polystyrene microplates, cultured in complete medium until 80-90% confluent, and then media was changed to include various concentrations of FMN. Samples were then exposed to light from the various sources for variable amounts of time.

To examine the cytocompatibility of FMN-mediated crosslinking with encapsulated cells, mouse NIH-3T3 fibroblasts were admixed with the 52μL M199 volume of the precursor solution and

distributed into the gels, which were prepared as above. Following irradiation with and without the presence of FMN, complete medium was added to the cell-encapsulated gels and they were allowed to culture in a humidified incubator at 37°C with 5% CO₂ for 24-48 hours. Following the culture period, cellular viability was assessed via standard live/dead staining assay and/or the MTS assay.

2.3.8 *Live/Dead Assay*

Live/Dead staining was adapted from the protocol that accompanies the documentation in the Invitrogen Live/Dead Viability/Cytotoxicity Kit for Mammalian Cells (Life Technologies). Following incubation, culture medium was removed, and samples were washed once with PBS. Live/Dead stain (PBS containing calcein acetomethoxy (calcein-AM, 2µM) and ethidium homodimer (EthD, 4µM) was added to cells and incubated at 37°C for 45 minutes to allow staining and then immediately imaged using an Olympus IX81 epifluorescent microscope. Calcein-AM is a membrane-permeant molecule that is cleaved by endogenous esterases in live cells. The cleaved calcein, which cannot exit live cells, is highly fluorescent and can be seen with a standard green fluorescence filter set (494nm excitation, 517nm emission). Ethidium Homodimer is a membrane-impermeant nucleic acid stain that only enters dead cells, which lack membrane integrity. When EthD binds to DNA, it increases its fluorescence 40-fold, and can be seen under standard red fluorescence (528nm excitation, 617nm emission). Thus, cells that stain green are counted as “live” whereas cells with red nuclei are counted as “dead”. Percent viability is then calculated as (number of live cells/(number live cells + number dead cells)) x 100. For 3-D culture experiments, viability was estimated semi-quantitatively due to difficulty counting cells due to overlapping fluorescence in adjacent focal planes.

2.3.9 *Antioxidants*

Two antioxidants were tested to determine if they could mitigate free-radical induced cell death observed as a by-product of photocrosslinking. Ascorbic acid, [L-Ascorbic Acid (LAA) and Ascorbic Acid 2-phosphate sesquimagnesium salt hydrate (AAS)], and reduced L-glutathione (GSH) were added to encapsulated gels after photocrosslinking. Concentrations ranged from 5 μ M-5mM.

2.4 Results

2.4.1 Rheometry

Frequency sweep tests showed that crosslinking collagen gels with 1mM FMN and the low-power Intensilight resulted in a slight increase in the storage modulus of the gels. A different light source, the EXFO lamp, with a rectangular fiber optic light guide, resulted in a modest increase in storage modulus.

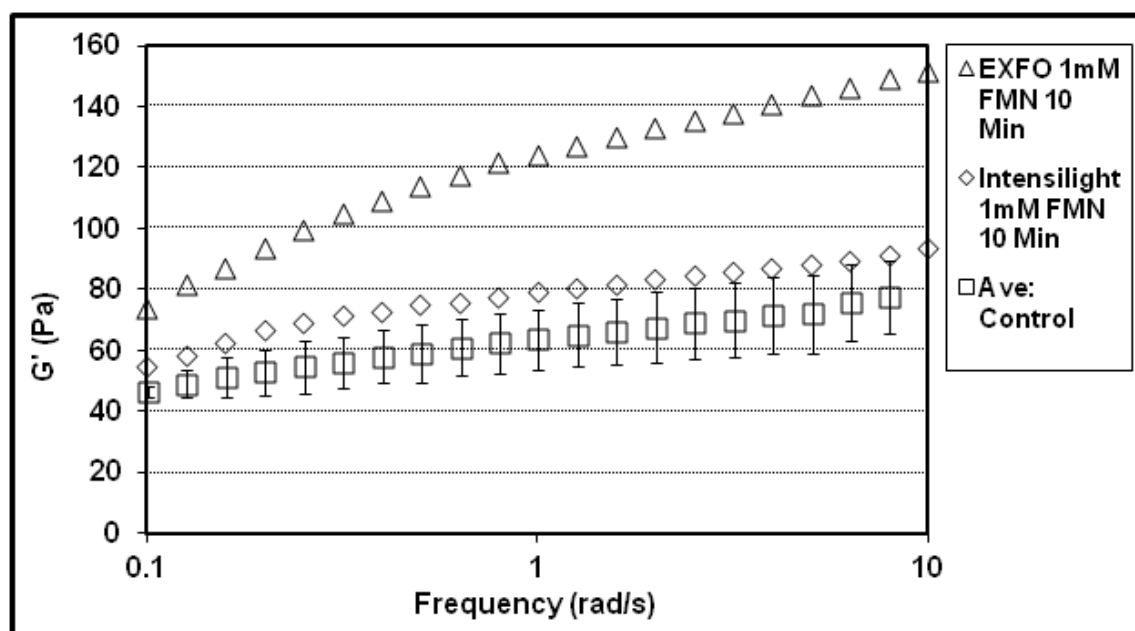


Figure 2-4: Frequency sweep of storage modulus of collagen crosslinked by FMN using different light sources

Further experiments which varied experimental parameters indicated that reducing FMN concentration increased photocrosslinking effectiveness. In addition, it was discovered that if the collagen solution was irradiated in the liquid phase, prior to gelation, then allowed to gel, the modulus was increased significantly higher than exposure after gel equilibration. These process changes are evident in Figure 2-5, which displays the increase in storage modulus obtained via photocrosslinking liquid collagen with an FMN concentration at 0.2mM.

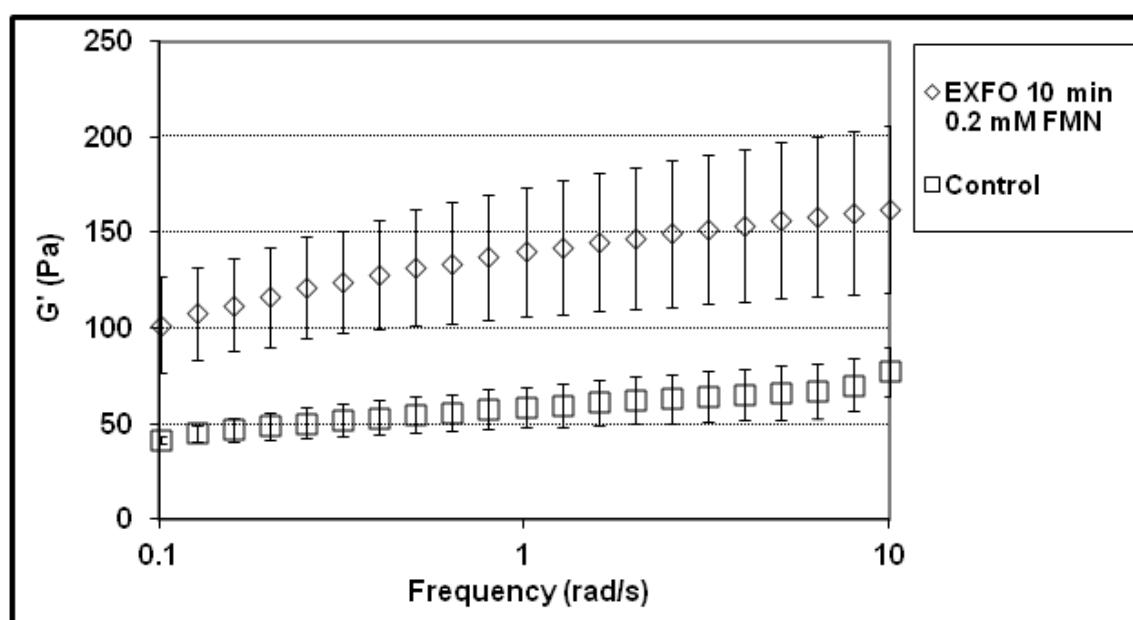


Figure 2-5: Frequency sweep of storage modulus of collagen crosslinked with FMN in the liquid phase prior to gelation

Using alternate light sources, it was determined 5 minutes of long-wave UV (UVA) light exposure at an FMN concentration of 0.1mM in the liquid phase yielded the best increase in storage modulus, nearly two-fold. Loss modulus was not significantly altered when compared to control collagen.

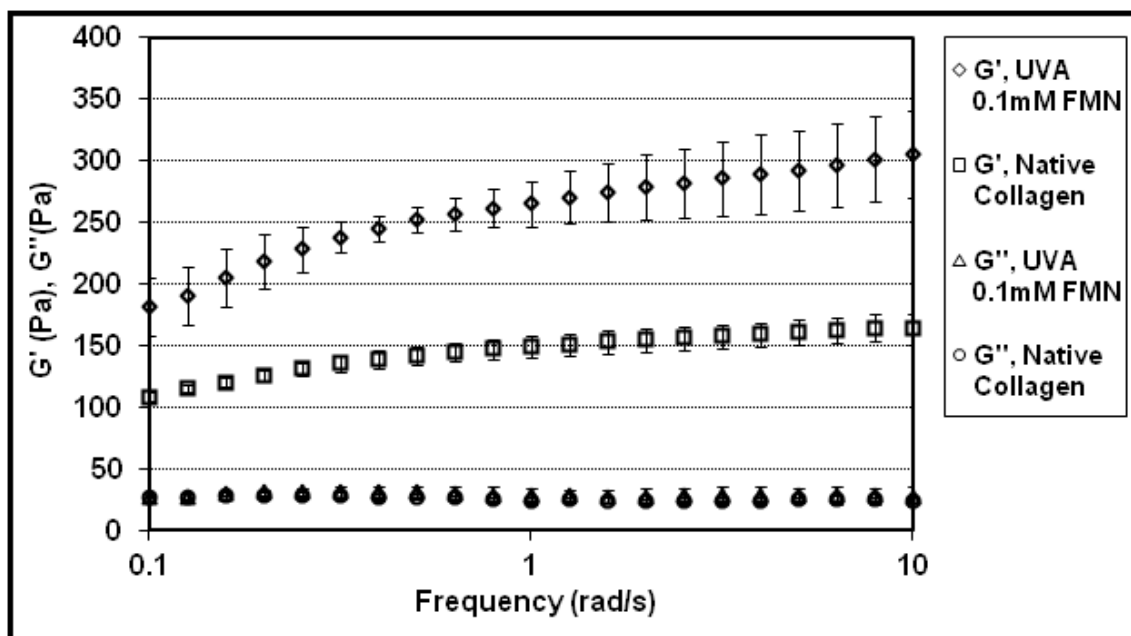


Figure 2-6: Frequency sweep of storage and loss moduli of liquid phase collagen crosslinked with FMN using longwave UV light

Indeed, in comparison with crosslinking collagen using 1mM genipin exposure for 24 hours, which our lab has shown resulted in biologically relevant modulation of the mechanical properties, 5 minutes of UVA exposure with 0.1mM FMN obtained nearly the same increase in storage modulus.

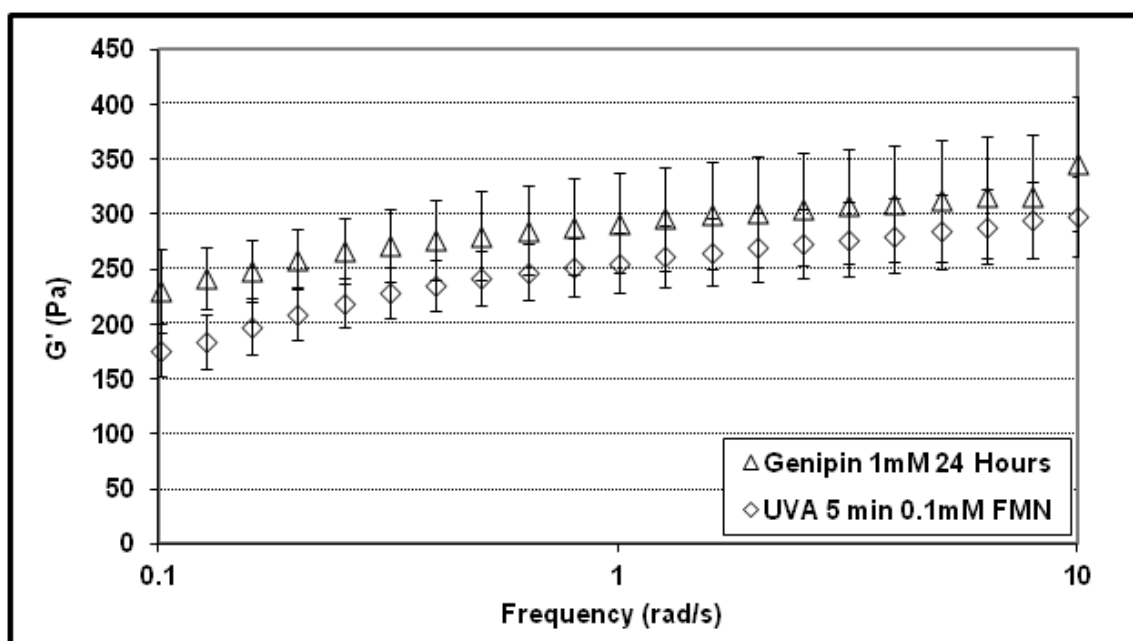


Figure 2-7: Frequency sweep of collagen gels photocrosslinked with FMN compared to 0.1mM Genipin crosslinking

FMN was also tested to see if it could be used to photocrosslink fibrin gels. Fibrinogen (10mg/mL) was dissolved in PBS without calcium or magnesium, cleaved using 1U/mL thrombin, and allowed to gel at 37°C in the incubator for 30min. To strengthen gels, 10mM calcium chloride was added to the thrombin solution. FMN (0.1mM) was included in a separate set of samples, also dissolved in the thrombin solution, and the gels were exposed to UVA for 5 minutes. One sample was not exposed to UV so serve as a control for FMN alone. All samples were tested on the rheometer in a similar mode to the collagen gels. Rheological analysis showed that FMN photocrosslinking was able to robustly increase the storage modulus of the fibrin gels more than 4-fold, although the effect was less pronounced at higher strain frequencies. In comparison, exogenous calcium addition increased G' by just over two-fold.

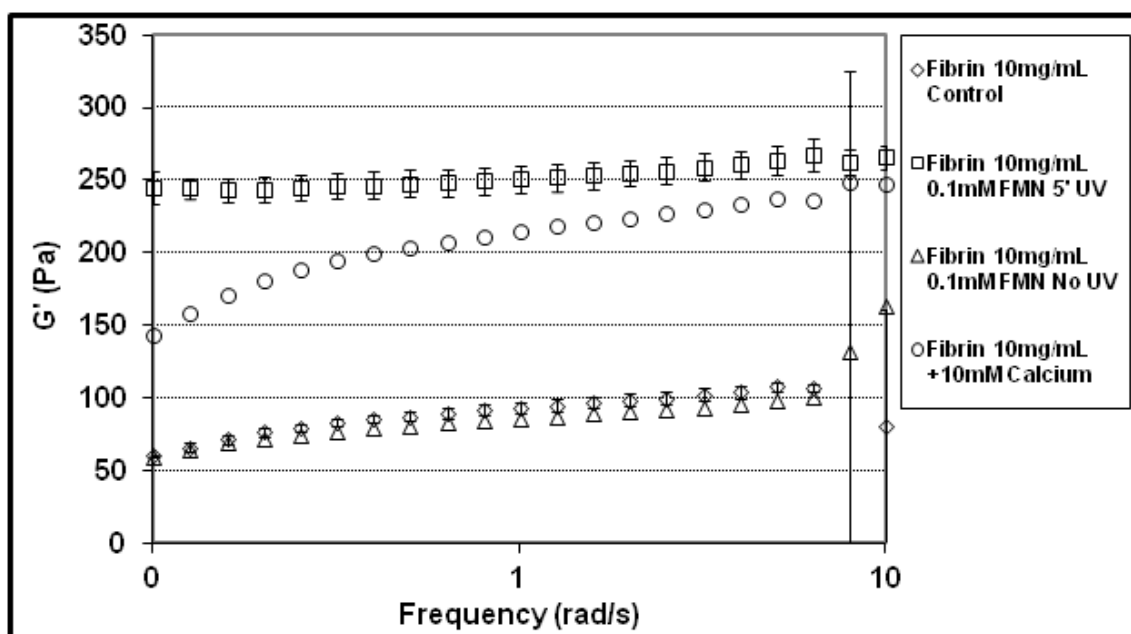


Figure 2-8: Fibrin 10mg/mL Rheometry: Effect of FMN X-linking and Exogenous Calcium

2.4.2 Light intensity Modulation via Masking

Masks on printed transparencies were placed in between the UV light source and the bottom of sample containers to impart variable light exposure. To test whether the mask successfully modulated the light exposure, we measured the irradiance of light masked with solid black filters of variable opacity. The result was an inversely linear dependence of light intensity on opacity.

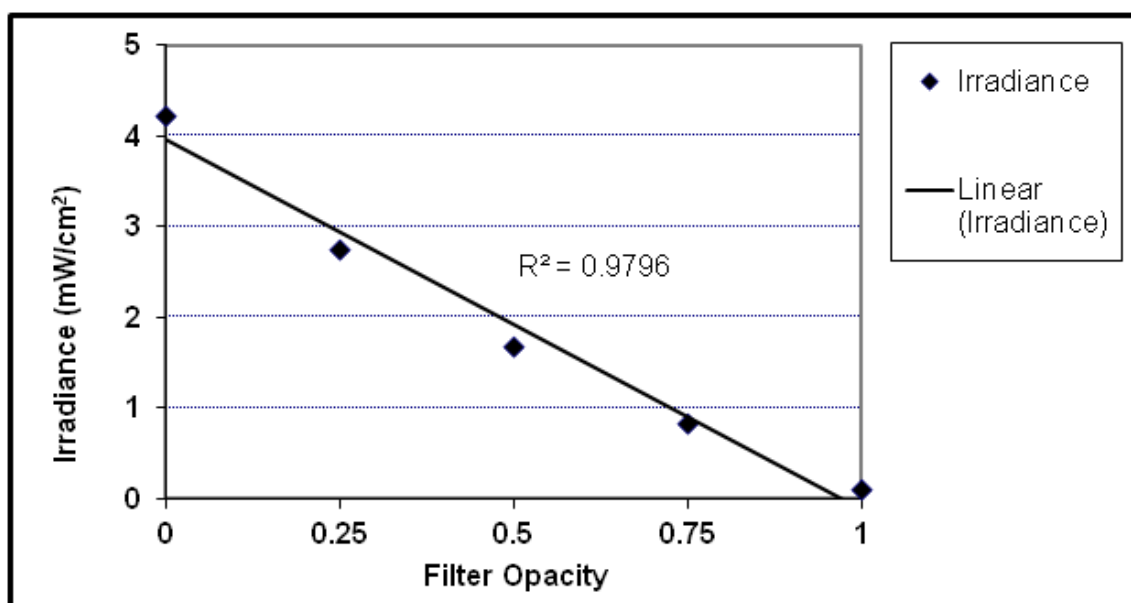


Figure 2-9: Modulation of light intensity using opacity filters

2.4.3 Cytotoxicity

Initial studies were carried out to assess the toxicity of FMN on NIH-3T3 fibroblasts with and without exposure to light. Culture medium with 0, 0.25, 0.5, and 1mM FMN was added to cells and then samples were exposed to 0 or 10 minutes of light from the EXFO source. After 24h, live/dead staining was performed to assess viability. For all three concentrations of FMN, viability was dependent on light exposure, i.e., 100% of cells died as evidenced by ubiquitous nuclear EthD staining. In contrast, cells exposed to either FMN or light, but not both, were near 100% viable as seen by calcein staining. Hence, FMN appears to be highly cytotoxic at these concentrations if light is exposed.

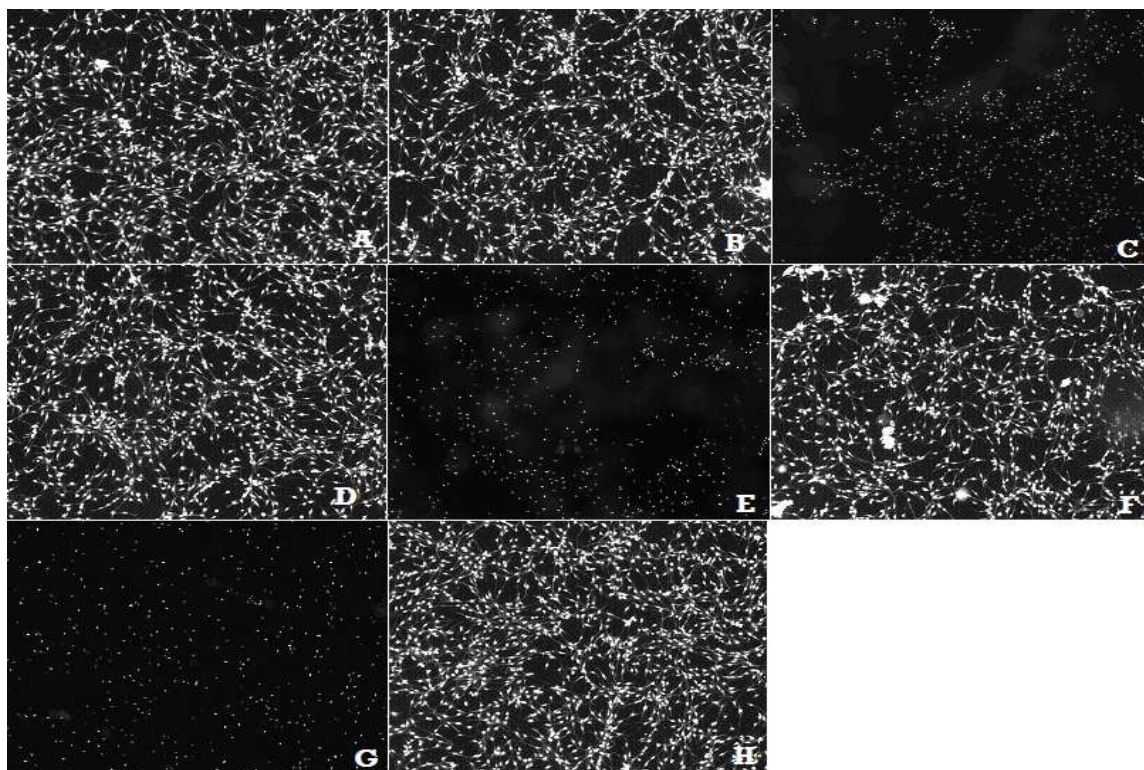


Figure 2-10 Cytotoxicity of FMN on NIH3T3: A, B, D, F, H: Calcein C, E, G: Ethidium. A- No FMN, +10min Exp; B- No FMN, No Exp, C- 0.25mM FMN, +10min Exp; D- 0.25mM FMN, No Exp, E- 0.5mM FMN, +10min Exp; F- 0.5mM FMN, No Exp, G- 1mM FMN, +10min Exp; H- 1mM FMN, No Exp

Further testing with 3T3s encapsulated in collagen, with and without 0.2mM FMN, and exposed to 2-5 minutes visible light showed that even at low exposure times (corresponding to minimal increases in storage modulus) there was pronounced toxicity (Figure 2-11).

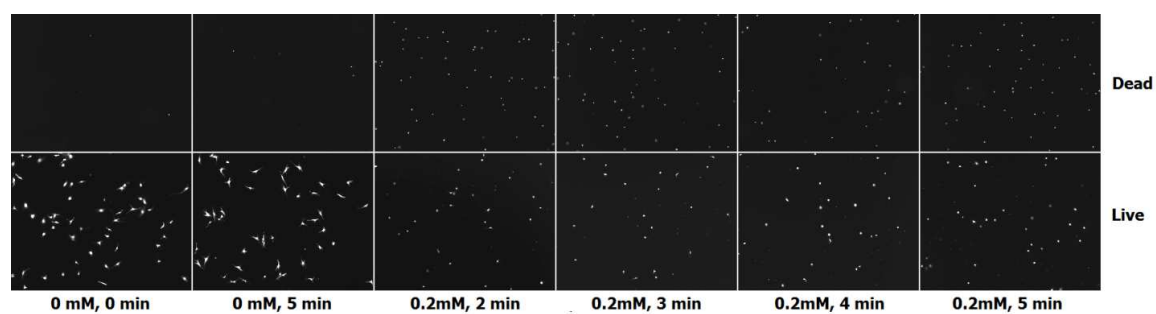


Figure 2-88: FMN Cytotoxicity on Encapsulated 3T3 Fibroblasts

To test the cytotoxicity of UVA activation of 0.1mM FMN, which was shown to have a significant effect on mechanical properties via rheometry, 3T3 fibroblasts were suspended in collagen with FMN, exposed to UVA for 5 or 10 minutes during the liquid phase, and then allowed to gel and culture for 24 hours. Both 5 and 10 minute exposures largely killed most cells as compared to control cells that were exposed to neither FMN nor light (Figure 2-12). However, the 5 minute exposure conditions had marginally more viable cells, and the cells that survived appeared to extend more robust processes than the cells exposed for 10 minutes.

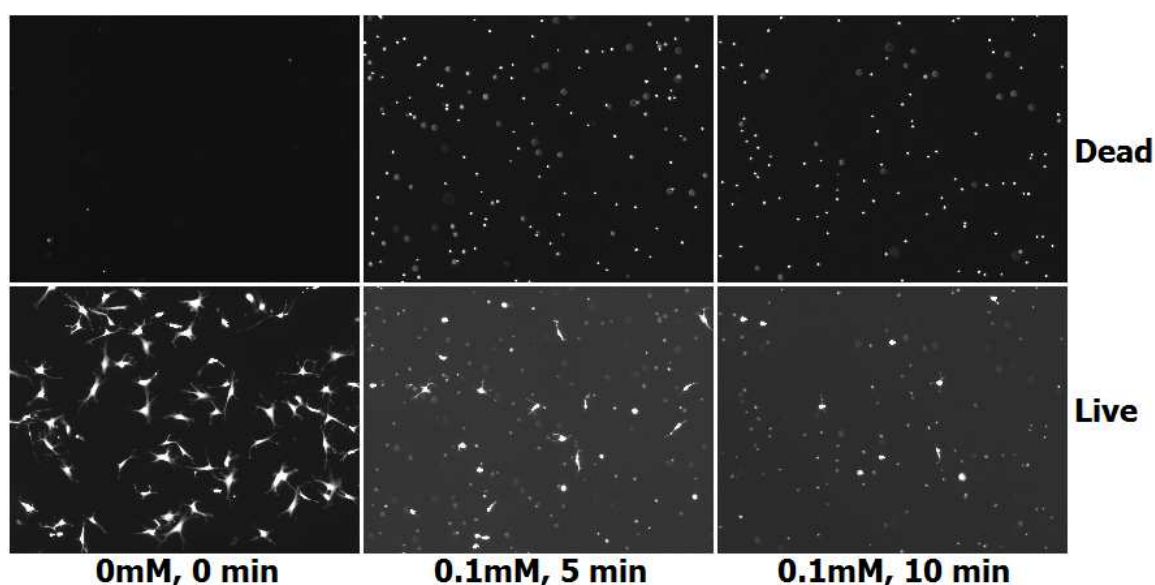


Figure 2-89: Cytotoxicity of Encapsulated 3T3 Fibroblasts in collagen crosslinked by 0.1mM FMN

Due to the incompatibility of the photocrosslinking process with live cells, we sought to investigate if free radical scavengers could be used to mitigate the observed cytotoxicity. We tested 2 well-characterized antioxidant agents, Ascorbic acid and Glutathione, to see if their presence before and/or after the photocrosslinking process had a beneficial effect on viability.

Ascorbic Acid was tested in 2 forms, LAA and AAS, with a standard “cytotoxic” crosslinking regime of 5 minutes UVA crosslinking with 0.2mM FMN, which normally produced ~95% cell death. LAA was added to the medium that was used directly after crosslinking and 45 minutes of gelation. In this case, LAA had no discernible effect at any dose, and viability was not improved by its inclusion as compared to negative controls.

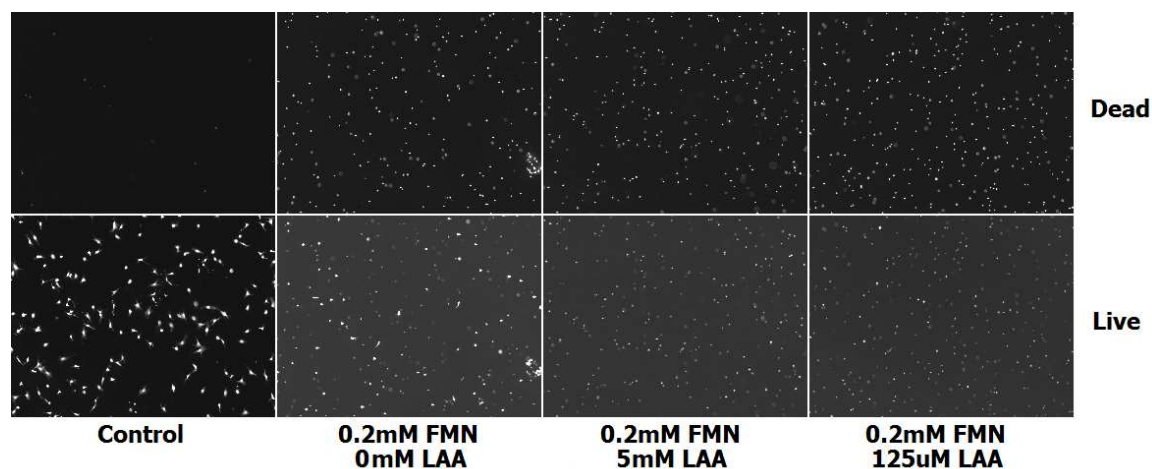


Figure 2-90: LAA effect on post-photocrosslinking viability

Another form of ascorbic acid, AAS, was tested in a similar manner, mixed into the medium that was added to the cell-encapsulated gels following crosslinking. AAS concentrations ranged from 5-125 μ M. Positive and negative control conditions were included for comparison. Here, a low, 5 μ m, dose of AAS, resulted in the rescue of ~5-10% viability compared to the crosslinked control condition. Ascending concentrations had a decreased effectiveness, with no benefit seen at 125 μ M.

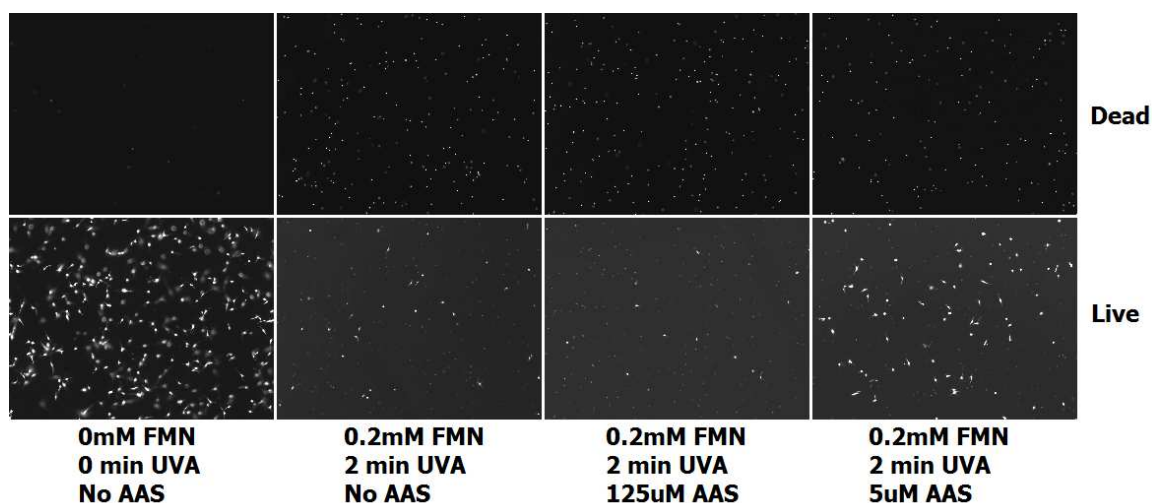


Figure 2-91: AAS effect on post-photocrosslinking viability

Glutathione, the oxidizing agent in the glutathione reductase enzymatic pathway involved in metabolism of reactive oxygen species, was also tested as a potential strategy for scavenging radicals. L-glutathione (GSH) was tested at 0.125-10mM. Again, FMN was kept at 0.2mM and light exposure was 5 minutes of UVA, with appropriate controls. A minor beneficial effect was also observed, with a broad range of GSH concentration conferring a similar benefit of ~5% increased viability.

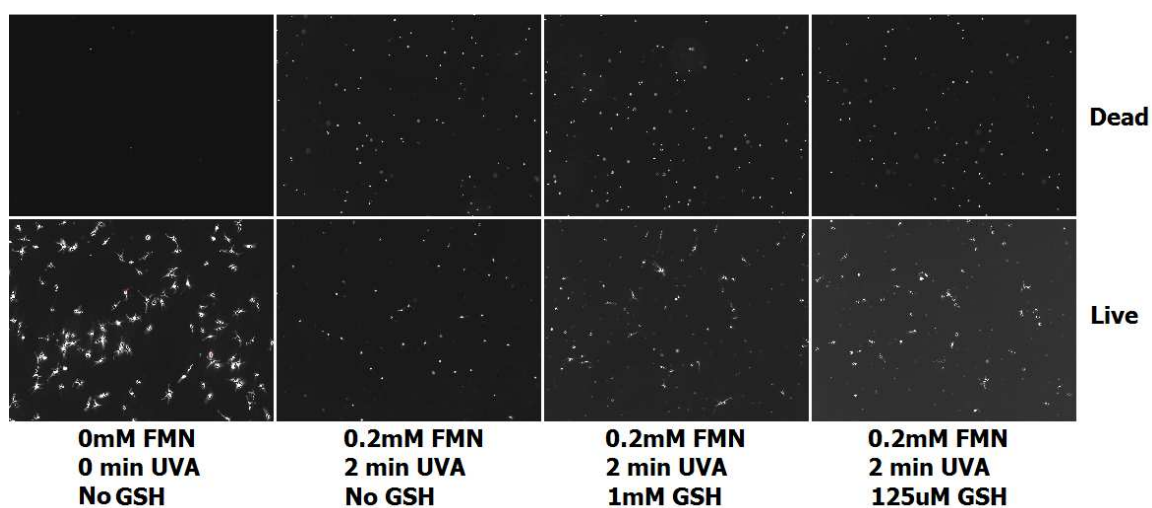


Figure 2-92: GSH effect on post-photocrosslinking viability

As the effect of both AAS and GSH were measurable but inadequate at restoring viability to acceptable levels, a combination of both was tested to determine if they would act additively or possibly synergistically. Using the same 0.2mM FMN, 5 minute UVA crosslinking paradigm, 5 μ M AAS was combined with 5, 50, and 500 μ M GSH. The antioxidant cocktail was again included in the medium added immediately following the gelation period. The most profound effect was seen with 5 μ M AAS plus 50 μ M - 5 mM GSH, where roughly 40-50% of cells were viable, whereas 5 μ M of each antioxidant produced only a 5-10% increase.

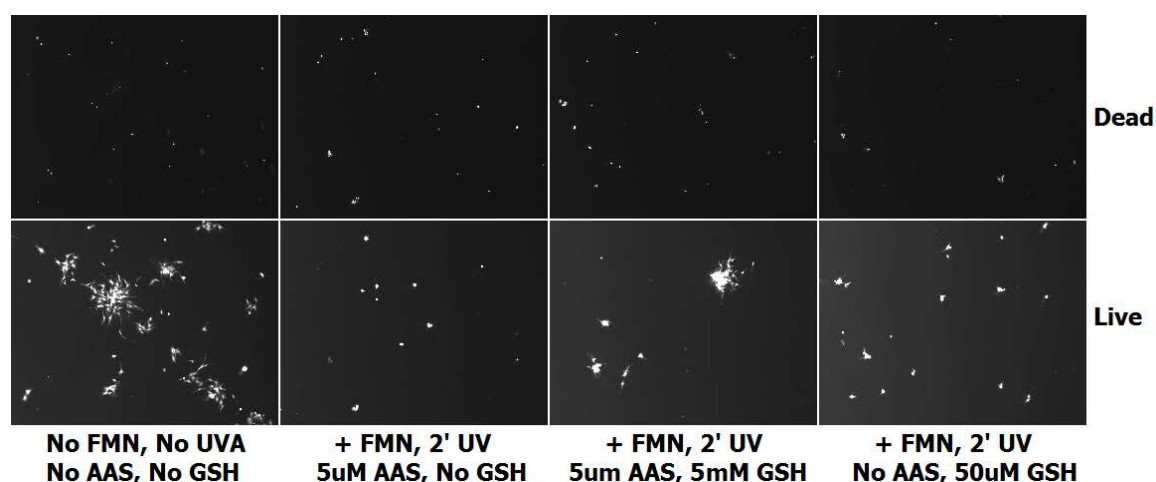


Figure 2-93: Effect of AAS + GSH on post-photocrosslinking viability

FMN photocrosslinking was also performed with chick DRG encapsulated in collagen gels. DRG were harvested from E8 chicks, immediately plated in collagen with 0.2mM FMN and exposed to UVA for 5 minutes. Following gelation, 5 days of culture in complete medium plus NGF, fixation, and staining for neurofilament-200, DRG were imaged to examine whether neurite outgrowth had taken place in the photocrosslinked collagen. Indeed, the FMN photocrosslinking process had no apparent effect on DRG viability or neurite outgrowth. Representative images, shown in

Figure 2-17, show equivalent morphology in terms of neurite number and outgrowth between DRG in uncrosslinked and crosslinked gels.

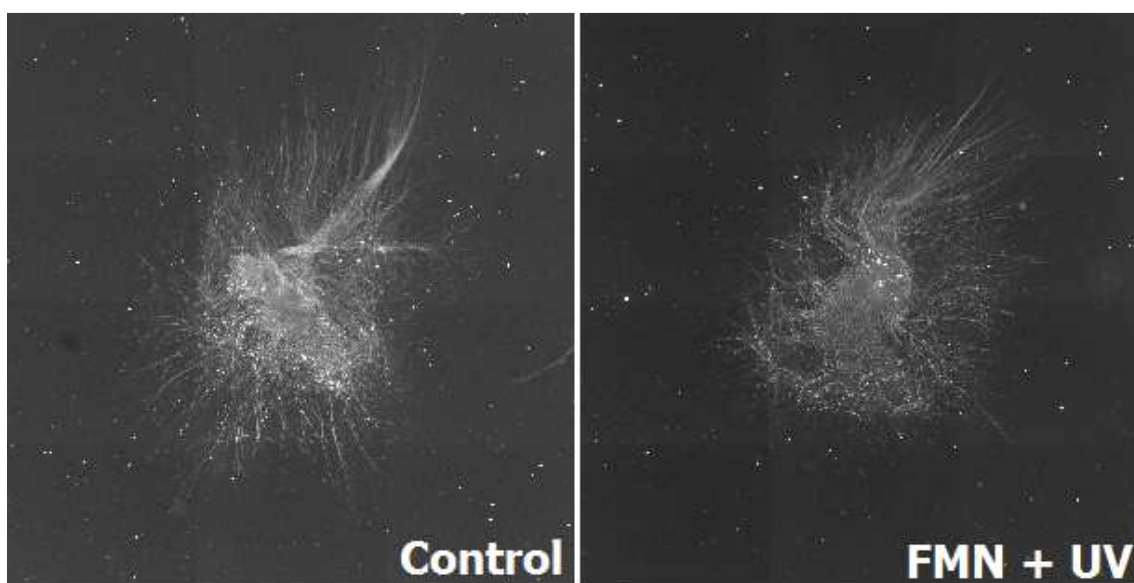


Figure 2-94: DRG encapsulated in collagen gels +/- FMN photocrosslinking

2.4.5 Fibrin Photocrosslinking with Encapsulated Cells

3T3 fibroblasts at concentrations from 4×10^4 – 1.4×10^6 cells/mL were encapsulated in fibrin gels and photocrosslinked to determine the effect of cell density on post-crosslinking viability. Briefly, cells in complete medium were admixed with an equal volume of fibrinogen (10mg/mL), and thrombin (10U final) and FMN a final concentration OF 0.1mM was included. Gels were allowed to form for 10 minutes at 37°C and then exposed to 5 minutes of UVA. Following exposure, medium was added to the gels and they were returned to the incubator for 24 hours prior to live dead staining. As seen in Figure 2-18, it appears that there is a direct positive correlation between cell concentration and post crosslinking viability.

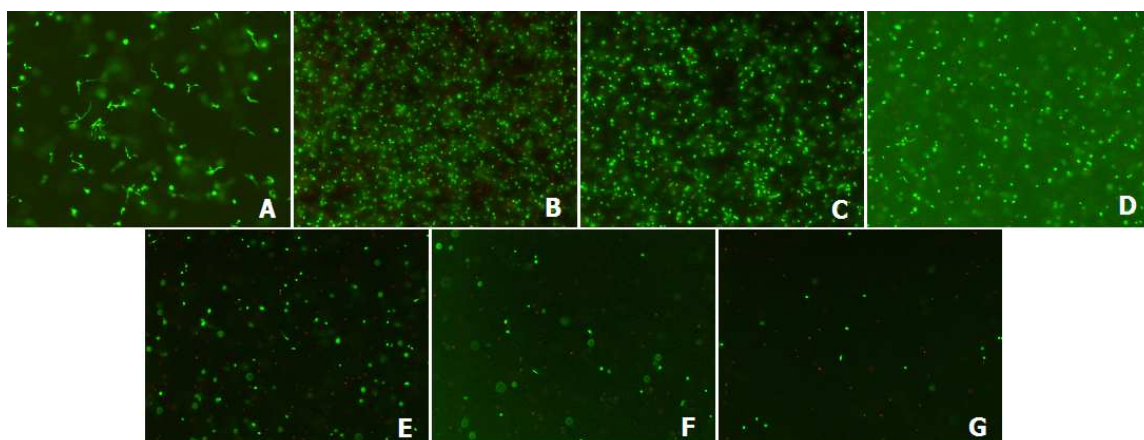


Figure 2-95: Effect of 3T3 Concentration in FMN Photocrosslinked Fibrin gels. A- Control (No FMN, UVA) 4×10^4 cells/mL; B- Crosslinked 1.4×10^6 cells/mL; C- Crosslinked 7×10^5 cells/mL; D- Crosslinked 3.4×10^5 cells/mL; E- Crosslinked 1.7×10^5 cells/mL; F- Crosslinked 8×10^4 cells/mL; G- Crosslinked 4×10^4 cells/mL;

Another factor that was tested with fibrin gels was time after photocrosslinking and gelation until medium addition. Fibrin gels with a high density of cells, NSC-34 in this case, were cast, crosslinked, and then medium was added 5, 10, 15, 20, 25, 35, or 45 minutes following 10 minutes allowed for gelation/FMN crosslinking. Here we observed that cells in gels where medium was added more than 30 minutes after gelation had a significant drop-off in viability.

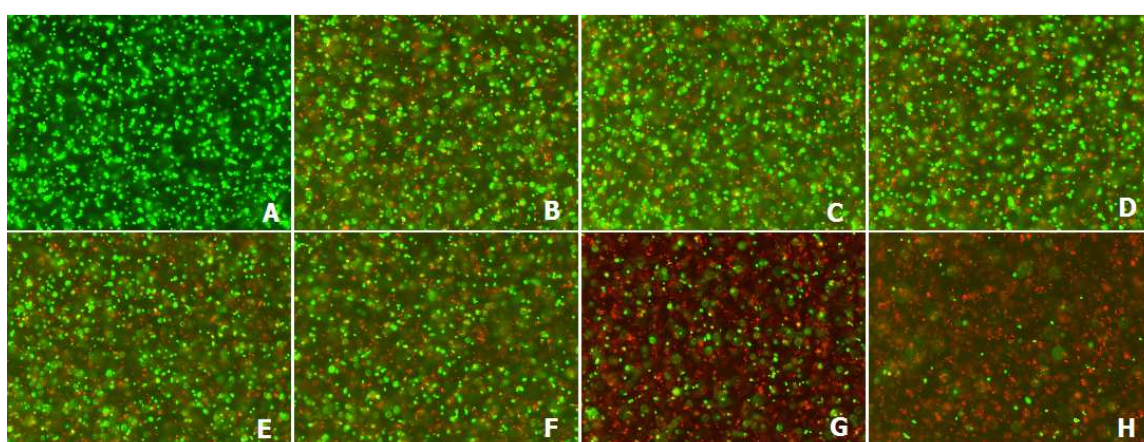


Figure 2-96: Effect of time of medium addition on post-crosslink viability. A- Control; B- 5min; C- 10min; D- 15min; E- 20min; F- 25min; G- 35min; H- 45min.

2.5 Discussion: FMN Photocrosslinking

Previously published work indicated that FMN could be used to modulate the mechanical properties of collagen gels. Our attempts to replicate these results were minimally successful in cases where the collagen was allowed to gel fully before light was applied. It appeared that regardless of light source or intensity, and across all tested concentration of FMN, crosslinking the liquid macromer solution on ice and then allowing self assembly resulted in much more robust changes in rheological properties than when crosslinking was attempted after self-assembly. The mechanism by which this occurs was unclear, but may be due to the availability of crosslinkable side chains which, in the liquid phase were available due to the mobility of the molecules in solution and that may have been physically constrained after self-assembly such that the distance between reactive groups was too far for FMN mediated crosslinking to have a significant effect. It was clear that the source of light was an important factor in achieving useful levels of crosslinking. Although FMN has absorption peaks in the visible range, the radicals that resulted from UV-based photoinitiation may be of higher energy and thus are able to catalyze a broader range of crosslinking reactions. Our results indicated that the most robust crosslinking resulted from using a low concentration, 0.1mM, of FMN with exposure to UVA for 5 minutes. We were thus successful in developing a process that allowed significant mechanical modulation of collagen gels, equivalent in magnitude to the change in mechanical stiffness resultant from 24 hour exposure to the chemical crosslinker genipin at 1mM. Previous work in our lab showed that neuronal cells were able to sense stiffness changes in this range, and that introducing gradients of stiffness could be used to preferentially direct neurite outgrowth. Attempts to replicate this phenomenon using FMN-crosslinked gels were unsuccessful. While DRG were able to survive the photocrosslinking process and extend neurites into FMN-crosslinked gels, we saw no preferential growth due to variable mechanical properties. Given that the crosslinking was

performed in the liquid phase, it is likely that any gradients in crosslinking formed were distorted after self assembly. Indeed, bulk flow of collagen was difficult to prevent in transferring gels into the incubator following crosslinking. Another possibility for the lack of differential neurite outgrowth observed may be due to the mechanism of crosslinking. If individual tropocollagen molecules are forming intra-fibril crosslinks, but there are no interfibril crosslinks, then the bulk properties of the gel might be changed, as seen by our rheology data, but the modulus may be minimally changed at the individual fibril level, thus neurites may not be able to sense a difference in stiffness at that scale. More experiments where the collagen was more constrained during the gelation phase might be useful for determining a lack of effect.

Another detriment to this method is the significant cytotoxic effect observed for encapsulated single cells. While DRG are large clusters of hundreds-to-thousands of cells, with multiple cell types and trophic support, single cell suspensions are a more vulnerable population. Indeed, with multiple cell types we observed a severe cytotoxic effect when exposing cell containing gels to FMN crosslinking conditions. Even short exposure times, which only induced small changes in storage modulus, resulted in significant cell death in as little as 12 hours after crosslinking. We were unable to find a regime where crosslinking was significant but cytotoxicity was not. Several strategies were tested to examine whether the detrimental effect of excess radicals could be mitigated. By adding a cocktail of antioxidants to the medium after crosslinking, increasing the concentration of cells present during crosslinking, and minimizing the time after photoinitiation until medium was added, cytotoxicity was reduced significantly. However, the number of dead cells resulting from radical exposure, as well as obvious changes in morphology observed in surviving cells, made it extremely difficult to decouple whether changes in cellular behavior were due to the change in mechanical properties or the insult from the radicals and reactive oxygen species produced as byproducts to the intended photocrosslinking.

FMN was also shown to be a potent crosslinking agent when used to modify fibrin gels. We showed that FMN-UVA crosslinking was able to increase the storage modulus, but not the loss modulus, of a fibrin gel by 3-4 fold across a range of oscillation frequencies, indicating that the material was more linearly elastic, which has a number of implications for modifying fibrin gels. However, in our application of designing tissue engineered constructs, since fibrin gels are quickly degraded in vivo, the effect of modifying mechanical properties is less useful since the mechanical environment likely changes too quickly for the relatively minor effect from photocrosslinking to be instructive. Furthermore, the cytotoxicity observed in collagen gels was also, as expected, present in fibrin gels.

In light of the numerous disadvantages of FMN-mediated crosslinking and the significant but limited range of mechanical properties achievable through its use, other methods of photocrosslinking collagen were investigated in the hope that more a more robust process could be developed. Specifically, a photocrosslinking protocol that could be performed after gelation to allow more spatial control of the mechanical environment, with a broader range of stiffness, and with less harmful byproducts would provide a superior tissue engineering material. Several groups have investigated using collagen as a starting material, but chemically modifying its side-chains with reactive to allow more material control than provided by the limited reactivity of the native amino acids.

2.6 Methacrylate Derivatized Collagen

Several groups have published on adding functional groups to collagen in order to augment the material properties with light. Poshusta and Anseth reported a method whereby photolabile acrylate groups were added to type I collagen in suspension in HCl via the addition of glycidyl acrylate [18]. The reaction was performed at low pH to prevent self-assembly, but the required

temperature of 37°C combined with the duration of the reaction (72h) resulted in significant denaturation of the collagen. Although the extent of the denaturation was not characterized, the authors did note that the material lost a significant portion of its collagenolytic degradability, indicating loss of triple helical structure. Additionally, while photopolymerization of this material was shown to be feasible through the formation of an artificial mandibular condyle purely via light exposure, the authors did not show whether self-assembly of this derivatized collagen was possible. Lastly, photocrosslinking this material in the presence of cells was not addressed; instead chondrocytes were exposed to photoinitiation in an acrylated PEO system. While they showed post-crosslinking viability and functionality, the question of whether the same holds true with their acrylated collagen was only hypothesized.

Another approach published by Dong et al., used a cinnamate group as the photoactive moiety and reported a photosensitive type-I collagen-based material that still retained the propensity to self-assemble upon pH neutralization, indicating preservation of secondary and tertiary structure [60]. Comparison of CD spectra showed no difference in the characteristic triple helix peak, providing further evidence that secondary structure was minimally perturbed. However, the wavelength of light required to initiate photocrosslinking, 254nm, is highly cytotoxic and cannot be used in the presence of cells. Thus, this approach is not useful in for crosslinking in vivo, a major consideration for a useful CNS regenerative therapeutic.

Lastly, Brinkman et al. published a methodology for derivatizing type I collagen to collagen methacrylamide (CMA) using methacrylic anhydride (MA)[20]. This method, based on a previously published protocol for derivatizing gelatin in a similar manner[61], claimed to produce a photosensitive type I collagen that could still self-assemble and could be photocrosslinked in the presence of live cells to increase the storage modulus of the gel by an

order of magnitude. In this method, the authors reacted type I collagen with MA at pH 7.5 using varying molar ratios of collagen:MA to achieve different amounts of derivatization. Based on their findings, this method seemingly met our criteria for producing a material that could be used to instruct neurite outgrowth in situ with minimal detrimental complications. While this method used rat-tail acid-solubilized type-I collagen, the high degree of sequence homology between murine and bovine collagen indicated that this method should work similarly with the type I collagen from fetal calf skin used by our lab.

2.7 Methods

2.7.1 Methacrylate Derivatization

Similar to that described in Brinkman et al., Type I collagen was dissolved in dilute acetic or hydrochloric acid overnight at concentrations from 1-3 mg/mL. Following dissolution, in some cases pH was neutralized with Na₂HPO₄ or NaOH to achieve pH 7.5. MA was added at various molar ratios, and the final product was dialyzed against multiple changes of dilute acetic acid, lyophilized for 48 hours, and reconstituted at 3mg/mL in 0.02M acetic acid overnight for further experiments. Other protocols involved using up to 50% v/v DMSO to facilitate dissolution at neutral pH.

2.7.2 Photoinitiation

4-(2-hydroxyethoxy)phenyl-(2-hydroxy-2-propyl)ketone, known by the trade name Irgacure 2959 (I2959), was a kind gift from Ciba Specialty Chemicals and was made in bulk solution (10% w/v) in either 70% ethanol or neat methanol. Further dilution into CMA solutions gave final concentrations of I2959 at 0.01-0.1% w/v. UVA exposure was applied either in liquid phase or following gelation. Light exposure times ranged from 1-60 minutes, with light intensity from the

UVL-21 measured at 4-8 mW/cm². Gels were prepared in similar fashion to studies performed using FMN. Samples were tested mechanically using the same rheometry test protocol as the FMN studies as well.

2.8 Results

Despite multiple attempts with a range of pH conditions, solvents, reactant concentrations, reaction times, and temperatures, we were unable to replicate the results published by Brinkman et al. In cases where the pH was neutralized prior to reaction, the collagen invariably gelled in the reaction container, even at low temperatures, concentrations, and reaction times. Attempts to re-solubilize the product following the reaction via addition of titrating amounts of HCl were unsuccessful, and while some product went back into solution a large proportion remained gelled despite extended exposure to acidic conditions. DMSO was also used to prevent gelation during the reaction by solvating the collagen, and while reaction gelation was avoided the DMSO caused a number of unwanted reactions with collagen and the result was unusable product. The reaction was also attempted at low pH, and while gelation during reaction was prevented, the end product either failed to gel properly upon standard gel formation assays, presumably due to denaturation from reaction conditions, or gelled normally but showed no change in stiffness upon exposure to UV-activated I2959. In cases where the collagen failed to gel properly, either small clumps would form, indicating some collagen was still intact but most had become disrupted, or it would fail to gel at all, even after extended incubation periods, indicating complete denaturation. Additional tests using I2959 and FMN with these liquid CMA solutions failed to produce any gelation either, indicating that not only was the fibrillar assembly disrupted, the derivatization efficiency was apparently too low to initiate hydrogel formation via photopolymerization.

2.9 Discussion: Methacrylic Anhydride Derivatization

Considerable effort was spent attempting to replicate the reaction described by Brinkman et al. with our collagen. This may have been due to some difference in collagen formulation that allowed the reaction to proceed without gelation, although our understanding of collagen assembly kinetics made this difficult to adapt with our system. We anticipated that collagen would self-assemble during the reaction, so it was not surprising; however, there is no mention of this issue in the published method. We contacted the corresponding authors for elucidation on this, although the authors had no recollection of this being a complication in their process. In any case, we attempted myriad strategies for circumventing this problem, none of which was successful. Either the end product would be liquid during reaction, but would stay liquid despite conditions that should initiate assembly, or the material would behave undesirably if gelation did occur. Reasons for these outcomes are poorly understood; some unknown sidechain reactions may have occurred during the low-pH derivatization attempts that prevented normal fibrillogenesis, or reactive groups may have formed premature crosslinks during reaction that caused a similar phenomenon. DMSO is a good solvent for collagen, in terms of solvent-solute interaction, but it does not appear to be useful as an adjuvant to methacrylate derivatization. Although cysteines are relatively scarce in type I collagen, comprising ~1% of all amino acids, the possibility for disulfide bridges forming at higher DMSO concentration is possible. In addition, since type I collagen truly is soluble in DMSO (compared to a quasi-soluble suspension state in acidic aqueous conditions), the unfolding of the triple helix due to the increased solubility may have been irreversible.

Whether it was due to differences in source material, an omitted crucial detail in the published method, or simply our inability to replicate this process, the overall results of our many

attempts was unfortunately an unusable material. Taken together, our results indicate this strategy for obtaining a useful, photocrosslinkable hydrogel based on type-I fetal calf skin collagen is less than optimal, and further efforts toward optimizing reaction conditions using methacrylic anhydride were abandoned. Instead, we devised a new strategy that took advantage of some of the beneficial aspects of the previously mentioned methods and combined them. Specifically, the EDC-based derivatization used in the cinnamate-derivatized method does not require neutral pH to proceed, while including a methacrylate as the photosensitive group allows photoinitiation with Irgacure 2959, which can be activated with UVA and has been widely used in the presence of cells using other photopolymers. Since our lab also has extensive expertise in using EDC to graft functional peptides onto free amines on type-I collagen via activation of the C-terminus, we evaluated a method using EDC to activate the carboxyl on methacrylic acid.

2.10 Conclusion

Several approaches for photonically modulating the mechanical properties of fibrillar collagen adapted from published literature were evaluated as the potential basis for further work utilizing photocrosslinking to impart anisotropic material properties to hydrogel scaffolds. Flavin mononucleotide was investigated in a direct photocrosslinking paradigm, whereby FMN was used to impart crosslinking of available side-chains on type-I collagen. In a separate modality, methacrylation of collagen via derivatization with methacrylic anhydride was attempted, with activation of a soluble photoinitiator used to catalyze crosslinking of reactive methacrylates with free radicals. FMN was only able to impart minimal differences in mechanical properties, and was effective at doing so only when photocrosslinking was performed prior to self-assembly. Furthermore, FMN-based photocrosslinking resulted in severe cytotoxic effects when used in the presence of live cells. Derivatization of collagen with methacrylic anhydride under several

reaction conditions resulted in either failure to impart photosensitivity or significant denaturation of protein structure. None of the methods tested was adequate for producing a self-assembling collagen-based biomaterial suitable for further investigation as a method to modulate cellular behavior with photonically induced heterogeneous mechanical properties. Further investigation is required to produce such a material.

3. Chapter 3: Collagen Methacrylamide Derivatization via EDC/Sulfo-NHS and Methacrylic Acid

3.1 Introduction: EDC Crosslinking as a Functionalization Modality

1-ethyl-3-(3-dimethylaminopropyl) carbodiimide (EDC) is a popular reagent used to alter protein chemistry (Figure 3-1). EDC is used to activate carboxylate groups by forming an unstable o-acylisourea ester that will readily react with

free amines to form a stable amide bond. The

main advantage of EDC functionalization is

that it can be performed in an aqueous

environment, does not require addition of

harsh solvents, and can be performed in a pH

range that is amenable to most proteins. The reaction conditions required for EDC therefore

typically don't result in significant denaturation of protein structure, allowing robust

modification of protein chemistry while maintaining existing functionality. EDC is a zero-length

crosslinker, meaning it catalyzes the formation of covalent crosslinks between carboxyls and

amines, but there is no spacer group and no part of EDC is

retained, so reactants can be completely removed after the

reaction is complete with no concerns about crosslinker leaching

out later as with aldehyde-based crosslinking. One drawback to

using EDC is that the o-acylisourea ester is highly unstable and will

quickly hydrolyze back to the original reactants, reducing the

reaction efficiency. As a result, *N*-hydroxysulfosuccinimide (sulfo-

NHS, Figure 3-2) is commonly used to form a semi-stable intermediary NHS-ester which has

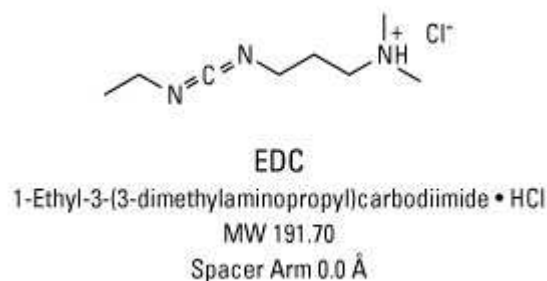


Figure 3-1: EDC; Source: Thermo Scientific, Pierce Protein Biology Division. Reproduced with Permission.



Figure 3-2: Sulfo-NHS; Source: Thermo Scientific, Pierce Protein Biology Division. Reproduced with Permission.

more longevity in an aqueous environment and allows for increased derivatization. This 2-step process allows for complete activation of the carboxyl of interest without carboxyls on the target protein being reacted. The standard process involves combining EDC, a carboxylic acid, and sulfo-NHS in MES (2-(*N*-morpholino)ethanesulfonic acid) buffer, which maintains the pH within the 4.7-6 range in which carboxyl activation occurs. After a 10 minute activation period at 37°C to fully react the two-step formation of the NHS-ester, the reaction milieu is added to a solution containing the target protein, and mixed well for the duration of the reaction. While the reaction of the NHS-ester is most efficient at a slightly alkaline pH (8-9) and higher temperature, it will still proceed, albeit slowly, at lower pH and temperatures, which makes it ideal for use with sensitive proteins such as type-I collagen. The general schematic of EDC crosslinking is outlined in Figure 3-3, showing amide bond formation with and without the presence of NHS.

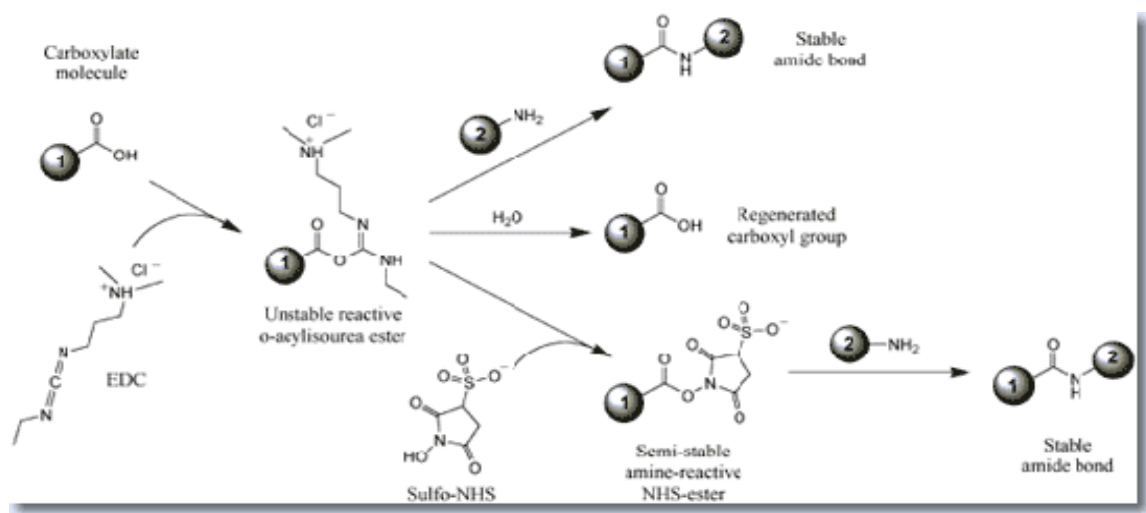


Figure 3-3: Schematic of EDC/NHS crosslinking reaction. Source: Thermo Scientific, Pierce Protein Biology Division. Reproduced with Permission.

3.2 Derivatization of Collagen to CMA via EDC and methacrylic acid

Initial attempts at derivatizing type I collagen with EDC were promising, in that that reaction conditions appeared to allow functional grafting of methacrylic acid (MAA) without the obvious detrimental effects observed with previous methods. After reaction of a collagen solution to EDC-activated methacrylic acid in MES buffer, dialysis, lyophilization, and reconstitution, the gelation assay indicated that self-assembly was not significantly disrupted. Additionally, rheological investigation indicated that I2959 photoinitiation could be used to increase the storage modulus significantly. However, a consistent product was not yet possible due to a lack of a developed reaction process, and optimization of the derivatization was necessary before further experiments were possible. Optimization of CMA synthesis via EDC required addressing a number of factors. Reactant concentrations, specifically molar ratios of EDC, sulfo-NHS, MAA and collagen, as well as overall collagen concentration and MES buffer volume were included as variables. Reaction time, dialysis parameters, lyophilization, and reconstitution were all considerations as well.

Previous work in our lab that incorporated EDC crosslinking has focused on grafting functional peptide sequences to the collagen backbone, and we have successfully added numerous molecules to type-I collagen while maintaining its positive attributes[62,63]. In these methods, due to the limited amount of expensive peptide used, the amount of EDC was relatively small given that the ratio of [peptide : EDC : primary amine] is constrained since excess EDC will aberrantly crosslink amino acid side-chains on collagen if there is not enough free amine available on the N-termini of the peptide. Using this as a starting point to determine the optimal molar ratios needed for methacrylate yielded extremely low derivatization, evidenced by minimal change in modulus upon photocrosslinking. However, since MAA is inexpensive, strategies utilizing large molar excesses were employed to maximize derivatization efficiency.

Concomitant increases in EDC and sulfo-NHS were then investigated to determine the optimal concentrations for maximum derivatization efficiency. Proton NMR and trinitrobenzenesulfonic acid assay were employed to characterize the extent of derivatization by direct analysis of CMA chemistry as compared to native collagen, while rheometry was used to assess photocrosslinking functionality. Rheometry was also used to optimize the photocrosslinking parameters by modifying the rheological setup with optical plates to allow real-time analysis of both self-assembly and photoinitiated crosslinking. Once optimization of CMA synthesis and photocrosslinking was considered complete, we further characterized the material properties to investigate whether derivatization with methacrylates resulted in ancillary modification of collagen structure. In particular, we examined tertiary and quaternary structure using circular dichroism (CD) spectroscopy, dynamic light scattering (DLS), and scanning electron microscopy (SEM). We also characterized the collagenolytic behavior of CMA gels before and after crosslinking compared to native collagen using a standard microplate assay as well as a novel rheological assay used to analyze the rate of change of mechanical properties in the presence of collagenase. Rheometry and viscometry were also used to investigate thermal stability of gels and molecular weight distribution, respectively.

3.3 Methods

3.3.1 CMA Derivatization Optimization

For optimization, CMA was derivatized in multiple, small (>10mL) batches where molar ratios of EDC, NHS, and MAA were varied between 1, 5 and 10 combinatorially and the ratio of MAA: free amine was varied from 1:10 to 40:1. The number of free amines was calculated based on published sequences of bovine type I collagen (Protein Database). Adding the number of lysines present on 2 α 1 chains and 1 α 2 chain, and using the average molecular weight of the collagen

provided by EPC, we determined that there are approximately 0.245mmol ϵ -amine groups per gram of lyophilizate. Molar ratios were calculated appropriately, and combinations of EDC, sulfo-NHS, and MAA were mixed, incubated for 10 minutes at 37°C, then cooled on ice and added to a solution of collagen, where stock collagen used was either 3 or 3.75 mg/mL. Reactions were allowed to proceed for 24-48h at 4°C on a rotator to ensure constant mixing. The reaction was then transferred to either dialysis tubing or a dialysis cassette, both employing the same regenerated cellulose membrane with a 10K MWCO (Thermo Scientific). After multiple dialysis bath changes in 0.02M acetic acid at 4°, the remaining protein product was extracted from the dialysis membrane and transferred into pre-weighed conical tubes and placed in a -20°C freezer for 4 hours, then transferred to -80°C overnight. Frozen samples were then uncapped, covered in perforated parafilm, then placed into a glass lyophilization jar and freeze dried for at least 48h to remove all liquid. Product was weighed, and reconstituted in 0.02M acetic acid similar to stock native collagen solutions.

3.3.2 *Proton NMR*

^1H Nuclear magnetic resonance (NMR) was used to analyze CMA for evidence of successful derivatization. Initial experiments aimed to use D_2O with 10mM DCl as solvent. However, while both native collagen and CMA became homogeneous solutions, spectra were unavailable due to improper solvation. Later experiments were performed with deuterated DMSO and acceptable spectra were resolved. NMR spectra were obtained with a Bruker Avance 360 MHz NMR. Lyophilized native collagen and CMA were dissolved in deuterated DMSO (10 mg/mL) overnight and NMR spectra were calibrated to the residual solvent peak (2.50 ppm).

3.3.3 *TNBSA Assay*

Derivatization efficiency was also evaluated using a trinitrobenzenesulfonic acid (TNBSA) assay, modified from Sheu et al.,[64] to quantify the free amine content before and after derivatization. To a sample of 100 μ L CMA (3 mg/mL), 100 μ L of 4% (w/v) sodium bicarbonate and 100 μ L of freshly prepared 0.5% (v/v) TNBSA solution in deionized water was added. After reaction at 37°C for 2 h, 200 μ L of 6 M HCl was added, and the temperature was raised to 60°C to solubilize CMA. The resulting solution was diluted with 500 μ L of deionized water, and the absorbance was measured at 345 nm. Native type-I collagen that was not reacted with methacrylic acid and 0.02 M acetic acid were used as controls.

3.3.4 Optimized CMA Synthesis Protocol

Type I bovine collagen was modified by reacting free amines with methacrylate groups to create collagen methacrylamide (CMA). Batches were made as follows: 100 μ g 1-ethyl-3-(3-dimethylaminopropyl) carbodiimide (EDC) and 50 μ g N-hydroxysuccinimide (NHS), both freshly dissolved in MES buffer were mixed with 100 μ L methacrylic acid (MA) and brought to 2 mL total volume with additional MES buffer. After thoroughly mixing, reactants were placed at 37°C for 10 minutes to fully react the EDC/NHS/MAA mixture. The mixture was then cooled on ice for 5 minutes and added to 30 mL collagen (3.75 mg/mL) in 0.02 M acetic acid and reacted for 24 hours at 4°C on a rotator with the tube set at a 45° angle to encourage continuous mixing. Following the reaction, the CMA reaction mixture was centrifuged at 2000 RPM at 4°C for 2 minutes to reduce foam, aspirated into a 60mL disposable sterile syringe using an autoclaved large bore stainless steel cannula and injected via 18G needle into a pre-soaked, γ -irradiated 12-30 mL capacity Slide-a-Lyzer dialysis cassette with a MWCO of 10,000. The reaction mixture

was dialyzed against 4 L 0.02 M acetic acid for 4, 12, and 24 hours to fully remove all reaction reagents. The purified product was frozen at -20°C for 4 h in pre-weighed 15 mL conical tubes wrapped in foil, transferred to -80°C overnight, and then lyophilized for 72 hours. Freeze dried samples were weighed to determine product yield and stored wrapped in foil at 4°C. For experiments, CMA was resuspended at 4°C overnight with gentle rotation in 0.02 M acetic acid at various concentrations from 3-5 mg/mL. Parallel plate rheometry was used to determine self-assembled and photocrosslinked storage moduli as a quality control (QC) metric after every synthesis, with a 4-fold increase in G' upon exposure to 2 minutes UV with 0.05% I2959 as the minimum benchmark for batch release. CMA solutions were initially stored for up to 2 months during experiments but later protocol used CMA within 2 weeks post-reconstitution to ensure minimal spontaneous reaction methacrylate groups. CMA solutions were stored, foil wrapped, at 4°C and kept on ice during experiments.

3.3.5 Rheometry

Rheology experiments were initially performed on the Rheometrics SR-2000 parallel plate rheometer with the same protocol used in the FMN crosslinking experiments. Initial optimization was performed in the original modality, creating samples in PDMS molds on glass slides, then removing the mold and transferring the gels to the rheometer plate. Further development led to a method in which vacuum grease was used to affix the glass slide to the bottom plate, and then samples were run sandwiched between the upper parallel plate and the glass slide. This method resulted in less manipulation of the gels due to the lack of a step requiring transfer from slide to rheometer. Additionally, a Bohlin Gemini II rheometer was used

during late stage CMA optimization due to maintenance issues with the SR-2000 that resulted in significant downtime. Similar but not identical experimental processes were performed on the Bohlin instrument based on differences in control modalities between it and the SR-2000. Later experiments, and the majority of the mechanical property characterization, were performed on a Kinexus Ultra rotational rheometer (Malvern Instruments, Worcestershire, UK). Sample loading for Kinexus experiments was initially performed using gels pre-formed on glass slides and immobilized on the lower parallel plate using vacuum grease. Late-stage optimization and mechanical characterization was performed using an *in situ* modality where the liquid macromer solution was loaded in between the parallel plates and allowed to self-assemble, which eliminated gel sample manipulation altogether. To form gels, 677 μL CMA (3-5.12 mg/mL) was added to 20 μL HEPES, 140 μL 0.15 N NaOH, 100 μL 10X PBS, 53 μL PBS, and 10 μL of a photoinitiator solution containing 2.5-10% (w/v) Irgacure 2959 (I2959) in methanol to form a 1 mL batch. In the preformed gel protocols this collagen solution was immediately loaded into PDMS molds, gelled for 1 hour, photocrosslinked, and then loaded on the rheometer using 10% compression of the sample to ensure a no-slip condition. In the *in situ* testing mode, 200 μL ice-cold collagen solution was pipetted onto the bottom parallel plate and then the upper geometry was lowered slowly to allow uniform flow of the macromer solution into a 600 μm gap between a 20 mm stainless steel top parallel plate and a custom-modified quartz glass lower plate with in-line diffusers and band pass filtration to provide uniform light in the UVA range (Figure 3-4).

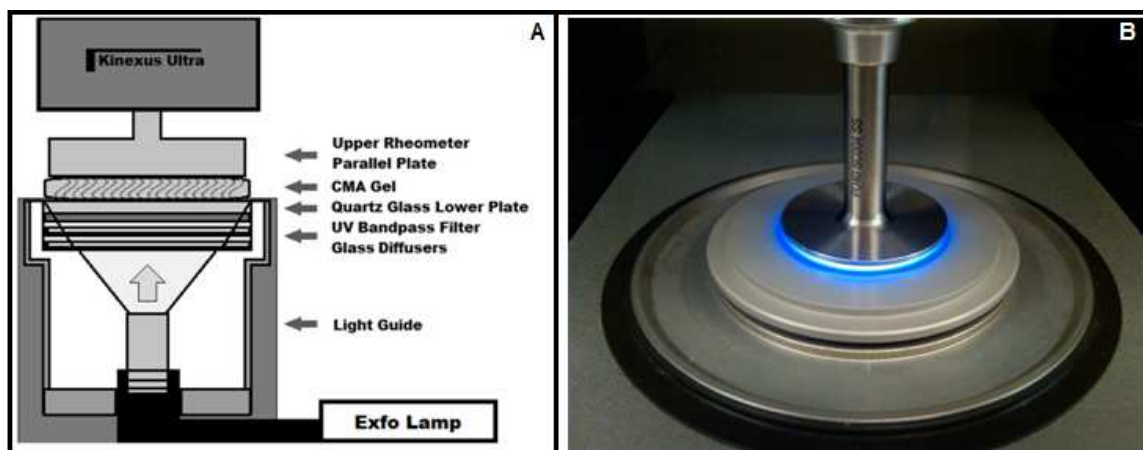


Figure 3-4: UV Rheometry Schematic (A) and Photo of parallel plates with UV light 'On' (B)

The solvent trap reservoir was filled with 700uL deionized water and the solvent trap covers were used to prevent evaporation during the test. The temperature was raised from 25 to 37°C with a Peltier-controlled stage to induce fibrillogenesis. After equilibration of fibrillogenesis, as evidenced by stabilization of storage and loss moduli, the sample was exposed to UV light (365 nm, 100 mW/cm²) from an EXFO mercury arc lamp connected via a liquid light guide through the quartz bottom plate for exposure periods ranging from 10-300s to photocrosslink the gel. The iris of the EXFO source was used to control light intensity and light exposure time was controlled using the digital timer mode on the light source. Light intensity was measured periodically with the photo detector to source intensity drift. Throughout the equilibration and photocrosslinking process, and continuing for 20 min after exposure, the sample was oscillated (0.5% strain, 1 rad/s), and the resultant torque was measured to obtain mechanical properties of the material during both self-assembly and photocrosslinking.

3.3.6 Circular Dichroism Spectroscopy

CD spectroscopy was performed in two sets of experiments. The first set was executed using an Aviv Model 400 Spectropolarimeter (Aviv Biomedical Inc., Lakewood, N.J.). Native collagen and

CMA at 0.1 mg/mL, along with a reference sample of 0.02 N acetic acid buffer, were injected into optically matched 0.1 cm path length quartz cuvettes (model 110-OS; Hellma USA). Ellipticity was averaged over 10 s and recorded from 290 nm down to 190 nm in 1 nm intervals. Samples were run at 10°C. A separate set of experiments was performed with similar cuvettes where collagen and CMA were in solution (0.1 mg/mL) in two separate buffers, 0.02 M acetic acid (as before) and 1X PBS to simulate physiological pH and initiate fibrillogenesis. Wavelength scans were conducted from 190 to 260 nm at 4°C (number of scans 1, averaging 1.0 s). CD spectra were plotted with buffer signal from the same cuvette subtracted out. Reported values were given as concentration normalized ellipticity, as molarity of solutions was unknown due to uncertainty of native collagen and CMA molecular weight. Here, a wavelength scan was repeated to determine peak ellipticity, and then a melting curve experiment was performed with a freshly prepared set of samples to examine thermal stability. The analysis of thermal stability was based on similar studies using triple helical synthetic peptides [65]. Thermal denaturation CD measurements were performed on the same instrument. Ellipticity was monitored at 222nm while temperature increased at 0.33°C/step with a 2 minute equilibration time. Apparent melting temperature, T_m , was calculated by estimating the fraction folded using:

$$F(T) = \frac{\theta(T) - \theta_U(T)}{\theta_F(T) - \theta_U(T)}$$

where $\theta(T)$ is the observed ellipticity and $\theta_F(T)$ and $\theta_U(T)$ are estimated ellipticities derived from linear fits to the folded and unfolded baselines. The melting temperature is estimated as T where $F(T) = 0.5$.

3.3.7 Dynamic Light Scattering

Dynamic light scattering (DLS) analysis was used to assess tropocollagen molecule size in acidic conditions as well as fibril formation at physiological pH. The methodology was based on a protocol published by Parmar et al [66] using a Zetasizer Nano S (Malvern Instruments) with a 3 mW He-Ne laser at $\lambda = 633 \text{ nm}$, collecting back-scattered light at $\theta = 173^\circ$. Collagen and CMA solutions (0.1 mg/mL) in 0.02 M acetic and 1X PBS were equilibrated to 37°C , controlled to within $\pm 0.1^\circ\text{C}$ by the built-in Peltier element. DLS analysis was performed at 0, 5, 30, and 60 minutes following thermal equilibration. Scattering intensities were determined from the average of five correlation functions, with a typical acquisition time of 60 s per correlation function. The derived count rate (DCR) was used to determine steady state, defined by lack of statistical difference ($P \geq 0.1$) between averaged DCR at a given time point. For acetic acid samples, steady state was achieved at 5 minutes and remained so throughout the remainder of the 60 minutes. For PBS, steady state was achieved at 30 minutes and remained at 60 minutes. Data within steady state groups were pooled and averaged. Only monodisperse data were analyzed. Acetic acid data consisted of the mean radius of the single monodisperse volumetric peak whereas PBS data consisted of both monodisperse intensity peak mean radii.

3.3.8 *Scanning Electron Microscopy*

Native collagen and CMA gels were prepared as previously described, except on 15mm diameter No. 1 circular glass coverslips. Following self-assembly and photocrosslinking with 2 minute exposure to the EXFO light source, gels were dehydrated in a series of aqueous acetone solutions (25%, 50%, 75%, 95%, 100% v/v) and critical point dried (CPD 020, Balzers Union Limited, Balzers, Liechtenstein). Samples were then sputter coated with gold/palladium (SCD 004, Balzers Union Limited, Balzers, Liechtenstein) and imaged via SEM (Amray 1830I, Amray Inc. Bedford, MA). Fibril diameter was measured on 20 separate images per condition. Diameter

was sampled on fibrils at the grid intersections of an overlaid 8x12 grid, and measured using ImageJ (ImageJ, NIH, Bethesda MD).

3.3.9 *Degradation via Collagenase*

Degradation of the mechanical properties of gels was evaluated via reduction in storage modulus (G') due to enzymatic cleavage of collagen fibrils. For rheological analysis during enzymatic degradation, collagen or CMA solutions were prepared as above and loaded onto the rheometer in a poly(dimethyl siloxane) (PDMS) ring, allowed to gel at 37°C, and exposed to UV for crosslinking. Samples were then cooled to 15°C and Type-I collagenase (0.1 mg/mL) was added and allowed to diffuse into the gel for 5 minutes. After aspiration of excess collagenase, the upper parallel plate was lowered onto the gels, the temperature was returned to 37°C, and the sample was exposed to 3 seconds of oscillatory shear (1 rad/s, 0.5% strain) every 5 minutes for 1 hour. Degradation of the fibrillar structure was evaluated with a separate assay, adapted from Damink *et al* [67]. Collagenase (0.01 mg/mL) was added to gelled native collagen, CMA and photocrosslinked CMA in a 96-well plate, where samples of the gel supernatant were removed every 30 minutes and the total liberated protein determined by the commonly-used bicinchoninic acid (BCA) assay for total protein.

3.3.10 *BCA Total Protein Assay*

A BCA Assay (Pierce BCA Protein Assay Kit, Thermo Scientific) was used to determine the concentration of protein in solution following collagenolytic degradation and following gelation to determine if both native collagen and CMA fully fibrillized. This assay was developed by Smith *et. al.*, and is commonly used to analyze general protein concentrations [68]. The BCA assay operates on the principle that peptide bonds reduce divalent copper ions (Cu^{2+}) to Cu^+ , which

then form chelates with bicinchonate to form a purple product [69]. Samples of protein supernatant (10 μ L) were plated into a 96-well clear-bottomed microplate. BCA Assay working solution was prepared freshly by adding 400 μ L of BCA Protein Assay Reagent B to 20 mL BCA Protein Assay Reagent A in a 50mL conical tube and vortexed. A 200 μ L aliquot of the working solution was then added to each sample well. After incubation for 30 min at 37°C, absorbance was read at 562nm using a DTX 880 Multimode Detector plate reader (Beckman Coulter, Fullerton, CA). Serially diluted native collagen and CMA standard curves were used to calculate labile protein concentrations from unknown sample absorbance.

3.3.11 Gel Mass Analysis

Gravimetric analysis was used to determine if CMA gels (\pm photocrosslinking) differed in mass of protein following fibrillization and equilibrated hydration compared to native collagen. CMA and native collagen solutions (50 μ L samples, 2.5 mg/mL, 1.25 mg protein/sample) were plated in 12-well plates, and allowed to self-assemble at 37°C for 1 hr. One set of CMA samples was photocrosslinked, and all samples were washed with 2mL diH₂O 4 times (15 min, 30 min, overnight, 5 minutes) and then aspirated dry. Gels were transferred to pre-weighed microcentrifuge tubes and lyophilized for 48h. Tubes were again weighed and dry weights were recorded.

3.3.12 Cold Melt Rheometry

Native collagen and CMA solutions were prepared as before and loaded onto the Kinexus Ultra with the standard parallel plate temperature-controlled lower module and stainless steel lower plate with the solvent trap setup included and filled with 700 μ L diH₂O to prevent sample evaporation. Gels were allowed to equilibrate for 10 minutes and then temperature was ramped

at 2°C/min down to 4°C and back up to 37°C. Storage and loss moduli were recorded to compare mechanical stability of native collagen and CMA gels at low temperature.

3.3.13 Viscometry

Native collagen and CMA in solution in 0.02M acetic acid (4.43mg/mL) were loaded onto a pre-cooled (4°C) stainless steel lower parallel plate and loaded using a 40mm upper cone with an angle of 4°. Samples were run in viscometry mode using a table of shear rates from 0.01-100 s⁻¹, 3 samples per decade, and the viscosity of the solution was recorded. A Moore model was fit to a plot of viscosity vs. shear rate and the zero-shear viscosity was determined through extrapolation using the Kinexus rSpace software.

3.4 Results

3.4.1 CMA Optimization

After testing multiple combinations of molar ratios of reactants, reaction times, and various other parameters, it was determined that a large molar excess of MAA: free amine (40:1) at a molar ratio of 5:2:1 (MAA:EDC:sulfo-NHS) reacted for 24h and dialyzed excessively (3 dialysate changes at 133-fold volume), lyophilized for 72 hours and reconstituted in a low shear mixing regime resulted in a type-I collagen based material with properties similar to collagen and the reactivity to increase its storage modulus five-fold via photocrosslinking via exposure to UVA for 2 minutes. Increasing reactant concentrations relative to collagen concentration past these ratios resulted in denaturation/crosslinking of collagen during the reaction and difficulty removing unreacted materials during dialysis. Decreasing ratios of reactants resulted in accompanied decrease in photocrosslinkable functionality.

3.4.2 Proton NMR

Multiple rounds of NMR experiments were necessary to determine both a successful NMR protocol as well as the optimal reaction conditions for CMA synthesis. Initial attempts using D_2O/DCI were unsuccessful due to the good suspension solubility of type-I collagen in dilute acid but poor molecular solubility. As a result, useable spectra didn't show up. After testing several solvents, DMSO seemed to provide suitable solubility. Samples were dissolved in deuterated DMSO (Sigma) and NMR spectra were obtained. Strangely, the native collagen was poorly soluble in this solvent despite it easily going into solution in standard lab grade DMSO. Thus comparisons between native collagen and CMA were meaningless. However, the NMR data did result in determination of some reaction condition parameters. Here, MAA: ϵ -amine ratios of 10:1, 1:1, and 1:10 were used as experimental conditions to determine whether large molar excesses of reactants provided increased derivatization. We discovered that only the 10:1 ratio produced resolvable peaks (seen near 5.3-6.1 ppm in Figure 3-5B) whereas in the 1:1 and 1:10 ratio conditions there were no observable peaks.

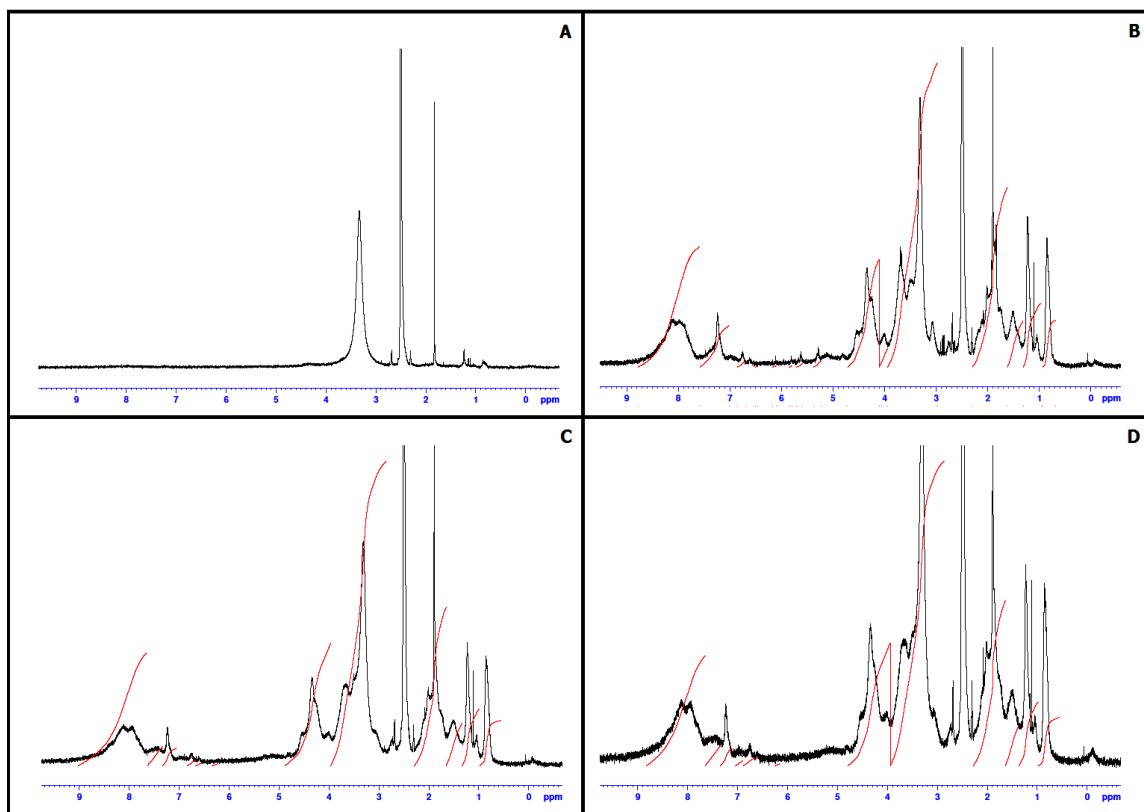


Figure 3-5: NMR of Native Collagen (A); CMA with MAA:ε-Amine ratios of 10:1 (B); 1:1 (C); 1:10 (D) in Deuterated DMSO

A second round of NMR experiments compared the spectra of native collagen, native collagen with MAA without EDC as an ‘undialyzed’ control, and CMA reacted with the 10:1 ratio of MAA:free amine with and without sulfo-NHS. Unlike the first round, native collagen was indeed soluble in deuterated DMSO (Figure 3-6A). Additionally, the ‘undialyzed’ control was included to determine where the methacrylate peaks would show up and to help determine in the future if our dialysis protocol was sufficient. The peaks from undialyzed concentrations of MAA showed up where expected and were massive compared to grafted methacrylate peaks (Figure 3-6B). Lastly, we saw that sulfo-NHS was necessary in the reaction as the EDC/MAA only condition did not produce measurable peaks, whereas the condition with EDC/sulfo-NHS/MAA had

discernible, albeit small, peaks equivalent to those seen in the first experiments (Figure 3-6 C&D).

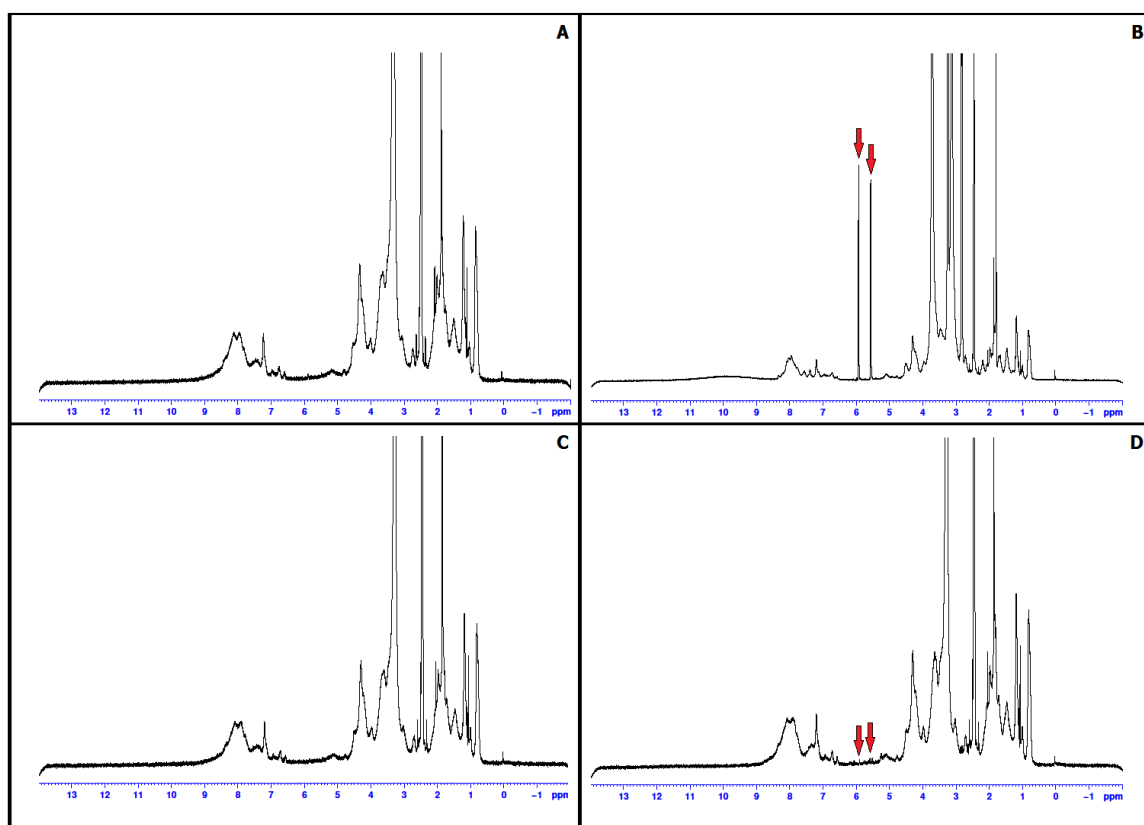


Figure 3-6: NMR spectra of native collagen (A); native collagen + 100µl free MAA (B); CMA without (C), and with (D) sulfo-NHS. Red Arrows Denote Methacrylate Peaks

Rheological data indicated that a MAA:ε-amine ratio of 10:1 was sufficient to impart photosensitivity, further increasing the concentration of reactants produced greater functionality. This is discussed in depth in Section 4.4. By increasing the MAA: ε-amine ratio to 40:1, and maintaining an MAA:EDC:sulfo-NHS ratio of 5:2:1 provided the best material from a mechanical properties standpoint. A last NMR experiment was performed to determine whether this functionality was visible as larger peaks at the characteristic section of the spectrum seen in

previous experiments. As seen in Figure 3-7, the peaks are indeed measurably larger than with previous experiments where reactant molar ratios were lower.

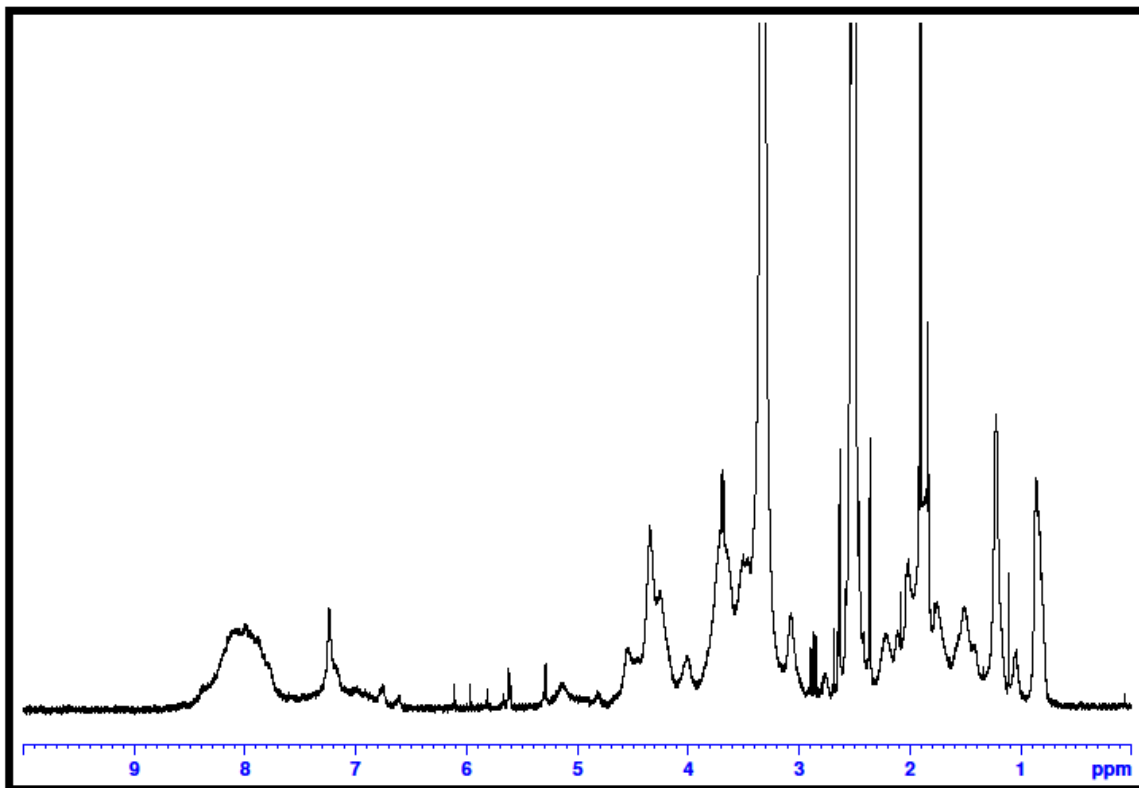


Figure 3-7: NMR spectrum of optimized CMA protocol showing derivatized methacrylate peaks at 5.3-6.1

However, while the peaks from the derivatization were evident, the noise associated with a complex spectrum of large protein like type-I collagen made quantification of derivatization efficiency difficult compared with similar reactions where the exact structure and concentration is known, such as with polyethylene glycol diacrylate (PEGDA). As such, a separate methodology used to quantify the percentage of free amines before and after the functionalization reaction was required.

3.4.3 TNBSA Assay for Amine Quantification

A literature search revealed previous work by Steffens et. al., who used EDC crosslinking to covalently graft VEGF onto collagen, and quantified their grafting efficiency using a colorimetric assay based on the reaction of TNBSA with the free-amines present on collagen [70]. Further details on this protocol were adapted from another published report using TNBSA to quantify amine concentration in collagen gels [64].

The assay was run in duplicate and data was averaged. The absorbance at 345nm, which is proportional to the amine concentration, was 2.19 ± 0.02 for CMA as compared to 2.24 ± 0.04 for native collagen. The absorbance of the acetic acid blank, 2.06 ± 0.05 , was subtracted from each sample value, and the resulting net absorbance was used to calculate the derivatization efficiency (E):

$$E = (ABS_{CMA} - ABS_{AcA}) / (ABS_{NC} - ABS_{AcA})$$

From this assay we determined that absorbance due to the amine concentration of CMA derivatization was 73.8% of the net absorbance of native collagen, hence the efficiency of methacrylamide functionalization was approximately 26%. TNBSA data was only obtained for the optimized CMA synthesis protocol. Results of the TNBSA assay are plotted in Figure 3-8.

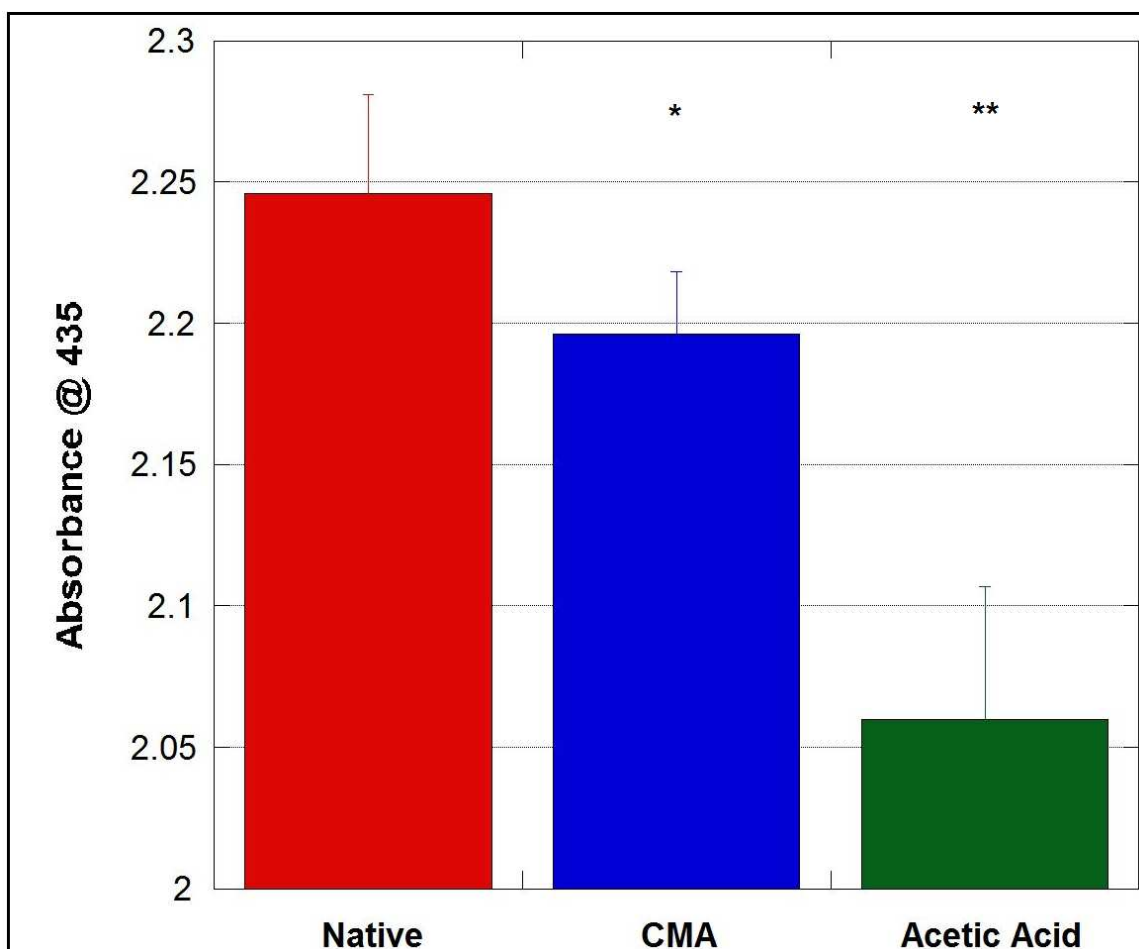


Figure 3-8: TNBSA Assay Data. Mean absorbance shown, error bars \pm SD

3.4.4 Rheometry

Substantial effort was involved in development of a robust rheological testing methodology simultaneous to optimization of CMA derivatization and crosslinking parameters, the bulk of which was driven by rheological data. The details of this optimization process are described in Appendix A. The results of the optimized photocrosslinking process, based on UV exposure during rheological measurement of moduli, can be observed in Figure 3-9 A, which shows a summary comparison of real-time gelation and photocrosslinking data of CMA vs. native collagen. Shown are G' and G'' vs. time for both materials at 2.5 mg/mL using an I2959 concentration of 0.025%. Rheological analysis of CMA gels demonstrates self-assembly of the

material into a fibrillar hydrogel as evidenced by the increase in storage modulus around 200-300 seconds after incubation at 37°C. The kinetics of self-assembly were slightly delayed compared to native collagen, which self-assembled from 100-200 seconds following the temperature increase. Photolabile functionality of CMA was demonstrated by the rapid, five-fold increase in storage modulus (G') upon irradiation with UV light in the presence of photoinitiator. A small increase in the loss modulus (G'') was observed during irradiation, however after the 90 s exposure period, the equilibrium loss modulus was slightly lower than prior to photocrosslinking. The large increase in storage modulus from pre-crosslinked (323.4 ± 7.8 Pa at $t=600$ s) to post-crosslinked (1316.8 ± 51.3 Pa at $t=1200$ s) along with the slight decrease in loss modulus (57.7 ± 4 Pa to 39.8 ± 6.5 Pa) indicates that photocrosslinking of CMA results in a mechanically stiffer and more elastic material (Figure 3-9 B).

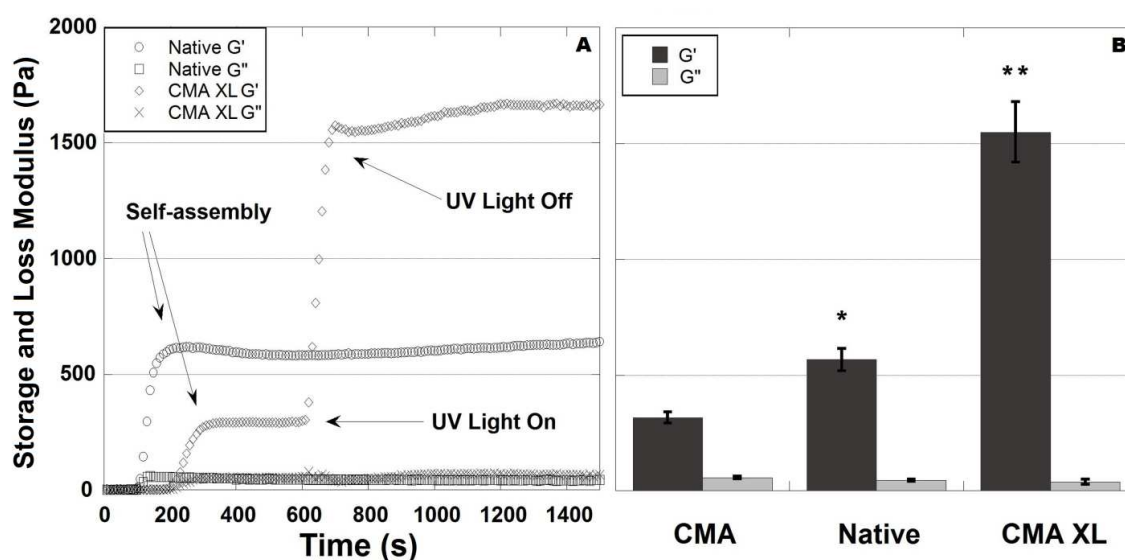


Figure 3-9: Summary of CMA vs. Collagen Storage and Loss Moduli. Full Real-time G' and G'' vs. Time (A) and average Equilibrium G' and G'' (B)

The final rheological analysis highlights the tunability of CMA via UV exposure time. Controlled stiffness modulation is demonstrated in Figure 3-10 A, where exposure for 30, 45, and 90

seconds resulted in 30%, 60%, and 100% crosslinking as determined by increase in storage modulus. Figure 3-10 B displays dynamic control of the material, as six distinct 15 s UV exposure periods incrementally and additively increased the storage modulus (~ 5, 30, 60, 80, 90, 100% of maximum) while maintaining a stable modulus immediately after removal of light.

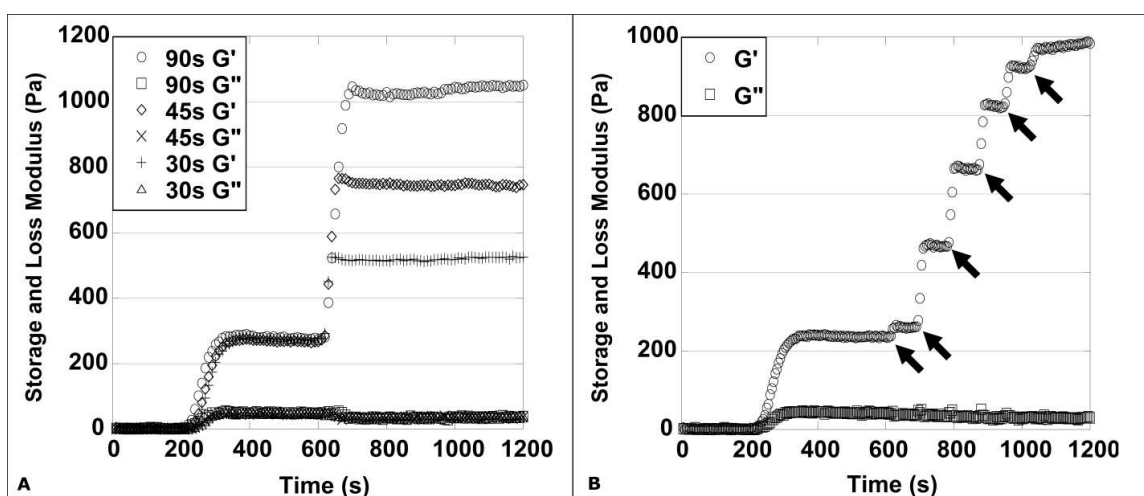


Figure 3-10: Mechanical Tunability of CMA Gels via Differential Light Exposure Periods (A) and Dynamic Temporal Control using Multiple Light Exposures (B). Arrows Indicate Onset of 15 s UV Exposure Period.

3.4.5 CD Spectroscopy

A preliminary CD experiment yielded curves that showed very little difference at the characteristic triple helix peak. Samples were dissolved in 0.02M acetic acid and CD measurements were obtained at 10°C. The ellipticity of CMA as compared to native collagen presented no significant differences in either wavelength shift or amplitude at the characteristic 222 nm peak, indicating an equal concentration of triple helix in both materials (Figure 3-11).

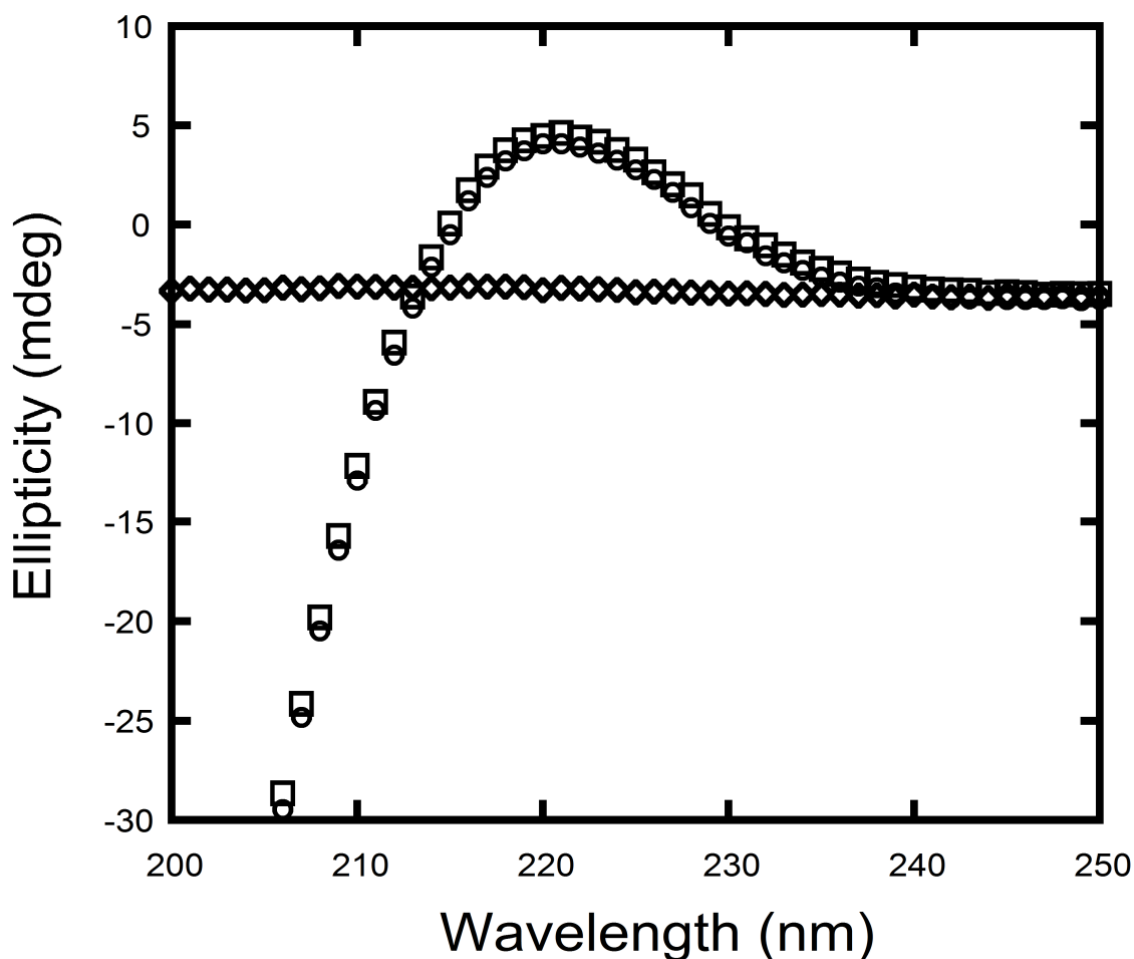


Figure 3-11: CD Spectra of CMA & Native Collagen in 0.02 M Acetic Acid

Due to sample preparation error, a second round of CD experiments compared 0.175 mg/mL native collagen and 0.1 mg/mL CMA in both the acetic acid buffer and a physiological-pH buffered PBS solution. Comparison of raw curves showed that CMA had the same peak wavelength but lower amplitude in both buffers, indicating a lower concentration of triple helix as compared to native collagen (Figure 3-12). However, when normalized to concentration, native collagen in PBS and acetic acid had ellipticities of 4.4 and 5.4 mdeg/mg, respectively, while CMA had measured at 4.6 and 5.5 mdeg/mg, respectively, indicating similar triple helix content between both materials in corroboration with previous data.

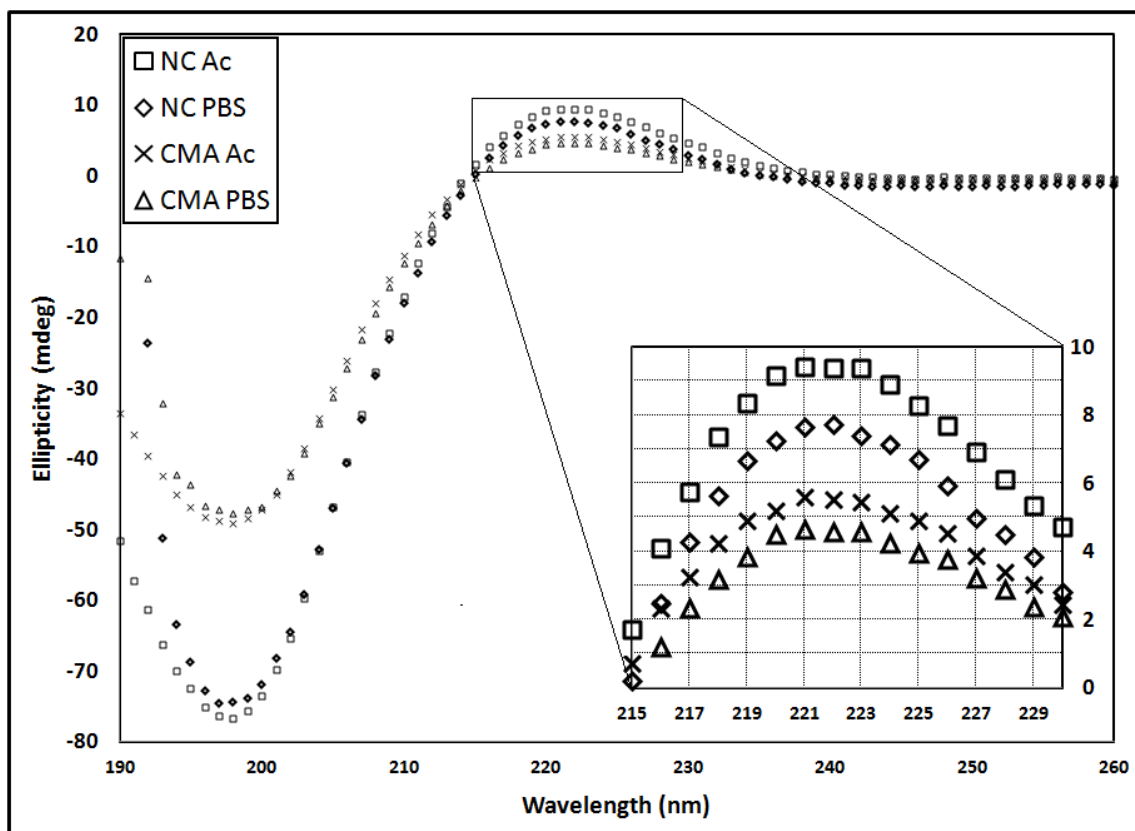


Figure 3-12: CD Spectra of CMA and Native Collagen (NC) in Phosphate Buffered Saline (PBS) and 0.02M Acetic Acid (Ac)

Next, melt curves were obtained for the same conditions by increasing the sample temperature from 4 to 60°C and measuring the ellipticity at 222nm to characterize the concentration of triple helix as a function of temperature (Figure 3-13). Melting temperature, calculated as described in the methods section, was similar for native collagen (41.9°C) and CMA in acetic acid (41.5°C), indicating that the soluble macromer stability was similar. However, looking at the melt curve of CMA, there are 2 apparent inflections during the melt phase, compared to only one for native collagen, indicating 2 distinct phase transitions for CMA and possibly implying the presence or absence of different molecular interactions between CMA and native collagen that are not recognized with the melt temperature calculation as is. In pH 7.2 PBS buffer, the melting temperature of CMA (33.2°C) was higher than native collagen (25.1°C).

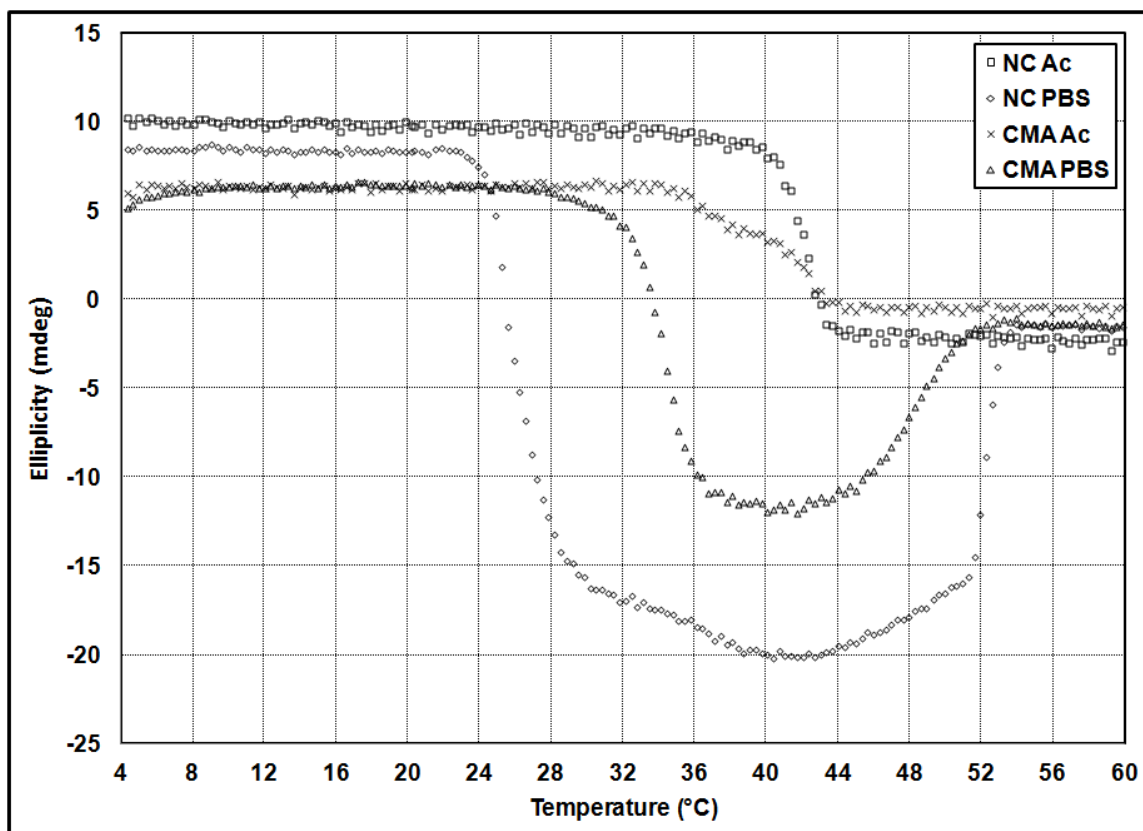


Figure 3-13: CD Melting Curve of CMA and Native Collagen (NC) in Phosphate Buffered Saline (PBS) and 0.02M Acetic Acid (Ac)

Repeats of the wavelength scan and melt curves were performed with all conditions at the same concentration of 0.1 mg/mL. Wavelength data verified that native collagen and CMA have identical concentrations of triple helix (Figure 3-14). In addition, the triple helical content was not distinguishable between buffers, indicating that negligible self-assembly had taken place during CD signal acquisition. Again, maximum ellipticity was observed to be near 222 nm for all samples. Thus, based on three sets of CD data, we have determined that triple helix content as measured by CD spectroscopy is not appreciably disrupted by CMA derivatization when compared to native collagen. In addition, at 4°C, there is not a measurable change in triple helix concentration of either CMA or native collagen during the 2 hour time period required to obtain CD data, a result which corroborates observations made during rheological testing in which pH

neutralized collagen was kept on ice for up to 3 hours with no observable change in self assembly kinetics or mechanical properties of the stable gels.

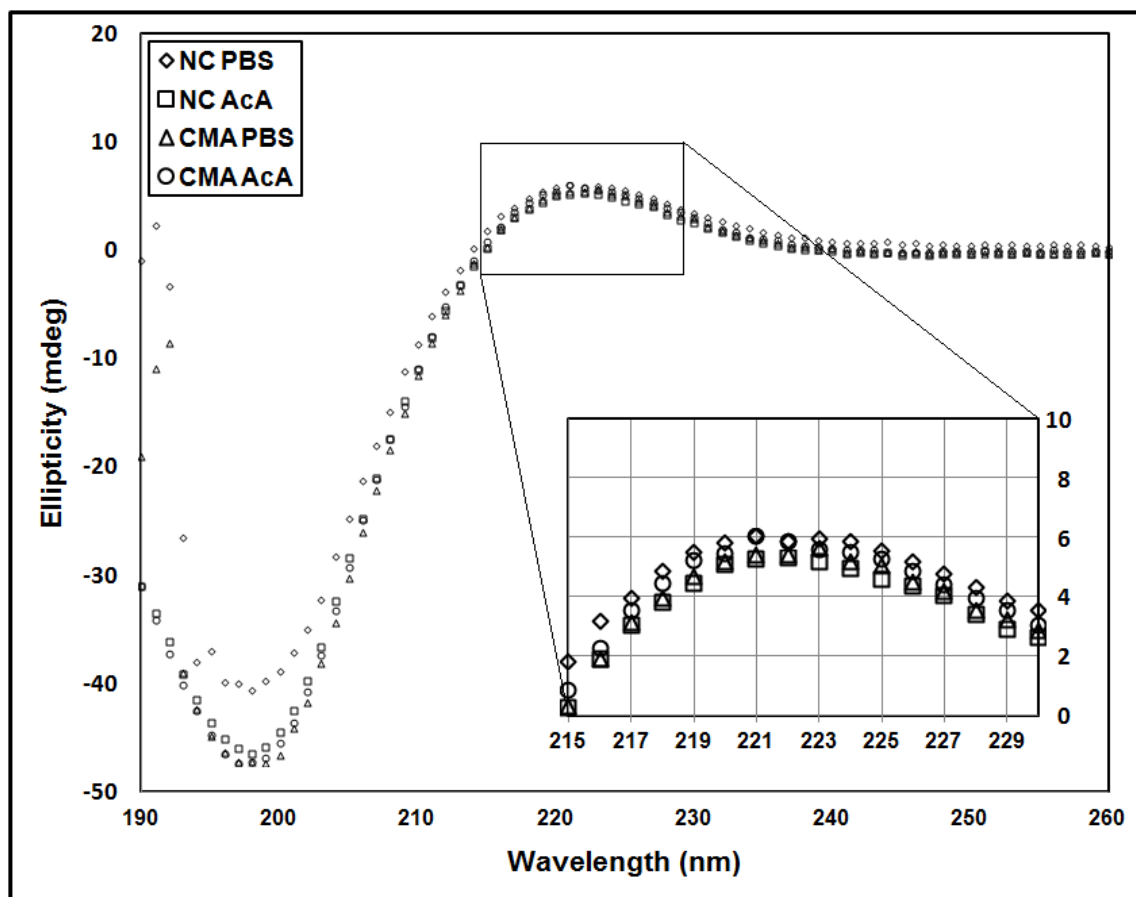


Figure 3-14: CD Spectra of CMA and Native Collagen (NC) in Phosphate Buffered Saline (PBS) and 0.02M Acetic Acid (Ac)

Melting curves of native collagen and CMA in PBS and acetic acid at 0.1mg/mL yielded largely similar results during this round of experimentation (Figure 3-15). Baseline ellipticity was highly consistent among all groups, in agreement with wavelength scan data, as was unfolded melted protein, which all measured close to zero as would be expected for denatured protein with no remaining helical structure. Melting temperatures were identical for native collagen and CMA in acetic acid (42.2°C), which was similar to results obtained previously. However, in this round, we

did not observe the double transition of CMA during melting that was seen previously, as curves for both native collagen and CMA were essentially identical and contained only one inflection. Another departure from the previous data was that here we saw T_M for native collagen in PBS increase slightly, to 28.0°C, while T_M for CMA in PBS decreased marginally to 30.6°C. Additionally, while comparison of the negative ellipticity in the PBS condition was not meaningful in the previous melt curve due to the protein concentration difference, here we can directly compare the curves, and we see that CMA presents a markedly larger ellipticity amplitude. However, it is unclear what type of structure this negative signal is resulting from, and yet further CD experiments are necessary to answer this question.

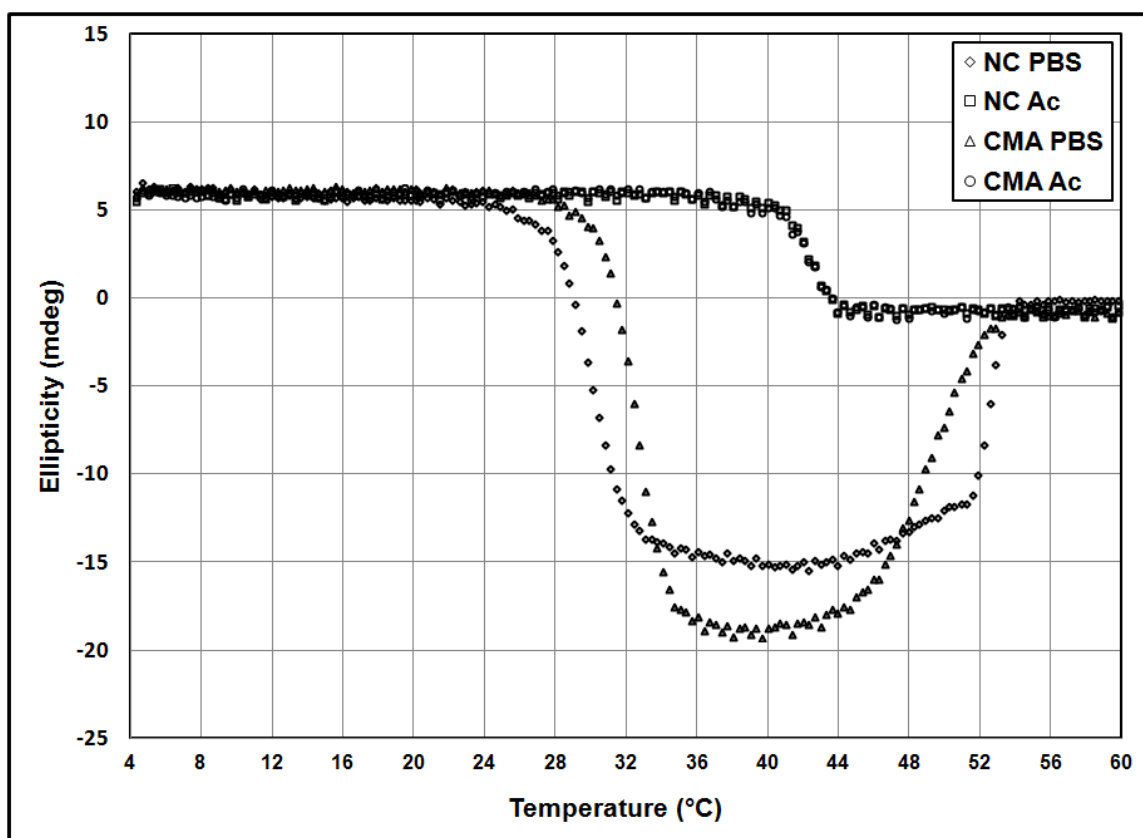


Figure 3-15: CD Melting Curve of CMA and Native Collagen (NC) in Phosphate Buffered Saline (PBS) and 0.02M Acetic Acid (Ac)

3.4.6 DLS

DLS was performed on native collagen and CMA in both PBS and 0.02M acetic acid at 37°C. Samples were all run in parallel, with readings taken at 0, 5, 30 and 60 minutes, and each reading averaging light scatter at 173° over 30 seconds. Steady state in PBS was achieved at 30 minutes, as per plateauing of the derived count rate, which is in agreement with fibrillogenesis kinetics seen via rheometry. Acetic acid steady state was reached at 5 minutes, and likely entailed simple temperature equilibration after sample loading. 5 minutes Comparison of mean peak intensity of CMA and native collagen in PBS at after steady state was achieved revealed that there were 2 distinct monodisperse peaks for both CMA and native collagen (Figure 3-16). Intensity and volume analysis indicated that the majority of the signal was due to the larger peak, likely corresponding to self-assembled fibrils. The smaller peak is likely due to unincorporated protein fragments, which other experiments (discussed later, *Gravimetric Analysis of Gel Mass*) show are negligible, also supported by the relative size of the DLS peaks seen in both the intensity and volume distributions, representative examples of which are shown in Figure 3-17.

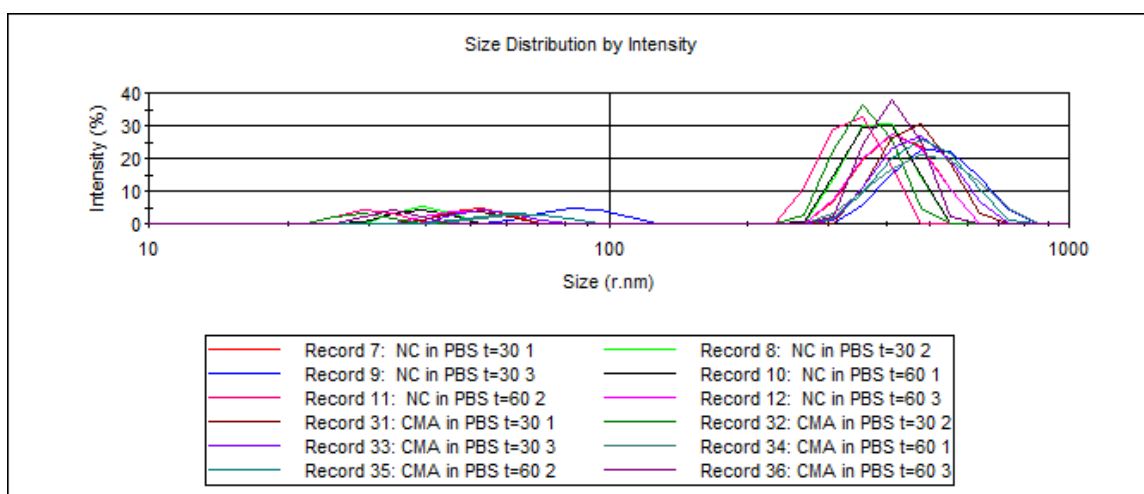


Figure 3-16: DLS Summary Plot of Intensity Peak Size of CMA and NC in PBS

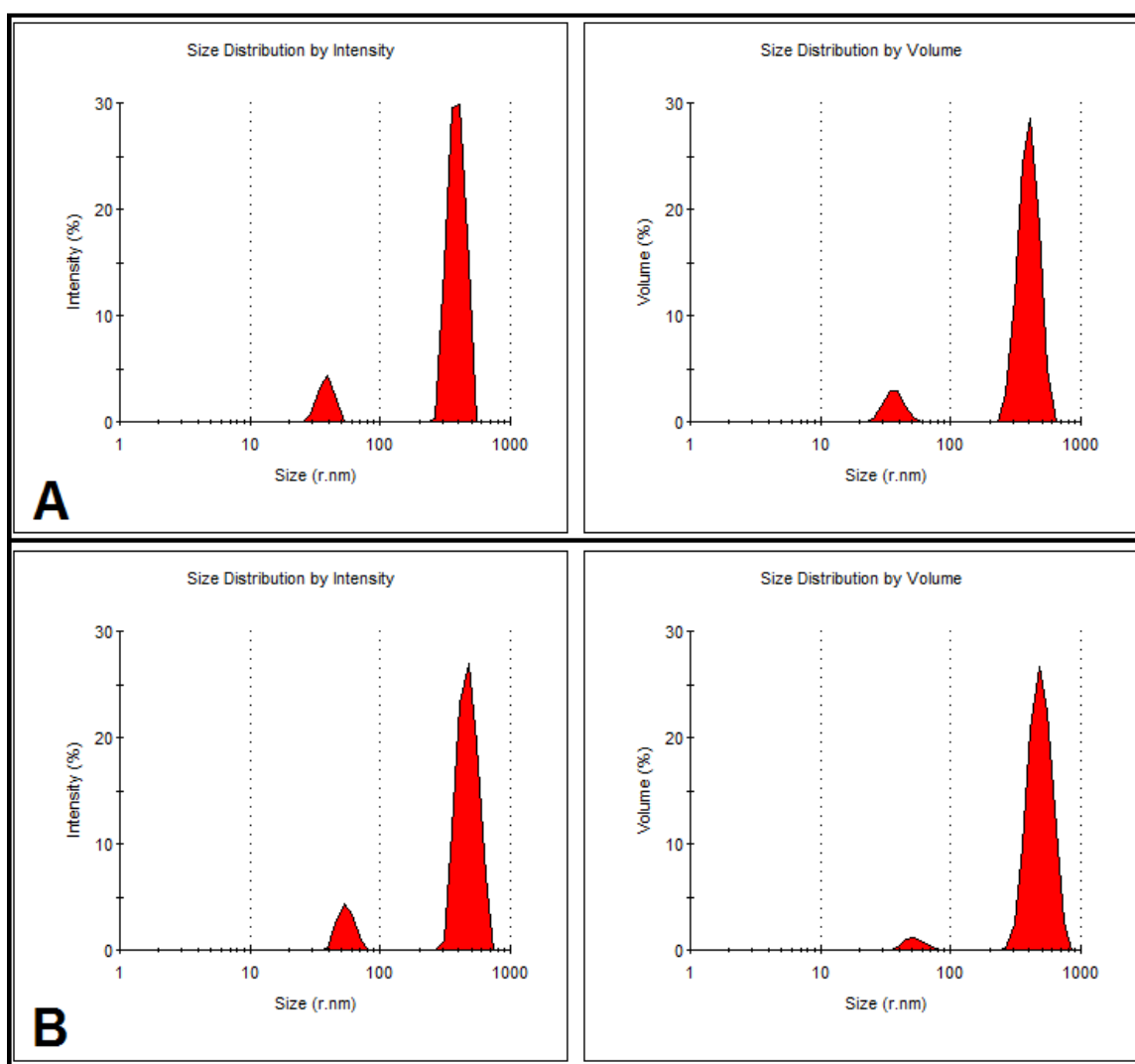


Figure 3-17: DLS Intensity and Volume Peaks for Native Collagen (A) and CMA (B) in PBS. Representative Plots

Average size of both intensity peaks was calculated from the combination of the mean peak size of each peak at 30 and 60 minutes (Figure 3-18). No statistical differences were found between native collagen and CMA for either peak, although the larger peak corresponding to the assembled fiber size trended as larger than native collagen (468.5 ± 56.7 and 430.1 ± 64.1 nm, respectively). Unincorporated/aggregated peptide fragment peaks were nearly identical in magnitude between CMA and native collagen (48.1 ± 14.5 and 48.0 ± 19.6 nm).

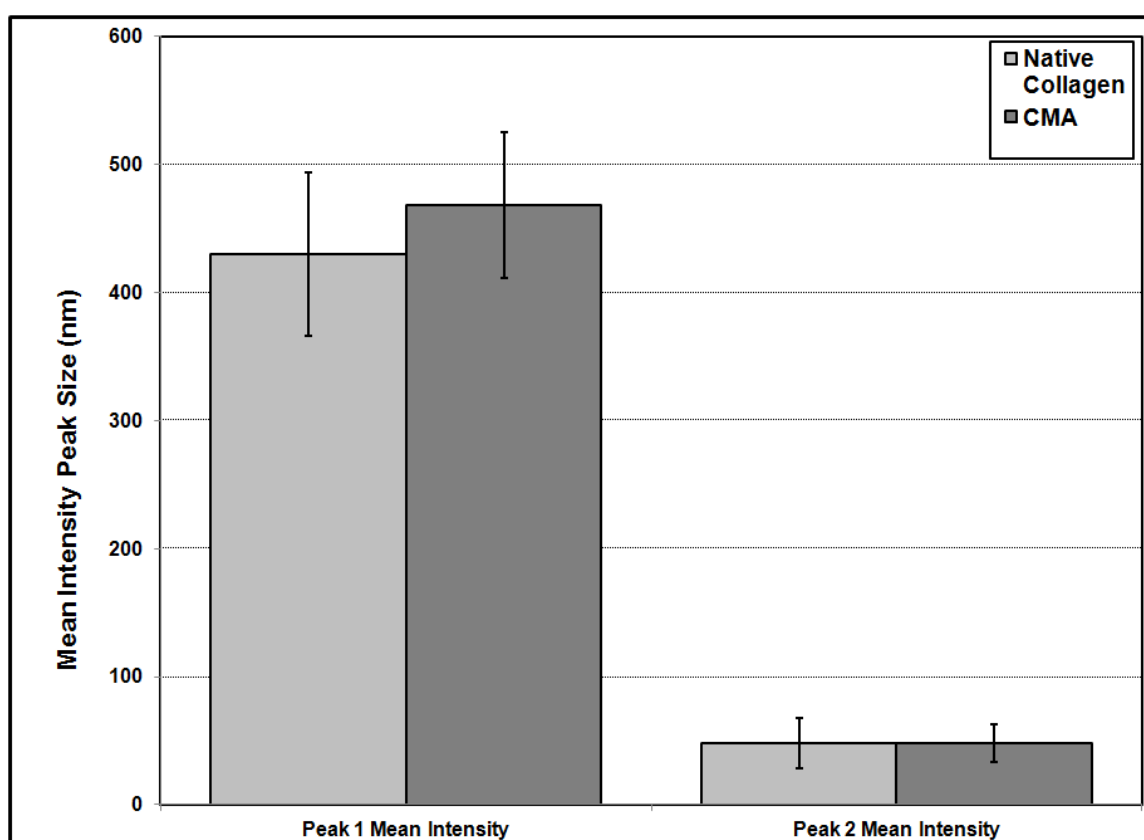


Figure 3-18: DLS Mean Intensity Peak Size (nm) for Native Collagen and CMA in PBS

Acetic acid solubilized native collagen and CMA DLS data was highly polydisperse, indicating the presence of a spectrum of macromer association states, likely due to random aggregation. Analysis of volume peaks in comparison to intensity peaks indicates that the volume fraction of

aggregated protein is small, especially higher order structures, as evidenced by the small volume peaks at larger radii. However, intensity data is skewed due to the higher intensity observed for larger radius objects due to the highly nonlinear relationship between object size and intensity that magnifies the signal of larger objects disproportionately (Figure 3-19). As we do not expect that any significant self assembly is occurring at the acidic pH of the 0.02M acetic acid, peaks corresponding to aggregate structures were excluded and only the single large volume peak was considered for analysis to compare sizes of single triple helical native collagen and CMA macromers.

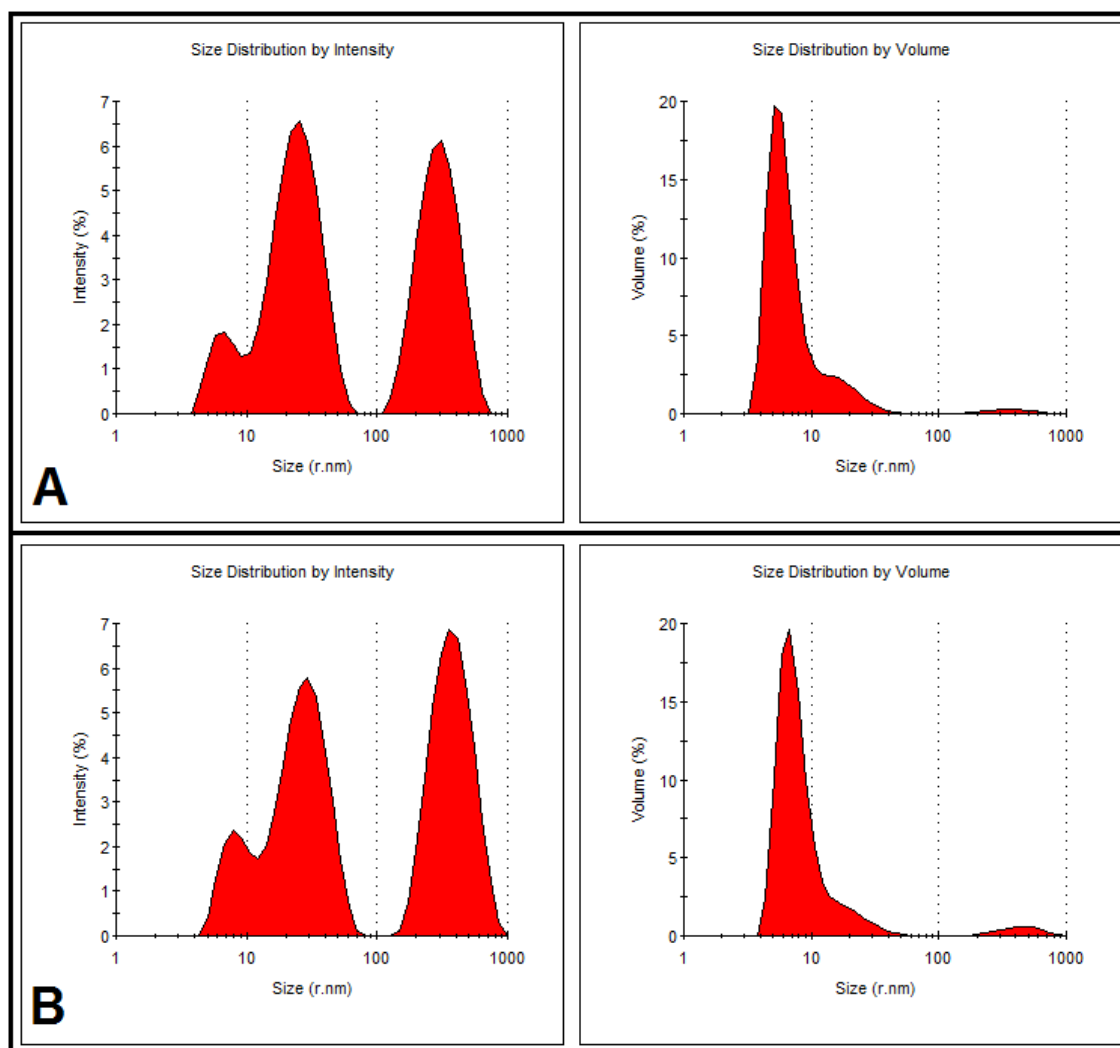


Figure 3-19: DLS Intensity and Volume Peaks for Native Collagen (A) and CMA (B) in Acetic Acid. Representative Plots shown.

Average size of volume peaks corresponding to single macromer was determined from the mean peak radius of the combined data from the steady state time period from 5-60 minutes (Figure 3-20). Analysis of individual macromer size indicated no significant difference between CMA and native collagen (10.6 ± 4.1 and 11.4 ± 4.2 nm, respectively), although overlap from nearby polydisperse peaks resulted in a large experimental error and made statistical numerical comparison of molecular size difficult.

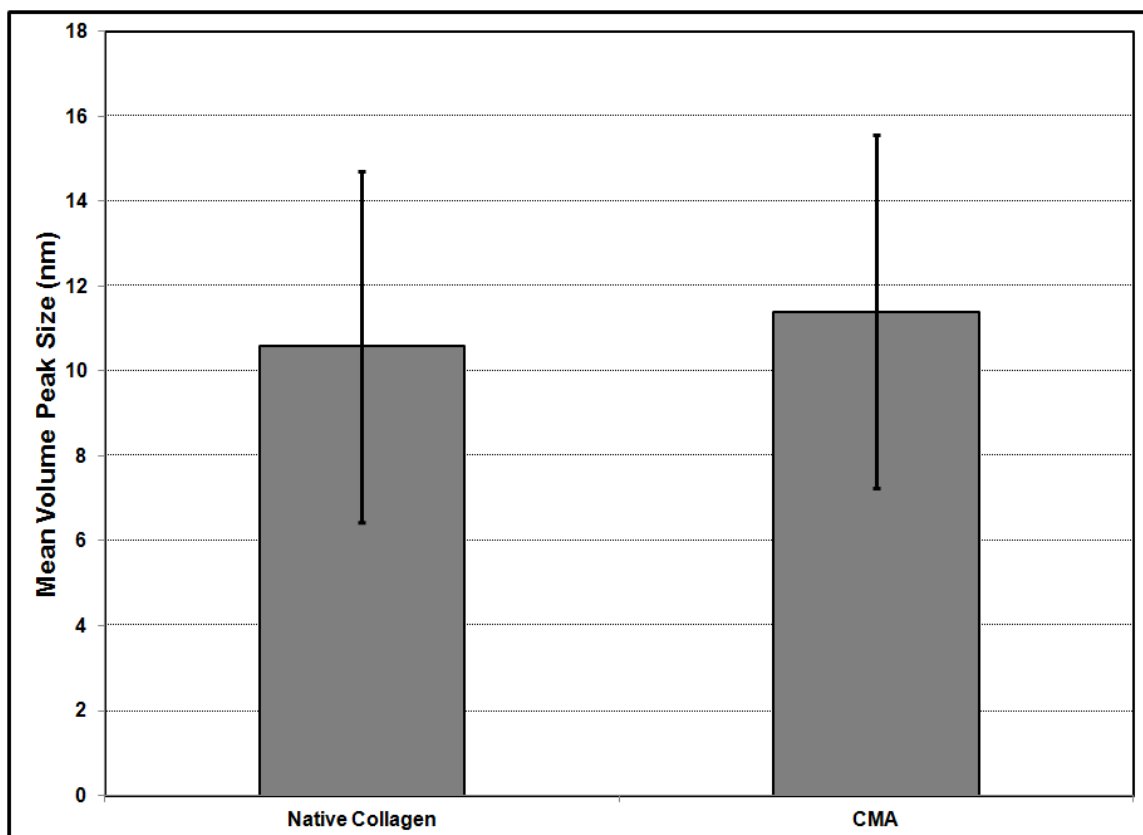


Figure 3-20: Mean Monodisperse Volume Peak Size (nm) for Native Collagen and CMA in 0.02 Acetic Acid

3.4.7 SEM

SEM revealed similar fiber morphology for CMA, photocrosslinked CMA, and native type I collagen (Figure 3-21 A-C). No substantial differences in fiber size, orientation, or quantity were observed, further indicating that the methacrylation reaction largely preserves the quaternary structure of the collagen, and that the photocrosslinking process does not significantly alter the fibrillar ultrastructure. Quantification of fiber diameter (Figure 3-21 D) confirmed that there were no statistical differences in average diameter or size distribution.

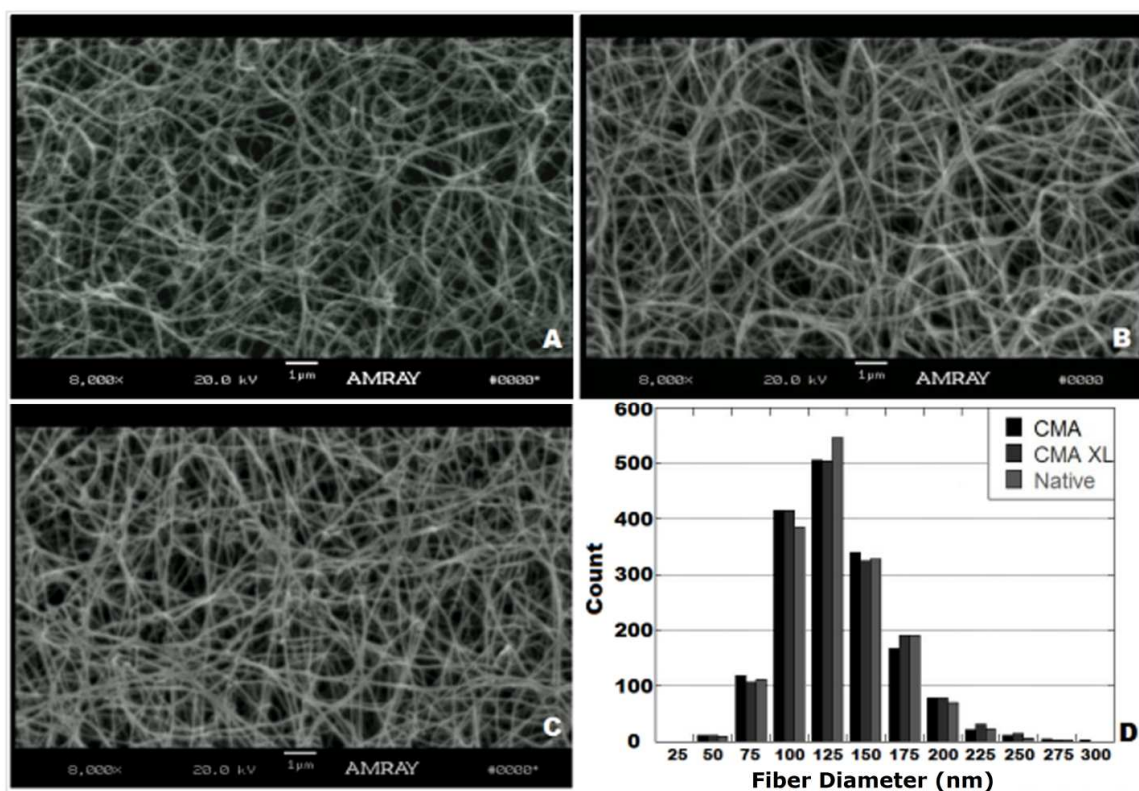


Figure 3-21: SEM of CMA (A), CMA Photocrosslinked (B), and Native Collagen (C); Histogram of Fibril Diameter (D)

3.4.8 Collagenase Degradation

Collagenase degradation assays were performed to assess whether the derivatization reaction or the photocrosslinking process had an effect on enzymatic degradation of the gels. The rate of mechanical degradation, reported here as the reduction in storage modulus as a percentage of initial storage modulus over time, was not statistically different between native collagen and CMA, indicating similar degradation kinetics. However, the degradation rate of photocrosslinked CMA was significantly lower ($P < 0.05$) than both native collagen and uncrosslinked CMA (Figure 3-22 A). A separate collagenase test assayed the percent of protein liberated from the gels following 3 hours of exposure to collagenase. A BCA assay determined the total protein in solution after the degradation time period (Figure 3-22 B). Native collagen ($72.8 \pm 0.2\%$ protein

liberated) was most degraded after 3 hours, followed by CMA ($55 \pm 2.8\%$), and finally photocrosslinked CMA ($35.9 \pm 4\%$).

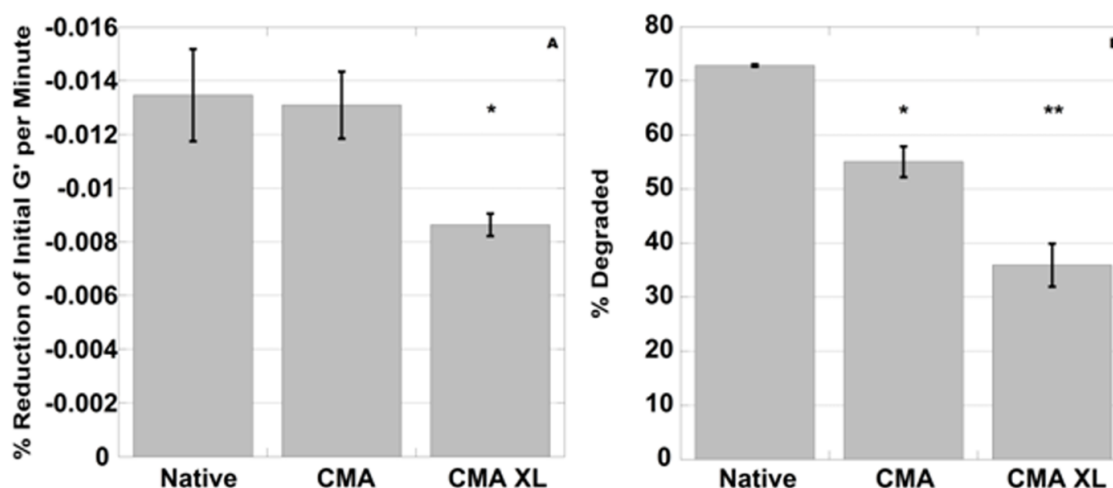


Figure 3-22: Rheological Collagenase Degradation Rate (A); BCA Assay Quantification of Collagenase-Liberated Protein (B)

Ancillary collagenase experiments that admixed enzyme into the precursor solution were developed that did not yield consistent data. This process required augmentation of the gelation kinetics. Previously, we observed that altering the salt concentration through substitution of 10X PBS with less concentrated solutions resulted in faster gelation. To characterize the effect of PBS concentration, we compared native collagen and CMA gelation kinetics with 5X, 7.5X, and 10X PBS as part of the precursor solutions.

At 5X, the native collagen gels began to self assemble as soon as they were plated, and thus were not able to be tested rheologically. Figure 3-23 shows the gelation kinetics for both native collagen and CMA at 10X and 7.5X PBS. Median gelation time, defined as the time when the storage modulus equals half of the average equilibrium G' , was 160 and 75s for native collagen with 10X and 7.5X PBS, and 330 and 210s for CMA with 10X and 7.5X PBS, respectively. The

average equilibrium G' for native collagen with 10X and 7.5X PBS was 514.9 ± 9.3 and 507.4 ± 12.2 Pa, respectively, and for CMA the average G' with 10X and 7.5X was 255.9 ± 6.7 and 253.0 ± 5.4 Pa. Median gelation time differences were statistically significant between 10X and 7.5X PBS among native collagen and CMA groups ($P < 0.05$), while equilibrium G' was not significantly different between PBS concentrations for native collagen or CMA. Thus, changing the PBS concentration can effectively alter native collagen and CMA gelation kinetics in a predictable manner without affecting the mechanical properties of the stabilized gel.

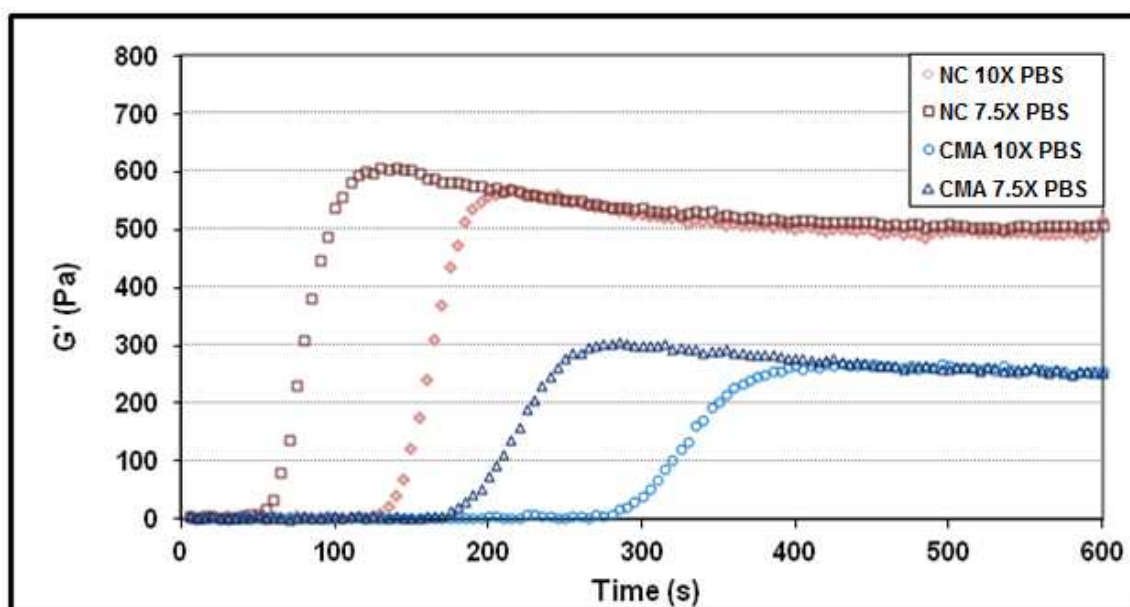


Figure 3-23: Real-time G' : Effect of PBS Salt Concentration on Native Collagen (NC) and CMA Fibrillogenesis Kinetics

3.4.9 Gravimetric Analysis of Gel Mass

Analysis of dry protein mass following self-assembly, extensive washing, and lyophilization revealed that there was no significant difference between CMA (\pm photocrosslinking) and native collagen, indicating that similar amounts of material comprise gels of both materials, and that photocrosslinking has no effect on the solid fraction of gels (Figure 3-24). Theoretical initial mass of protein was calculated as 1.25mg for each sample ($50\mu\text{L} \times 2.5\text{mg/mL}$). Percent of macromer

that underwent incorporation into the fibrillar network was calculated as final mass divided by initial theoretical mass. Acetate and salts included in the precursor solution were considered negligible. Results were $96\pm0\%$, $99\pm5\%$, and $101\pm17\%$ incorporation for native collagen, CMA, and photocrosslinked CMA, respectively.

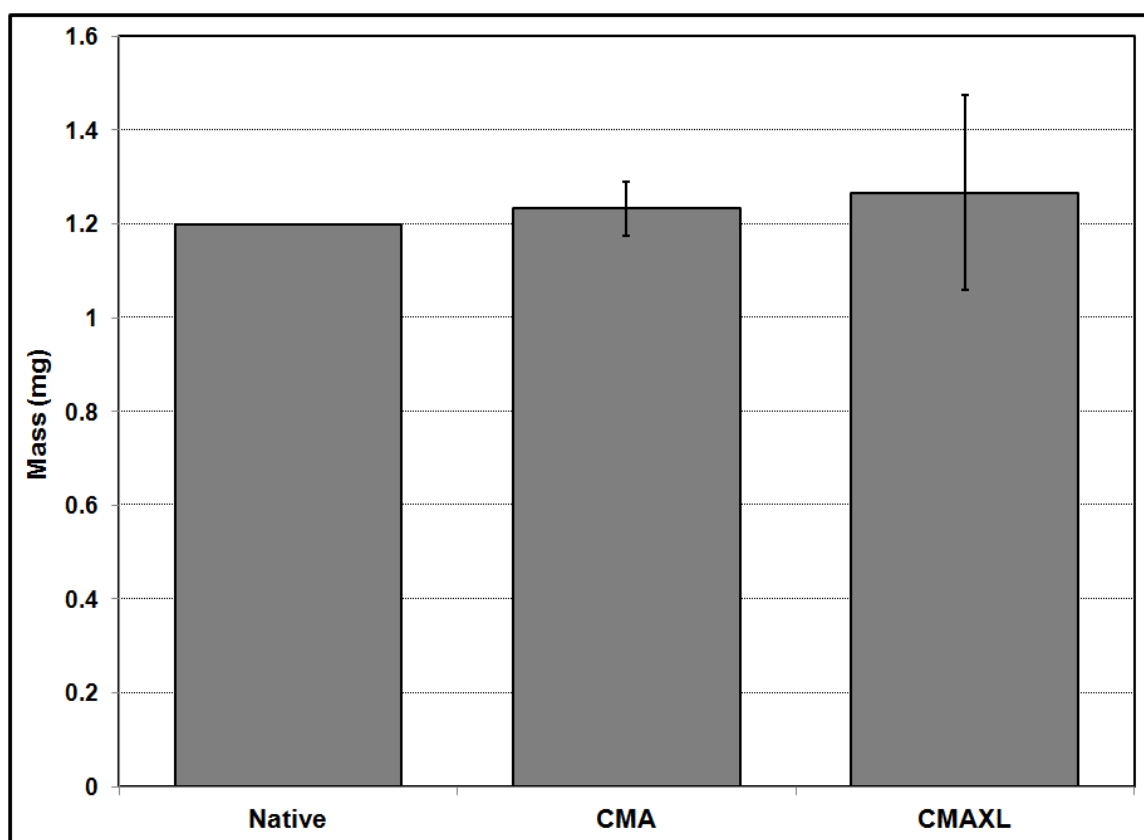


Figure 3-24: Dry Weight of Native Collagen, CMA, and Photocrosslinked CMA Gels

3.4.10 Viscometry

To analyze whether the molecular weight distributions were the different between native collagen and CMA solutions in acetic acid, the viscosities of high concentration (4.4 mg/mL) samples were analyzed over a table of shear rates from 0.01 - 100s^{-1} . Fitting the data to a Moore model, the zero shear viscosity (η_0) for each was extrapolated, with $\eta_0 = 1.0 \pm 0.2$ and 0.68 ± 0.01 Pa s for native collagen and CMA, respectively (Figure 3-25). Zero shear viscosity is assumed to

be proportional to the 3.4th power of the average molecular weight for a polydisperse mixture of polymers [71]. The zero shear viscosity of CMA was significantly lower than that of native collagen, indicating a difference in either molecular weight distribution or hydrodynamic radius of the macromers.

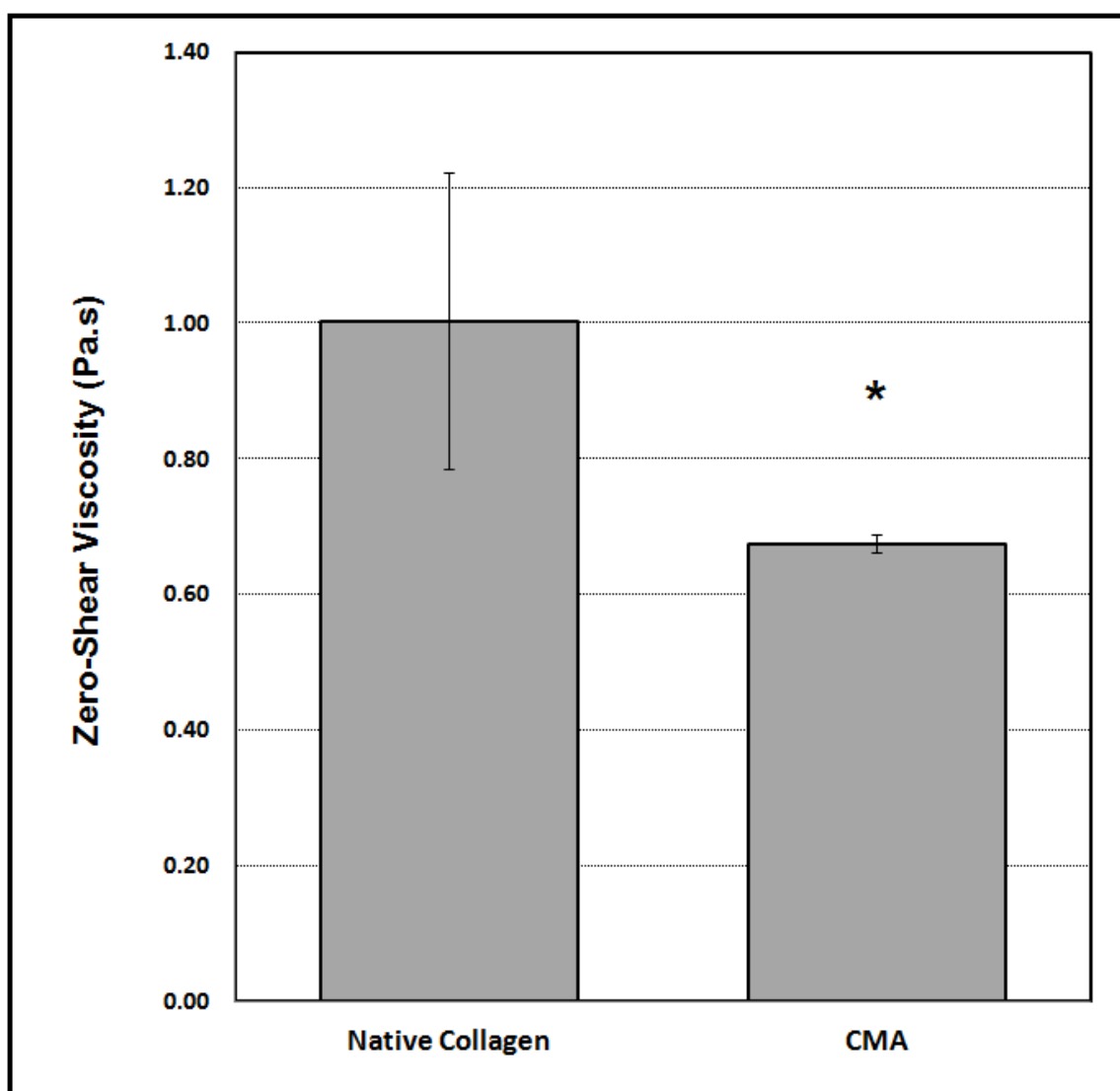


Figure 3-25: Zero shear viscosity of 4.4 mg/mL Native Collagen and CMA at 4°C from Moore fit

3.4.11 Cold Melt Rheology

It was observed previously, including experimentation with CMA for use in biological sponges [72], CMA gels liquefy when stored at 4°C, which was unexpected. To investigate the thermal stability profile of CMA gels compared to native collagen, a rheometry test was performed to measure storage modulus over time as the temperature was first raised to initiate gelation, then lowered at 2°C/min down to 4°C, and back up to 37°C (Figure 3-26). Native collagen and CMA both followed the same trend initially, with G' increasing until the temperature decreased from 37°C to ~30°C, whereupon both gels' G' sharply decreased. However, native collagen G' reached a minimum at around 10°C, and then began to increase again, whereas CMA returned completely to liquid phase, as evidenced by the G'/G'' crossover at 9°C. Upon raising the temperature back up, native collagen again showed a minimum near 10°C, then raised back up to approximately the same stable modulus as prior to the temperature ramping. CMA remained liquid until the temperature was raised back to ~34°C, indicating that fibrillogenesis had to restart completely. Interestingly, CMA G' was more than 100 Pa higher after re-assembly as compared to G' before temperature ramp.

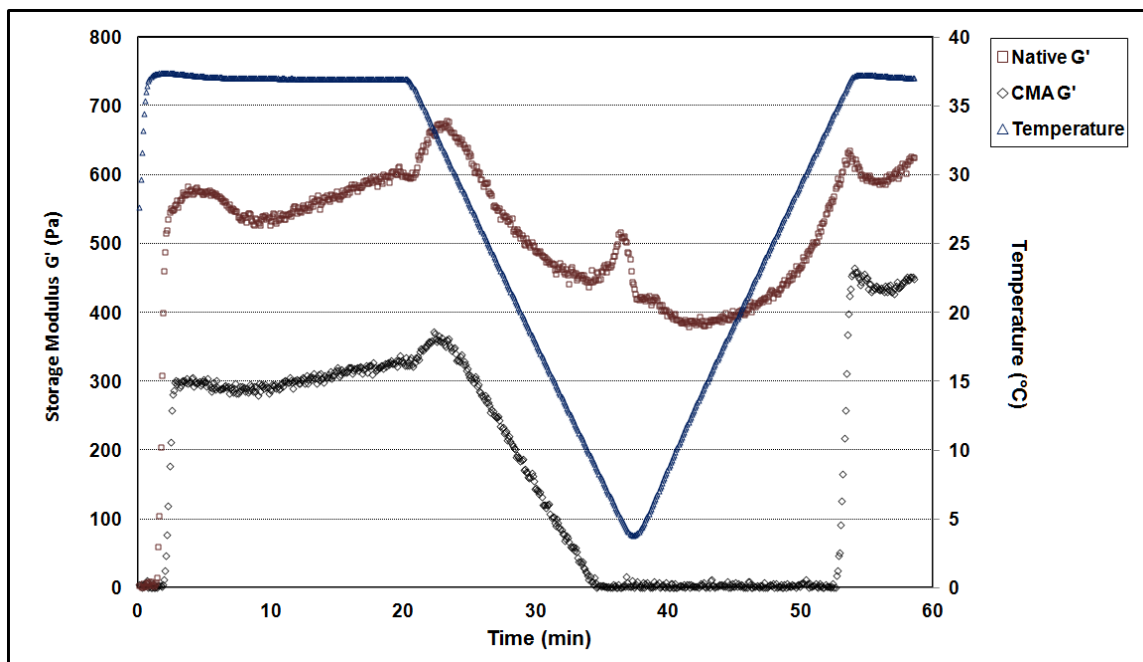


Figure 3-26: Cold melt and reassembly curves of Native Collagen and CMA

A separate experiment was performed with the UV crosslinking module to determine if photocrosslinked CMA exhibited a similar thermal stability profile (Figure 3-27). G' Curves are not directly comparable between data in Figures 3-26 and 3-27 due to differences in thermal response times, although it seems that crosslinked CMA does not exhibit any cooling-induced mechanical instability. Indeed, similar to native collagen and CMA, photocrosslinked CMA increases in modulus upon cooling. However, instead of then entering a phase of decreasing G' , the storage modulus continues to increase by a full order of magnitude as the temperature reaches a nadir of 5°C.

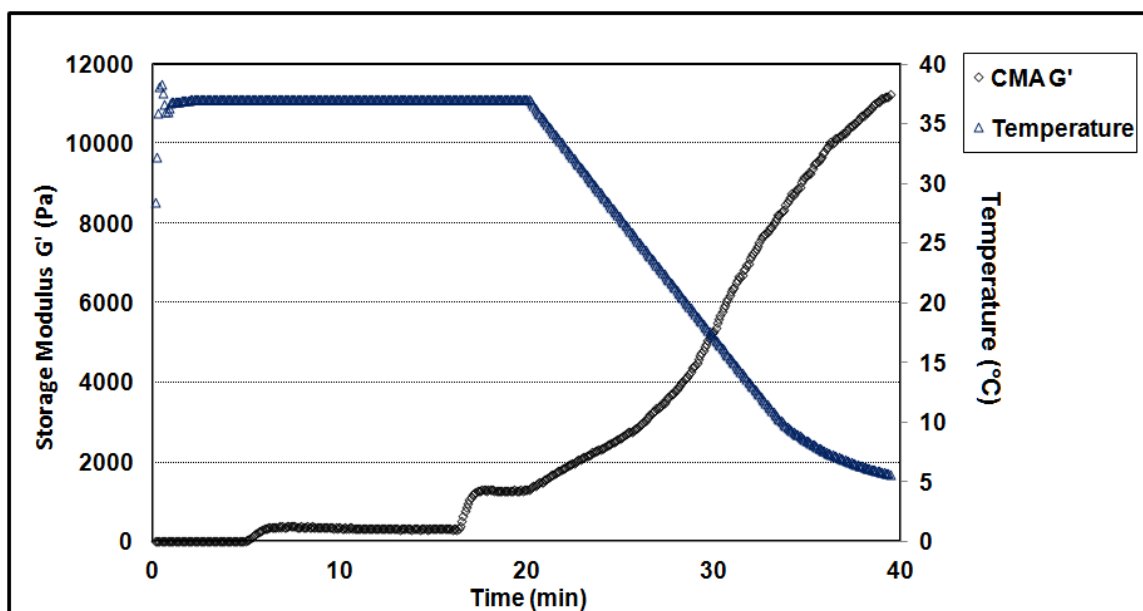


Figure 3-27: Cold Melt Rheology of CMA with Photocrosslinking

<u>Method</u>	<u>Properties Analyzed</u>	<u>Characterization Results</u>
^1H NMR	Chemical Structure	EDC/sNHS derivatization results in grafting of methacrylate groups; no other differences observed Between NC and CMA
TNBSA Assay	Chemical Structure	EDC/sNHS derivatization decreases free amine concentration of CMA to $\sim\frac{1}{4}$ of NC
Rheometry	Hydrogel Mechanicals	Basal CMA G' is half of NC; photocrosslinking increases CMA G' ~ 3 fold over NC
	Kinetics of Self-assembly	NC self-assembly time is $\sim 50\%$ of CMA
CD Spectroscopy	Macromer Structure and Stability	CMA and NC macromers have similar triple-helical content and thermal denaturation temperature
	Fibrillogenesis Thermodynamics	Significant thermodynamic and structural differences exist between CMA and NC at physiological pH and temperature
DLS	Z-average Size/Hydrodynamic Radius	CMA appeared marginally larger than NC; data difficult to interpret due to aggregation, polydispersity, protein linearity
SEM	Fibrillar Structure	CMA and NC have similar average fibrillar diameter and size distribution
Collagenase Degradation	Enzymatic Degradation: Mechanical	Mechanical degradation rate is similar for NC and CMA, lower after photocrosslinking
	Enzymatic Degradation: Chemical	Liberation of cleaved peptide fragments is reduced for CMA; photocrosslinking greatly reduces peptide liberation.
Viscometry	Zero-Shear Viscosity/Hydrodynamic Radius	CMA zero shear viscosity is significantly lower than NC, indicating smaller hydrodynamic radius
Cold-Melt Rheology	Low Temperature Structural Stability	Fibrillized CMA reversibly disassembles at $< 10^\circ\text{C}$; NC remains a solid hydrogel.

Table 3-1: Comparison of Native Collagen and CMA Properties with Various Characterization Methods

3.5 Discussion

We have developed, optimized and characterized a robust, photosensitive material based on type-I collagen to modulate hydrogel mechanical properties via the application of light. Optimization of multiple reaction and process parameters resulted in a repeatable and robust method for reacting commercially available type I collagen with readily available reagents, and is relatively easy to carry out, making it attractive as a platform material for many applications. This method allows us to synthesize CMA by derivatizing a large percentage of the available free amines with reactive methacrylate groups without significantly altering the structural and functional properties that make type I collagen an attractive and versatile scaffold material. These methacrylate groups impart CMA with reactive groups that provide significant mechanical control compared to native collagen. CMA derivatized with this methodology is able to self-assemble from a liquid macromer solution into a fibrillar hydrogel at physiological pH and temperature, with similar assembly kinetics and resultant structure as compared to native type I collagen, although the onset of self-assembly of CMA following the temperature ramp is delayed. This discrepancy might be caused by subtle changes in the protein structure or by loss of low-molecular weight protein fragments during dialysis of the reaction milieu. We also developed an advanced characterization platform utilizing modern rheological testing equipment that allows full temporal characterization of hydrogel behavior during self-assembly and photocrosslinking in real-time. Analysis of photocrosslinking kinetics allowed us to identify and characterize a large parameter space spanning a range of photocrosslinking factors such as macromer concentration, gelation time, light intensity, exposure time, and photoinitiator concentration. This body of data allows predictive design of optimized conditions for application-driven scaffold modulation in cases where biological constraints dictate specific material properties.

Rheological analysis revealed that both CMA and native collagen formed mechanically stable gels less than 10 minutes after temperature was increased to 37°C. Following photocrosslinking for 90 seconds, the storage modulus of the crosslinked CMA is increased nearly 6-fold, and is almost 3 times that of native collagen at the same concentration. The 5-6 fold increase of storage modulus from uncrosslinked CMA to the fully crosslinked state represents a significant range of mechanical properties achieved through this system, with addition control afforded by varying the starting CMA concentration. The storage modulus of uncrosslinked CMA hydrogels is slightly lower than that of native collagen, potentially due to unwanted crosslinking between collagen molecules during the synthesis step, which, while minimized through the large molar excess of MAA during synthesis, may still occur to some degree over the course of the 24 reaction. Another possibility is that the reduction in storage modulus is due to the loss of intrafibril ionic associations between the positively charged amine groups and negatively charged residues, which form stabilizing salt bridges [73].

Analysis of triple helix content and protein structure stability through CD spectroscopy provided insight into differences between CMA and native collagen in various states and temperatures. In the acid-solubilized state, triple helix content appeared similar for CMA and native collagen. In the physiological pH-buffered PBS, ellipticity was similar for both CMA and native collagen, although in the initial comparative wavelength scan it appeared that overall ellipticity was slightly lower than acetic acid, which might be expected due to some self-assembly resulting in overall triple helix concentration going down as macromers polymerized. However, in the second set of experiments, there was no difference in ellipticity between any group in either buffer, indicating that triple helix concentration was equal and that self-assembly was not occurring to an appreciable extent. Given the inconsistencies in the data of the initial data, experimental error was likely responsible. Taken together, the wavelength scan data implies

that derivatization of collagen to CMA does not appreciably disrupt the macromeric triple helical structure, a claim strengthened by the similarity of our native collagen spectra with previously published results elsewhere [74]. Furthermore, pH-driven conformational changes produced no significant differences in CD signal at 4°C. However, CD spectra for the melt curves showed intriguing differences in fundamental thermal stability properties between CMA and native collagen. Based on our calculations of melting temperature, native collagen had essentially an identical melting temperature than CMA in the soluble, acidic environment, a trend observed in both experiments. However, analysis of curve geometry in the first melt experiment revealed an inflection in ellipticity present in CMA that is not seen in native collagen. Since this inflection is minor compared to the major drop in ellipticity due to complete protein unfolding, it was not picked up in the melting temperature calculation, but it does indicate that there may have been a subtle change in macromer stability before the triple helix completely denatured. However, this phenomenon was not seen in the second melt curve experiment. Hence, we can't conclude whether this was due to some experimental error during CD sample preparation, aberrant crosslinking during synthesis, or a fundamental reason such as fewer stabilizing salt bridges in CMA compared to native collagen. Further CD studies are planned to evaluate structure at different temperatures and wavelengths to help answer these questions. Interestingly, CD analysis of CMA and native collagen at physiological pH indicated that CMA had a significantly higher melting temperature than native collagen, which would imply that CMA is somehow more stable than collagen. However, following the initial melt, we observed development of a large negative ellipticity, indicating that another structure may be formed at this temperature, likely a product of the self-assembly into a coiled coil with optical properties different than those of the triple helical macromer. Thus, the higher melting temperature of CMA may actually be related to the latent self-assembly we have observed with rheological experiments. The

considerable gap in negative ellipticity between native collagen and CMA observed in the second melt experiment may imply that there is a substantial difference in either the geometry or stability of the fibrillized quaternary structure. Additional wavelength/temperature scans near the respective transition temperature will need to be performed in the future to resolve the nature of the assembled structure and may improve our understanding of the fundamental properties of both CMA and native collagen. These results may have important biological consequences in terms of *in vivo* remodeling of fibrillar networks, as one theory suggests that evolution of mammalian collagen sequences has resulted in thermodynamically stable molecules that are intentionally unstable at normal body temperature to facilitate matrix remodeling [75]. Whether CMA or native collagen can be remodeled more readily *in vivo* at physiological temperature remains unknown.

DLS experiments provided another avenue for determination of molecular structure of CMA as compared to native collagen. Acid solubilized protein size intensity spectra were highly polydisperse due to random protein aggregation, although filtering the size peaks from volume data and focusing on the peaks due to single macromers indicated that protein size was similar for both CMA and native collagen. However, error due to the polydispersity makes drawing conclusions about the structure of CMA impossible. A different methodology designed for discerning between the sizes of large, linear polymers might allow better resolution of whether CMA macromers are appreciably different from native collagen in molecular weight. Gel Permeation Chromatography (GPC) may be a suitable method, although at present our laboratory is not equipped to perform these experiments. DLS analysis of self assembled CMA and native collagen in PBS was more readily interpreted due to the monodispersity of intensity peaks. These data indicated that CMA and native collagen fibrils were similar in size, although CMA appeared to be marginally larger. Again, large error suggests that DLS may not be a

particularly effective method for analyzing CMA due to the size and aspect ratio of the molecules involved. Overall, DLS data corroborated information obtained in other experimental modes leading us to believe that structurally CMA and native collagen are similar.

Analysis of quaternary structure via SEM image analysis indicated that average fibril diameter and fibril size distribution were essentially identical between native collagen and CMA, which is expected tertiary structure has been preserved, as the CD data propose. While fibrillar structure was qualitatively similar, there were occasional rosette-like structures seen within the CMA gels. These rosettes could be due to branching incidents during self-assembly, which could be a result of multiple collagen molecules being crosslinked during the CMA synthesis reaction, or from spontaneous reaction between methacrylates of CMA macromers in solution after reconstitution. These rosettes may potentially disrupt the local mechanical properties of the gels by forming small discontinuities within the fibrous network that may be prone to microscopic tears, thus resulting in a lower bulk storage modulus. This reduction in bulk material properties can be offset by altering the initial CMA concentration. However, there is the possibility that localized differences in material properties exist at the microscale, and these pockets of heterogeneity may have undesired consequences with respect to the cell matrix interface. A more in depth examination of the mechanical microenvironment with a more appropriate testing modality such as atomic force microscopy [76] may help elucidate these questions in the future. Minimizing the storage time and light and heat exposure of CMA solutions prior to use in forming gels may also minimize this phenomenon, although the presence of these rosettes in gels from freshly synthesized and reconstituted CMA indicates this may not be the dominant mechanism responsible and that some ectopic crosslinking between collagen macromers is unavoidable in the derivatization reaction as developed.

Viscometric analysis of CMA and native collagen solutions in acetic acid showed significant differences that appear to contradict other experimental data. Specifically, DLS and SEM data indicate that CMA macromers are similar in size to native collagen, and that the assembled fibrils are similar in size as well. Extrapolation of zero shear viscosity from a Moore model fit of viscosities at various shear rates indicates that CMA has a significantly lower average molecular weight compared to native collagen. While these data likely indicate an actual difference, there is some question about the validity of the data at lower shear rates, the curve fitting had significant error at that part of the curve. What appears to be an artifactual torque signal may be caused by small torque provided by the relatively inviscid fluid at the low shear rates. Further experimentation with this modality using larger samples with a larger diameter tool may provide more reliable data.

We also compared protein mass of CMA gels with and without photocrosslinking to native collagen to determine if there was a difference in the amount of protein that was incorporated into the fibrillar structure. If during the self-assembly process a specific fraction of CMA was sufficiently modified or denatured such that it could not undergo fibrillization, then it should diffuse out of the network and the gel would have less mass. Less protein per unit volume would potentially help explain the lower mechanical properties seen in CMA compared to native collagen at identical macromer concentrations. However, there was no significant difference in protein mass between any of the three groups analyzed, which leads us to conclude that CMA and native collagen gels contain the same percentage of protein, thus CMA derivatization doesn't prevent any fraction of the macromer solution from fibrillizing. This result further strengthens our hypothesis that CMA is highly similar to native collagen, and that the

mechanical differences are likely due to subtle differences in triple helical stability rather than higher order protein structure.

Collagenase degradation assays were performed to determine if the methacrylate derivatization had any effect on the enzymatic degradation of the CMA gels before crosslinking, and if photocrosslinked CMA gels were significantly less degradable than the uncrosslinked CMA and native collagen samples. Since type-I collagenase requires an intact triple helix to effectively degrade fibrillar collagen, if the tertiary structure was indeed altered significantly then collagenase degradation rates should also be affected, which may influence the biodegradability of the material as well as the extent that cells may remodel the scaffold [77]. Also, crosslinking of collagen has previously been shown to decrease the collagenolytic degradation rate, as crosslinks between collagen molecules increase the number of ligations necessary to liberate protein fragments and affects the availability of recognizable triple helical segments [78,79]. We evaluated separately the mechanical degradation and the chemical degradation of pre- and post-photocrosslinked CMA gels as compared to native collagen. Rheological testing was performed to evaluate the percent reduction in initial storage modulus over time during a continuous hour-long test. Chemical degradation was assessed via sampling collagenase-exposed gels over a three hour period. Rheological tests showed that the mechanical degradation rate was not statistically significant between native and uncrosslinked CMA gels, while photocrosslinked CMA gels showed a significantly lower degradation rate ($P < 0.05$). The chemical degradation assay indicated that the degradation rate of CMA was lower than that of native collagen gel, and that crosslinking CMA further decreased the degradation rate. This apparent discrepancy between the rheological and chemical assays may again be attributed to ectopic crosslinks that result in anomalous structure formation during fibrillogenesis. These non-helical structures may be protected from collagenase degradation by a lack of enzyme binding

sites as well as stabilizing covalent bonds. Thus, they are not liberated into solution, as seen by the BSA assay, and do not contribute to the mechanical strength of the gels. As such their lack of degradation has no effect on the storage modulus during the rheological collagenase degradation assay. Most importantly, in both assays the photocrosslinked CMA was significantly less degradable. This aspect may prove extremely useful, as photocrosslinking may be exploited to spatially control the degradation rate of individual regions of the scaffold.

Additionally, characterization of the thermal stability of CMA gels compared to native collagen revealed that CMA gels could be quickly liquefied upon reducing temperature below 10°C, and that this liquefaction was completely reversible upon restoration to physiological temperature. Our understanding of this process is quite underdeveloped at this time, as native collagen does not exhibit this trait. Such a characteristic is unique, and could possibly be exploited for a number of applications. For instance, for tissue culture, *in vitro*, CMA could be used as a ‘smart polymer’, in which a layer of CMA would be gelled as a substrate for cell adhesion and then returned to a liquid phase to harvest cells later simply by cooling the flask on ice, and without the use of potentially detrimental proteolytic enzymes such as trypsin. Furthermore, since photocrosslinking appears to completely remove this cold melting behavior, patterned crosslinking followed by cooling and washing could be used to control gel geometry quickly and easily using only temperature and light. Further investigation of this phenomenon, while tangential to this thesis, may coincide with better understanding of the structure of CMA.

3.6 Conclusions

We have created and characterized a novel method for derivatizing type-I collagen with photocrosslinkable methacrylate groups, resulting in a robust material that can be mechanically

tuned via the application of light. We can effect up to a 6-fold increase in the storage modulus with application of UV light for only 90 seconds, and the change in stiffness can be easily tuned within that range by adjusting the amount of UV exposure. Our laboratory has previously shown that modulation of the mechanical properties of collagen via chemical crosslinking provides cues that can be used to direct cellular behavior [52]. While a multitude of strategies exist for chemically crosslinking collagen to affect bulk material properties [80,14] these techniques cannot easily be applied in a localized manner, nor can they affect the properties as rapidly. The power to locally tune the mechanical properties within a gel is desirable for creating a soft-tissue scaffold with controlled heterogeneity. This material largely retains the characteristic structure and attributes of fibrillar collagen while also being mechanically dynamic, resulting in a self-assembling, bioactive, biocompatible hydrogel that provides a high degree of spatial material control. We believe this material has utility as a potential scaffold for regenerating soft tissues with irregularly shaped defects which require an injectable, self-assembling scaffold to fill the wound site without further disruption of nearby viable tissue. This material may be particularly useful as a scaffold material for central nervous system injuries, as the range of stiffness allowed from uncrosslinked to crosslinked CMA is similar to that of native CNS tissue [81]. Following stabilization of the hydrogel within the defect, mechanical heterogeneity may be introduced, allowing the creation of complex, customizable scaffolds that mimic the structure of the lost tissue and increase the chance of restoring function by recapitulating some aspects of the original tissue.

CMA retains a large number of the attractive attributes of native collagen as a degradable, self-assembling, fibrillar hydrogel. Furthermore, there are significant differences in other qualities that may be further exploited in applications beyond the scope of this thesis. Most notably, the mechanical properties of CMA are unique at low temperatures, after fibrillization, and upon

thermal denaturation. In addition, enzymatic degradability is altered following derivatization. Making use of these differences may allow for creation of novel cell and tissue scaffolds that afford utility in a variety of desired situations untenable with conventional collagen scaffolds. However, further characterization of the molecular structure is necessary as our understanding of the molecular structure of CMA is incomplete, which may hamper our ability to take full advantage of its capabilities as a dynamic biomaterial.

3A Appendix: Optimization of CMA Photocrosslinking and Rheological Testing

Utilizing the same rheometry protocol as with previous experiments, CMA derivatized with the 10:1 MAA:E-AMINE ratio was shown to be readily modulated following photoinitiation of 0.1% (w/v) I2959 with the UVL-21 lamp. Storage modulus of CMA was more than doubled after crosslinking (Figure 3A1), while loss modulus was minimally changed (not shown). While storage modulus was markedly lower for CMA as compared to native collagen at the same concentration, gelation appeared similar and manual manipulation of gels revealed similar bulk properties, although CMA gels did appear to be more fragile during sample loading.

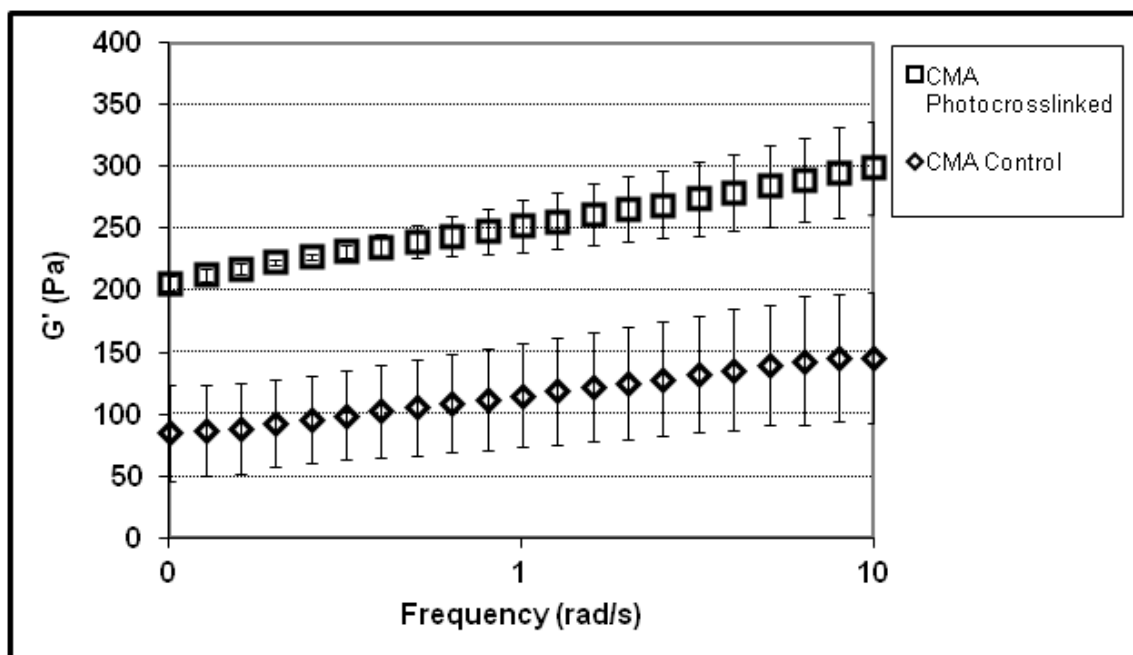


Figure 3A-1: G' : CMA +/- Photocrosslinking via SR-2000

During this period of optimization, the SR-2000 rheometer became unusable due to instrumentation breakdown, and further testing was transferred to a similar rotational rheometer, a Bohlin Gemini II. While this rheometer operates with the same basic principle as the SR-2000, some differences in instrument control were somewhat different, with sample loading being the most impactful on this research. Specifically, the rate at which the upper geometry lowered onto the sample was less manually operated, with the result being that samples were loaded under different compressive rates and forces. We compared SR-2000 data with native collagen gels run with similar oscillatory frequency sweep parameters to the Gemini to determine the effect that the difference in loading conditions had on the storage modulus data. As seen in Figure 3A2 below, there was a significant difference in the rheological behavior of native collagen gels between the 2 instruments, with storage moduli measuring higher on the SR-2000 compared to the Gemini II across all shear frequencies. Additionally, whereas on the SR-2000, the storage modulus displayed a logarithmic dependency on frequency, on the Gemini

If the storage modulus appeared to increase exponentially at higher frequencies. However, both instruments provided measurements in the same general stiffness range, and the variability between samples was acceptable, so the Gemini II was used to further optimize CMA as the relative difference between crosslinked and uncrosslinked materials was quantifiable even if a direct comparison with previous moduli data was not.

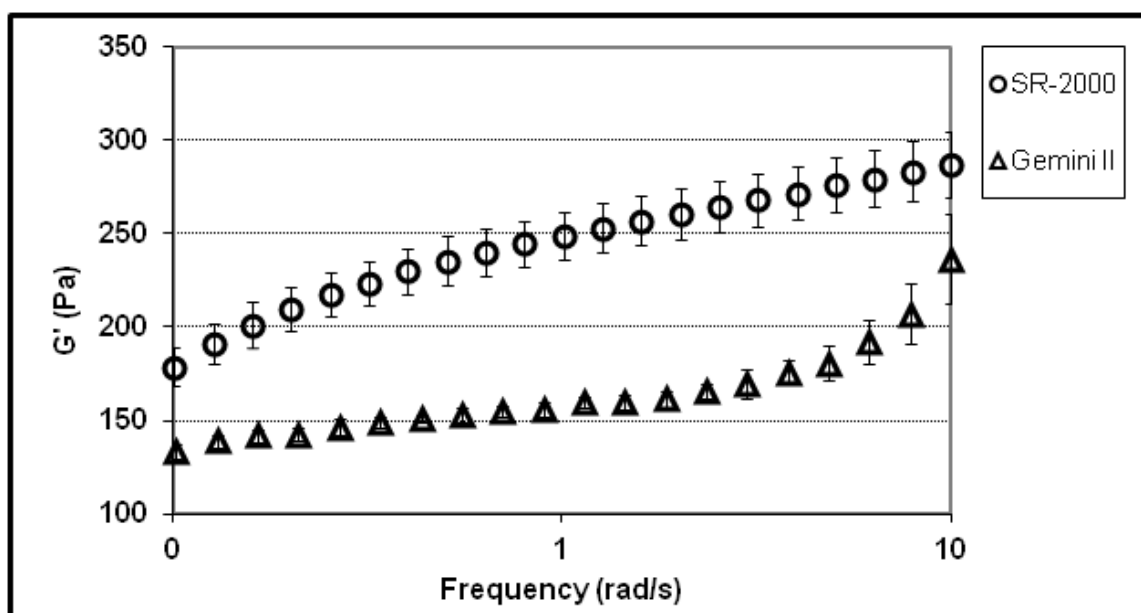


Figure 3A-2: Native Collagen: Rheometer Comparison

Next, we analyzed whether CMA photocrosslinking rheology curves were comparable between the two instruments in order to continue optimization studies. As seen in Figure 3A3, a more than two-fold increase in storage modulus due to photocrosslinking was observed on data from both instruments, although the G' data distribution is again different. In particular, the storage moduli of the CMA control conditions were on average much higher than seen on the SR-2000. There also appeared to be more variability between CMA control samples on the Gemini II, as seen by the larger standard deviation. As CMA gels are inherently weaker than either native

collagen or photocrosslinked gels, successful loading of the sample onto the instrument without disrupting the gel structure is challenging. Accordingly, the variability in observed mechanical properties due to gel manipulation may be exacerbated by the change in loading procedure. Whether this was effect was due to loading conditions or from another intangible factor such as difference in heat transfer or parallel plate surface properties of the Gemini II versus the SR-2000 was not determined. Additional operator practice and development of the state of the art with this system may have produced decreased variability.

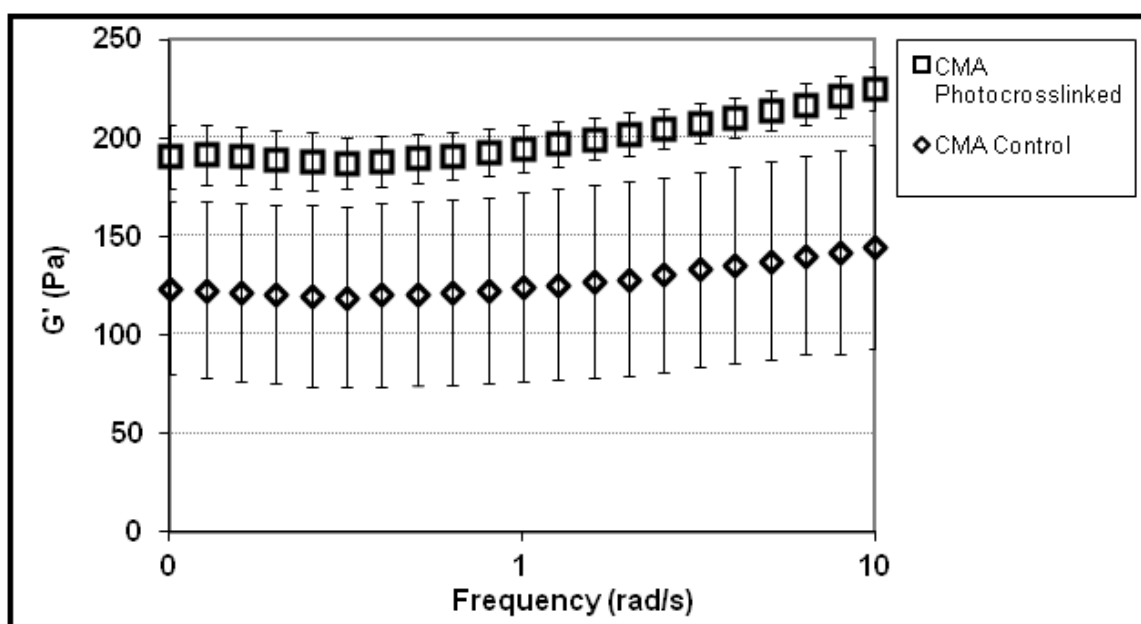


Figure 3A-3: G': CMA +/- Photocrosslinking via Gemini II

We next looked at what effect CMA macromer concentration had on the relative increase in storage modulus of the gels achieved by photocrosslinking. Final CMA concentrations of 2, 2.5, 3, and 3.5 mg/mL were looked at. All samples were crosslinked under the same conditions, 0.1% I2959 and 5 minutes exposure to UV from the UVL-21. Due to the nonlinearity of storage modulus at higher shear frequencies on the Gemini II, comparisons were made at an

intermediate frequency of 1 rad/s, which was typically in the linear viscoelastic range regardless of which rheometer was used. The results indicate that storage modulus increases linearly with macromer concentration (Figure 3A4). Variability among CMA groups made statistical analysis of this linearity difficult, as the storage modulus was not significantly different between adjacent concentration groups. However, the average fold increase of G' after photocrosslinking of 2.2, 2.2, 2.5, and 2.2 for concentrations of 3.5, 3, 2.5, and 2 mg/mL, respectively, indicate that the fold change is invariant of the CMA concentration within this range of concentrations.

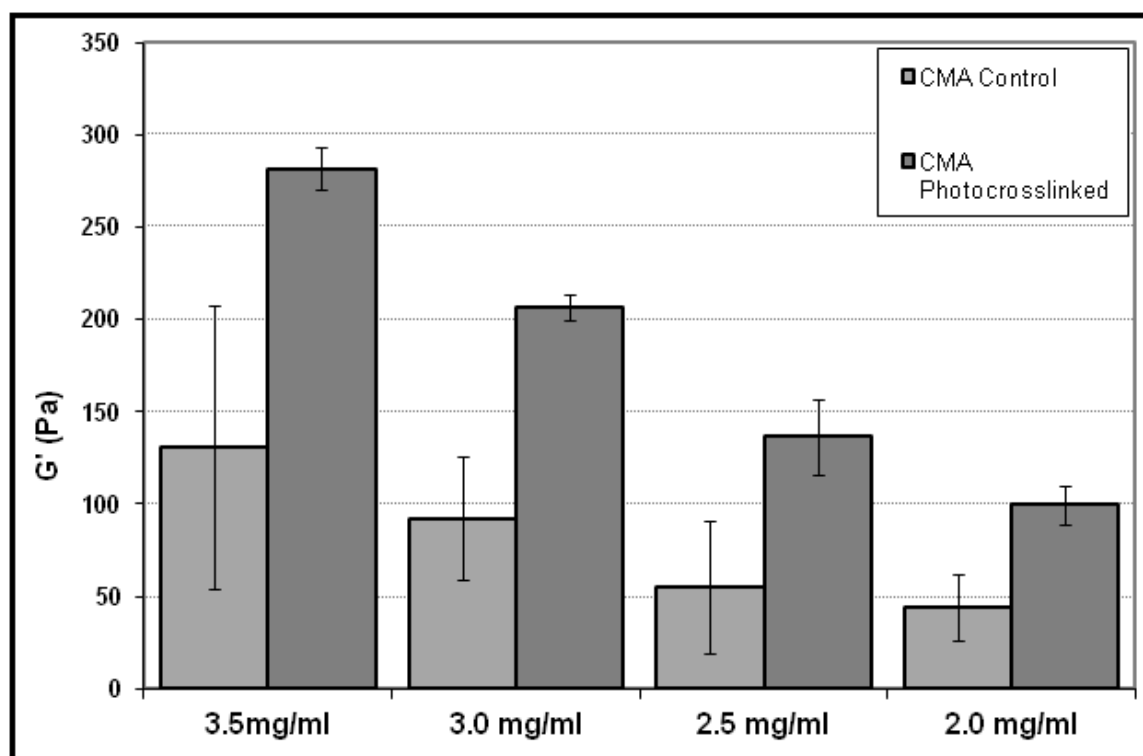


Figure 3A-4: G' : Effect of CMA Concentration +/- Photocrosslinking

Next we examined whether increasing the UV exposure time had a discernible effect on the photocrosslinking efficiency. Standard protocol was used to make CMA (3 mg/mL) gels containing 0.1% I2959, and exposed to UV light for 0, 1, 2, 3, 5 and 10 minutes using the UVL-21 source. Samples were run in triplicate. Full frequency sweeps were obtained for all conditions to

ensure valid data, although for clarity of comparison storage moduli at only one frequency were analyzed. Again, 1 rad/s was used.

These results, displayed in A5, indicate that under these conditions, there was no significant difference between 1 and 10 minutes of exposure, implying that maximal photocrosslinking occurs during the first minute and that subsequent exposure does not result in any further increase in stiffness. Conversely, while not statistically different, the modulus after 5 or 10 minutes did appear to be slightly lower than the modulus after 1-3 minutes.

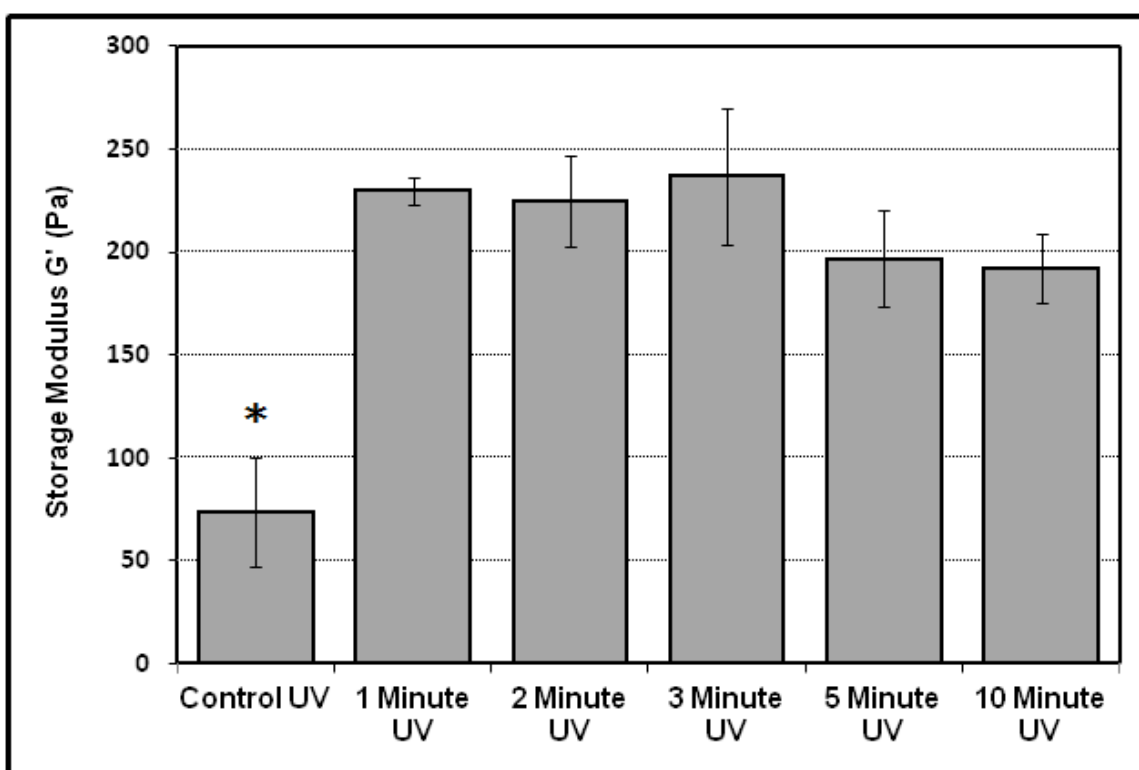


Figure 3A-5: G': Effect of UV Exposure time on Photocrosslinking

Continual optimization of the CMA derivatization protocol through rheological analysis and NMR studies led to increasing the molar ratio of MAA:E-AMINE to 40:1 to drive the conversion of more amine groups toward the methacrylamide product, including sulfo-NHS in the reaction,

and more thoroughly dialyzing the unreacted MAA. Photocrosslinking parameter optimization dictated that CMA at 2.5mg/mL, crosslinked by exposure to UVA for 3 minutes provided the greatest increase in storage modulus. Furthermore, optimization of the loading procedure to remove the gel transfer step, instead loading and testing the gel directly on the glass slide affixed to the lower plate via vacuum grease, resulted in a reduction in experimental variability. These optimizations are evident in Figure 3A6, which shows a 3-fold increase in storage modulus at low shear frequencies, as well as the greatly minimized variability in both control and photocrosslinked samples. The storage modulus of the uncrosslinked CMA is slightly lower than with the previous derivatization protocol.

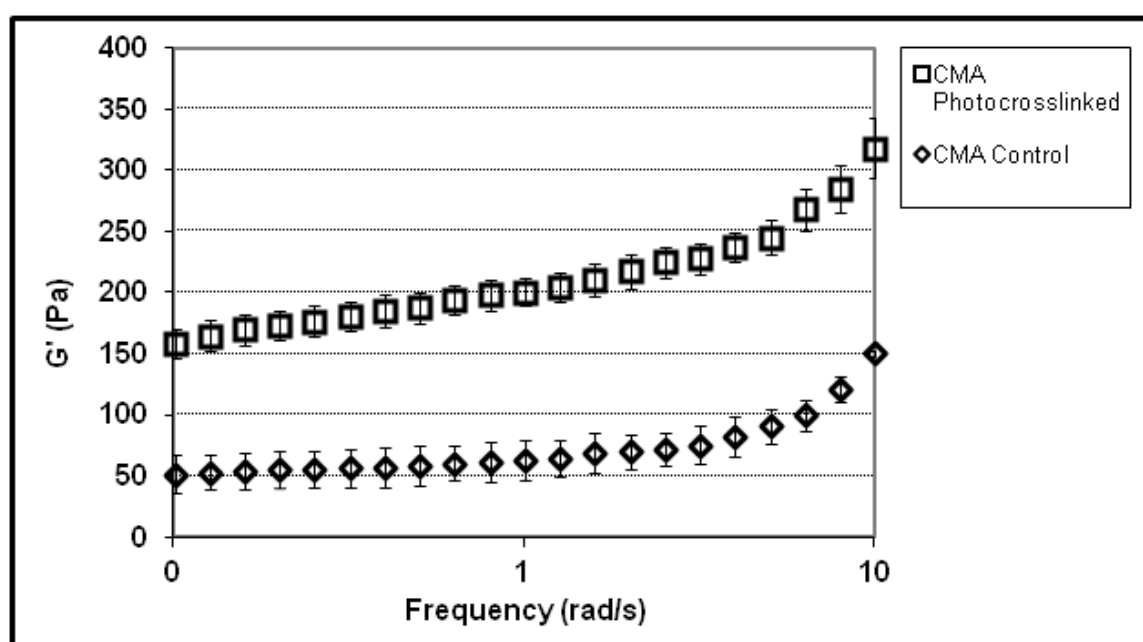


Figure 3A-6: G': Optimized CMA +/- Photocrosslinking. Data From Bohlin Gemini II

The procurement of a new, state-of-the-art Kinexus Ultra rotational rheometer allowed a substantially improved characterization of the material properties. In particular, torque sensitivity, system response, temperature control, and displacement resolution on the Kinexus Ultra allowed us to obtain better data with smaller samples, with a greater throughput provided

by much quicker temperature equilibration. While the previous data was useful for optimizing the derivatization and photocrosslinking protocols to the present state, some tests were rerun on the Kinexus to provide data continuity going forward. Using the optimized reaction and crosslinking protocols described previously, samples were tested using a standard frequency sweep with similar parameters to the Gemini II settings. Loading of samples was markedly easier due to customizable subsequences available using the rSpace software package. Briefly, the upper plate was lowered quickly until the sample was barely in contact with the plate, and then an exponentially slower mode was used to move the geometry into testing position at the standard gap height. Results of the frequency sweep (Figure 3A7) show that equivalent data is obtained with the Kinexus platform as compared to previous modalities, and that the loading conditions are repeatable, seen by the low variability. Furthermore, the exponential tail that was observed with the Gemini II curves was not present, possibly due to enhanced loading control which provides better fidelity to the material properties by maintaining structure during loading.

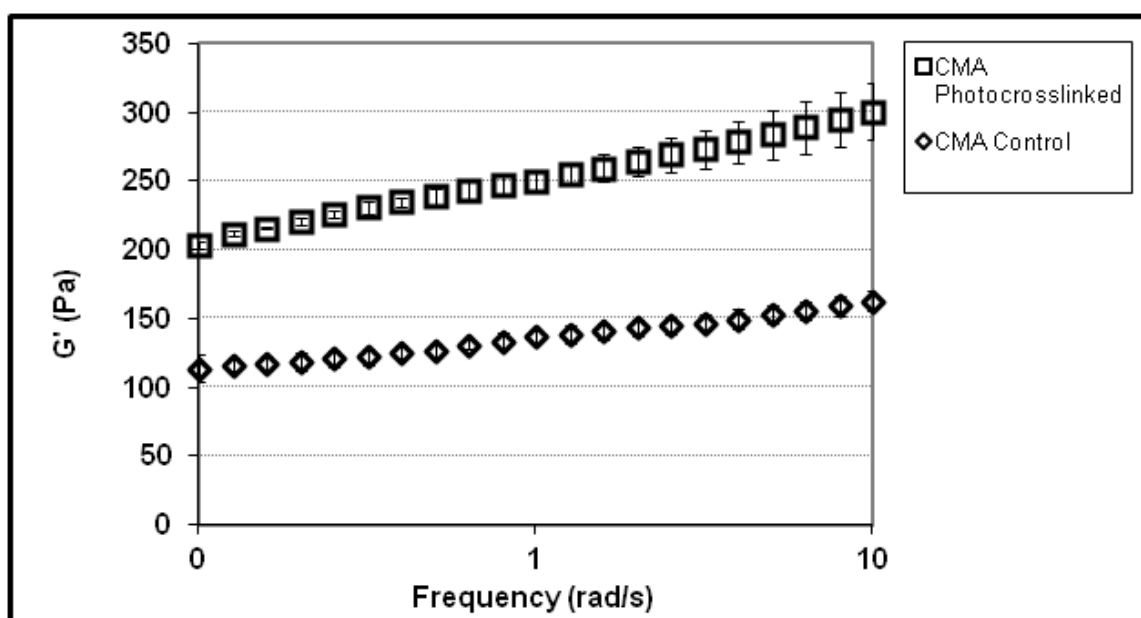


Figure 3A-7: G' : Kinexus Validation - CMA +/- Photocrosslinking

Concurrently, to verify that the increase in stiffness from photocrosslinking was due solely from the presence of the derivatized methacrylamide groups and not from existing side-chain moieties, we exposed stock collagen to the standard photocrosslinking conditions. To test this, unmodified native collagen gels (2.5 mg/mL) containing 0.1% I2959 were exposed to 2 minutes UVA to determine if any change in mechanical properties occurred. Here, we saw that there was no difference in storage modulus after exposure of native collagen to photocrosslinking conditions (Figure 3A8). Thus, it was concluded that methacrylation is the sole mechanism by which CMA becomes sensitive to the UVA/I2959 photoinitiation system.

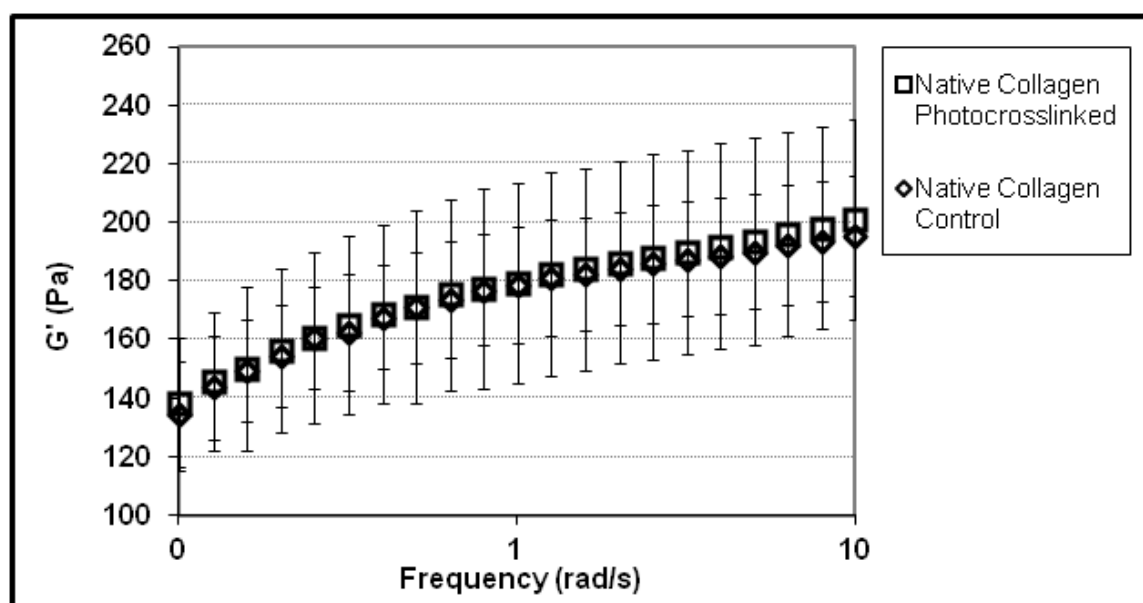


Figure 3A-8: G': Native Collagen +/- Photocrosslinking Conditions

Additionally, it was observed that the foam content in CMA was substantially higher compared to native collagen following reconstitution. To measure the effect of the final product of reconstitution shear conditions, CMA was put into solution with high and minimal shear via adjustment of mixing angle, which resulted in negligible foam formation in the low shear condition. CMA storage moduli with and without photocrosslinking were compared between

the 2 mixing regimes using the standard frequency sweep. Figure 3A9 shows the marked increase in moduli both before and after photocrosslinking using the low shear reconstitution protocol.

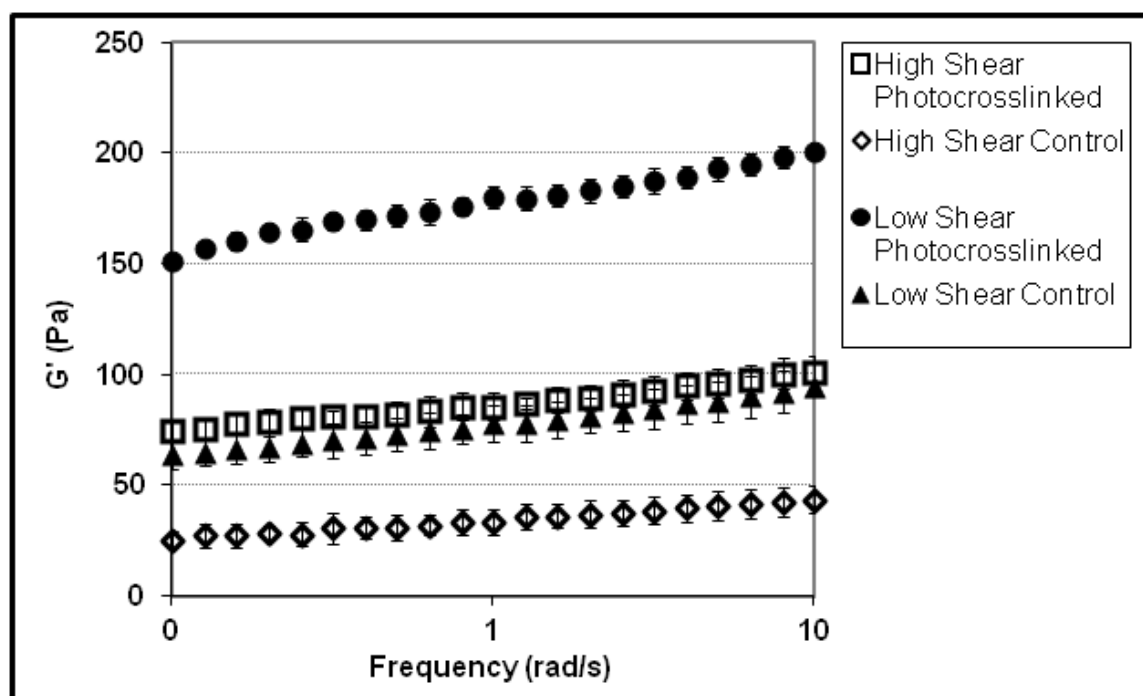


Figure 3A-9: G': Effect of Shear during CMA Reconstitution +/- Photocrosslinking

Another issue that was producing variable results was the consistency of the source material, type I collagen. While it is generally accepted that biological materials will have lot-to-lot variability, it was unclear how severe this might be and what parameters that might change with respect to our process. Heretofore, the same Lot of collagen, #141, had been used for the majority of the CMA optimization experiments. This lot was no longer in stock, and Lot 159 was instead supplied. We ran a standard frequency sweep with native collagen from both lots and compared storage moduli. As evidenced by Figure 3A10, native collagen from Lot 159 has a significantly lower storage modulus than Lot 141.

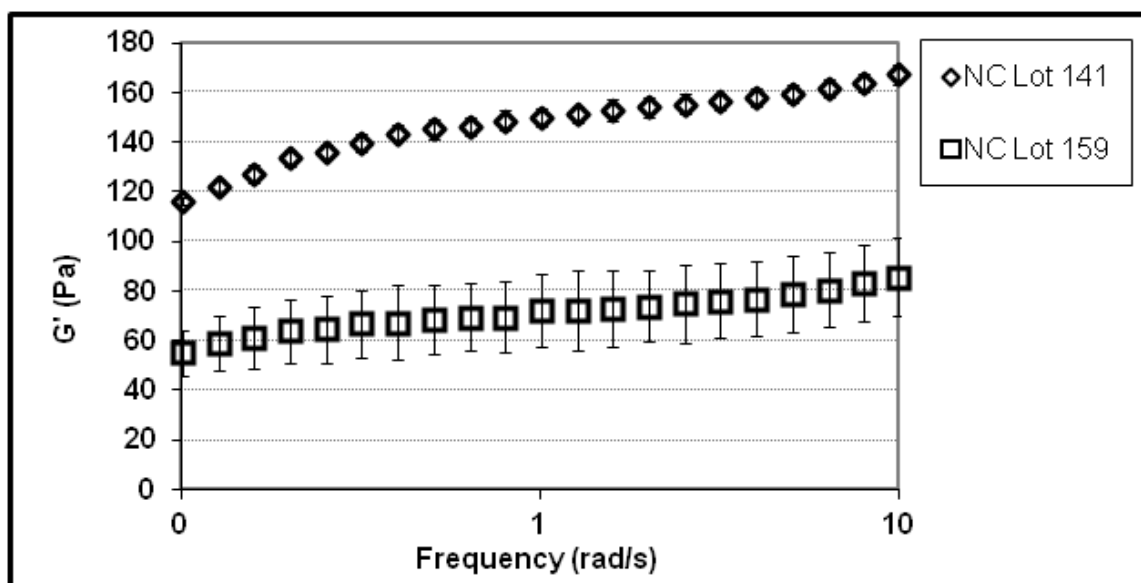


Figure 3A-10: G': Native Collagen QC Lot 141 vs. 159

To Compare how this translated to CMA modulus, since previously it was seen that methacrylate derivatization significantly reduced the basal G', a frequency sweep of a newly synthesized batch of CMA from Lot 159 was performed. Here, as displayed in Figure 3A11, we saw that the storage modulus of CMA from this lot was similar to that of CMA made with the previous collagen Lot. Thus, it seems that comparisons of raw G' values on CMA batches made from different Lots of collagen are reasonable even if the mechanical properties of native collagen are inconsistent. The limited difference in basal CMA G' between Lots 141 and 159 after derivatization, in comparison with the significant difference between native collagen G', indicates that methacrylate derivatization or the associated processing results in a more consistent starting material.

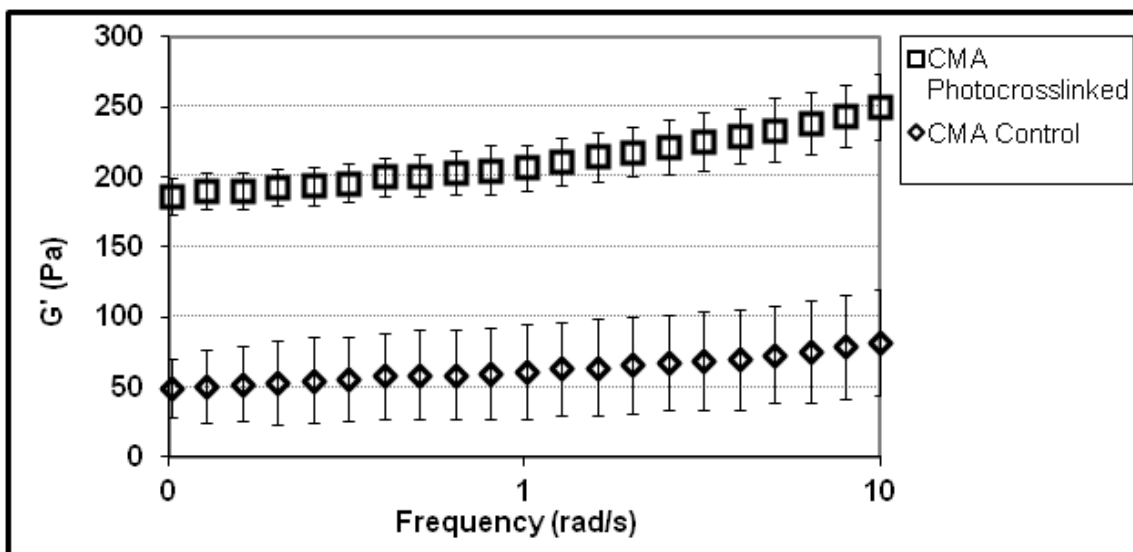


Figure 3A-11: G' : CMA Synthesis QC: NC Lot 159

A process development breakthrough came about upon the acquisition of a prototype UV-crosslinking lower module. Using a lower Kinexus module designed for in-cup rheometry, we inserted a modified geometry that contained a quartz glass upper plate. Using a liquid light guide connected to the EXFO lamp, we were able to form gels in the testing geometry, and then apply UV light while testing. This modality provides more accurate material properties through the omission of loading steps that not only disrupted material structure, as well as no longer requiring exogenous compression of the sample to obtain data, which is of particular concern with viscoelastic materials. Using the 'in situ' testing modality, the gel forms in the exact shape that it is tested in, providing data that directly corresponds to the true material properties. Utilizing the superior torque sensitivity and temperature control capabilities of the Kinexus platform, we were able to develop a methodology for analyzing the gelation kinetics of collagen and CMA, as well as characterizing the photocrosslinking process in real time by looking at the change in storage and loss moduli over time at a single oscillation frequency. The oscillation frequency of 1 rad/s was used according to previously discussed rationale. 200 μ L aliquots of

liquid phase, ice-cold, pH-neutralized collagen or CMA macromer solutions were loaded onto the quartz plate and the upper 20mm plate was lowered in 2 steps to allow the solution to flow symmetrically into the gap, forming an ideal cylinder. Solvent traps were used to minimize evaporation, and then temperature was raised to 25 or 37°C to initiate gelation. Moduli were measured continuously during and after gelation to obtain complete gelation curves. Time until gelation initiation (marked by G'/G'' crossover), gelation rate (linear slope of increase in G'), and equilibrium moduli were used to quantify gel and crosslink formation and kinetics. Real-time analysis was also used for quality control of collagen to validate new EPC Lots and verify that batches prepared by newly trained personnel conformed to expected parameters, as previous QC procedures were purely qualitative (Figure 3A12).

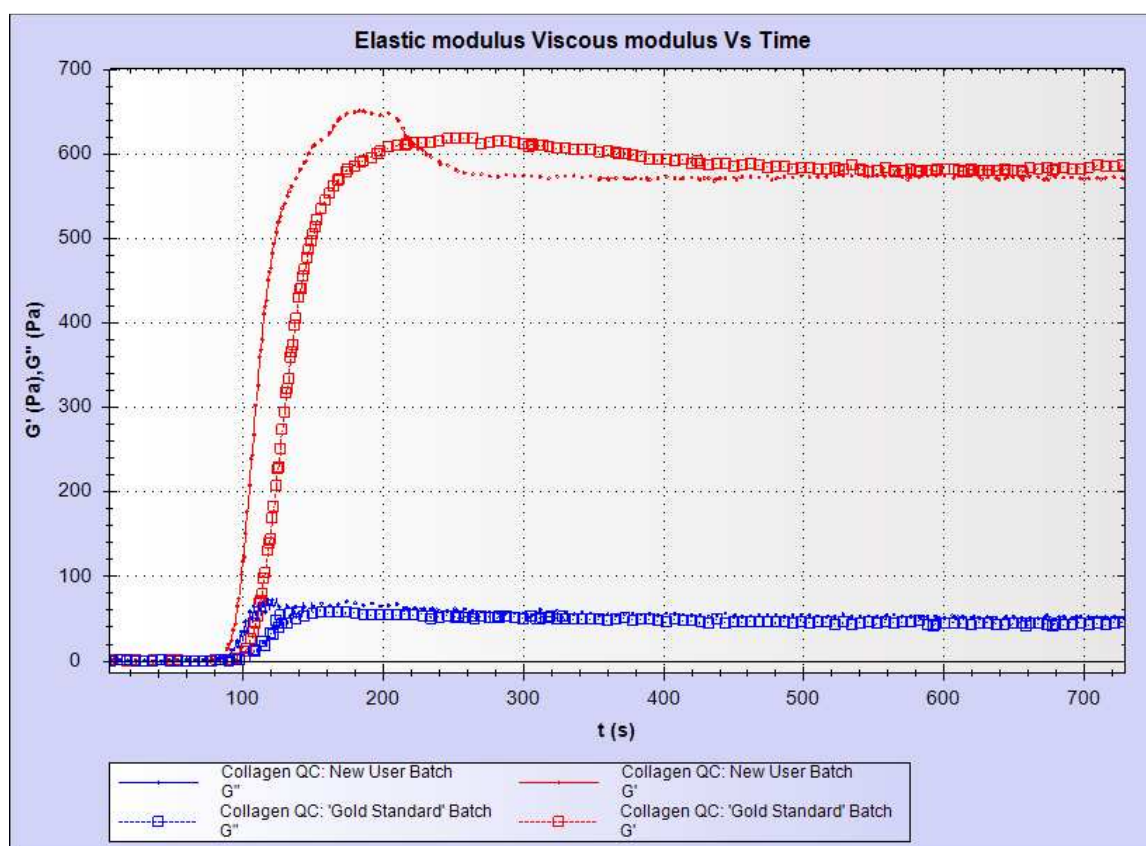


Figure 3A-12: Kinexus rSpace Software Output Chart of QC Validation of a New Native Collagen Batch

By analyzing the rate of modulus increase, as well as being able to directly observe when crosslinking was complete, it was possible to quickly optimize a number of parameters simultaneously, as exposure time no longer needed to be independently controlled. For photocrosslinking parameter optimization, samples were gelled for 10 minutes and exposed to UV light for 2 minutes. Light intensity was varied by adjusting the lamp iris across multiple concentrations (0.01-0.1%) of I2959, and rate of photocrosslinking fold increase of storage modulus were compared across conditions. The optimal fold increase occurred using an iris setting of 12%, corresponding to a light intensity measured at $100\text{mW}/\text{cm}^2$ (Figure 3A13). The optimal I2959 concentration was broader, with 0.025-0.05% (w/v) resulting in similar increases in modulus, although rate of increase was lower with higher I2959 concentrations (Figure 3A14).

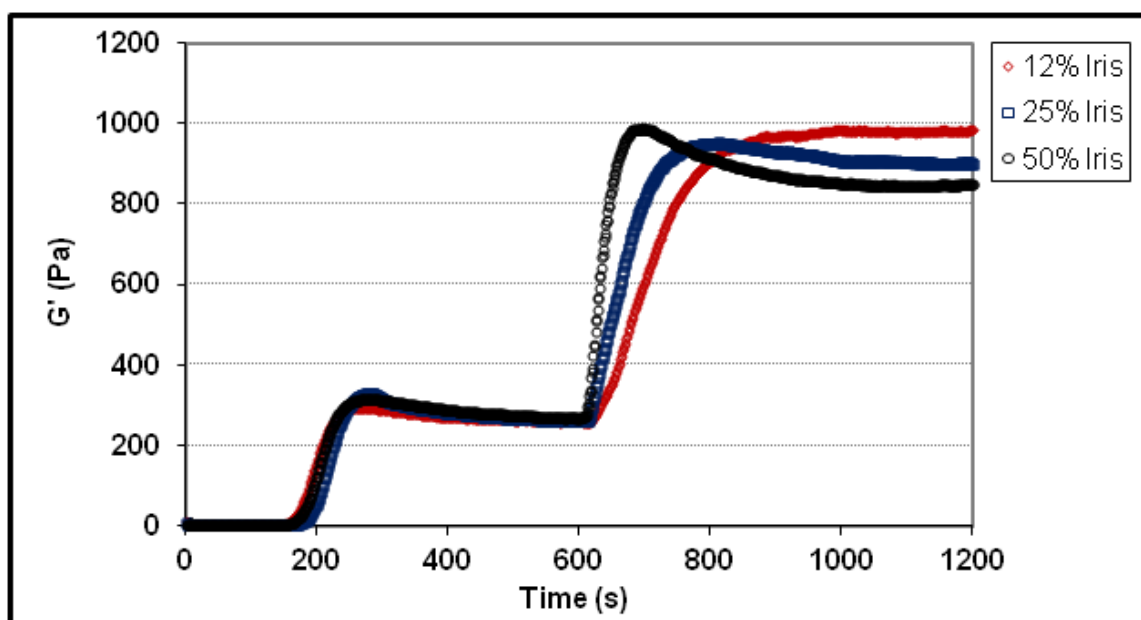


Figure 3A-13: Real-time G' : Effect of Light Intensity Modulation

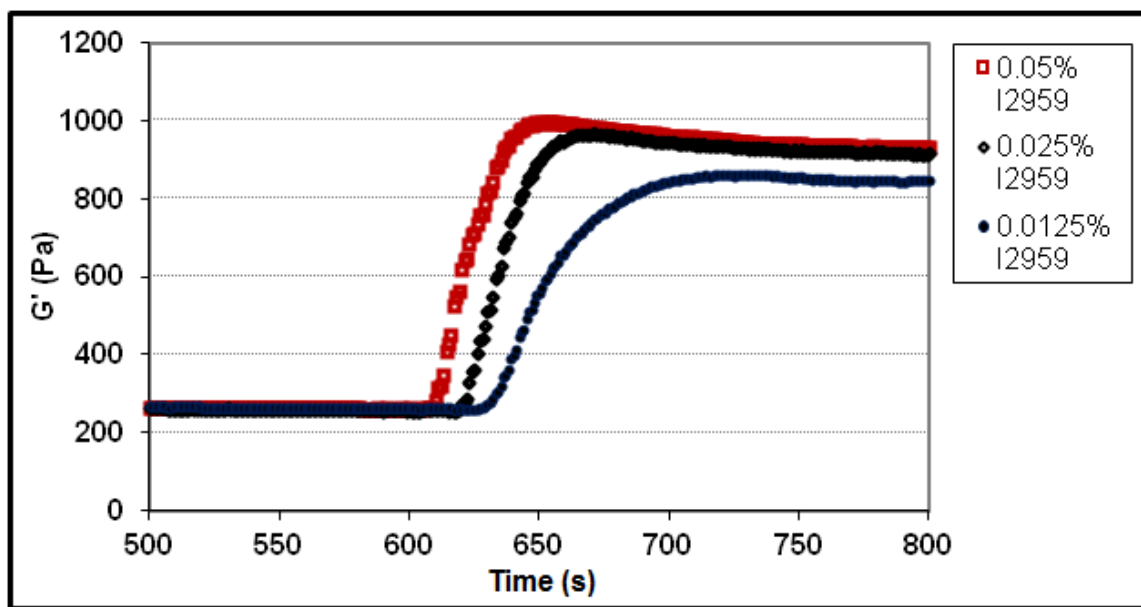


Figure 3A-14: Real-time G' : Effect of Photoinitiator Concentration

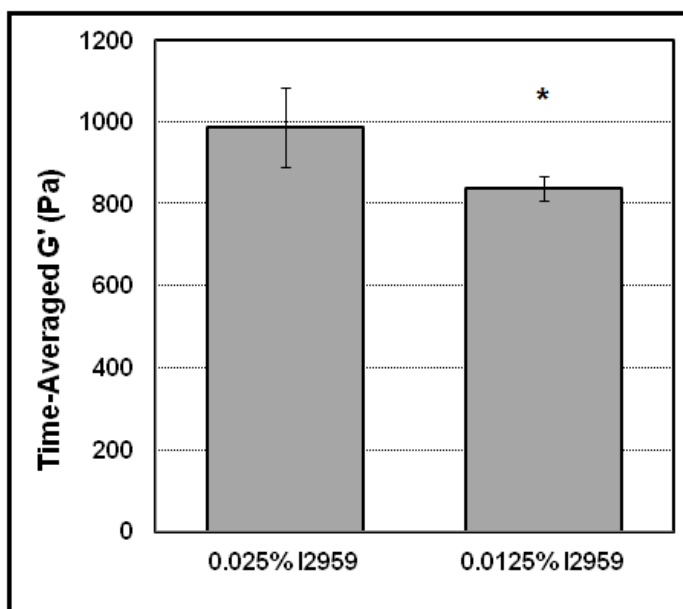


Figure 3A-15: Effect of I2959 Concentration on Photocrosslinked CMA Equilibrium G' . $P < 0.05$.

To verify that 0.025% is the optimal concentration, a repeat experiment was performed to compare 0.025% I2959 with 0.0125%. Briefly, 4 samples of CMA were created with each photoinitiator concentration, and the post crosslinked G' was time-averaged from 750-850s to minimize rheometer and sample variability. The averaged storage

moduli, plotted Figure 3A15, show that CMA photocrosslinked with 0.025% I2959 is significantly stiffer after photocrosslinking compared to 0.0125% I2959. Thus, it was determined that the

optimal photoinitiator concentration of 0.025% (w/v) provides the maximal benefit while minimizing excess photoinitiator.

Thus far, storage modulus has been used primarily as the metric for analysis of material property modification. This is due to the minimal change observed in the loss modulus, which contributes a negligible amount to the calculated complex shear modulus. However, it is worth noting that the loss modulus does exhibit a measurable change during the UV exposure. A small peak is present during the initial phase of photocrosslinking, which then decays to a stable G'' concomitant with the stabilization of G' as seen in Figure 3A16 A, with a zoomed in image of G' and G'' during the UV exposure in Figure 3A16 B to enhance the details. The sinusoidal behavior is an aliasing artifact due to the sampling rate.

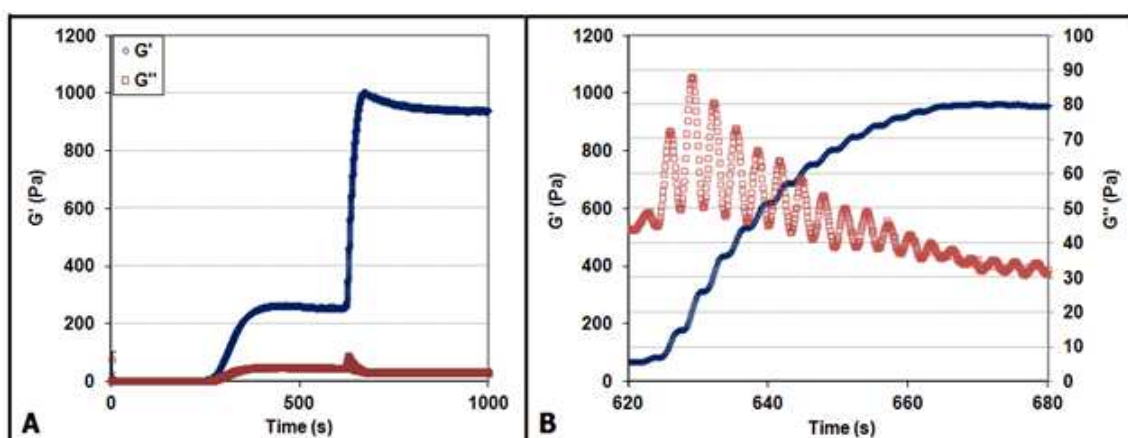


Figure 3A-16: Complete CMA G' and G'' Curves (A) and Magnification of UV exposure period (B)

Due to the profound differences in mechanical properties observed using the preformed gels versus the real-time data as well as various small protocol changes such as EDC storage conditions, we re-ran several rheometry experiments to gain further insight into the material properties of CMA gels as derived from a more ideal testing geometry and with a further optimized protocol. CMA at 2.5, 3.0, and 3.5 mg/mL were photocrosslinked with standard

optimized photoinitiation parameters. Figure 3A17 displays the storage moduli of these conditions, which represent the present state-of-the-art of photocrosslinked CMA hydrogels. Average equilibrium moduli of CMA at 2.5, 3.0, and 3.5 mg/mL before photocrosslinking ($t = 600$ s) were 261.4 ± 19.7 , 387.8 ± 2.6 , and 537.6 ± 9.1 Pa, respectively. After Photocrosslinking, average equilibrium moduli ($t = 1100$ s) were 1697.7 ± 298.5 , 2411 ± 131.4 , and 3299.3 ± 41.3 Pa, respectively.

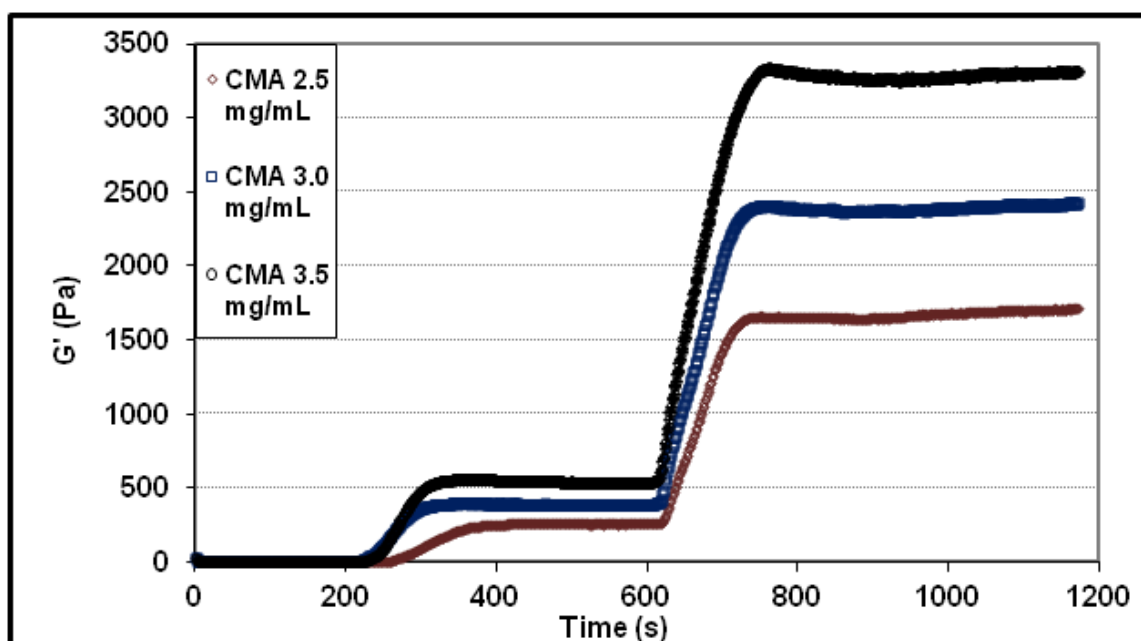


Figure 3A-17: Real-time G' of CMA at 2.5, 3.0 and 3.5 mg/mL

4. Chapter 4: CMA PEG hybrids and CMAX2

4.1 Introduction: Hybrid Hydrogels

However, collagen hydrogels typically have poor mechanical strength and the mechanical properties are not easily controlled, except through changing the macromer concentration or chemical crosslinking [10,11]. Furthermore, cellular adhesion to collagen matrices is highly variable and cell type-specific, and has profound implications on cell migration, proliferation, and other phenotypic behaviors [12]. These qualities limit or prevent the use of collagen in many applications. Another material,

polyethylene glycol (PEG), has been used in medical implants and pharmaceuticals in a

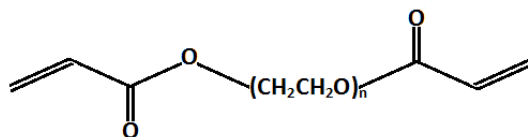


Figure 4-97: Poly-(Ethylene Glycol) Diacrylate (PEGDA)

number of formulations for decades. In 1995 West and Hubbell modified PEG by adding reactive acrylate groups to the end of the PEG macromer to form PEG diacrylate (Figure 4-1), which was then photopolymerized and used to form synthetic hydrogel matrices in which encapsulated cells could be grown [22].

More recently, photopolymerizable PEG-based materials have been produced for use as highly tunable tissue scaffolds and drug delivery systems [23,24]. The mechanical properties of PEG hydrogels can be precisely controlled by altering the polymer chain length and degree of branching [25]. Although PEG is well tolerated by both encapsulated cells and host tissues, it is also inherently non-adhesive and non-degradable. This prevents cells from either infiltrating the scaffold or remodeling it unless modified to include biodegradable moieties [26].

Hybrid materials, which contain a mixture of biomaterials and synthetic components, are becoming popular as tissue engineering matrices due to the combination of their respective advantages. Several groups have successfully used combinations of natural and synthetic

materials to optimize and tailor the properties of tissue engineering scaffolds to the particular application [27-29]. However, simply combining biomaterials with synthetics has limitations, due to the drawbacks of having both materials everywhere within the scaffold. In the case of PEG, this could prevent cell attachment. Other approaches using hybrid materials involve using collagen as a base material, and admixing additional natural or synthetic components such as hyaluronic acid and polyethylene oxide to form interpenetrating networks. Limited control over where materials interact remains a major drawback of this approach, and it may be hard to determine with which material cells might interface due to the presence of two independent matrices [30-32]. A more useful application of hybrid materials would be to insert synthetic materials in places where additional mechanical strength is needed while maintaining the availability of the biomaterial's functionality in other areas. Furthermore, living tissues are highly variable in their localized properties, with different mechanical and biochemical properties within different parts of the tissue. To truly regenerate tissues with any real similarity to the original structure and functionality, an efficient scaffold requires ability to be tailored with a heterogeneous structure.

Although CMA is a useful material, it has limitations imposed by the relatively small percentage of crosslinkable groups even with the optimized derivatization method outlined previously. Furthermore, the small size of the methacrylate groups combined with the large inter-fiber distances within the collagen network limits the possible number of interactions between methacrylate groups, which in turn limits the ability to modulate the mechanical properties across multiple orders of magnitude. The inclusion of synthetic bridging agents such as PEG may allow for increased tunability within the material. As it is synthetic, PEG can be made at molecular weights from the hundreds to the hundreds of thousands, allowing precise control of mechanical properties as well as porosity as a property of the polymer chain length. PEG can

easily be modified to have one or more acrylate or methacrylate groups attached to the end of the polymer chain, and PEG molecules can be linear or branched, allowing control over the density of functional groups which may be used as a tool to decouple crosslinking density (mechanical modification) from porosity (geometric modification). Previous studies that have used photocrosslinked polymers to control matrix stiffness also invariably created differences in matrix porosity and network geometry, as stiffness can typically be tuned by varying either the macromer concentration or molecular weight, both of which have significant effects on matrix geometry. Using CMA in combination with PEG-variants of similar molecular weights but different numbers of functional groups, allowing more crosslinks per unit mass, may provide a platform whereby control of mechanics and geometry can be studied independently. A schematic of this concept can be seen in Figure 4-2.

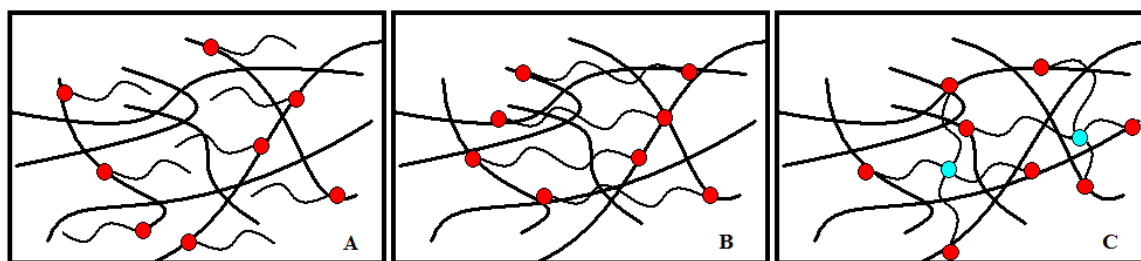


Figure 4-98: Schematic of CMA gels crosslinked with PEG linkers with 1 (A), 2 (B), and 4 (C) functional groups.

Branched PEG may also be used to multiply the number of functional groups, for instance by using 4-arm PEG end-capped on each arm with a reactive group. By crosslinking one arm to the methacrylated collagen backbone, 3 additional functional groups may be added dendritically with each 4-arm PEG resulting in an exponentially larger number of photocrosslinkable groups. As such, the inclusion of PEG variants into the hybrid hydrogels may allow a robust synergy, taking advantage the natural benefits of collagen as well as the precision afforded by synthetic material in a single hybrid material.

Here, we evaluated whether PEG-based photopolymers could be used in conjunction with CMA to create heterogeneous hybrid hydrogels in an effort to exploit the advantages of both materials. We examined material properties of composite photocrosslinked gels containing a variety of PEG variants with a range of molecular weights and reactive functional groups including acrylates, methacrylates and thiols, as well as 4 and 8 arm PEG-based dendrimers. We also examined a method for derivatizing carboxyl groups on CMA utilizing a functionalization scheme based on EDC grafting of aminoethyl methacrylate.

4.2 Methods

4.2.1 PEGDA Synthesis

PEGDA was synthesized based off previously described methods [82]. Triethylamine (5 molar excess) was added to PEG (Average Mw = 2000, Sigma) dissolved in benzene. Acryloyl chloride (5 molar excess) was added drop-wise under nitrogen and reacted on ice for 6 h, followed by reaction at room temperature for 12 h. The product was vacuum filtered in benzene, concentrated via rotovap, precipitated via drop-wise addition of excess hexane, re-dissolved in methylene chloride, dried overnight in nitrogen, and stored at -20°C in powder form before use. The reaction efficiency was characterized using ^1H nuclear magnetic resonance (Bruker Advance 360 MHz, Bruker, Billerica, MA).

4.2.2 PEG/CMA Hybrid Rheology

Standard CMA (2-3mg/mL) containing 0.1% (w/v) I2959 was admixed with reactive PEG variants at 0.1-1% (w/v) and plated into PDMS molds. PEG variants included acrylated and methacrylated PEG with molecular weights from 258-10,000 Da and 2 or 4 functional groups/molecule. PEG2KDA was synthesized in-house, whereas other molecular weight PEGDA, PEGDM, and

single acrylate/methacrylate PEGs were purchased from Sigma-Aldrich. Four-armed PEG species were purchased from Laysan Bio (Arab, AL) and Creative PEGWorks (Winston Salem, NC). After self-assembly, samples were fully crosslinked by exposure to UV light ($4\text{mW}/\text{cm}^2$) via UVL-21 for 5 min. Rotational rheometry using the previously described frequency sweep method was used to determine the storage moduli.

4.2.3 PEG CMA Cytotoxicity

Cytocompatibility studies were performed with PEG variants with and without CMA and/or crosslinking to determine whether PEG variants had any effect on cell viability directly or through secondary effects from photoinitiation. To test direct cytotoxicity of low Mw PEG variants, NIH 3T3 Fibroblasts were plated at 20,000 cells per well in a 96 well plate. After 24 hours of culture, media was changed to contain 0.1% (v/v) of PEGDA at molecular weights of 258, 575, and 2000 Da, as well as monoacrylated PEGs (PEGMEA) with molecular weights of 480 and 1100 Da. Following 24 h in culture, cells were assayed for viability using Live/Dead staining described in Chapter 1 and the MTS assay.

4.2.4 MTS Assay

The MTS assay measures mitochondrial activity, and thus reports both cellular viability as well as metabolic functionality, as both are necessary to produce colorimetric signal. This protocol is based on the CellTiter 96® AQueous One Solution Cell Proliferation Assay (Promega, Madison, WI). In this assay, 3-(4,5-dimethylthiazol-2-yl)-5-(3-carboxymethoxyphenyl)-2-(4-sulfophenyl)-2H-tetrazolium, inner salt (MTS), is reduced in metabolically active cells via the NADh/NADPH pathway, catalyzed by an included electron coupling reagent (phenazine ethosulfate; PES). The resultant product, Formazan, can be detected using absorbance spectroscopy at 490nm following 1-4 incubation. MTS typically requires 20 μL stock MTS per 100 μL culture medium. A

standard curve of known numbers of viable cells is used the internal calibration to determine the number of viable, active cells in the unknown conditions and ensure that assay was performed within the linear range of product development.

4.2.5 *Collagen-PEG-Acrylate and Collagen-PEG-Thiol*

We investigated whether functional PEG groups could be grafted onto the collagen backbone using similar derivatization chemistry to CMA synthesis. Heterobifunctional PEGs from Creative PEGWorks, acrylate-PEG-succinimidyl carboxy methyl ester (APS, Mw = 2000 Da) and thiol-PEG-carboxyl (TPC, Mw = 1100) were used to synthesize collagen-PEG-acrylate (CPA) and collagen-PEG-thiol (CPT), respectively. For CPA synthesis, a 10:1 molar excess of APN:ε-amine was reacted directly, as the succinimidyl ester is readily reactive with the free amines of collagen in an identical fashion to the 2-step EDC/NHS esterification of methacrylic acid. Collagen in 0.02M acetic acid (3.75mg/mL) and APN were mixed on ice and reacted for 24h on a rotator at 4°C. CPT was synthesized with a similar 10:1 molar ratio of TPC: ε-amine, and a 1:1:2 ratio of EDC:sulfo-NHS:TCP. Following a 10 minute activation of the carboxyl group via EDC/NHS in MES buffer at 37°C, the reactants were cooled on ice and mixed with ice-cold collagen solution in 0.02M acetic acid (3.75mg/mL) and reacted for 24h on a rotator at 4°C. For both CPA and CPT, the reaction mixture was then transferred to a dialysis cassette with a 20,000 Da MWCO and dialyzed excessively with 5 changes of 250-fold volumes of 0.02M acetic acid dialysis buffer. Products were then frozen and lyophilized, weighed, then resuspended at 3.75mg/mL for experiments.

4.2.6 *CMAx2 Synthesis*

An additional method for optimizing CMA derivatization efficiency was investigated in an attempt to utilize carboxyl groups present on type-I collagen as methacrylation targets. The

initial methacrylation step targets the free amines on collagen, of which there are approximately 164 per tropocollagen molecule. Although this number of potential grafting sites is large enough to allow a functional modification of collagen, if more methacrylate groups could be added, then CMA could be a more robust material in terms of the range of material properties achieved through photocrosslinking. Another site of potentially graftable residues is on the carboxyl group present on the amino acids glutamate and aspartate, of which there are a combined 387 per triple helical collagen molecule. After the free amines on collagen have been converted into methacrylamides, a second round of EDC functionalization targeting the free carboxyls is possible due to the paucity of amines present which would otherwise result in the collagen crosslinking to itself and rendering the material an unusable gelatinous mass during the reaction. After derivatization of native collagen with methacrylic acid and dialysis of the excess reagents, the resultant CMA was then further derivatized using the same general reaction scheme as with the methacrylic acid derivatization but instead using aminoethylmethacrylate (AEM), which can form amide bonds with the EDC/sulfoNHS-activated carboxylic acid groups on collagen (Figure 4-3). AEM:Carboxyl ratio was targeted at 10:1, with an AEM:EDC:NHS ratio set at unity. The reactants were mixed on ice and added to a solution of CMA at 3.75mg/mL, then reacted at 4°C for 24h. The product was then dialyzed, frozen, lyophilized, and reconstituted similarly to the standard CMA process. The resulting material, which we dubbed CMAX2, could theoretically have over 3 times the number of photocrosslinkable groups than the first generation CMA due to the large number of carboxyls present on type-I collagen.

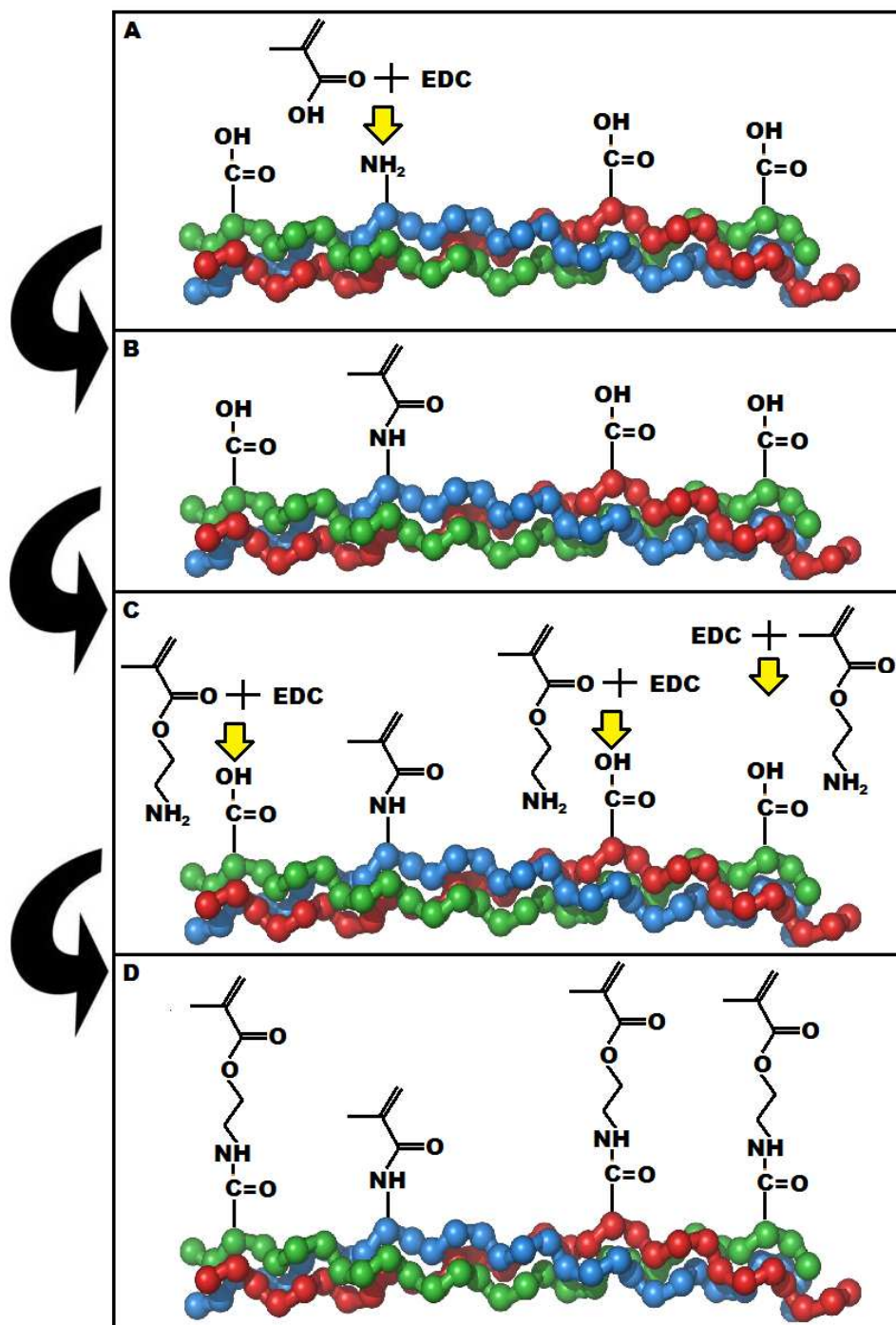


Figure 4-99: CMAX2 Derivatization Schematic

4.2.7 CMAX2 Characterization

Proton NMR similar to that used for CMA characterization was used to analyze derivatization of CMA to CMAX2. CMAX2 was cast into gels using the standard collagen recipe used previously. Standard rheology frequency sweep analysis of storage and loss moduli was used to characterize the mechanical properties of CMAX2 before and after photocrosslinking. Functional PEG variants were also included in photocrosslinking experiments to determine if CMAX2 allowed additional interaction between collagen-bound methacrylates and functional PEGs compared to CMA.

4.3 Results

4.3.1 NMR: PEGDA Synthesis

PEGDA synthesis was straightforward and resulted in an efficiency of >98% acrylation of the PEG as per analysis of the peaks from the NMR spectrum (Figure 4-4). The product was an off white powder that was readily soluble in water. Gelation tests involved admixing a 10% (w/v) aqueous solution of the PEG2KDA with I2959 (0.1% w/v, final concentration) and exposing to 10 minutes of UV light from the UVL-21. The result was the formation of a solid gel after light exposure, indicating that the PEGDA was readily photopolymerizable. PEG2KDA, having no inhibitors to prevent spontaneous polymerization, was stored desiccated at -20°C in foil-wrapped tubes to prolong functionality. Aliquots were weighed individually for each new experiment and solutions were prepared freshly immediately before each experiment.

4.3.2 PEG Solubility

Lower molecular weight PEG-based molecules (< 1000 Da) were first dissolved in 70% ethanol to create 10% (v/v) solutions, and then diluted appropriately. Higher molecular weight species (>

1000) were readily soluble in aqueous solutions and were dissolved in diH₂O, PBS, or cell culture medium prior to further dilution for experiments.

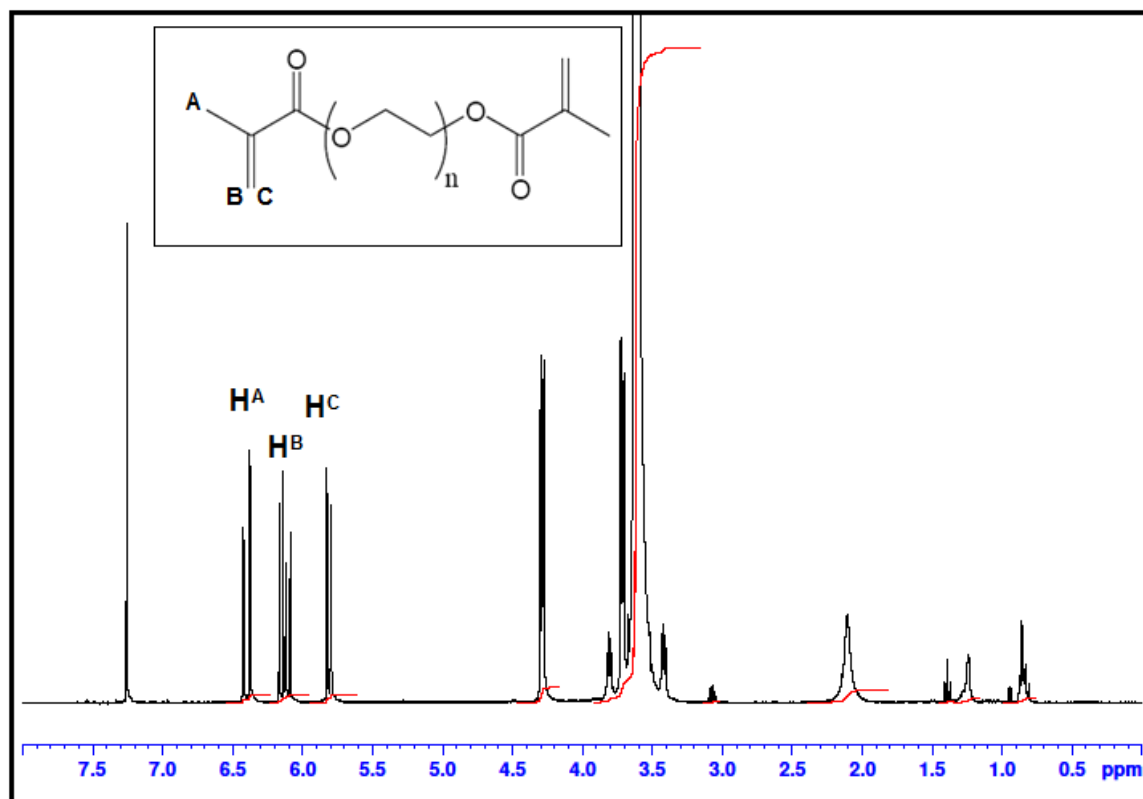


Figure 4-100: ¹H NMR spectrum of PEGDA. Peaks Corresponding to Derivatized Acrylate Hydrogens seen at 5.5-6.5 ppm

4.3.3 CMA-PEG Hybrid Gel Rheometry

Initial hybrid tests focused on low M_w acrylated PEG. PEG258DA (Sigma) was admixed with native collagen and CMA (2mg/mL) containing 0.1% I2959 for a final concentration of 0.1% (v/v) and exposed to UV light for 5 minutes following a 1 hour gelation period. The excess photoinitiator and light exposure time was included to ensure complete activation of photosensitive groups on CMA and from the PEGDA. Native collagen mixed with PEGDA, with and without photoinitiation, was included as conditions to test whether PEGDA would react

independently of methacrylate derivatization and whether PEGDA would affect the mechanical properties of native collagen, possibly through interfering with fibrillogenesis. Native collagen conditions in Figure 4-5 showed no significant effects from PEG258DA, as G' was similar for native collagen with and without PEGDA, regardless of photoinitiation. On the other hand, CMA storage modulus, which when photocrosslinked alone, increased by 2-3 fold, was increased further by nearly 50% in the presence of 0.1% PEG258DA. Thus, PEG258DA changed the storage modulus of methacrylated, and not native, collagen upon 5 minutes of photoinitiation.

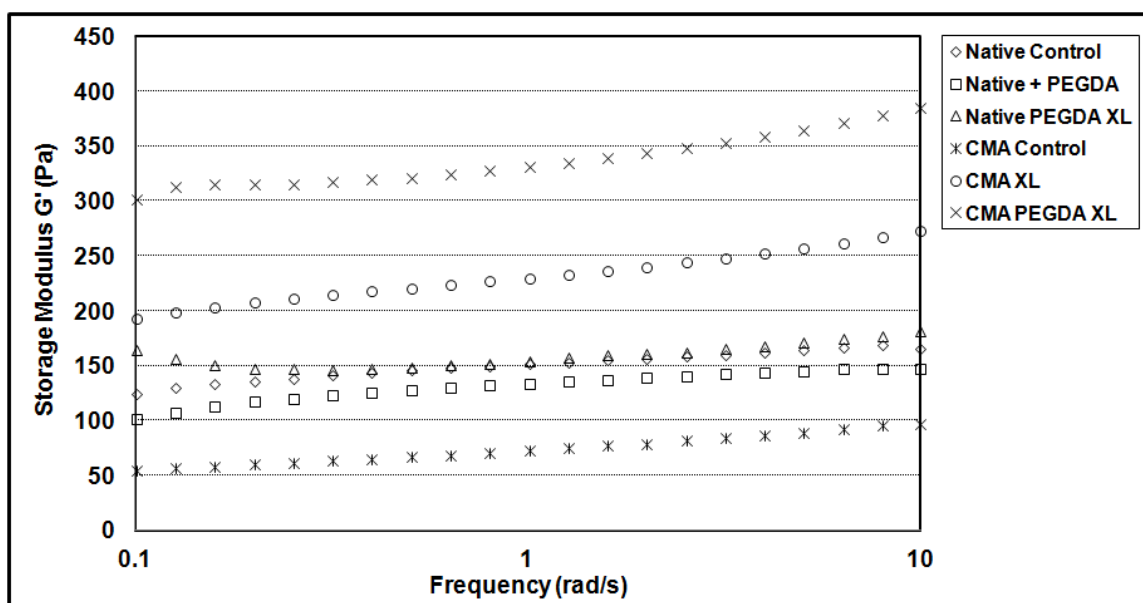


Figure 4-101: Effect of 0.1% (v/v) PEG258DA on Storage Modulus of Native Collagen and CMA Hydrogels

We next evaluated whether the increase in G' was correlated to the CMA concentration. CMA at 2, 2.5, 3, and 3.5 mg/mL was admixed with 0.1% (v/v) PEG258DA and photocrosslinked with 0.1% I2959 and 5 minutes of UV exposure. A frequency sweep from 0.1-10 rad/s for all conditions was performed, and the storage modulus at the median frequency (1 rad/s) was compared after verification that behavior at this frequency was within the linearly viscoelastic portion of the data. Figure 4-6 summarizes the storage moduli of all conditions. A linear

correlation was inferred between CMA concentration and G' increase from PEG258DA-mediated photocrosslinking, with PEG258DA increasing the storage modulus threefold from the basal value. The greatest net modulus value was obtained with CMA at 3.5mg/mL.

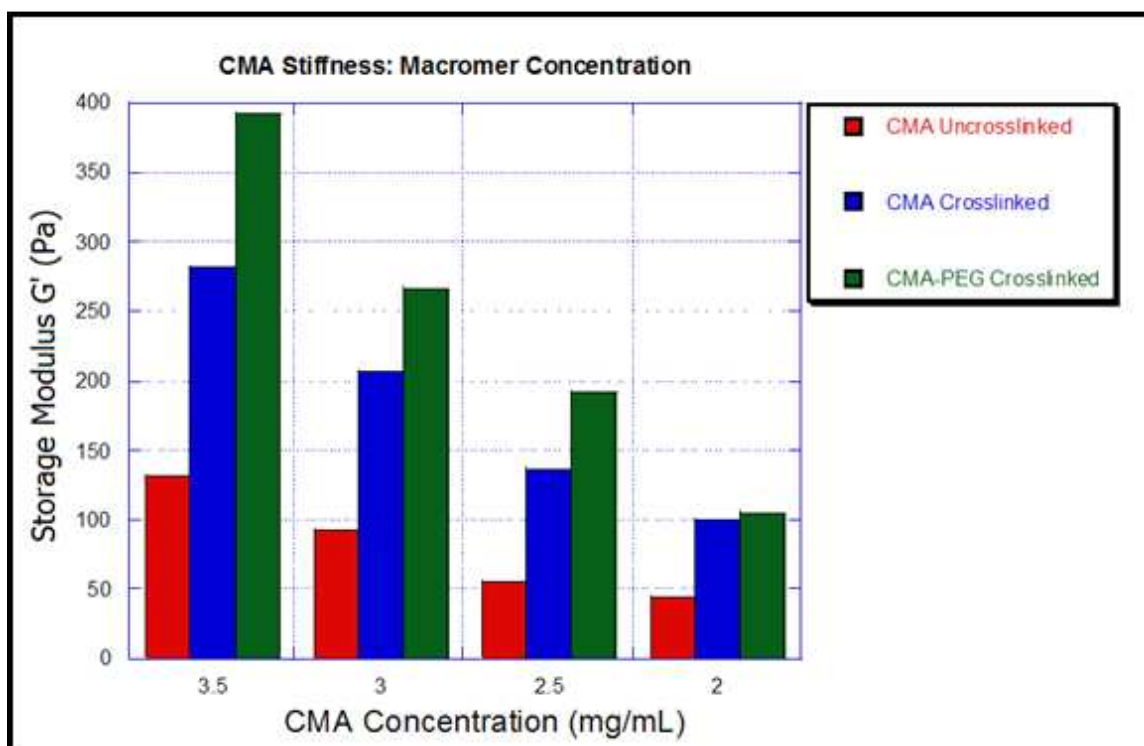


Figure 4-102: Effect of CMA Concentration Photocrosslinked with 0.1% PEG258DA on Gel Stiffness

Continued optimization of CMA synthesis and the rheological testing procedure necessitated a repeat of the CMA photocrosslinking characterization to obtain updated mechanical properties. Figure 4-7 shows frequency sweep (0.1-10 rad/s) data of storage and loss moduli of CMA at 3 mg/mL photocrosslinked with and without PEG258DA. Here, CMA G' was increased ~2-fold via photocrosslinking alone, and ~4-fold increase in G' when PEG258DA was included. G'' was not significantly different between any conditions, indicating that photocrosslinking, especially with PEGDA, resulted in a stiffer and more elastic material at the strain rates tested here.

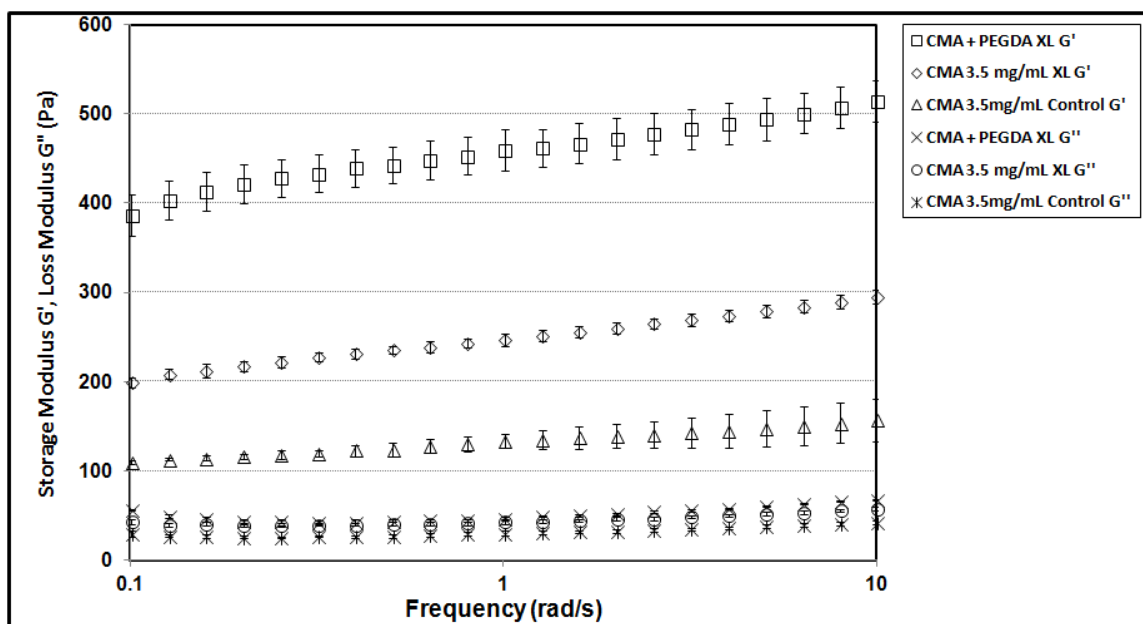


Figure 4-103: G' and G'' Characterization of 3.0 mg/mL CMA Photo \pm 0.1% (v/v) 258 Da PEGDA

We next evaluated whether similar mechanical modulation would result from the inclusion of other acrylated PEG variants of different molecular weights and structures. PEG258DA and PEG575DA, both from Sigma (0.1% v/v), and a four armed PEG-acrylate (PEG10KTA), (0.1% w/v, Mw = 10KDa, Laysan Bio) were admixed with CMA (3.5 mg/mL) and frequency sweeps from 0.1-10 rad/s were performed. Figure 4-8 summarizes the effect of photocrosslinking on G' under these conditions at the median frequency of 1 rad/s. PEG258DA again significantly increased storage modulus, but PEG575DA and PEG10KTA were not statistically different from CMA photocrosslinked alone. It was concluded that the molecular weight of the PEG variant has a profound effect on its ability to modulate the mechanical properties of CMA gels through photoinitiation.

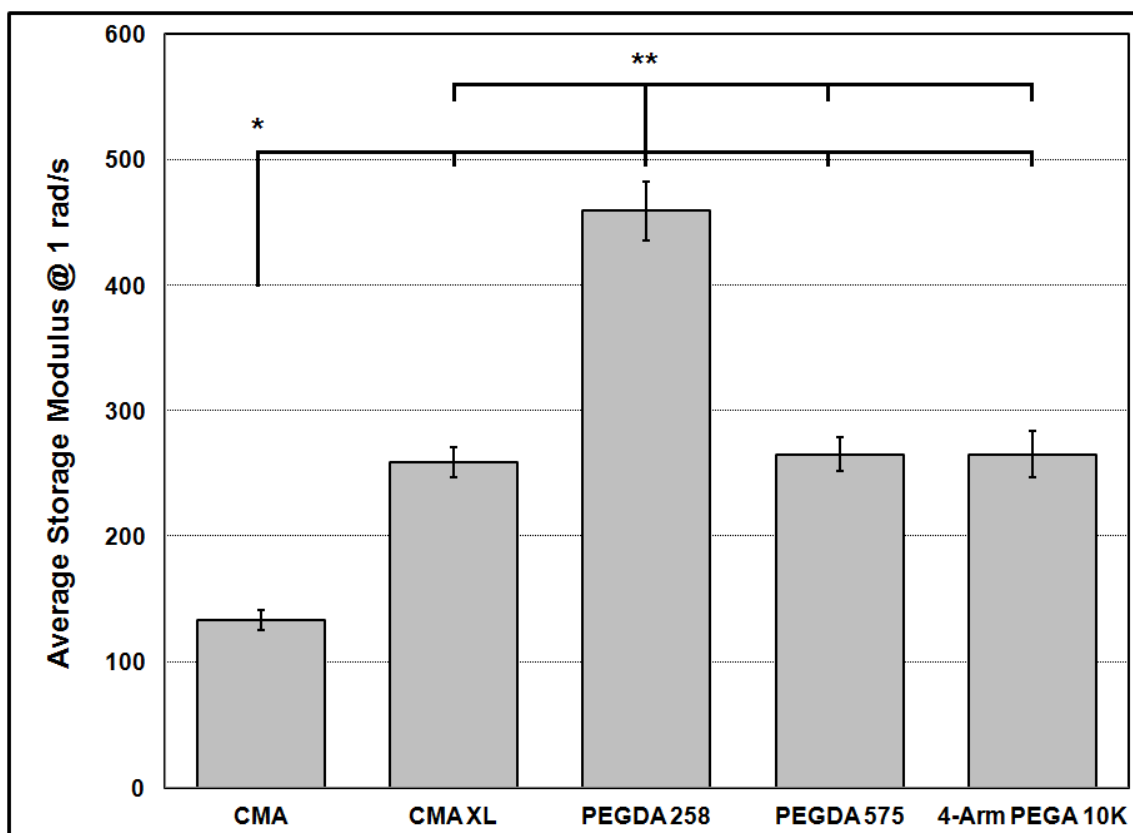


Figure 4-104: Summary of G' at 1 rad/s of CMA \pm photocrosslinking with Acrylated PEG Variants. $p < 0.01$.

Several other PEG variants, PEG2KDA, synthesized in-house, PEG dimethacrylate with $M_w = 2000$ (PEG2KDM), purchased from Sigma, and a four-armed PEG-acrylate (PEG2KTA, $M_w = 2000$, Laysan Bio) were tested at a higher concentration of 1% (w/v) to determine if any had a significant effect on storage modulus following photocrosslinking. Here, we saw that all three PEG variants had a quenching effect on the photocrosslinking G' increase (Figure 4-9). G' was increased only minimally when these acrylated PEGs were included, but the increase was significantly lower than for CMA photocrosslinked alone. These data imply that at a concentration of 1%, acrylated and methacrylated PEGs with 2 or 4 functional groups did not contribute to the photoinitiation-mediated augmentation of storage modulation; rather, these species appeared to interfere with the crosslinking.

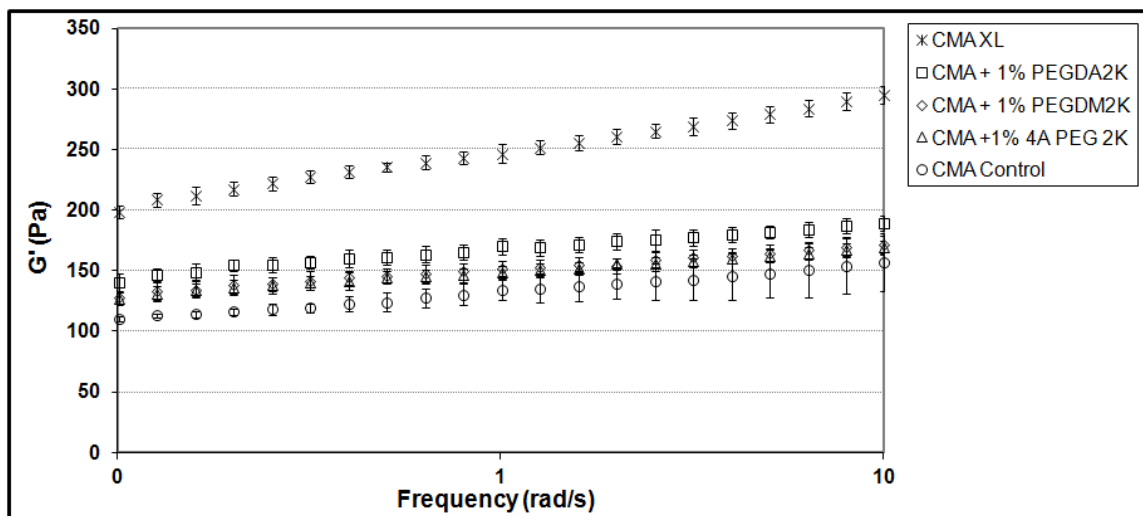


Figure 4-105: CMA G' with crosslinking \pm 2000 Da PEG Variants

4.3.4 CPA and CPT Functionalization

Another strategy was examined that aimed to graft photosensitive PEG chains onto collagen, then photocrosslink the resulting material under the premise that the additional spacing provided by the presence of the PEG chains would increase photocrosslinking efficiency through

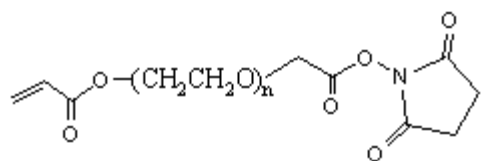
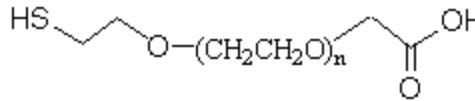


Figure 4-106: Acrylate-PEG-SCM

increasing the number of possible crosslinking interactions. A first attempt used Acrylate-PEG-SCM, where SCM was used to directly derivatize free

amines. Multiple attempts with this method resulted in a product that failed to self-assemble, either from denaturation of the collagen during the reaction or by disruption of the triple helical structure through the presence of the grafted PEG chain. As a result, no meaningful rheological data was obtained, and photocrosslinking was not evaluated.

A different strategy using thiol-PEG-carboxyl was attempted by using EDC chemistry to graft the functional PEG onto the collagen backbone. As the 2000 Mw APS disrupted the collagen self-assembly, a



smaller 1100 Mw TPC was used (Figure 10). The

Figure 4-107: Thiol-PEG-COOH

result of this reaction was a material that did self-assemble, although the storage modulus of the gel was lower than native collagen and visible heterogeneity was observed in the gel. In addition, photoinitiation conditions appeared to actually lower the storage modulus, and inclusion of PEGDA258 in the photocrosslinking mixture further reduced the storage modulus (Figure 4-12). Further attempts at grafting functional PEG moieties onto collagen were discontinued due to the lack of additional functional benefit and obvious disruption to the fibrillogenesis of collagen networks.

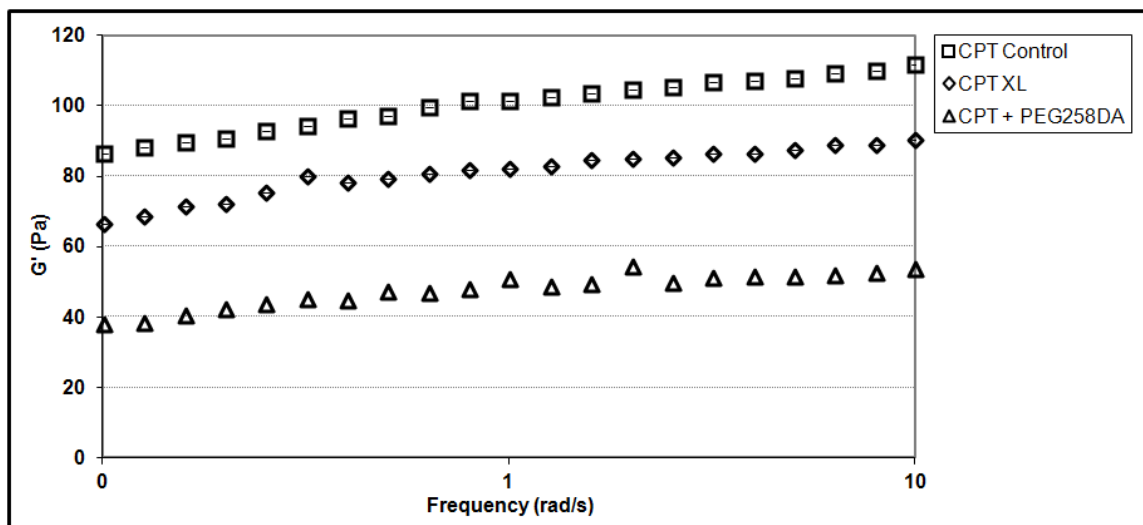


Figure 4-108: Storage Modulus of Collagen-PEG-Thiol Photocrosslinked ± PEG258DA

4.3.5 PEG Cytotoxicity

NIH-3T3 fibroblasts were used to screen PEG variants for cytotoxicity both directly and through indirect secondary effects following photocrosslinking. In the former case, NIH-3T3 cells cultured

on TCP were exposed to PEG258DA, PEG575DA, PEG480MEA, PEG1100MEA, and PEG2KDA in culture medium. After 24 hours in culture, medium was removed and medium containing MTS was added and allowed to develop color based on the presence of live, metabolically active cells. Cells were stained using the Live/Dead assay following MTS absorbance readings. MTS data (Figure 4-13) indicates that PEG species below 1000 Da are highly toxic, with near 0% viability following PEG exposure. In contrast, PEG1100MEA and PEG2KDA showed no significant effect on viability.

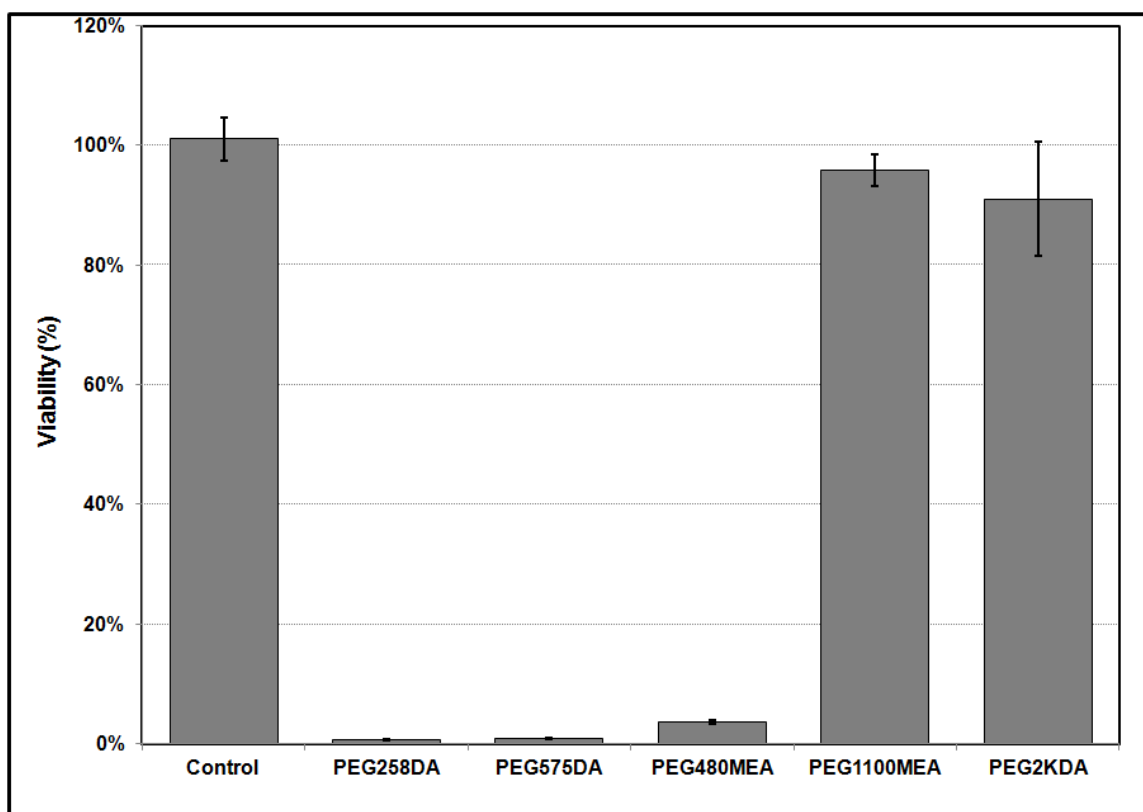


Figure 4-109: Cytotoxicity of Diacrylated and Monoacrylated PEG Variants of Different Molecular Weight

This drastic cutoff was also seen in the Live/Dead staining images, where all of the cells in the sub-1000 Mw PEG groups (Figure 4-14 B-D) appear necrotic as per the ethidium positive pyknotic nuclei and lack of cytoplasmic calcein staining, whereas cell morphology was similar

between control condition cells and the higher Mw PEG conditions (Figure 4-14 A, E, F). The significant number of dead cells in the latter group, in contradiction with MTS data, is likely due to MTS toxicity as the same cells were used for both assays.

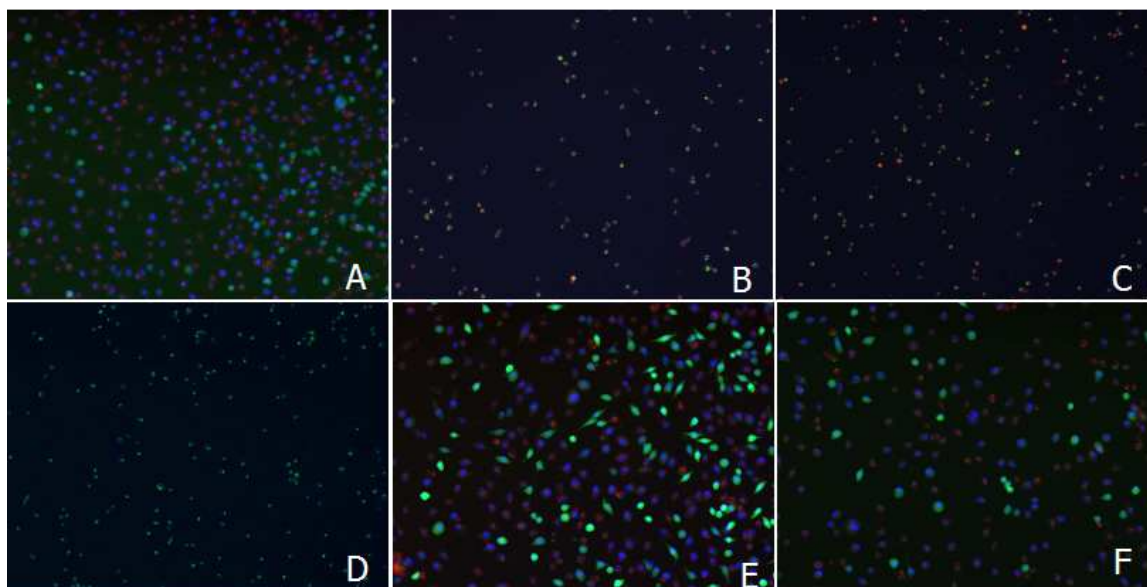


Figure 4-110: Live/Dead Staining of PEG Variant Exposure. Control (A), PEG258DA (B), PEG575DA (C), PEG480MEA (D), PEG1100MEA (E), PEG2KDA (F)

To understand the mechanism behind the cytotoxicity of the low Mw variants, we tested whether the same cutoff for toxicity was observed for non-acrylated PEG molecules of similar size. PEG (Sigma) of molecular weights 200, 400, 600, 1000, and 2000 was put into solution in ethanol, diluted into culture medium at 0.1% (w/v), added to NIH-3T3 fibroblasts on tissue culture plastic, cultured overnight, and tested for viability via MTS and Live/Dead assays. Controls including Positive Control, Etoh at vehicle concentration (less than 1%), and a known cytotoxic Negative Control with 10% Etoh were included with the MTS assay. The vehicle control served as the only control condition for the Live/Dead staining. MTS data, shown in Figure 4-15, indicated that none of the PEGs tested showed any significant cytotoxicity. These data were confirmed by Live/Dead staining images (Figure 4-15), in which all cells stained positive for

calcein and very little ethidium staining was observed. Cellular morphology looked similar for all conditions as well. From this study we concluded that the acrylated PEG toxicity is not due to the PEG molecular weight, but has some other, unknown toxic mechanism.

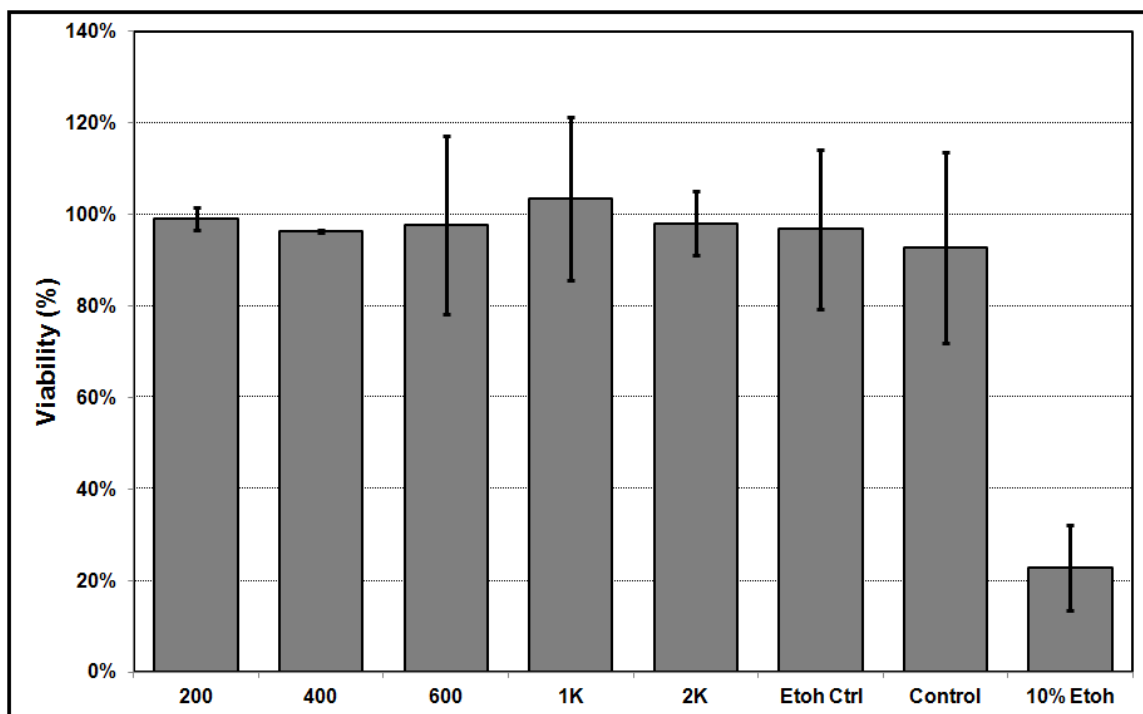


Figure 4-111: MTS cytotoxicity screen of PEG macromers. Columns "200-2K" indicate PEG Mw, "Etoh Control" replicated PEG vehicle solution (0.63% Etoh), "Control" was Culture Media only (Positive Control), "10% Etoh" was the Negative Control

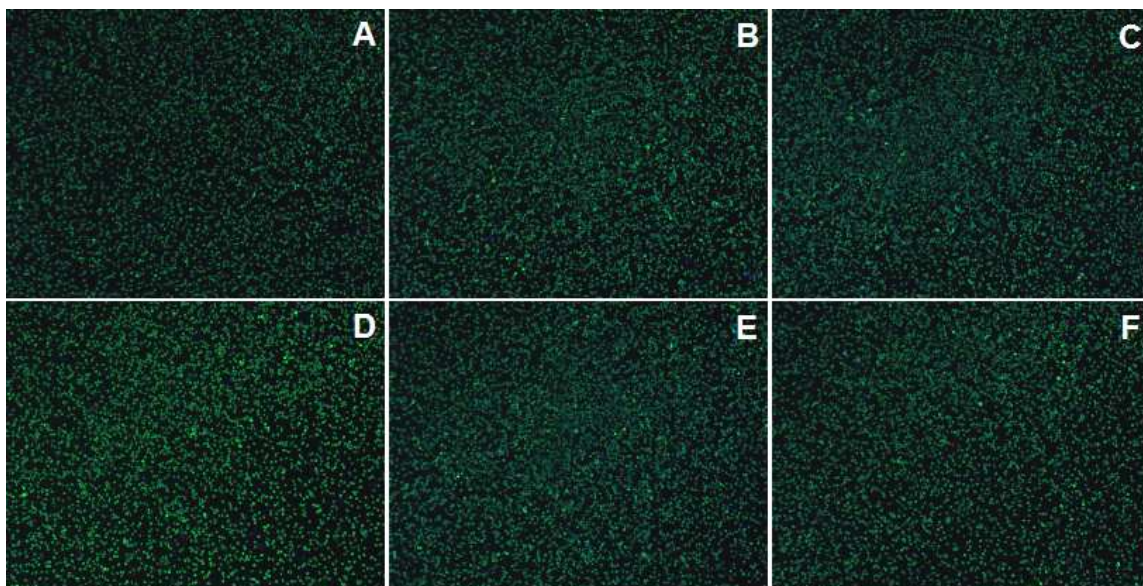


Figure 4-112: PEG Molecular Weight Effect on Cytotoxicity. 200 Da (A), 400 Da (B), 600 Da (C), 1 kDa (D), 2 kDa (E), EtOH Vehicle (F). Positive and Negative Control Conditions Not Shown.

To further elucidate the mechanism by which PEG258DA induces cytotoxicity, we looked at whether PEG258DA was cytotoxic after being exposed to photoinitiation. NIH-3T3 fibroblasts were plated on native collagen gels, photocrosslinked CMA, and 0.1% PEG258DA photocrosslinked CMA. A positive control of 3T3 on tissue culture plastic (TCP) and a negative control of TCP with 0.1% PEG258DA in culture medium were included. After 24 hours of culture, Live/Dead staining was performed to analyze viability of fibroblasts in each condition. As seen in Figure 4-17, NIH-3T3 fibroblasts adhered and were viable on native collagen gels and photocrosslinked CMA gels, although there were fewer cells adhered to the CMA gels as compared to the TCP control well. Cells on PEG258DA-photocrosslinked CMA gels were highly viable as per nearly ubiquitous calcein positive/ethidium negative staining, but very little cell spreading was observed indicating that adhesion to this material was limited. The PEG258DA TCP control condition showed 100% toxicity, as expected from previous experiments. Hence,

exposing PEG258DA to photoinitiation conditions appears to greatly mitigate its toxicity, although cell adhesion may potentially be affected.

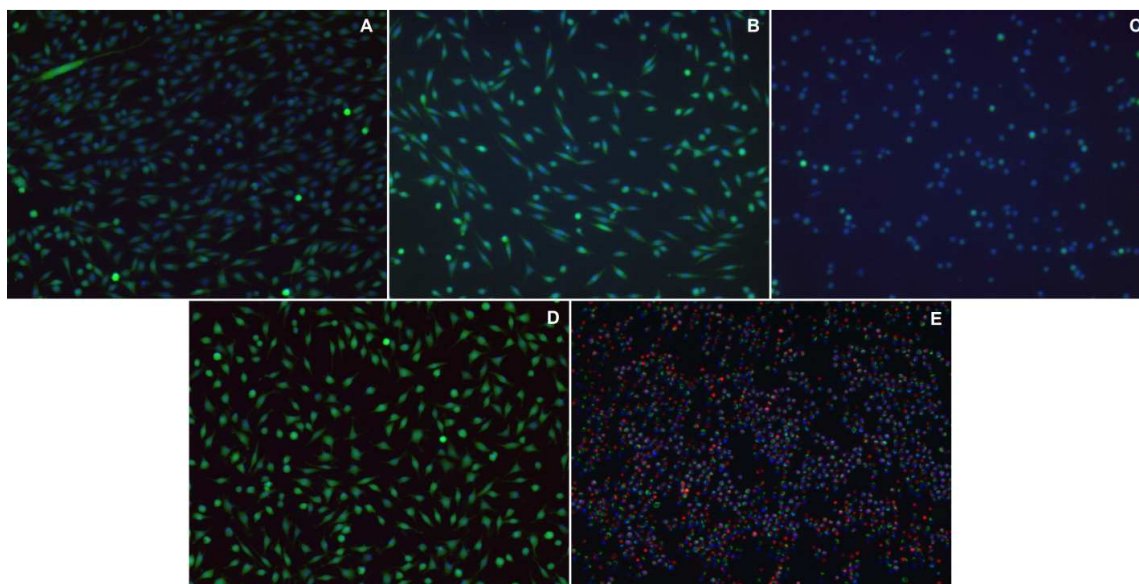


Figure 4-113: Live/Dead Staining of NIH-3T3 Fibroblasts on Native Collagen (A), CMA XL (B), CMA + 0.1% PEG258DA (C), TCP (A), TCP + 0.1% PEG258DA

A dose response experiment was conducted to determine if adhesion to CMA-PEG258DA hybrid hydrogels could be modulated by adjusting the concentration of PEG258DA prior to photocrosslinking. CMA was admixed with 0.5, 0.1, 0.01, and 0.001% (v/v) PEG258DA, cast into 2 sets of gels, and half were photocrosslinked. Immediately after crosslinking and/or gelation, NIH-3T3 fibroblasts were seeded on the gels and cultured for 24 hours. MTS assay was used to assess viability, with a standard curve of cell concentration plated on TCP and used to quantify viable cell number in the gel conditions. In both (UV \pm) CMA conditions, there were fewer viable ($49 \pm 3\%$, $40 \pm 6\%$) cells compared to native collagen ($65 \pm 1\%$, $69 \pm 6\%$), as seen in the previous experiment. In conditions containing PEG258DA, there was a dose-dependent decrease in cell viability ($21 \pm 7\%$, $9 \pm 3\%$, $7 \pm 1\%$, $-2 \pm 1\%$) with increasing concentrations (0.001, 0.01, 0.1, 0.5%, respectively) of PEG258DA in the photocrosslinked conditions, whereas in the uncrosslinked

PEGDA gels there was a measured negative viability ($-5\pm1\%$, $-4\pm1\%$, $-5\pm1\%$, $-3\pm1\%$) for all conditions (0.5, 0.1, 0.01 and 0.001%, respectively). The negative viability seen in the PEGDA conditions is likely due to interference of the MTS conversion by either the PEGDA itself or the trace polymerization inhibitors in the stock PEGDA solution.

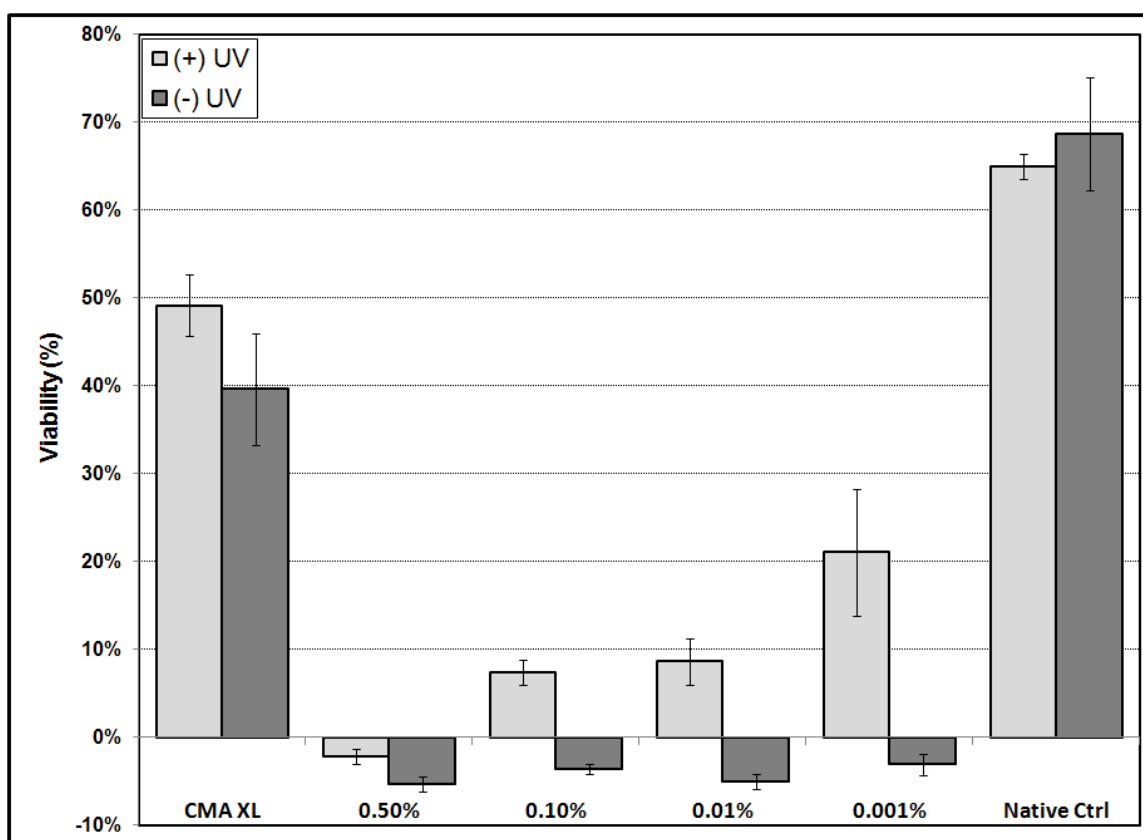


Figure 4-114: MTS Assay Data: Dose Response Cytotoxicity of CMA Photocrosslinked with Various Concentrations of PEG258DA

4.3.6 CMAX2 Characterization

Initial rheological characterization of CMAX2 photocrosslinking via frequency sweep analysis of the storage modulus showed that the double methacrylation synthesis process resulted in a material that still formed a stable hydrogel, although with a lower storage modulus after fibrillogenesis compared to CMA, indicating some additional disruption to the triple helical or fibrillar structure. Upon photocrosslinking with 5 minutes UV light and 0.1% I2959, the result

was approximately a four-fold increase, significantly higher than the 2-fold increase obtained from photocrosslinking the intermediate batch of CMA alone (not shown). In the presence of 0.1% PEG2KDA, which showed no effect with CMA, G' was increased further to nearly 8-fold above basal CMAX2 values (Figure 4-19).

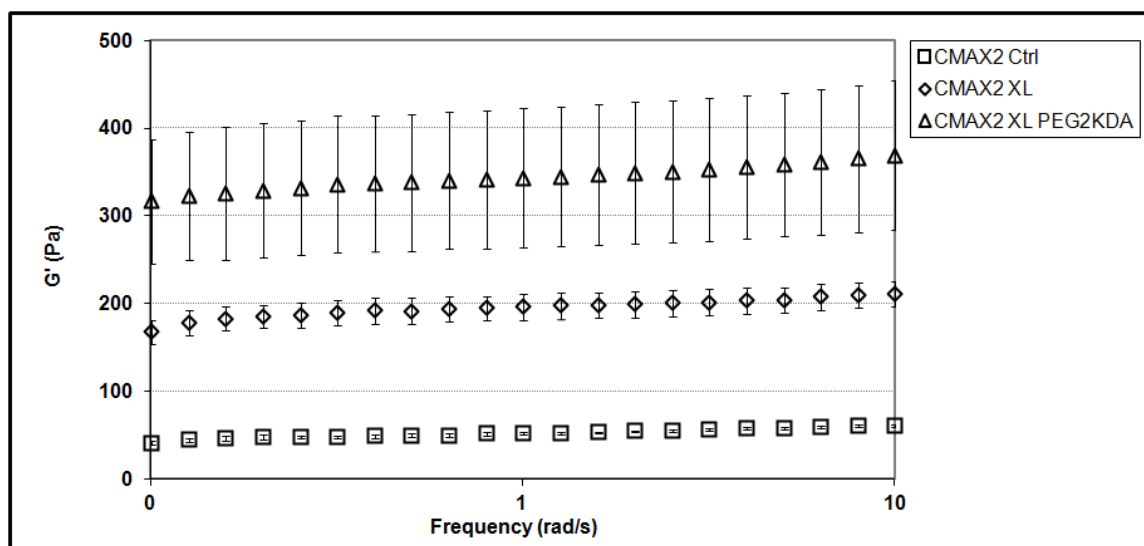


Figure 4-115: Storage Modulus of CMAX2 (Batch 1) with Photocrosslinking \pm 0.1% PEG2KDA

While the rheological results with CMAX2 were initially promising, subsequent batches of CMAX2 showed a trend toward decreasing functionality, with almost negligible increase seen in G' by Batch 3, and no difference in modulus with PEG2KDA as compared to photocrosslinking alone (Figures 4-19, 4-20). Self assembly appeared consistent, with basal values similar among all batches.

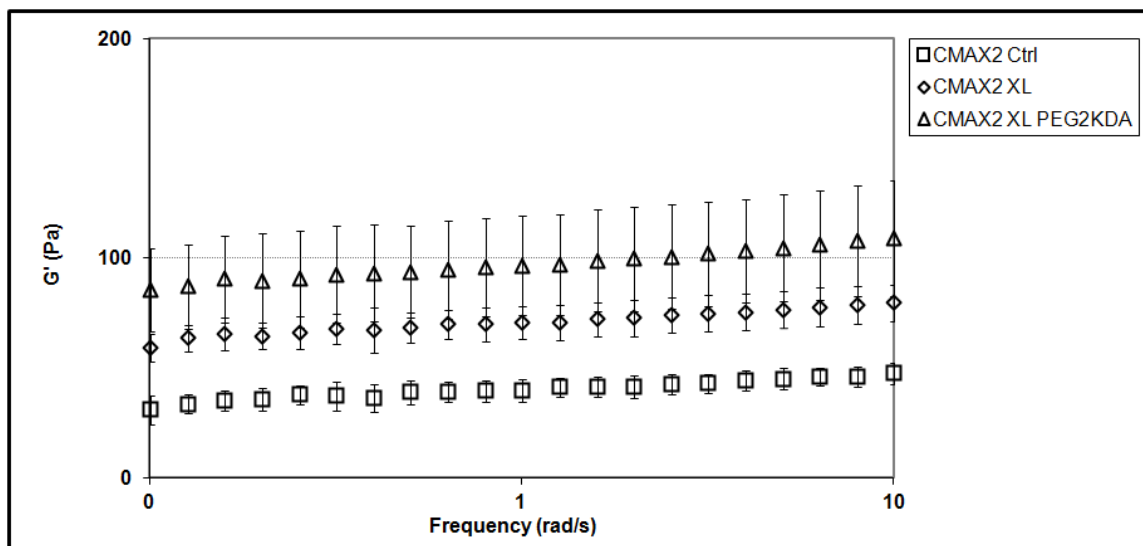


Figure 4-116: Storage Modulus of CMAX2 (Batch 2) with Photocrosslinking \pm PEG2KDA

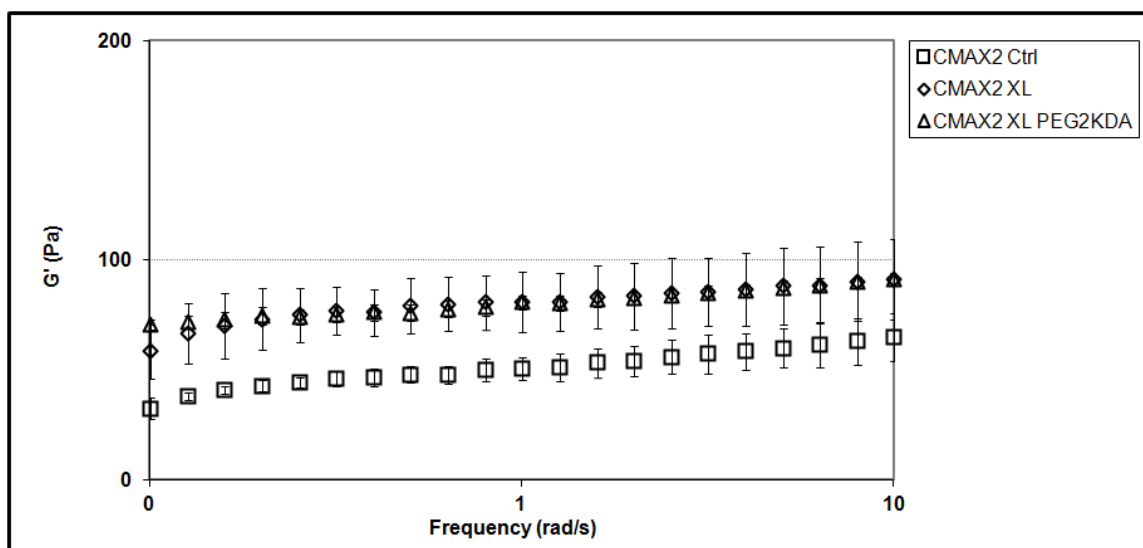


Figure 4-117: Modulus of CMAX2 (Batch 3) with Photocrosslinking \pm PEG2KDA

Troubleshooting was performed to determine if collagen lot number was potentially responsible for the decreased functionality. CMAX2 was synthesized in parallel using two different lots of native collagen, 141 and 159, and photocrosslinked samples of each were tested rheologically. Basal storage modulus was higher for CMAX2 from Lot 159, a trend seen previously when comparing CMA derivatized from these same lots. However, the increase in storage modulus

was close to 2-fold for both batches of CMAX2, and it was concluded that collagen lot was not responsible for the reduced CMAX2 functionality (Figure 4-22).

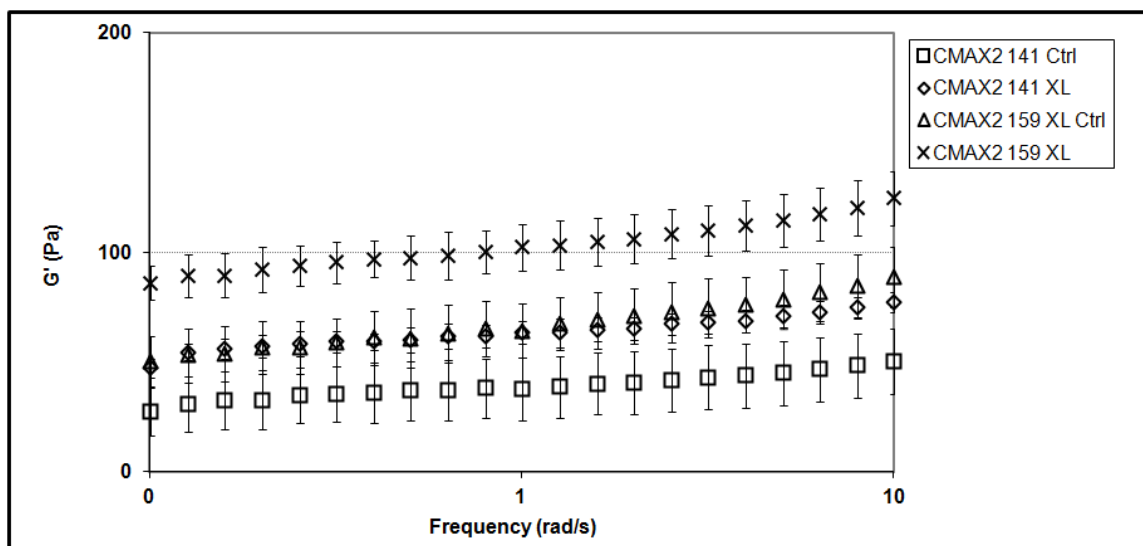


Figure 4-118: Storage Moduli ± Photocrosslinking of CMAX2 from 2 Different Native Collagen Lots

Additionally, frequency sweep analysis including PEG2KDA at 0.1% and 1% (w/v) was included with CMAX2 from lot 159 to evaluate whether the different collagen lot had any effect on the ability of the resultant CMAX2 interaction with PEG2KDA. CMAX2 from lot 159 did not replicate the results seen in the initial CMAX2 rheology experiments. Storage modulus with 0.1% PEG2KDA was not different from photocrosslinking alone, and 1% PEG2KDA significantly decreased the increase in G' upon photoinitiation, similar to results seen previously with CMA (Figure 4-23).

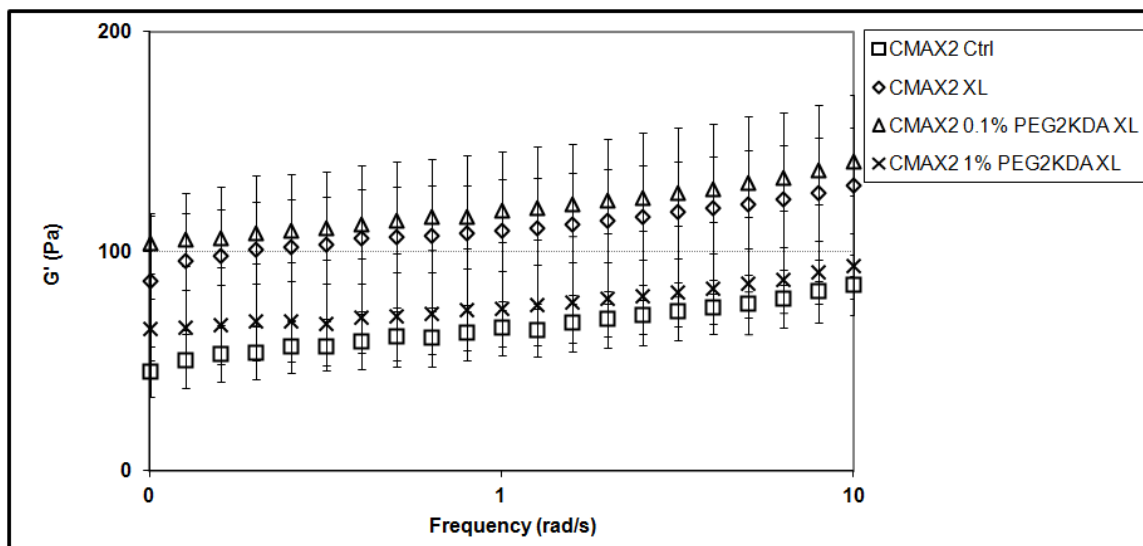


Figure 4-119: Storage Moduli of CMAX2 Photocrosslinked +/- 0.1% and 1% (w/v) PEG2KDA

NMR spectra were obtained from CMA the resultant derivatized CMAX2. From these spectra, seen in Figure 4-24, the peaks corresponding to CMA methacrylate grafting (5.5-6.5 ppm, Figure 4-24A) have disappeared on the CMAX2 spectrum (Figure 4-24B), which looks more similar to spectra obtained from native collagen in previous experiments.

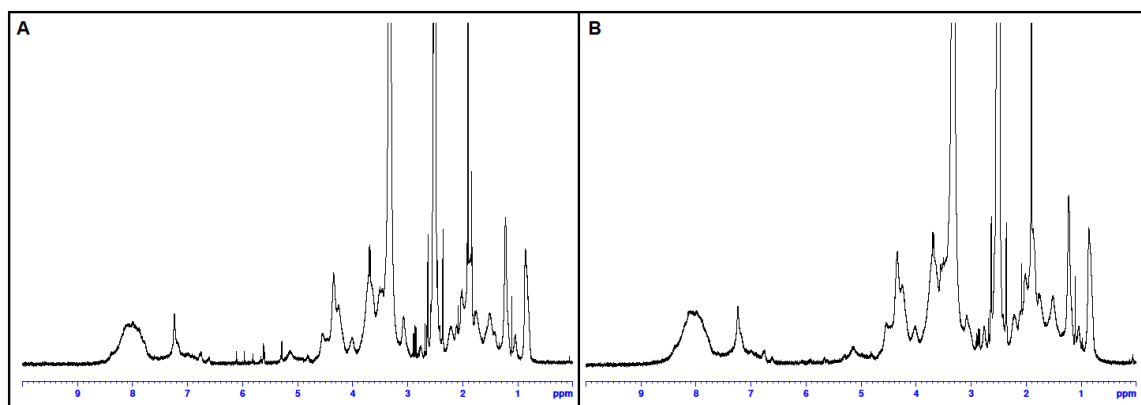


Figure 4-120: NMR of CMA (A) Further Derivatized to CMAX2 (B)

4.4 Discussion

Photocrosslinking type-I collagen-based gels in the presence of photolabile PEG-based reactive macromers resulted in a range of outcomes. We encountered difficulty in predicting the changes in mechanical properties depending on the particular properties of the PEG variant used, which underscores the complexity of the system, and to some degree our lack of understanding as to the molecular nature of the photocrosslinking mechanisms. Using CMA as the base material, we were able to achieve a significant increase in storage modulus upon photocrosslinking in the presence of 0.1% PEG258DA, a low molecular weight homobifunctional macromer. As this concentration of PEG258DA is far too low to form a hydrogel by itself, we can infer that the increase in CMA storage modulus is due to the PEG258DA interacting with the methacrylate groups on CMA, and forming intrafibril and/or interfibril crosslinks that serve to stiffen the fibrillar matrix. Given the length of the PEG involved compared to the relatively large interfibril distances, we believe that the former is more likely, as significant PEG258DA polymerization coupled with the probability of successfully linking CMA groups is unlikely at the concentrations used. This theory is supported by the fact that the relative increase in modulus was linearly related to CMA concentration, as at higher gel density the average interfibril distance is smaller, thus it can be expected that if interfibril crosslinking was a significant contributor to matrix stiffness, a linear increase in CMA concentration would lead to an exponential increase in modulus, which was not observed. Further supporting the theory that intrafibril crosslinking is the primary mechanism responsible for the synergistic G' augmentation in CMA-PEG258DA hybrid gels is the observation that higher molecular weight PEG macromers were not able to effect a significant increase in CMA gels' storage modulus under the conditions we tested. It is possible that only the smallest PEG, $M_w = 258$, was able to effectively enter the intrafibril space to allow crosslinking between available methacrylate groups, and that these

interactions, in addition to the CMA-CMA photocrosslinking, was responsible for the higher G' . A more complete knowledge regarding the position of the methacrylamide groups relative to the orientation of the triple helix would be helpful towards validating this hypothesis, and may require successful modeling of the CMA molecular structure, which we are currently attempting. Another possibility is that the increased hydrophobicity of the PEG258DA compared to higher Mw (and therefore more hydrophilic) PEG variants results in increased interaction with the hydrophobic portions of the collagen molecule and allow photocrosslinking of groups that are modulation unavailable to the higher Mw species.

While the additional mechanical modulation afforded by the inclusion of PEGDA in the photocrosslinking process represents a useful tool for increasing the range of mechanical properties achievable through this platform, it also has serious limitations. Foremost is the severe cytotoxicity that results from including low Mw functional PEGs. Our data indicates that only 258 Da PEGDA is effective at achieving a significant improvement over photocrosslinking CMA alone. PEG species of Mw 500 and greater did not show efficacy at similar concentrations, and when concentrations were increased, the increase in G' compared to photocrosslinking alone was reduced, presumably due to lack of crosslink formation while simultaneously acting as a radical sink and preventing CMA from crosslinking to itself. However, all acrylated PEGs that we tested with Mw less than 1000 exhibited strong cytotoxicity even at very low concentrations. The reason for this toxicity is unclear. Additional studies using non-acrylated PEG macromers did not show significant toxicity at similar concentrations at any of the molecular weights we used, which spanned both toxic and non-toxic molecular weight variants. Another hypothesis was tested, that inhibitors, included to prevent spontaneous polymerization in some of the commercially available functional PEGs, could be responsible, as these inhibitors included benzene, MEHQ, and BHT. However, after comparing inhibitors to viability data, it was clear that

the PEG575DA, which contained no listed inhibitors, was highly toxic while PEG1100MEA, which contained 100ppm MEHQ and 300 ppm BHT, was not toxic. PEG258DA contained 100ppm MEHQ and was highly toxic, as was PEG480MEA which contained 0.5% benzene, 100 ppm MEHQ, and 300 ppm BHT. PEG2KDA had no inhibitors. Thus, no inhibitor proved to be responsible. Singly acrylated PEGs did not seem to differ in toxicity compared to diacrylated PEGs, although a more thorough dose response may have elucidated whether toxicity was correlated to functional group number.

As such, it does not appear that there is a parameter space within the CMA/PEG combinations that we tested that would allow for modulation of gel mechanics in the presence of encapsulated live cells, which was a major motivation for this platform. However, when PEG258DA was photocrosslinked with CMA prior to cell seeding, the cytotoxic effect appeared to be largely mitigated as seen by Live/Dead staining. It was observed that while photoinitiated PEG258DA was not toxic, it did greatly limit fibroblast adhesion and spreading compared to pure CMA gels. This effect is not entirely surprising, as PEG is commonly used to coat biomaterials where adhesion is disadvantageous. Thus, photocrosslinking CMA gels with PEG258DA could potentially be used to spatially control cellular adhesion in tissue engineering constructs or in vitro experiments where differential adhesion is beneficial.

One other major motivation for creating CMA-PEG gels was the goal of using this platform to study cellular behavior in 3D scaffolds of different stiffness, and using PEG-based photocrosslinking to modulate mechanical properties while controlling matrix geometry. However, as CMA did not appear able to form crosslinks with PEG variants that could be used to develop this methodology, we were unable to pursue this goal. Instead, we focused on further development of methacrylate derivatized collagen in the hopes that by adding more

methacrylate groups, and on different side chain targets, PEG variants would be more effective in forming crosslinks.

Given both the relatively low concentration of amines on collagen per unit mass and the constraint of achieving ~25% derivatization of those, we investigated whether other amino acid side chains could be methacrylated along with the free amines. The success in using EDC crosslinking to derivatize collagen while maintaining its inherent advantages led us to attempt to use a similar method to activate the carboxyls on collagen, rather than methacrylic acid, and graft an amine-containing methacrylate. While it was previously impossible to do so with native collagen, as the amines present on collagen would crosslink to the activated carboxyls, we hypothesized that CMA, with a large percentage of its amines already derivatized, would result in less unwanted crosslinking. Thus, we investigated a second round of methacrylation that used aminoethyl methacrylate at the amine target to derivatize the activated carboxyls on CMA to create the double-derivatized CMAX2. Initial results were promising, as we observed a much larger range of crosslinking from basal CMAX2 to a photocrosslinked state, indicating that we had indeed added more functional methacrylates. Additionally, it seemed that the orientation of these additional methacrylates was such that PEG variants that were previously ineffective in modulating the material properties of CMA were able to interact with CMAX2, as PEG2KDA showed a significant increase in modulus and represented almost an order of magnitude of dynamic stiffness range through crosslinking. However, the enthusiasm for this method was quickly tempered as replication of the initial results proved difficult, and functionality of CMAX2 decreased with each successive batch despite our best efforts at keeping synthesis conditions as similar as possible. Much effort was spent troubleshooting this phenomenon, but we were unable to replicate the functionality of the first batch or understand the reason for this failure. It was have been due to unique environmental conditions, a particular lot of reagent that was no

longer available, or simply serendipitous error during the first batch that was not successfully replicated in later attempts. NMR data was the most nonplussing, as not only did it show a failure to additionally add methacrylate peaks to the spectrum, but instead showed that there was less methacrylate present than before the second derivatization. One hypothesis to explain this is that the methacrylates were potentially reacting with each other during some of the reactions, thus rendering them unavailable to form crosslinks later during photocrosslinking. Eventually it was decided that, given consistent, robust functionality of CMA, it was prudent to focus on using that material without the viability constraints of low Mw PEGs, and investigate how cellular behavior could be modulated using the stiffness range available along with evaluation of photografting ligands to the CMA methacrylate groups.

4.5 Conclusion

The stiffness of CMA can be significantly mechanically modified using 0.1% (v/v) of very low molecular weight (258Da) PEG diacrylate in the photocrosslinking reaction, although higher molecular weight functional PEGs had no effect at low concentration (0.1%) and actually mitigated the desired increase in modulus afforded by crosslinking alone at higher concentration (1%). The mechanism by which PEG258DA allows this additional stiffness increase is unclear. Furthermore, use of PEG258DA with live encapsulated cells is not plausible due to its severe cytotoxicity even at lower concentrations than will produce significant mechanical effects, although the cytotoxic effect appears to be greatly reduced after photocrosslinking is conducted. Cytotoxicity appears unique to low molecular weight acrylated PEG, as PEGs lacking of acrylate or having a molecular weight above 1KDa resulted in no significant toxicity. One possible use of a hybrid CMA/PEG258DA gel would be in designing hydrogel materials where mechanical and adhesive properties can be tuned for specific applications, where subsequent

cell interaction will occur. Other methods for incorporating functional PEGs into hybrid hydrogels, such as grafting heterobifunctional PEGs onto the collagen backbone, resulted in significant disruption of the fibrillar self-assembly, and were not pursued further due to this drawback. Lastly, derivatizing carboxyl moieties on collagen may be an avenue for increasing the degree of functionalization of CMA gels, although our attempts at further derivatizing CMA in a second reaction resulted in variable and irreproducible results. It appeared that in some cases, but not others, that the second round of methacrylation produced a more derivatized material with a broader range of stiffness available via photo initiation, and allowed for interaction with larger, non-toxic PEG diacrylates. However, due to these inconsistencies and the high cost of both time and materials in optimizing the CMAX2 reaction process to a useful state, further development on this material were halted.

Chapter 5: In Situ Photomodulation of Hydrogels for Cellular Instruction

5.1 Introduction: CNS Tissue Scaffold Engineering

Mechanically tunable hydrogels have the potential to be used in a broad range of applications where heterogeneous control of the material properties is desired. One possible clinical application is in central nervous system (CNS) injury. The native tissue in the CNS has mechanical properties similar to those of collagen gels, and neural tissue behavior has been shown to be highly responsive to changes in stiffness [33]. Moreover, CNS injuries can result in lesion cavities with non-uniform geometries that are not amenable to solid scaffold implantation without the risk of additional damage to the injury site [34]. One major advantage of type I collagen is its ability to self-assemble, which will allow the material to be injected into a defect of almost any geometry with minimal invasion, and then automatically become a solid to provide a stable matrix. Photocrosslinking could then be accurately introduced into any spatial pattern where light application is accessible. As long as the photocrosslinking process is cytocompatible with the cells of interest, a liquid scaffold/cell mixture can be injected into a defect, followed by scaffold modulation *in situ* to create an optimal environment for tissue regeneration that is customizable to an individual situation. Hydrogel scaffolds also allow for controlled release of therapeutic agents such as growth factors, enzymes, and anti-inflammatory agents [37,38,35,36]. Here, the release rate of the therapeutic can be controlled locally by increasing the crosslinking density and hence the degradation rate of the scaffold. Localized patterns and gradients of neurotrophic agents encapsulated within the matrix could provide another method for guiding cellular behavior. It is well known that chemotactic gradients present during neurogenesis contribute to proper axonal targeting; this phenomenon has also been recreated in the adult rat brain facilitating properly targeted axonal outgrowth [39].

Defined, anisotropic presentation of cues, such as adhesive ligands or matrix stiffness, can also provide critical directional information to regenerating neural tissue to potentially accelerate functional recovery. Neural recognition molecules, such as L1, Neural Cell Adhesion Molecule (NCAM), poly-sialic acid (PSA), and Tenascin-R, have been implicated in the recruitment and/or repulsion of neuronal cell migration and peptide mimics of these ligands may provide attractive options for photopatterning of neuroactive molecules [40,41]. In another instance, using a microfluidic-based assay, our laboratory has demonstrated that the growth of regenerating neurites from dorsal root ganglia is directed and enhanced down gradients of compliance. However, the scope and profile of these gradients were limited by the tolerable concentrations of the soluble crosslinker used, and by dimensional constraints associated with maintaining laminar flow regimes in microfluidic networks. Moreover, guidance of cell types other than neurons, such as astrocytes and Schwann cells, has been shown to cause a secondary alignment of neurons [83,42]. Taking advantage of these phenomena may allow reorganization of either the glial scar or infiltrating Schwann cells, both present in many CNS injuries. This in turn could allow modulation of neuronal ingrowth through the injury site and could provide strategies to encourage proper targeting, a crucial step toward promoting functional recovery [84].

Another potential arena for employing tunable hydrogels is toward directing and maintaining stem cell differentiation. The microenvironment surrounding a stem cell, including the mechanical and biochemical properties of the extracellular matrix, has been shown to have a profound effect on the proliferation rate of stem cells as well as differentiation fate [43]. More recently, human mesenchymal stem cells (hMSC) have been shown to not only differentiate into functional neuronal lineages ^[44], but also that the mechanical properties of the matrix were directly and solely responsible for the resultant differentiation fate ^[45]. Engler *et al* demonstrated that hMSC differentiation on 2D substrates was determined by substrate

stiffness. Substrate stiffness of 0.1-1 kPa, 8-17 kPa, or 25-40 kPa resulted in neurogenic, myogenic, or osteogenic lineages, respectively [46]. It was also shown recently that the combination of substrate stiffness and the presentation of adhesive ligands may act synergistically to drive hMSC differentiation. Rowlands *et al* showed, for instance, that hMSC differentiation could be pushed towards an osteogenic lineage via a stiff (80kPa) substrate coated with type-I collagen, but that type IV collagen on the same substrate resulted in differentiation into a myogenic lineage [47].

Several groups have recently used collagen gels as matrices for stem and neural precursor cell-based therapies in CNS injury models [48,49]. While their results show that collagen gels are suitable for supporting both stem cell proliferation and differentiation into neural tissues, thus far these materials lack the ability to produce localized, controlled heterogeneity, which may be necessary to completely regenerate damaged tissues and restore function to pre-injury levels. In addition, endogenous neural progenitor cells involved in CNS regeneration may also be instructed through the presence of exogenous functional ligands. Previous studies performed in our laboratory showed that Schwann cell proliferation and process extension could be augmented by culture on collagen gels grafted with a peptide mimic of PSA [85]. Schwann cells present an attractive option for nervous system injury regeneration, and have been implicated both as part of the innate CNS injury repair mechanism as well as a possible cell type for transplantation into CNS injury lesions [86-89]. Furthermore, laminin patterning on 2D substrates has been used to align Schwann cells *in vitro* [90]. However, strategies for guiding Schwann cell ingrowth in clinically relevant situations are severely lacking.

Here, we investigate the use of CMA as a self-assembling hydrogel scaffold for fostering growth and differentiation, and for manipulating cellular behavior via photoinitiated modulation of

scaffold mechanics and biochemistry. We begin by examining biocompatibility via comprehensive screening of multiple cell types in the presence of photoinitiator activation. Following identification of robust cell types, we test whether photocrosslinking can be used to affect neuronal differentiation and outgrowth within 3D gels as well as on 2D gel interfaces through both stiffness augmentation and biochemical modification using photosensitive bioactive peptides. The successes and failures with these approaches are discussed with discussion of future implications for using CMA hydrogels as self-assembling soft tissue constructs.

5.2 Methods

5.2.1 *Cell Culture*

NIH-3T3 Fibroblasts (ATCC) were cultured on tissue culture-treated polystyrene (TCP) flasks in Complete Medium, (CM: Dulbecco's Modified Eagle Medium (DMEM), 10% Fetal Bovine Serum (FBS), 2mM L-glutamine, 1X penicillin/streptomycin (P/S)). Cells were routinely subcultured when 90-95% confluency was reached. Cells were passaged by detachment using 0.25% Trypsin/EDTA, inhibition with CM, and centrifugation at 400RCF for 2 minutes. Cells were then replated at between 3-10-fold dilution for further expansion. For experiments, 3T3 cells were harvested, centrifuged, resuspended in CM and used immediately for experiments in native collagen and CMA gels as well as on TCP. Rat Aortic Smooth Muscle Cells (SMCs) were cultured similarly in a medium consisting of a 50% DMEM 50% Ham's F-12, supplemented with 20% FBS, 1% L-Glutamine, 1% P/S.

Intact chicken dorsal root ganglia (DRG) were dissected from embryonic day 8 chicks (Charles River). Briefly, chicks were decapitated, skin and internal organs removed in room temperature PBS, and limbs were bluntly dissected away from the spinal column to expose DRG. #5 Forceps

were used to transfer DRG by the 'tail' to a dish containing HBSS on ice. DRG were kept in HBSS for up to 1 hour post dissection before plating on or in collagen gels. DRG were cultured in CM supplemented with 50ng/mL recombinant rat β -NGF (R&D Systems).

Human embryonic stem cells (hESC) were cultured according to a protocol developed by Carlson et al[91]. Briefly, NIH-approved hESC WA09 (H9) from the WiCell Research Institute (Madison, WI, USA) were maintained under feeder-free conditions on $\frac{1}{4}$ Matrigel-coated dishes (BD Biosciences) in mTeSR1 maintenance medium for hESCs (Stem Cell Technologies), as described previously[92]. Cells were routinely passaged every 5–7 d using 1 mg/ml dispase (BD Biosciences). Other ES cells, including Sox1-expressing mouse ES (Sox1-mES) were cultured in a similar manner.

L2.3 rat neuroglial precursor cells were a kind gift from the Grumet Lab, and were cultured according to a previously published protocol[93]. L2.3 were grown in neurosphere culture in 100mm Petri dishes in an incubator containing 10% CO₂. Culture medium comprised a base medium of DMEM/F-12, 25mM glucose, 1X P/S, supplemented with fresh 1X B27 supplement, 2 μ g/mL heparin, and 10ng/mL bFGF (Peprotech). Cultures were fed daily with a 10X concentrated feed medium consisting of base medium supplemented with 10X B27, 20 μ g/mL heparin, and 100ng/mL bFGF. Neurospheres were cultured until spheres started to show necrotic cores, at which time the population was passaged. To passage, L2.3 spheres were centrifuged at 100RCF for 2 minutes, supernatant aspirated, and triturated with 0.25% trypsin/EDTA for 2minutes to dissociate neurospheres. Following inhibition with a soybean-based trypsin inhibitor, cells were centrifuged at 100RCF for 5 minutes, aspirated, and resuspended for further culture or use in experiments. Other experiments using intact neurospheres were sedimented for 20 minutes and the supernatant carefully aspirated. Intact

neurospheres and dissociated cells were encapsulated in native collagen and CMA gels or exposed to I2959 and UV in culture medium for cytotoxicity testing. Later experiments with cortical neuron precursor (CTX-8) neurospheres, also from the Grumet Lab, were cultured similarly to L2.3 cells.

H1 hESC-derived RG8 neural stem cell (RG8-NSC) were kindly donated from Jocie Cherry of the Moghe Lab. RG8 were grown on ¼ Matrigel-coated flasks in Neural Proliferation Medium (NPM), consisting of 50% DMEM/F-12, 50% Neurobasal medium, 0.5X N2 supplement, 0.5X B27 (w/o vitamin A), and 20ng/mL bFGF. For use in experiments, cells were cultured to 95% confluency, detached with Accutase, centrifuged and resuspended for use in cytotoxicity screening in gels as well as on tissue culture plastic.

Adult human mesenchymal stem cells (hMSC) were provided by the Texas A&M Health Science Center College of Medicine Institute for Regenerative Medicine. hMSC were seeded at 1000 cells/cm² in tissue culture flasks and expanded until 60-70% confluency to prevent contact mediated spontaneous differentiation as determined by morphological analysis under bright field microscopy. hMSC were cultured in α -MEM (Invitrogen, Carlsbad, CA) supplemented with 20% FBS (Atlanta Biologicals, Norcross, GA), 1% penicillin/streptomycin, and 2ng/mL bFGF (Peprotech, Rocky Hill, NJ). Following expansion, hMSC were detached via 0.25% trypsin/EDTA, washed in culture media, and replated for cytotoxicity on TCP or encapsulated in NC/CMA at densities from 1-100x10⁴ cells/mL. hMSC were also induced to a neural phenotype using several published protocols. Initially, a protocol based on Woodbury et al. [94], adapted to incorporate elements from several subsequently published works[95-100], was used to induce neuronal differentiation. Briefly, hMSC were encapsulated in native collagen and CMA gels at a density of 1x10⁶ cells/mL, and gels were photocrosslinked. TCP with 1000 cells/cm² served as a

2D control. Cells were grown in pre-induction medium (PIM; α MEM, 20% FBS, 10ng/mL bFGF, 1X P/S) for 2 days. On day 2, medium was changed to neural differentiation medium consisting of Neurobasal medium, 1% FBS, 1X N2, 10ng/mL bFGF, 20ng/mL BDNF, 50ng/mL NGF, 10 μ M Forskolin, 2% DMSO, 200 μ M BHA, 1 μ M β ME, 1X L-Glutamine, and 1X P/S. Cells were cultured for 2 weeks, changing medium once per week. Additionally, a separate method published by Long et al.[101] was evaluated for inducing neuronal differentiation. Medium was changed from standard proliferation medium to a neural induction medium consisting of Neurobasal, 1X B27m, 1mM db-cAMP, 0.5mM IBMX, 20ng/mL EGF, 40ng/mL bFGF, 10ng/mL FGF8, and 10ng/mL BDNF.

Induced pluripotent stem cell-derived neural stem cells (iPS-NSC) were obtained through collaboration with Kristina Hernandez under the auspices of Dr. Bonnie Firestein. iPS-NSC were derived from human foreskin-derived iPS cells, and further differentiated to a neural stem cell phenotype. Briefly, iPS cells were grown in mTeSR/Neurobasal media supplemented with 500ng/ml Noggin. Noggin is a morphogen which plays a key role in neural induction and in the inhibition of neuronal differentiation. After 11 days in this culture, cells were dissociated and plated onto 20 μ g/ml laminin coated dishes in Neurobasal media. Eight days later, the media was changed to neural proliferation medium NPM (50% DMEM/F-12 with Glutamax, 50% Neurobasal, supplemented with 0.5X N2, 0.5X B27 without vitamin A, and 20ng/ml bFGF, at which point cells were characterized as neural stem cells. For further culture, iPS-NSC were seeded at 30×10^4 cells/cm² on ¼ Matrigel-coated tissue culture plastic flasks. Cells were expanded in NPM until 95% confluent, at which they were harvested for experiments or passaged for further expansion. For neural differentiation, confluent flasks were switched to neural induction medium (NIM) to induce neural differentiation for 24h, then cells were replated on PDL/Laminin, or later, ¼ Matrigel, upon which medium was changed to neural

differentiation medium (NDM) to terminally differentiate cells into neurons for 5-7 days. NIM consisted of NPM without bFGF, while NDM was made up of Neurobasal medium supplemented with 1X B27 (w/o vitamin A) and 10ng/mL BDNF (Peprotech).

Adult spinal cord progenitors (aSCP) were obtained from Dr. Audrey Petit at the University of British Columbia in the lab of Dr. Jane Roskams. aSCP were expanded as neurospheres in NeuroCult NSC Basal Medium (Stem Cell Technologies) supplemented with 10% NeuroCult NSC Proliferation Supplement (Stem Cell Technologies), 2µg/mL heparin, 20ng/mL EGF and 20ng/mL bFGF. To passage, cells were trituated in 0.25%trypsin/EDTA until a single-cell suspension was obtained, washed in culture medium, and resuspended using a split ratio of 1:10. For differentiation into glial cells, medium was changed to Neurobasal medium supplemented with 2 mM glutamine, 1XB27, and 1X P/S.

Skin-derived precursor-derived Schwann cells (SKP-SC) were a kind gift from Dr. Wolfram Tetzlaff at the International Collaboration on Repair Discoveries (ICORD) in Vancouver, British Columbia. SKP-SC were cultured on TCP coated with 2ug/mL poly-D-lysine (PDL) and 2ug/mL Laminin-1 from Engelbreth-Holm-Swarm murine sarcoma basement membrane. To coat flasks, PDL/Laminin in deionized water was sterile pipetted into flasks and incubated overnight at 37°C. Flasks were washed 2X with PBS prior to plating cells. SKP-SC were plated and at 2×10^4 cells/cm² and cultured in Schwann Cell Medium (SCM), which consisted of 75%DMEM, 25% F-12, 2%N2 supplement, 5µM forskolin, 50ng/mL neuregulin1-β. Cells were expanded until 95% confluent, then passaged using 0.25% trypsin/EDTA, washed in PBS with 10% FBS to inhibit trypsin, centrifuged at 200RCF for 2 minutes, and resuspended in SCM for further expansion or used in experiments.

5.2.2 Immunohistochemistry (IHC)

Cell phenotype was characterized through IHC staining of expressed protein markers. Primary antibody targets included are listed in the table below.

Cell Type	Protein Target	Species	Source	Dilution
hMSC, iPS-NSC, aSCP	Nestin (neural stem cell marker)	Mouse	Millipore	1:500
hMSC, iPS-NSC, aSCP, SKP-SC	Class III β -tubulin (Tuj1) (neuronal marker)	Mouse	Covance	1:1000
DRG aSCP	Neurofilament Heavy Chain (NF-200) (neuronal marker)	Mouse	Sigma, AbCam	1:500
DRG	Neurofilament Medium Chain (NF-M) (neuronal marker)	Mouse	AbCam	1:500
iPS-NSC	PAX6 (neural stem marker)	Mouse	Millipore	1:500
hMSC	CD105 (mesenchymal stem cell marker)	Mouse	AbCam	1:500
hMSC, iPS-NSC, aPSC	Glial Fibrillary Acidic Protein (GFAP) (glial marker)	Rabbit	Dako	1:100
hMSC, iPS-NSC,	Microtubule-Associated Protein 2 (MAP2) (mature neuronal marker)	Rabbit	Millipore	1:500
iPS-NSC	Synaptophysin (SYN) (neuronal synapse marker)	Rabbit	AbCam)	1:500
iPS-NSC	Vesicular Glutamate Transporter 1 (VGLUT1) (glutamatergic neuron marker)	Rabbit	Millipore	1:500
SKP-SC	S-100 (Schwann cell marker)	Rabbit	AbCam	1:50

Table 5-1: Primary Antibodies used in Immunohistochemistry

For IHC of cells grown on 2D substrates, cells were fixed in 4% paraformaldehyde (PFA) for 15min at RT then washed 3X with immunobuffer (IB) consisting of PBS, 1% bovine serum albumin, 0.5% Triton-X. Following fixation and permeabilization via IB, cells were blocked for 1 hr at RT with IB + 10% goat serum. Blocking buffer was removed and primary antibodies at working dilutions were then added and allowed to conjugate protein targets overnight at 4C. Cells were then washed 3X with IB, and fluorescently-conjugated secondary antibodies at 1:1000 working

dilution (Alexa Fluor, Life Technologies) were allowed to bind appropriate primary antibody isotypes for 2 hr at RT. Cells were then washed 3X in IB, with DAPI included in the 2nd wash for nuclear counterstaining, and imaged. For 3D gel samples, samples were fixed with 4% PFA for 30min, followed by 3 washes with IB of 5, 10, and 30 minutes to allow complete diffusion of PFA out of gels. Blocking was performed for 2 hours at RT, with primary antibody incubated at 4°C overnight. Primary antibody was washed with 10, 15, and 30 minute incubations with IB at RT. Secondary antibody was incubated for 4 hours at RT on a rocker, followed by washes of 30 minutes, 1 hr, and 4 hr at RT on a rocker, then overnight at 4°C to completely remove unbound secondary antibody. DAPI was included in the 4 hour wash. Imaging was performed using an Olympus IX81 inverted epifluorescent microscope with an Olympus IX2-DSU spinning disc confocal attachment. Images were captured with a Hamamatsu ORCA (Hamamatsu City, Japan) or Hamamatsu ImagEM digital camera for 2D and 3D samples, respectively. Images were obtained and processed with Olympus Microsuite and Olympus Metamorph software, with further processing and quantification using ImageJ and Matlab.

5.2.3 Irgacure 2959

4-(2-hydroxyethoxy)phenyl-(2-hydroxy-2-propyl)ketone, trade name Irgacure 2959 (I2959), was chosen as the photoinitiator due to its water solubility and purportedly low cytotoxicity as compared with other photoinitiators[102]. I2959 was supplied as a kind gift from Ciba Specialty Chemicals and was stored in opaque containers at room temperature. Fresh stock solutions of 10% (w/v) I2959 were mixed weekly. I2959 stock solutions were made by weighing out powdered I2959 and adding the requisite amount of solvent, initially 70% ethanol and later 100% methanol due to increased cytotoxicity with the former. Stock I2959 solutions were kept at 4°C in foil wrapped tubes until needed, and all work done using I2959 was performed in a

dark room with UV-masked fluorescent bulbs. All samples were foil wrapped and kept from light when unreacted I2959 was present.

5.2.4 Photoinitiator Cytotoxicity Screening

Various cell types were seeded onto TCP 96 microplates, allowed to adhere (if necessary) and cultured 0-2 days under the conditions described previously depending on the cell type. Medium was then changed to either cell-specific culture medium or PBS containing from 0.01-0.1% (w/v) I2959, exposed to UV light from the UVL-21 source for variable times of 1-10 minutes, and then cultured for 24-48 hours, at which time viability was assessed using Live/Dead staining and the MTS Assays as described in Chapter 1.

5.2.5 3D Cell-containing Gel Photocrosslinking

Various cell types were encapsulated in native collagen and CMA hydrogels to examine the compatibility of that cell type with both the hydrogel culture environment and the photocrosslinking process. Briefly, Native collagen or CMA solutions were mixed on ice, similar to the process described for rheological tests. The 1X PBS/medium volume (52 μ L per 1mL) was reserved for cell suspensions, which were added in concentrated form to the other mixed reagents to prevent pH and osmolarity induced toxicity from the precursor solution. Macromer/cell solutions were then triturated to distribute cells evenly, plated for gelling, and transferred to a 37°C incubator for 30 minutes to self-assemble into stable hydrogels. Following this, gels were exposed to UV light to initiate photocrosslinking, immediate after which culture medium was added and cells were returned to the incubator for culture. Cell compatibility in 3D photocrosslinked gels was assessed quantitatively with MTS assay, semi-quantitatively with Live/Dead staining, and qualitatively by morphological analysis using bright field and fluorescence microscopy.

5.2.6 Adhesion Assay

Cell adhesion using hMSC and smooth muscle cells was tested on both collagen/CMA gels as well as an adsorbed layer of dilute protein in acetic acid. For gels, native collagen and CMA (\pm photocrosslinking) were pre-formed in 100 μ L aliquots in 48-well plates, washed with PBS and hMSC were plated for 0.5-3 hours and allowed to adhere. Cells were then gently washed 3X with medium to remove unadhered cells. Remaining adhered cells were then quantified either by staining with Calcein-AM and Hoechst 33342 and counting via fluorescent microscopy or via quantification using the MTS assay. For the adsorption assay, 0.1 mg/mL of four ratios of CMA:NC (1:0, 1:1, 3:1, 0:1) in 0.02 acetic acid were coated onto a 48-well plate and incubated at 4°C overnight and allowed to adsorb. Following aspiration of the protein solution and washing with PBS, plates were seeded with 100 μ L of a 5×10^4 cell/mL cell suspension of SMC. The cells were incubated for 1.5 hours to allow adhesion to the substrates. TCP with no protein served as a control. Cells were washed 3X with PBS to rinse unadhered cells an MTS assay was used to quantify remaining adhered SMC.

5.2.7 Photopatterning

Differential crosslinking was achieved through masking incident light exposure. Aluminum foil or high resolution printed transparencies were used to spatially control UV light exposure. Imaging of photopatterning was performed by admixing acrylated fluorophores, such as fluorescein-o-acrylate (FOA), Methacryloxyethyl thiocarbamoyl rhodamine B (Polyfluor 570, Polysciences), or Nile Blue Acrylamide (NBA, Polysciences) into the macromer solution, allowing self-assembly, exposing gels to masked UV, and then washing labile fluorophores out of the gels with multiple rinses of PBS before imaging with epifluorescent microscopy.

5.2.8 Photolabile Peptides Crosslinking

Acrylated peptides were custom synthesized by Biomatik (Biomatik USA, Wilmington, DE). N-termini were targeted for acrylation. Acrylate groups were spaced from peptide sequences using a six glycine (G6) repeat or a miniPEG oligomers chain. Laminin peptide sequences were as follows: Methacrylate-GGGGGG-YIGSR (YIGSR) Methacrylate-GGGGGG-IKVAV (IKVAV), and the scrambled control peptide Methacrylate-GGGGGG-VIVAK (VIVAK). Poly-sialic-acid (PSA) mimetic peptide sequences were as follows: Acrylate-miniPEG-SSVTAWTTG (PSA) and Acrylate-miniPEG-SVSATTWTG (PSA Scramble). Laminin peptides were first dissolved in DMSO due to poor water solubility, then admixed with CMA macromer solutions at 0.1-1mg/mL. PSA peptides were more soluble due to the miniPEG spacer, and were dissolved directly into 10X PBS, which was then mixed in as part of the CMA precursor solution at final concentrations of 0.1-2mg/mL. Gels were formed as 80-100 μ L cylinders in Mat-Tek glass bottom petri dishes, with 14mm diameter cutouts and No. 0 coverslips as the base. UV light was exposed from the bottom up through the gels. Gels were washed 3X with culture medium (30 minutes each) to remove unbound peptide. Cells were either admixed into macromer solutions or plated on top of gels after washing. For $\frac{1}{2}$ gel photocrosslinking, aluminum foil was used to mask one half of the gel from light.

5.3 Results

5.3.1 *hMSC Culture in 3D Photocrosslinked Hydrogels*

A multitude of stem and precursor cell types were screened for compatibility with I2959 photoinitiation (see Appendix A at the end of this chapter for details). Based on this cytotoxicity screen, nearly all neural stem cell populations, with the exception of RG-8 cells with which further development was discontinued due to federal funding conflicts with the source hESC line, appeared incompatible with UV-I2959 photoinitiation. Conversely, hMSC were able tolerate

I2959 at concentrations sufficient to crosslink CMA. Summary of photoinitiation toxicity, including cell types discussed later in the chapter, is provided in Table 2 below.

Cell Type	Species	0.1%	0.05%	0.025%	0.01%	Notes
NIH-3T3	Mouse	--	-	+	++	Significantly affected at photocrosslinking-effective I2959 Concentrations
hESC	Human	--	--	--	-	Highly incompatible, even at lowest I2959 concentrations tested
CTX-8	Rat	--	--	-	-	Few viable cells; only observed in neurosphere cores at < 0.05% I2959
RG-8	Human	--	-/+	+	++	Suitable viable at I2959 concentrations suitable for photocrosslinking
L2.3	Rat	--	-	-	-/+	Marginally viable at low (0.01%) I2959 concentrations at high cell density
hMSC	Human	-	-/+	++	++	Largely tolerant of I2959 concentrations below 0.05%, highly viable at 0.025%
DRG	Chicken	+	++	++	++	Minor negative effects observed only at highest concentration (0.1%)
iPS-NSC	Human	n/a	-	-/+	+	Tolerant of 0.025% when pre-differentiated and at 1×10^7 cells/mL in 3D
aSCP	Rat	n/a	n/a	-/+	+	Marginally tolerant of 0.025% when pre-differentiated and at 1×10^7 cells/mL in 3D
SKP-SC	Rat	n/a	n/a	--	-	Highly susceptible to I2959 at concentrations useful for photocrosslinking

Table 5-2: Summary of Irgacure 2959 Photoinitiation Cytocompatibility with Various Cell Types

Given these results, we then began to investigate whether photocrosslinking-mediated modulation of matrix stiffness could be used to control neuronal differentiation in 3D CMA gels. As 0.025% I2959 seemingly had a minimal negative effect on hMSC viability, and recent

rheological testing implied that 0.025% I2959 could be used to impart significant mechanical stiffness to CMA gels with 2 minutes of UV exposure, we compared hMSC encapsulated in native collagen and CMA gels with and without photocrosslinking at 1×10^6 cells/mL. Using Live/Dead staining and the MTS assay, we analyzed how hMSC morphology and viability were affected under these optimized photocrosslinking conditions to assess whether differences in differentiation fate could be attributed to matrix stiffness alone. Intriguingly, we saw that while viability in the gels was similar to results determined previously, several distinct differences in cell behavior were apparent. Foremost was the difference in contraction of the CMA gels as compared to the other conditions. After 48 H in culture, uncrosslinked CMA gels had contracted to ~25% of their original size, as seen by the increased cell density in Figure 5-1 A. Additionally, cellular morphology of hMSC in photocrosslinked CMA (Figure 5-1 C) was distinct from the other conditions in that cellular processes appeared to be more branched as compared to native collagen, in which the hMSC morphology looked more bipolar (Figure 5-1 B).

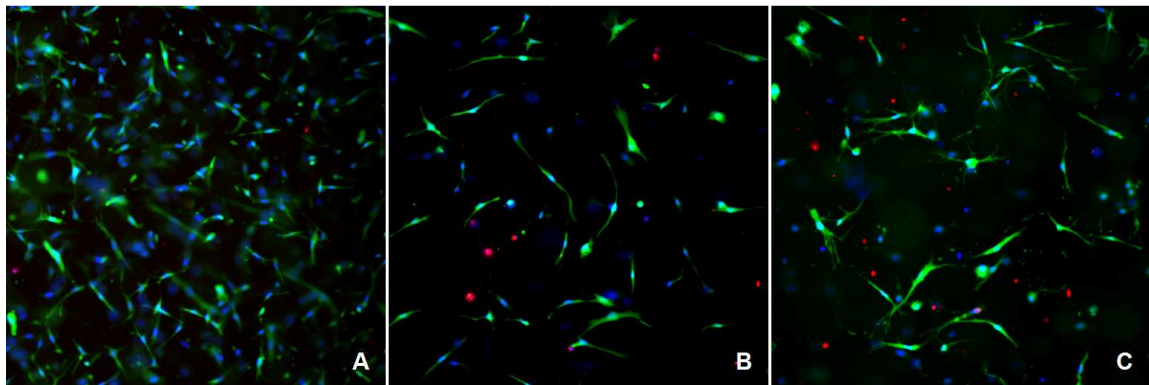


Figure 5-121: hMSC in 3D Gels 48 H after Photocrosslinking with 2 minutes UV and 0.025% in Mat-Tek Dishes. A: CMA Uncrosslinked Control, B: Native Collagen Photocrosslinked, C: CMA Photocrosslinked

A subsequent experiment employing MTS (Figure 5-2) further supported the Live/Dead images, with absorbance at 490 nm of hMSC in photocrosslinked native collagen and CMA only slightly lower than the native collagen control, implying similar cell viability and mitochondrial activity.

Absorbance from hMSC in uncrosslinked CMA gels was significantly higher than native collagen control gels. It was unclear whether this was caused by an actual increase in cell number due to proliferation, an increased metabolic rate of the cells, or an artifactual signal caused by the large difference in gel volume due to the cellular compaction. Control gels that contained no cells did not imply that MTS interacted differently with native collagen compared to CMA.

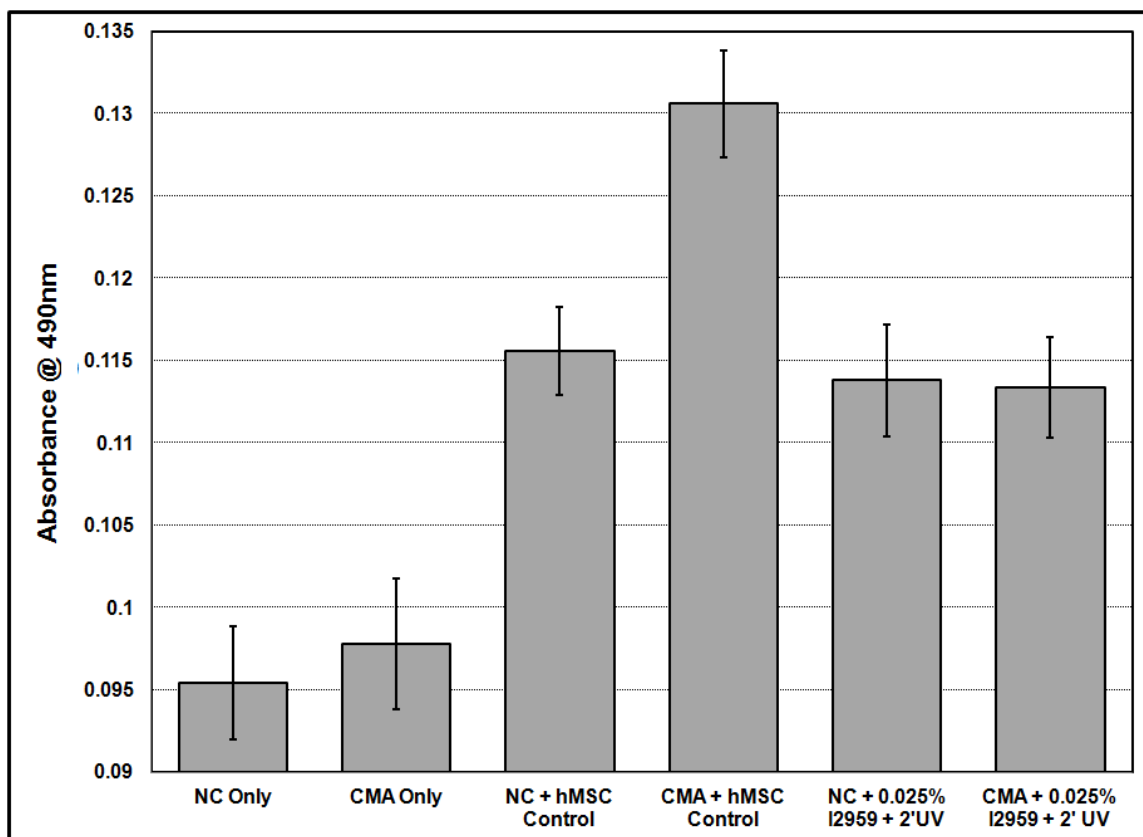


Figure 5-122: MTS Assay. hMSC in Native Collagen and CMA 48 H after Photocrosslinking

It was also unclear whether 48 hours was an appropriate culture period for assessing viability. To evaluate the effect of post-crosslinking culture time on viability, we quantified viability of entrapped hMSCs in native collagen without photocrosslinking and compared to CMA photocrosslinked with 0.025% I2959 and 2 minutes of UV exposure. Following the photocrosslinking process, hMSC were cultured for 24 (Figure 5-3) and 72 hours (Not shown).

Live/Dead stain was added and cells staining positive for each were manually counted and used to determine viability. Again, hMSC appeared at 24H to tolerate the photocrosslinking well, with similar numbers of calcein positive cells in both conditions, as well as only a modest increase in the number of ethidium positive cells. Morphology of cells in photocrosslinked CMA again appeared to be more highly branched than those in native collagen, although overall cell size did not appear to be different.

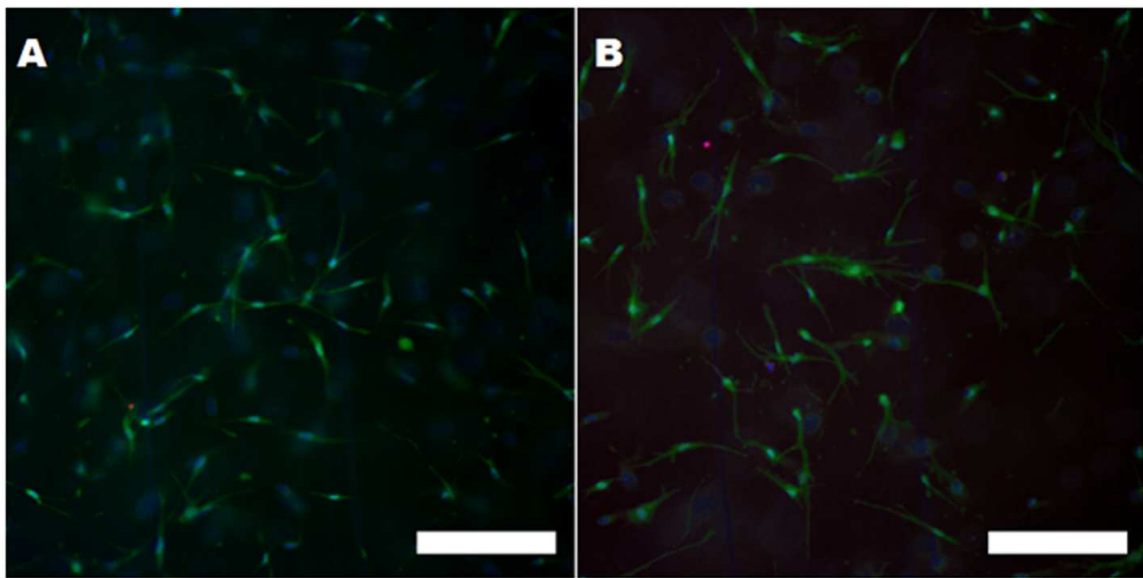


Figure 5-123: Cytocompatibility of hMSC encapsulated in (A) native collagen or (B) photocrosslinked CMA. Images taken 24 hours after UV exposure. Scale bar = 200 μ m

Viability quantification was performed by thresholding and binarizing images from standalone Hoechst and ethidium channels, and using ImageJ to count the number of total and necrotic nuclei in each. As outlined in Figure 5-4, minimal cell death was observed in the control condition of native collagen ($98\pm 1\%$ and $97\pm 1\%$ viable at 24 and 72 hours, respectively) without UV/photoinitiator exposure, whereas in the photocrosslinked CMA condition there was a significant drop in viability ($71\pm 5\%$) at 24 h that recovered to $81\pm 2\%$ at 72 h. There was no significant difference in total cell number between any of the groups. Activation of the

photoinitiator in the presence of hMSC within CMA has a noticeable effect on cellular viability, although the majority of the photocrosslinked cells were viable at both time points.

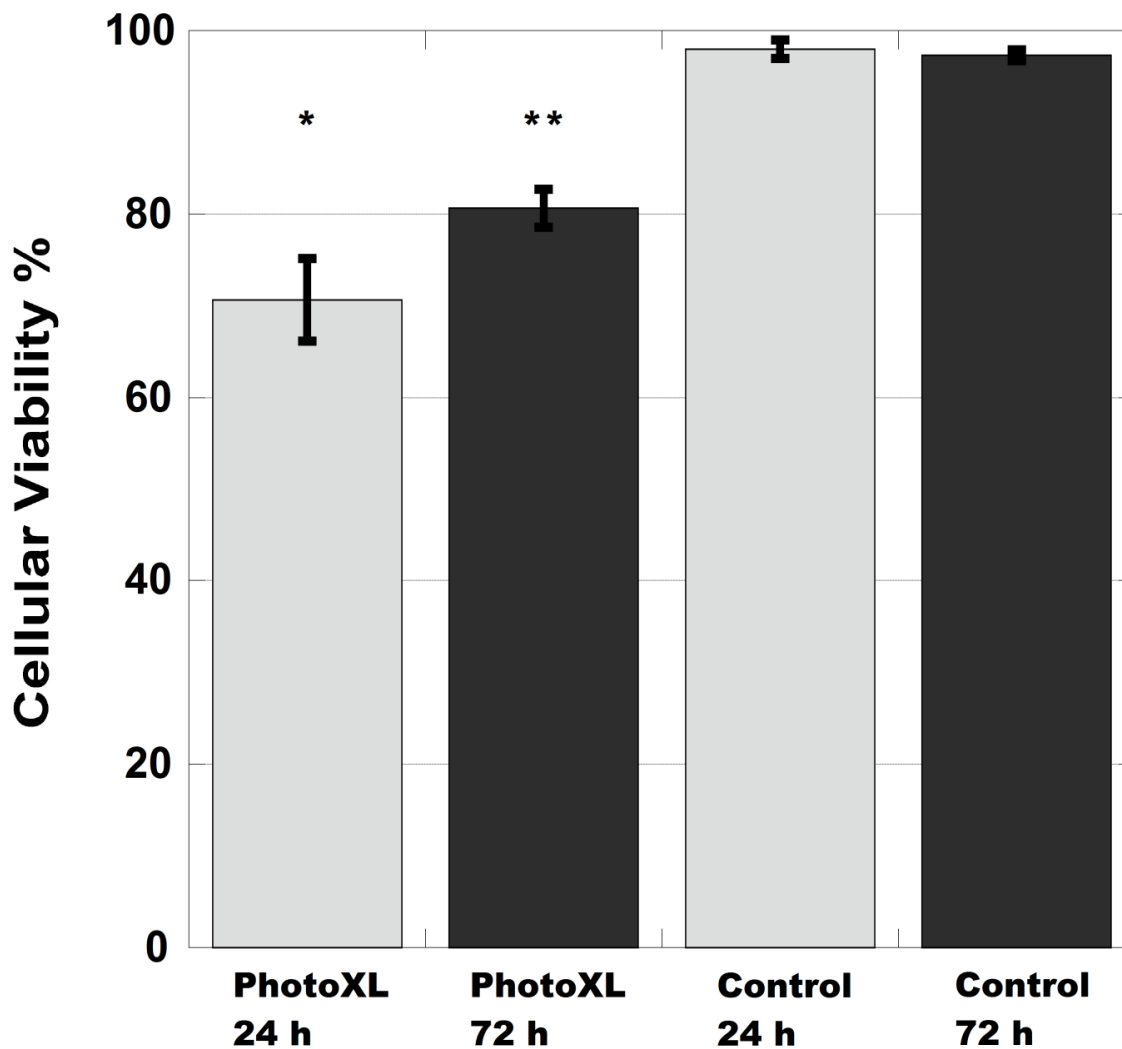


Figure 5-124: Quantification of hMSC viability at 24 and 72 hours after encapsulation and/or photocrosslinking. Photo XL is photocrosslinked, while Control is native collagen without exposure to UV or I2959

5.3.2 hMSC Neuronal Induction

Following validation that hMSC could survive photocrosslinking in CMA gels, we sought to investigate whether hMSC would differentiate into neurons in CMA gels based on the mechanical properties alone, as published research by Engler et al., indicated that matrix

mechanical properties similar to native CNS tissue was a sufficient to induce neuronal differentiation[46]. Additionally, neural induction medium (NIM) was also used to induce neuronal differentiation simultaneously to investigate whether soluble factors along with matrix stiffness could have a synergistic effect on the resultant lineage of neutrally induced cells. Differentiation potential of hMSC was initially evaluated on tissue culture plastic by growing cells in standard growth medium (GM) or NIM. Cells were plated at 1000 cells/cm² and cultured in either medium for 7 days, after which they were fixed and stained for the neural progenitor cell marker nestin, the neuronal dendritic marker microtubule associated protein 2 (MAP2), the axonal marker Class III β -tubulin (β T3), and the glial cell marker glial fibrillary acidic protein (GFAP). This population of hMSC appears to have neurogenic potential, as seen by the presence of nestin in hMSC grown on TCP in standard growth factor (Figure 5-5 A), which is downregulated after 7 days in NIM as would be expected for cells undergoing differentiation (Figure 5-5 E). MAP2 was not highly expressed in either GM or after 7 days in NIM (Figure 5-5 B & F), whereas β T3 was slightly expressed in GM and upregulated in NIM (Figure 5-5 C & G). GFAP appeared to be highly expressed in GM and even more so after NIM culture (Figure 5-5 D & H). Overall, we take these data to imply that these hMSC are inherently capable of differentiating into neural-type cells, and that 7 days of culture NIM increases the expression of characteristic neural markers β T3 and GFAP while downregulating the neural stem cell marker nestin.

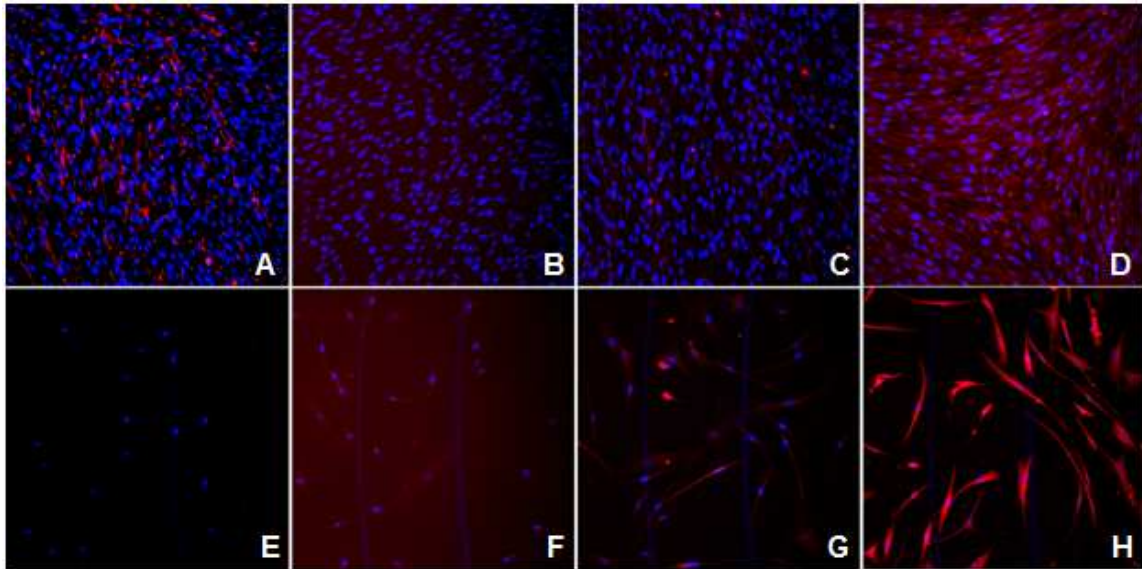


Figure 5-125: hMSC after 7 days in GM (A-D) and NIM (E-H) on TCP. Nestin (A & E), MAP2 (B & F), β 3T (C & G), GFAP (D & H)

hMSC were also grown in 3D culture in native collagen and uncrosslinked CMA in both GM and NIM. hMSC in native collagen followed similar, but not identical, trends for neural differentiation protein marker expression as compared to TCP (Figure 5-6). Nestin was again present in hMSC in GM, and expression disappeared after 7 days in culture in NIM. MAP2 was not expressed in hMSC in GM, but was slightly more expressed in native collagen than TCP. β 3T was highly upregulated in NIM-cultured cells in native collagen, similar in expression to TCP. However, GFAP appeared to be expressed less prevalently in hMSC in native collagen with GM, and was downregulated following NIM culture, in stark contrast with GFAP expression in TCP. While 3D culture in native collagen gels does not appear drastically different than on TCP, the lack of GFAP upregulation may imply that hMSC are preferentially differentiating to a neuronal rather than glial lineage.

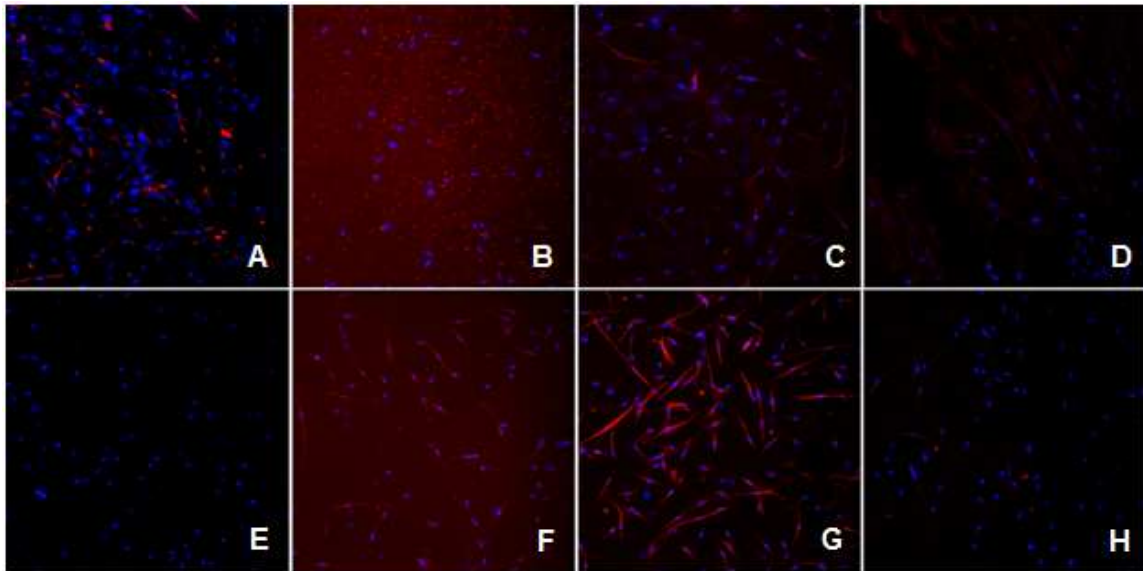


Figure 5-126: hMSC after 7 days in GM (A-D) and NIM (E-H) in Native Collagen. Nestin (A & E), MAP2 (B & F), β T3 (C & G), GFAP (D & H)

Uncrosslinked CMA was highly contracted by hMSC grown in GM as observed previously, making direct comparison of protein expression somewhat difficult. However, similar trends were observed in comparison to native collagen (Figure 5-7). Notably, hMSC grown in NIM did not contract CMA gels to any noticeable degree after 7 days. Overall nestin expression appeared somewhat higher in CMA in GM, although cell density was much higher in the compacted gels. Some nestin expressing cells were still present in NIM cultures, although again the sheer number of cells is likely responsible for this effect. MAP2 upregulation from GM to NIM appeared minimally higher compared to native collagen, but overall expression was still low. The most striking expression difference was observed in β T3 expression, which appeared to be highly expressed in hSMC grown in GM, contrasting both TCP and native collagen. NIM culture did not appear to change the expression level of β T3. Basal GFAP expression and its concomitant downregulation after NIM culture were similar to native collagen.

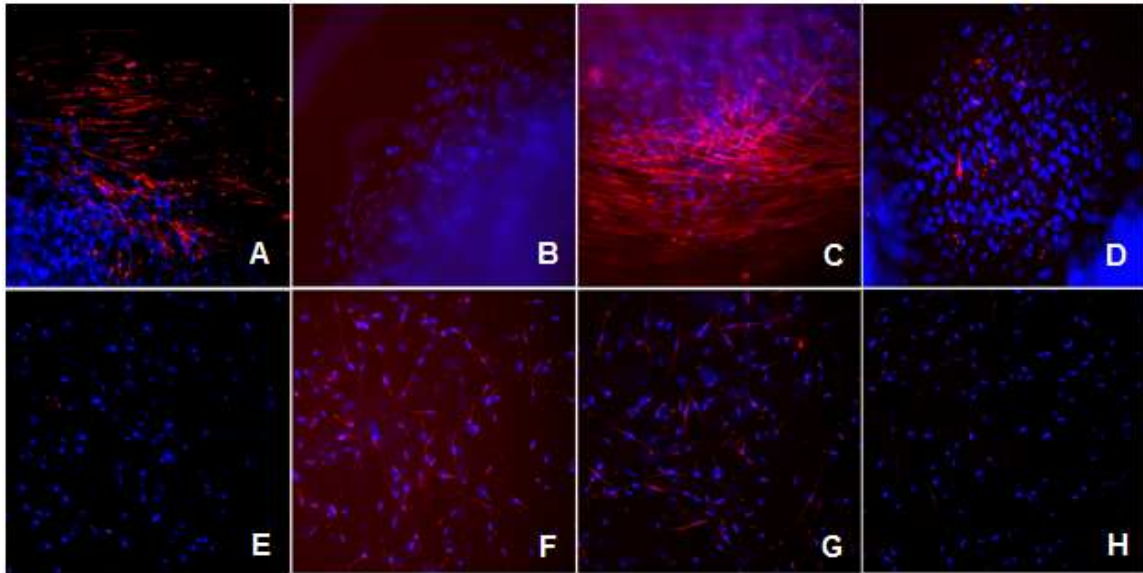


Figure 5-127: hMSC after 7 days in GM (A-D) and NIM (E-H) in CMA. Nestin (A & E), MAP2 (B & F), β 3T (C & G), GFAP (D & H)

A more thorough follow-up experiment was performed to examine differences in hMSC phenotype in photocrosslinked CMA gels along with uncrosslinked CMA and native collagen. Additionally, primary rat cortical neurons and rat brain-derived astrocytes were cultured in 3D native collagen gels in parallel to examine β 3T and GFAP expression levels of hMSC in different substrates to cells with characteristic expression levels. All images were taken under identical optical conditions with exposure times and threshold levels set based on optimal parameters for primary cells. As shown in Figure 5-8, β 3T expression was similar for hMSC regardless of substrate, and staining intensity appeared similar to primary neuronal expression levels. Astrocytes were typically negative for β 3T, although a small percentage of cells, presumably contaminating neurons, did stain positively.

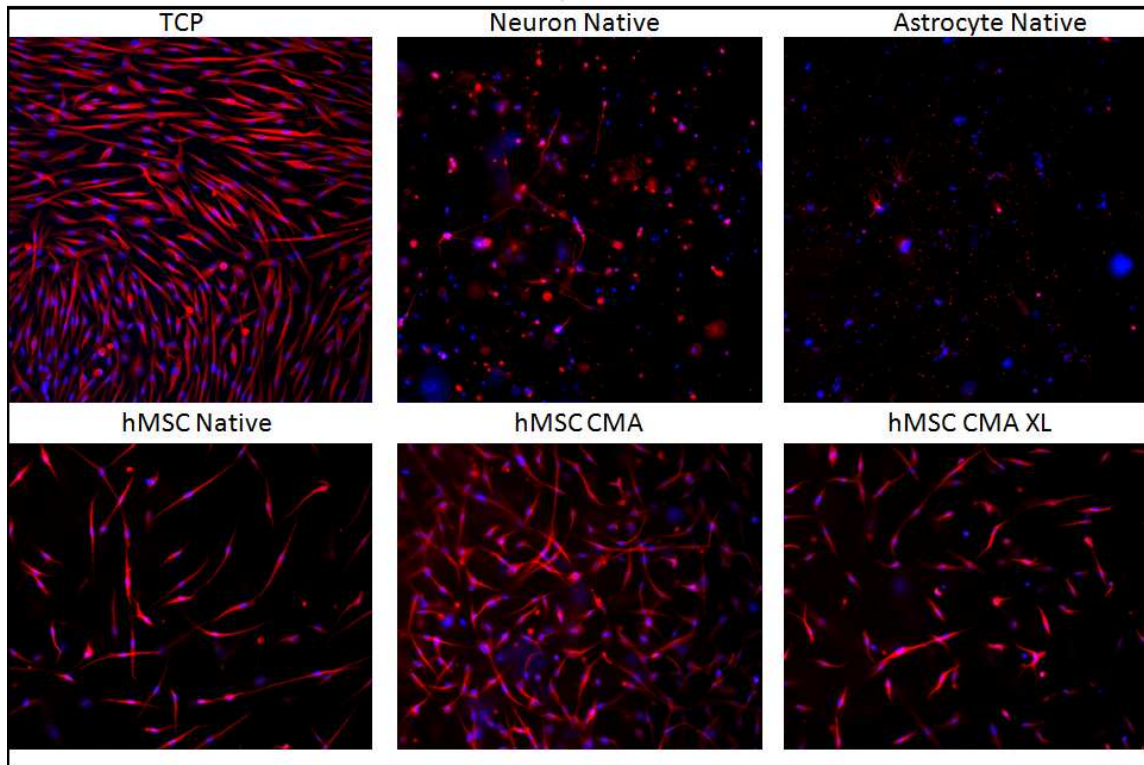


Figure 5-128: β 3-Tubulin Staining of hMSC in Growth Medium in Different Culture Conditions compared to Primary Neurons and Astrocytes

GFAP expression (Figure 5-9) was similarly poor in hMSC in both photocrosslinked and uncrosslinked CMA, with slightly higher expression observed in native collagen gels. Interestingly, hMSC on TCP expressed higher levels of GFAP than in any of the gel conditions, which was morphologically distinct in that it appeared as tortuous bundles of protein ostensibly on top of the hMSC monolayer, whereas in 3D conditions GFAP expression appeared colocalized to the cytoplasm. Neuron controls were expectedly lacking in GFAP expressing cells except for a small number of what appear to be contaminating astrocytes, and astrocyte control cells stained appropriately for GFAP and presented with the standard stellate morphology.

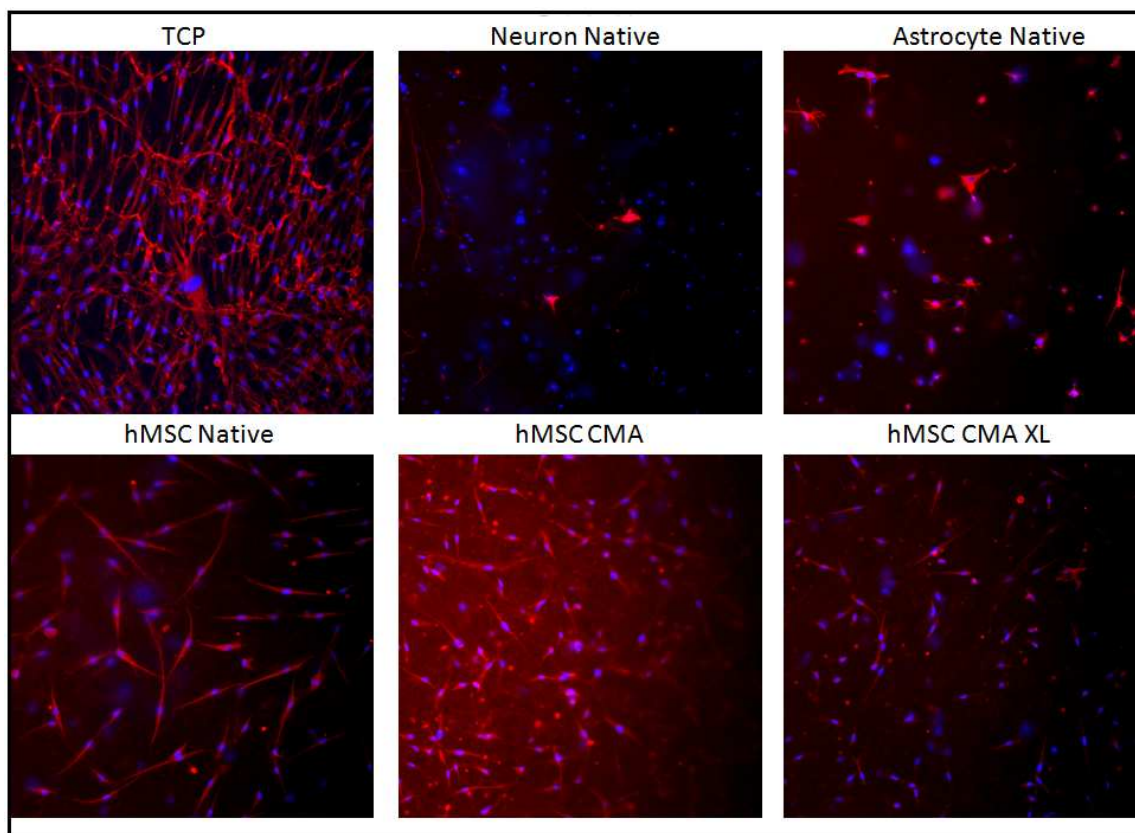


Figure 5-129: GFAP Staining of hMSC in Growth Medium Different Culture Conditions compared to Primary Neurons and Astrocytes

The overall results of these data implied that, although our staining protocols were successful, (a concern given the unexpectedly high levels of constitutive expression on neural markers in hMSC), the panel of markers chosen was not appropriate for determination of differentiation lineage. β T3 expression was high regardless of substrate or medium, MAP2 was not sufficiently expressed by hMSC even after neural induction, and GFAP appeared highly expressed in hMSC on stiff TCP and in GM while it was poorly expressed when cultured in softer 3D gels with NIM. Nestin appeared to be the only useful marker, as its downregulation was predicted for cells transitioning from a neural progenitor state to a more mature neural lineage, although the lack of nestin expression alone is not sufficient to make any conclusions about neural differentiation.

Additionally, we investigated how modulating the stiffness of CMA gels through controlling UV light exposure time affected the viability of neurally-induced hMSC. Figure 5-10 outlines the viability as per Live/Dead staining of hMSC in CMA with growth medium (Figure 5-10 A) as compared to hMSC in CMA cultured with NIM following photocrosslinking of 0, 30, 60, 90, 120, 150, and 180 seconds (Figure 5-10 B-H).

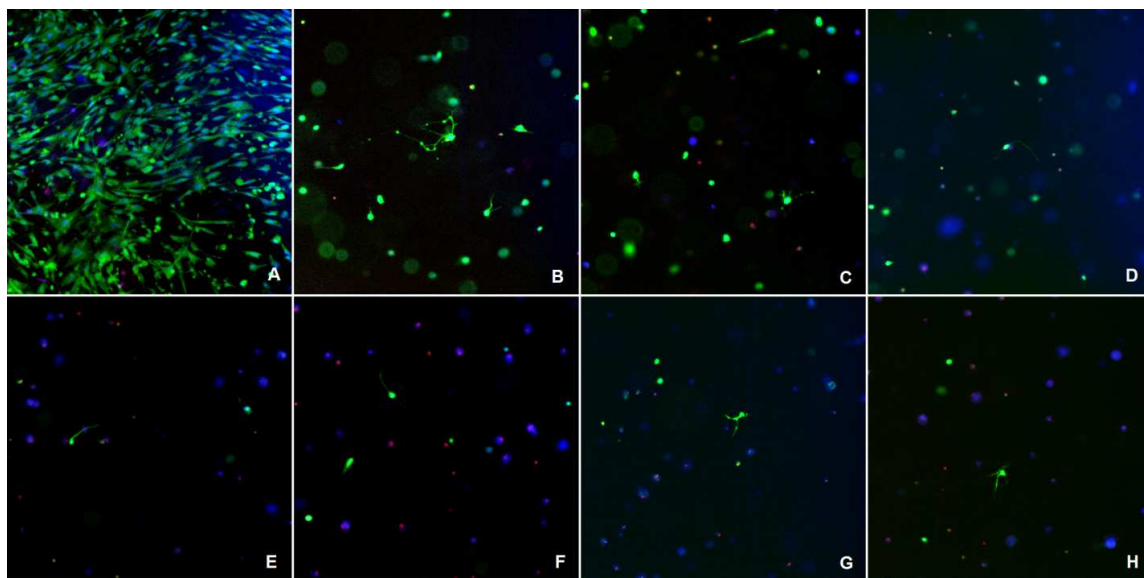


Figure 5-130: Live/Dead staining of hMSC in 3D CMA Gels. A: Growth Medium, no I2959, B: NIM + 0.025% I2959 No UV C: NIM + 0.025% I2959 + 30s UV, D: NIM + 0.025% I2959 + 60s UV, E: NIM + 0.025% I2959 + 90s UV, F: NIM + 0.025% I2959 + 120s UV, G: NIM + 0.025% I2959 +150s, H: NIM + 0.025% I2959 +180s

Here, we saw that increased light exposure time spanning none to more than necessary to achieve maximum crosslinking resulted in a noticeable decrease in live cell number when light exposure was longer than 30s. However, live cells with neuronal morphology were still observed even in the highest exposure time, indicating that at least some neurally induced cells could survive the full range of exposure parameters of the photocrosslinking process.

5.3.3 Patterned Contraction

Although hMSC contraction of CMA was problematic with respect to analyzing differentiation, the robust compaction of the gel, combined with the ability to spatially restrict contraction via photocrosslinking has myriad applications for tissue engineering applications [103]. A proof of

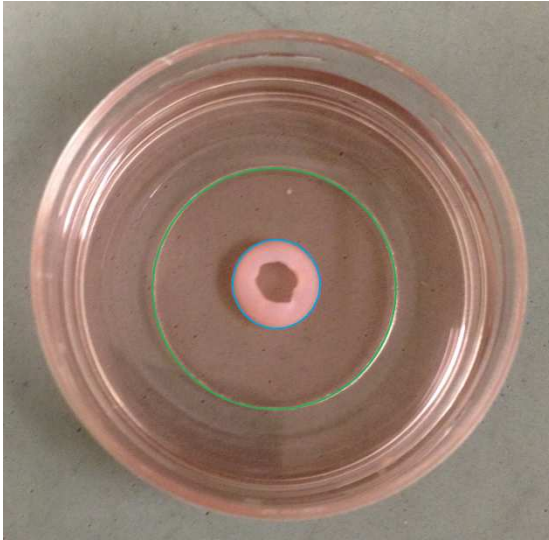


Figure 5-131: Annular-contracted hMSC-encapsulated photopatterned CMA disk

principle experiment was conducted to show that spatially controlled application of UV light could be used to constrain the geometry of the resulting contracted gel. Briefly, CMA gels with 1×10^6 hMSC were plated as thin disks in Mat-Tek dishes with 20mm cutouts. The center of the disks was photocrosslinked while keeping the outer radius of the disks uncrosslinked with an annular photomask with a 7mm aperture.

The gels were then cultured for 5 days in GM and allowed to contract fully. As seen in a representative image in Figure 5-11, the outside diameter of the gel, initially 20mm (green circle overlay), is reduced by 13mm, to the exact diameter of the hole in the photomask (blue circle overlay). Additionally, not only is the overall geometry of the gel constrained to the geometry of the photocrosslinked region, the contraction of the gel by the hMSC results in orientation cells as well as the collagen fibers within the gel network. Live/Dead staining was used to show that the cells in the crosslinked center are still viable, and that they are oriented randomly. The cells in the contracted annulus, constrained to contract the gel circumferentially, also align the CMA fibers circumferentially as seen in Figure 5-12 at 4X (left) and 10X (right) magnifications.

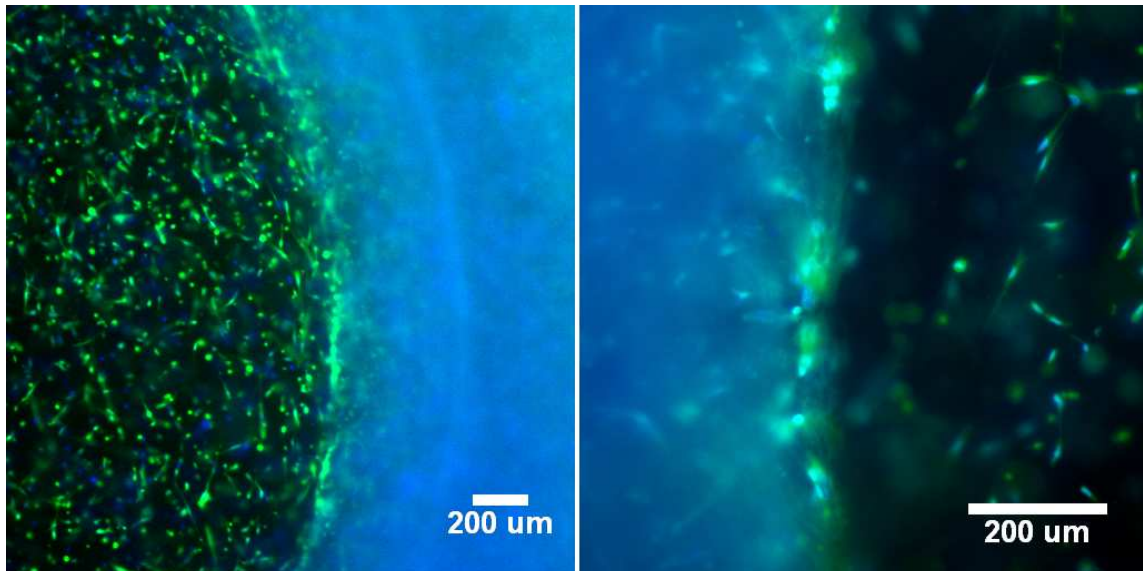


Figure 5-132: hMSC in a 3D CMA Gel 5 72 H after Photocrosslinking Circular Pattern in Center of Gel

5.3.4 hMSC Adhesion Assay

To further understand the mechanism behind the contraction of CMA and not native collagen gels, we tested whether there was a difference in the adhesion of hMSC to CMA gels \pm photocrosslinking as compared to native collagen and TCP. Two modes of quantification were employed to quantify hMSC adhesion. An image-based method made use of Hoechst labeling to stain and count nuclei following a 90 minute adhesion period and three washes with PBS to remove unbound cells. Results are outlined in Figure 5-13 where we observed that significantly more cells adhered to all 3 gel conditions as compared to TCP, although no difference was observed between gel conditions. These data indicate that CMA with and without photocrosslinking and native collagen are all highly adhesive substrates, but no difference between gel conditions was concluded. However, this method results in large standard deviations in cell count due to unequal distribution of cells on gels and the physical forces involved in washing.

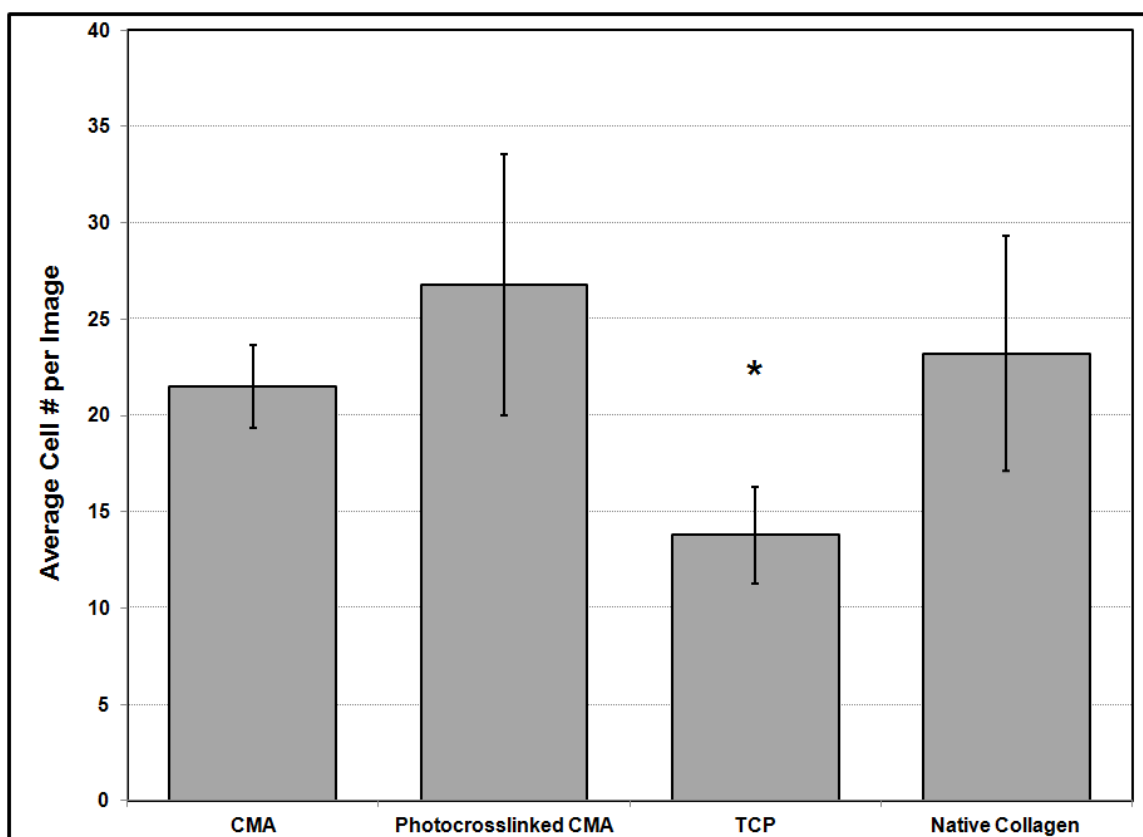


Figure 5-133: Image-based Adhesion Assay. hMSC on Various Substrates for 90 Minutes. $p < 0.05$.

Minimizing this sampling error would require exhaustive image collection. Another method for quantification based on the MTS assay was implemented. In addition, 3 time periods were used to monitor if the rate of adhesion or the overall adhesion window was dynamic between groups. Cells were again seeded on the 4 substrates, then subgroups were washed immediately, and at 30, 60, and 90 minutes with culture medium added after the wash to keep adhered cells alive. Following the last wash, MTS was added and absorbance was measured after 4 hours of incubation. Figure 5-14 displays the results. Again, it was observed that for all time points, 3D gels were more adhesive than TCP. Additionally, adhesion increased for all groups from 0 to 30 minutes, but additional incubation past 30 minutes did not increase adhesion of cells, indicating that hMSC adhesion kinetics stabilize in a matter of minutes on these substrates. There were no

significant differences in adhesion between 30, 60, and 90 minutes within any group. Uncrosslinked CMA and native collagen were not statistically different at any time point, although the averaged signal across the 30-90 minute time points was marginally lower for CMA as compared to native collagen. However, photocrosslinked CMA was significantly ($p < 0.05$) lower at all time points as compared to native collagen and uncrosslinked CMA.

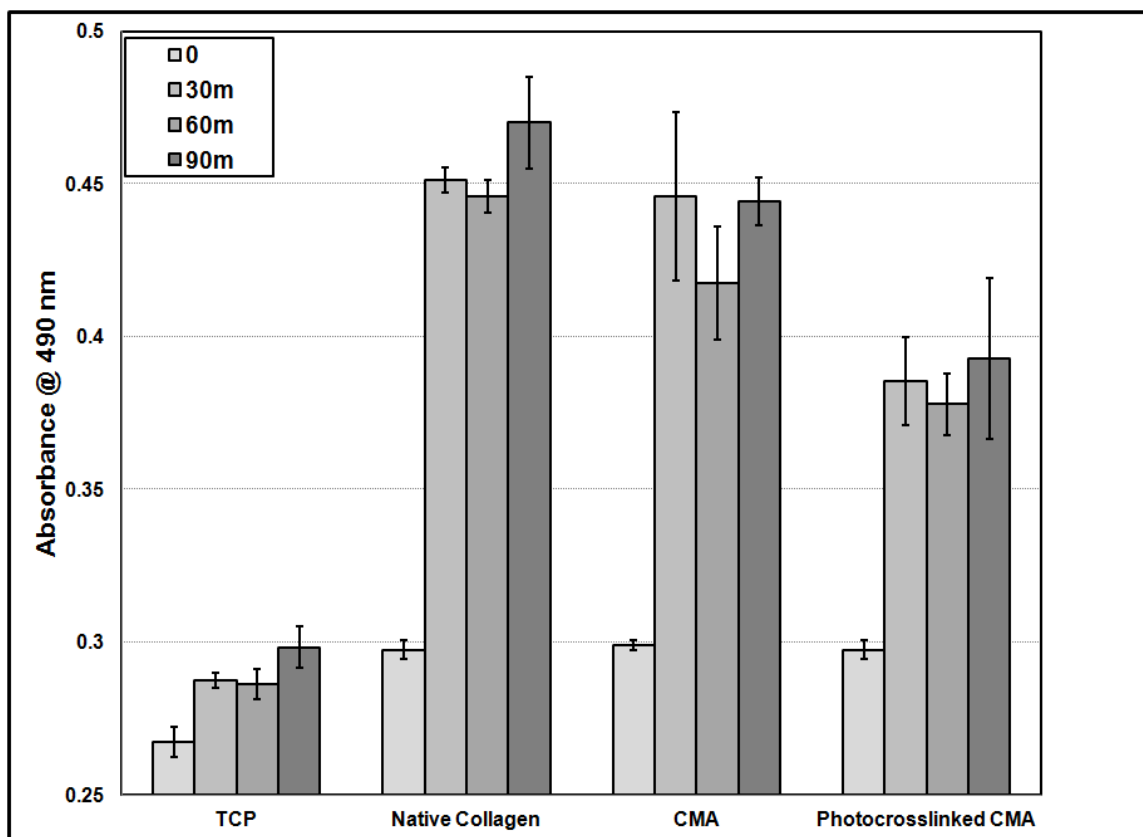


Figure 5-134: MTS Adhesion Assay. hMSC on Various Substrates for 0, 30, 60, & 90 Minutes

Rat smooth muscle cells (SMC) were also tested for adhesion to CMA. Briefly, CMA, native collagen and a 50/50 and 75/25 ratio of CMA to native collagen were used to form gels, to which SMC were allowed to adhere for 60 minutes. MTS was used to quantify the % of cells adhered after this period compared to the number seeded initially. TCP was included for comparison. As Figure 5-15 indicates, SMC preferentially adhered to all gel conditions compared to TCP. CMA

was significantly less adhesive than pure native collagen as well as 3:1 CMA:native collagen ($p < 0.05$). CMA appeared less adhesive than the 1:1 CMA:native collagen, although the difference was not significant ($P = 0.051$). Thus it appears that the presence of even 25% native collagen in the composite gels resulted in an increase in SMC adhesion.

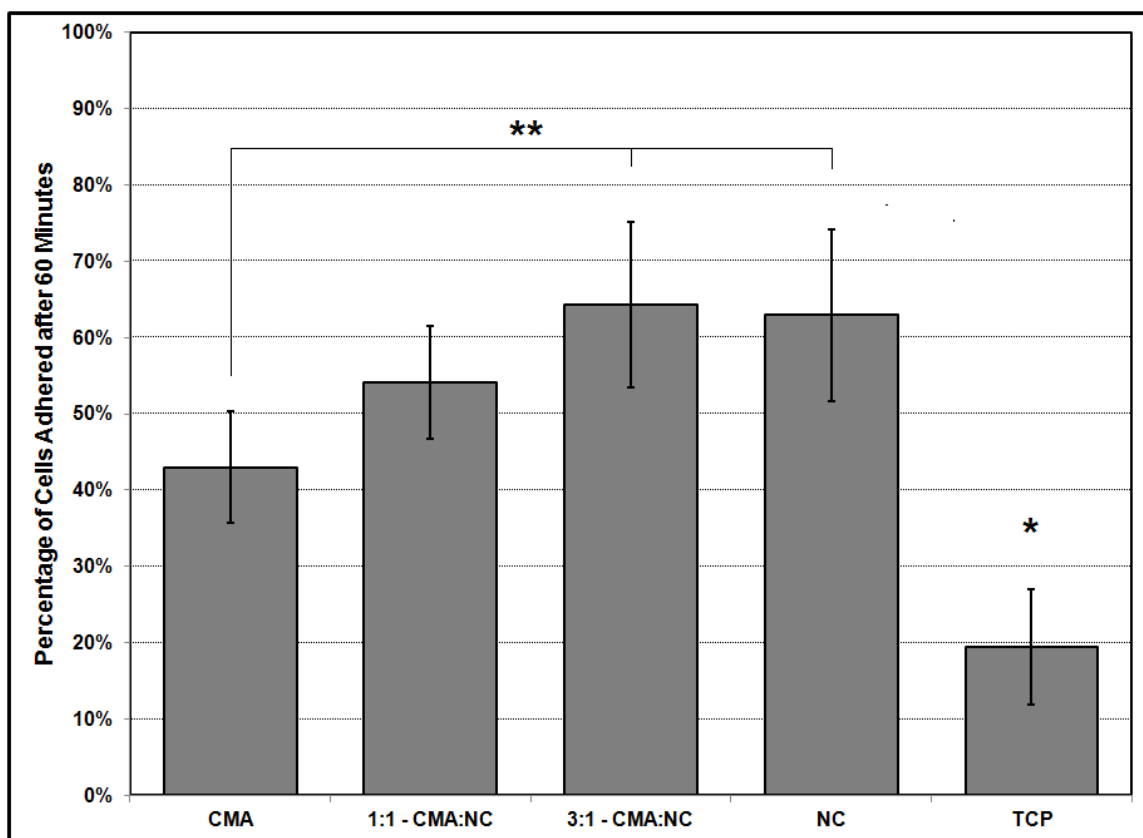


Figure 5-135: Adhesion of SMC on Varying Ratios of CMA and Native Collagen

5.3.5 iPS-NSC Culture in 3D CMA Photocrosslinked Gels

Difficulty in determining actual hMSC neurodifferentiation, controversy over functionality of hMSC derived neurons, batch variability in hMSC phenotype, and contraction of uncrosslinked CMA gels by hMSC resulted in a decision to veer away from hMSC as a platform cell for neural tissue repair. Recent work performed in the Firestein lab, with which our lab has collaborated previously, resulted in a new research direction involving iPS derived neural stem cells (iPS-NSC).

Given the huge potential for iPS-NSC in personalized regenerative medicine as well as in vitro diagnostics, we evaluated whether iPS-NSC could be cultured in 3D CMA gels, which we postulated could be tuned to recapitulate either native or pathological CNS mechanical properties via photocrosslinking. Furthermore, we investigated whether Photolabile bioactive peptides could be used to modulate biochemical microenvironment to tailor the stem cell niche for specialized applications.

Development of protocols to allow photocrosslinking of iPS-NSC encapsulated CMA gels required substantial optimization, including modification of the standard differentiation procedure. Briefly, iPS-NSC undergoing differentiation were able to tolerate photocrosslinking significantly better than proliferating iPS-NSC. However, harvesting significant numbers of viable cells from PDL/Laminin coated flasks was not possible, resulting in the modified protocol. The optimization of these processes is described in Appendix B at the end of this chapter. Using this modified protocol, we were able to increase cell density to 1×10^7 cells/mL, which along with the gentler harvesting process and the inclusion of Y-27632, resulted in iPS-NSC derived cells that looked morphologically like viable neurons and formed extensive networks of neurite-like processes in CMA gels after 72 H (Figure 5-16 A). Furthermore, these differentiating iPS-NSC were able to tolerate photocrosslinking much more robustly, although cellular density and neurite extension was reduced following crosslinking compared to uncrosslinked gels (Figure 5-16 B). In addition, we evaluated whether crosslinking could be constrained by masking one half of the gel from UV (Figure 5-16 C, dotted line). Given that the boundary of neurite-like process extension is confined to the mask edge, we show that the photocrosslinking effect on cells is localized to the immediate area of light exposure (Figure 5-16 C), validating our hypothesis that excess free radicals have a sufficiently short half-life such and don't appreciably diffuse away

from their location during photoinitiation. However, further experiments are needed to precisely define the fidelity of masked photocrosslinking in cellularized CMA gels.

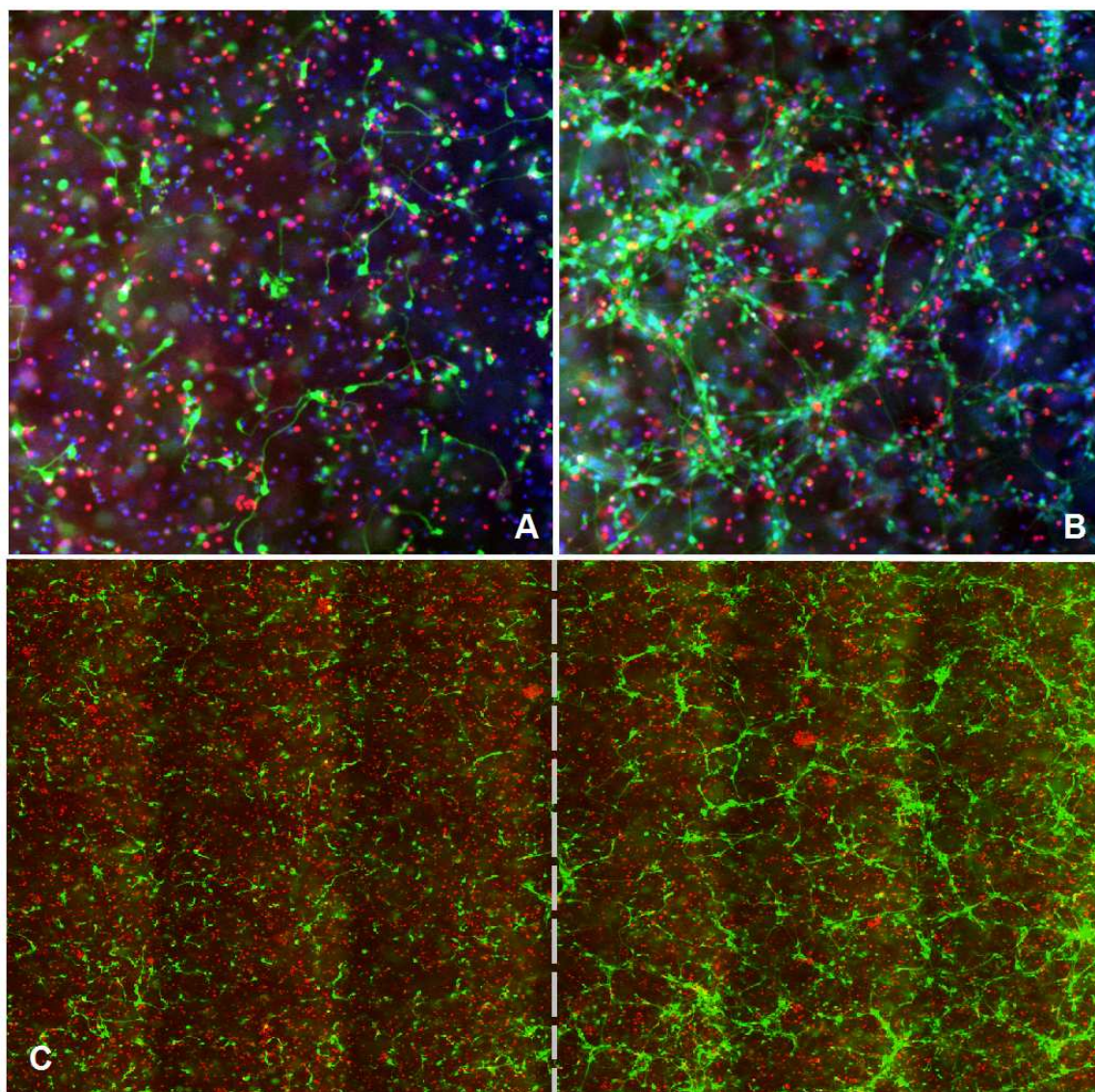


Figure 5-136: Pre-differentiated iPS-NSC in photocrosslinked CMA (A), uncrosslinked CMA (B), and a masked gel (C), where dotted line indicates boundary of mask, with area left of line exposed to UV. A & B taken at 10X, C at 4X magnification.

Despite acceptable post-photocrosslinking viability, the effect of the photoinitiation still appeared to have a profound negative impact on cellular compatibility as evidenced by the

severe reduction in neurite outgrowth. As such, decoupling the effect of substrate stiffness from free radical induced damage was sufficiently challenging to cause a shift in strategy. Another avenue that we deemed worthwhile was the photografting of bioactive peptides containing a photosensitive group. We posited that photografting could be used to attach functional peptides to the CMA network, and that spatially patterning these peptides could be used to guide neurite outgrowth. In addition, we sought to test whether post crosslinking viability was improved by having a labile radical 'sink' which would reduce the free radical concentration. While some cell death due to excess radicals is unavoidable, previous results with hMSC and PEG2KDA were promising; at 1% w/v it was able to substantially mitigate even 0.1% I2959 induced cytotoxicity. Here, due to cost limitations of custom peptide synthesis, we first tested whether low concentrations of methacrylate-conjugated laminin peptides with a 6-glycine (G6) spacer would be able to affect post-crosslinking viability following 0.05% I2959 crosslinking, and whether neurite outgrowth was affected due to increased adhesion via qualitative image analysis. The G6 spacer was included based on published work by Wang et al., that suggested that G6 spaced laminin peptides have improved functionality over unspaced peptides due to increased availability of ligand [104]. In addition, CMA concentration was increased to 3.5mg/mL to increase the number of functional grafting sites. Methacrylate-G6-Peptide, where peptide was either of the functional laminin sequences IKVAK or YIGSR or the scrambled control peptide VIVAK, was dissolved in DMSO and mixed into the CMA-cell macromer solution at a final concentration of 0.1mg/mL and plated 100 μ L each into Mat-Tek dishes and gelled for 20 minutes in the incubator. After exposure of UV light for 150s to ensure complete photoactivation of all methacrylate groups, samples were washed with PBS, and then culture medium was added and samples were cultured for 24 H. Live/Dead staining was used to assess viability and cellular morphology. Visual inspection on Figure 5-17 implies no differences between uncrosslinked

groups (Figure 5-17 A-D) or photocrosslinked groups (Figure 5-17 E-H), indicating that inclusion of 0.1mg/mL methacrylate-G6-Peptide had no effect on either viability or apparent cellular adhesion/outgrowth. Furthermore, 0.05% I2959 caused almost complete loss of iPS-NSC viability.

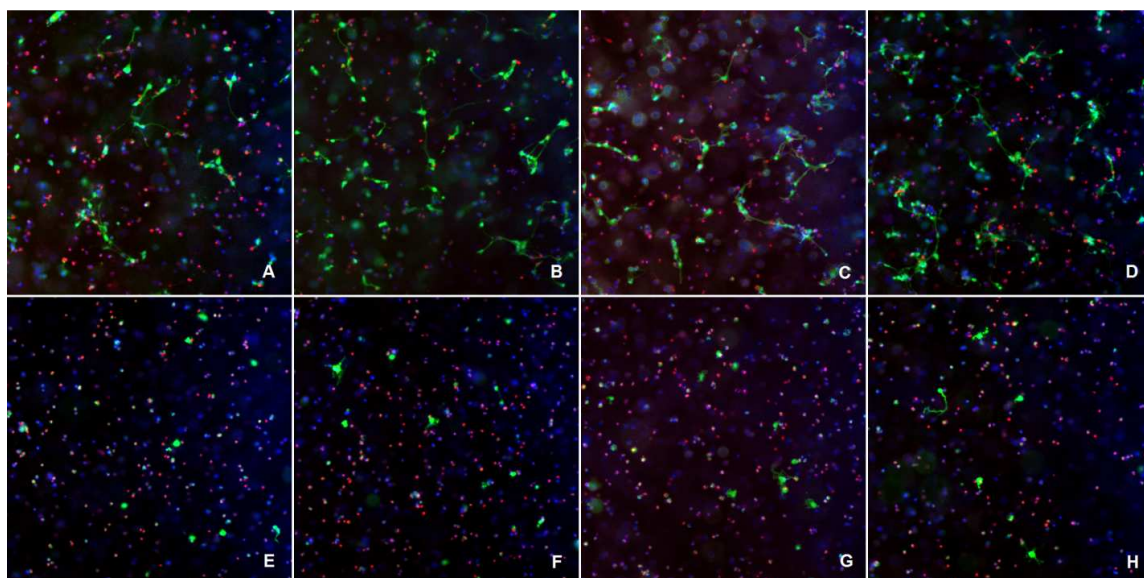


Figure 5-137: Differentiating iPS-NSC in CMA gels 72 H after encapsulation. Control (A, E), IKVAV (B, F), YIGSR (C, G), VIVAK (D,H). A-D were in uncrosslinked CMA, E-H photocrosslinked with 0.05% I2959 and 150s UV exposure.

A final set of analysis was performed using a high concentration (1mg/mL) of methacrylated peptide in 3.5 mg/mL CMA (10% DMSO) with 1×10^7 pre-differentiated iPS-NSC encapsulated therein. Gels were ½ masked and the unmasked portions were photocrosslinked with 0.025% I2959 and 180 s UV exposure. Samples were washed 2X with PBS and NDM + 10 μ M Y-27632, then cultured for 5 days and Live/Dead stained to assess viability. No apparent differences were observed between any group, as the photocrosslinked areas displayed typically poor process extension, and the presence of methacrylates peptide did not appear to provide any benefit, at least from a photoinitiation toxicity standpoint (Figure 5-18).

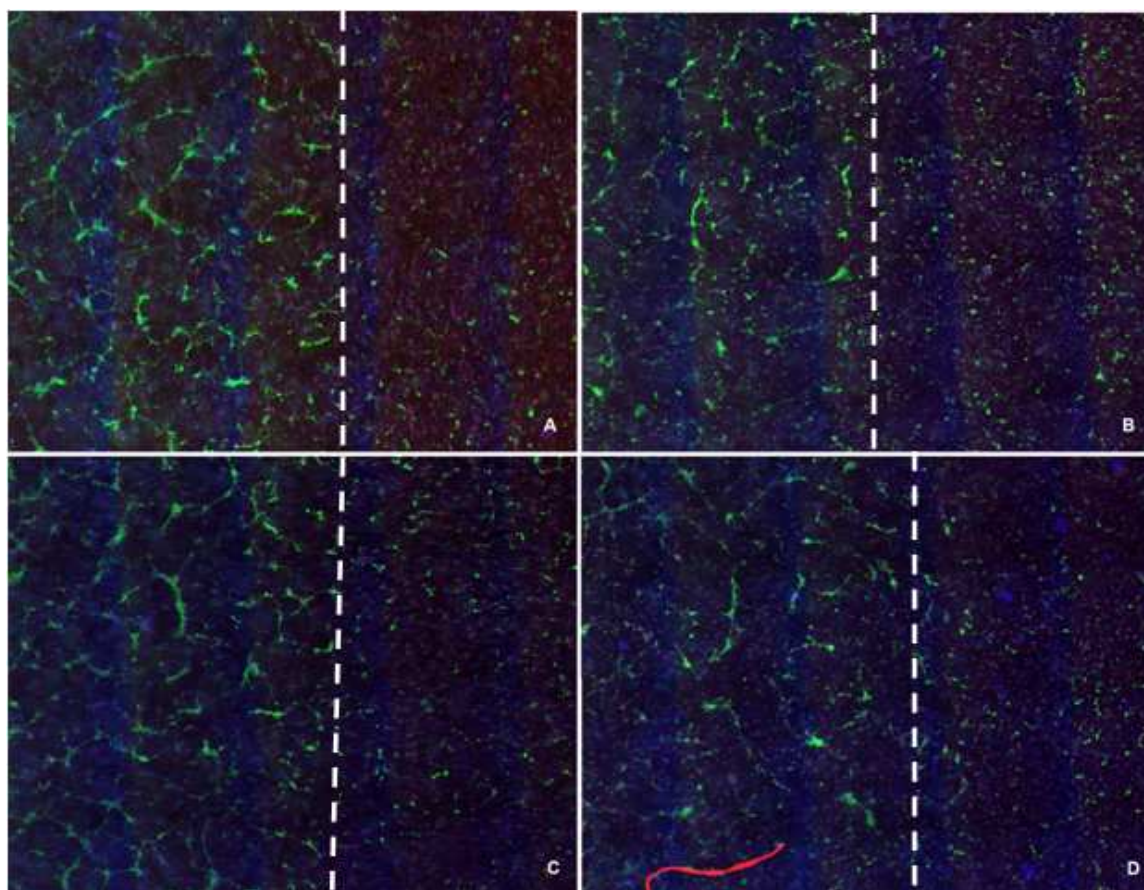


Figure 5-138: Montaged images of iPS-NSC in 1/2 Photocrosslinked CMA Photografted Peptide Gels. 10% DMSO Control (A), Me-G6-IKVAV (B) Me-G6-YIGSR (C) and Me-G6-VIVAK (Scramble Control). Area at Right of Dashed Lines is Photocrosslinked.

A repeat experiment was performed, except that instead of Live/Dead staining, samples were fixed and stained using immunohistochemistry for the neural stem cell markers nestin and Pax-6, the neuronal markers class III β -tubulin (Tuj1), microtubule associated protein (MAP2), and neurofilament medium chain (NF-M), and glial fibrillary acidic protein (GFAP). A number of issues were apparent in the analysis of images obtained from this experiment. Foremost, non-specific interaction between the anti-rabbit secondary antibody and methacrylated IKVAV peptide highlighted a serious problem that was previously unnoticed, namely that the peptide was aggregating. Previously, it was not apparent that peptide was aggregating as the concentration was too low. However, upon re-inspection of all peptide groups, small clusters of

amorphous debris were present. Analysis of IHC images of iPS-NSC in uncrosslinked samples (Figure 5-19) in the IKVAV conditions, confirms the presence of these fluorescently bound-aggregates readily apparent as red aggregates. Additionally, it appeared that the anti-rabbit secondary antibody (red in all images in Figure 5-19) may have been dysfunctional. Neither GFAP nor MAP2, for which differentiated iPS-NSC had previously stained positively, showed up in any images. Another issue with these samples was the noticeably lower cell density compared to previous experiments, possible caused by a number of problems such as improper cell suspension quantification or low viability. Indeed, crosslinked samples looked mostly devoid of viable cells with little staining of any of the protein markers (not shown). We also observed that cells in all conditions were expressing nestin as well as β -tubulin III, indicating that a large proportion of cells were still in the process of differentiating. Finally, we observed that in the scrambled VIVAK condition, the neurite outgrowth was noticeably more extensive than other conditions, particularly apparent in the NF-M staining. A literature and peptide database search produced no evidence that VIVAK has any known function, although sample variability might have been more responsible given the overall condition of the cells in this experiment.

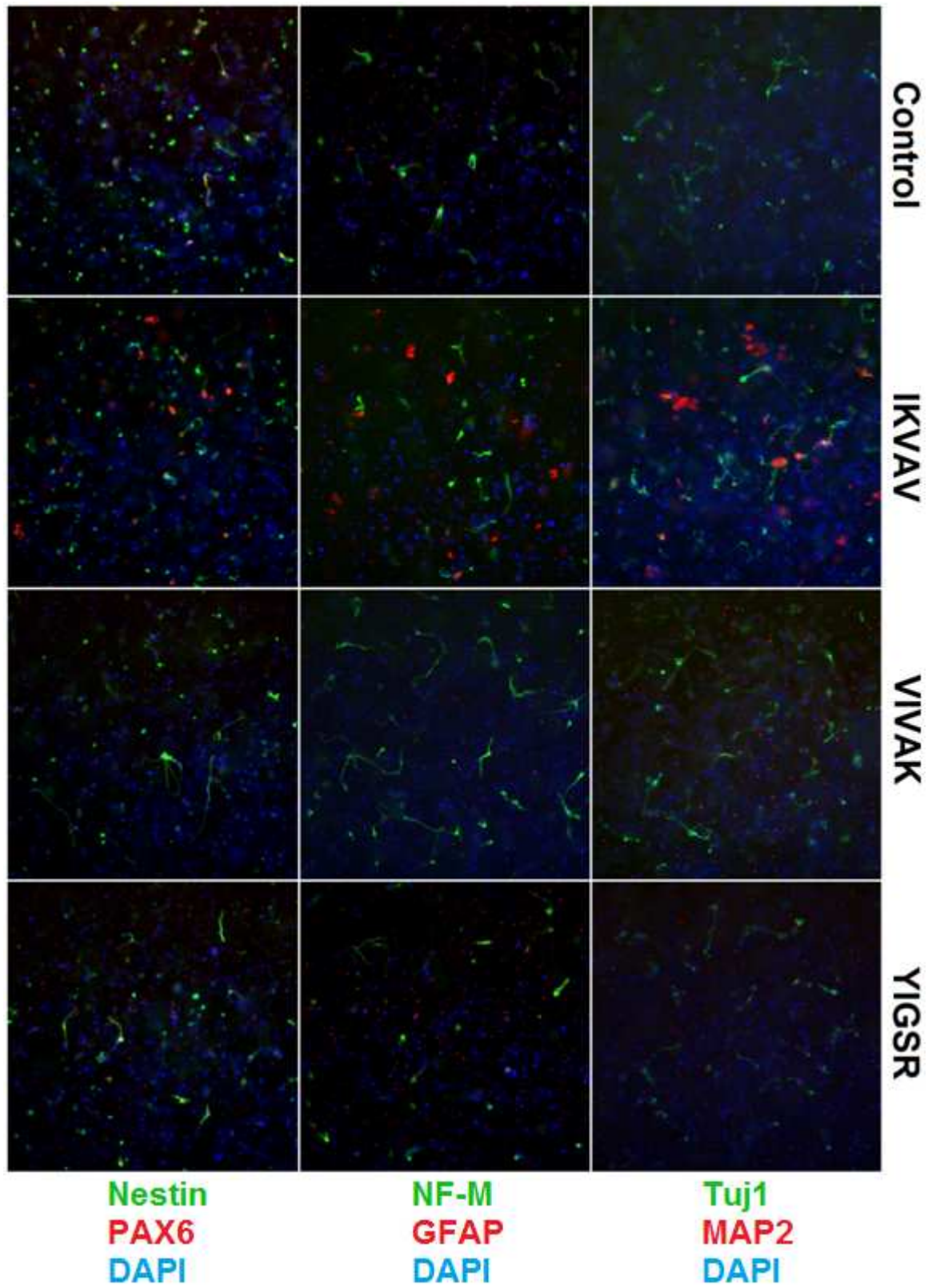


Figure 5-139: IHC staining of iPS-NSC after 5 Days in culture in CMA gels. Uncrosslinked Region Shown. 10X Magnification.

Another attempt at investigating the effect of photografting peptides into 3D gels was made with *ad hoc* revisions to the methodology reflective of the previously encountered problems. Primarily, peptide was solvated in DMSO for 1 H at 37C, then sonicated for 10 minutes, and finally added to the premixed macromer solution in an attempt to minimize pH and aqueous phase-induced aggregation. To address cell quality concerns, cells from a lower passage were used, and cell counts were repeated after harvest to ensure proper cell concentration and maximal viability. In addition, logistical changes were made concerning timing of mixing and gelation to minimize time after gelation/photocrosslinking until medium was added. Finally, a new batch of anti-rabbit secondary antibody was used. However, despite these efforts, the results were essentially the same (Figure 5-20), with peptide actually aggregating into larger chunks, as seen in the IKVAV condition. Interestingly, iPS-NSC in VIVAK containing gels, in both uncrosslinked and photocrosslinked conditions, displayed increased neurite outgrowth compared to control gels.

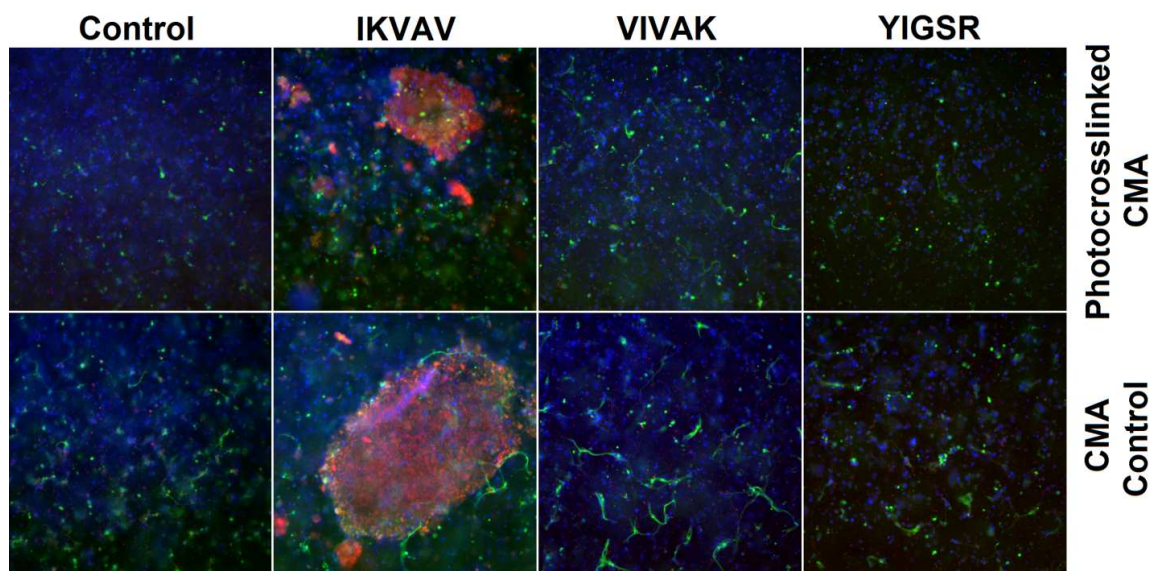


Figure 5-140: Tuj1 (Green) and GFAP (Red) staining of pre-differentiated iPS-NSC in CMA hydrogels \pm Photocrosslinking after 5 days in culture. Nuclei are counterstained with DAPI (Blue). Images taken at 10X.

Analysis of iPS-NSC morphology with other neuronal markers revealed similar augmentation of expression in VIVAK conditions compared to control CMA. MAP2, synaptophysin (SYN), and vesicular glutamate transporter (VGLUT) were all expressed more highly in VIVAK gels (Figures 4-21, 4-22, 4-23).

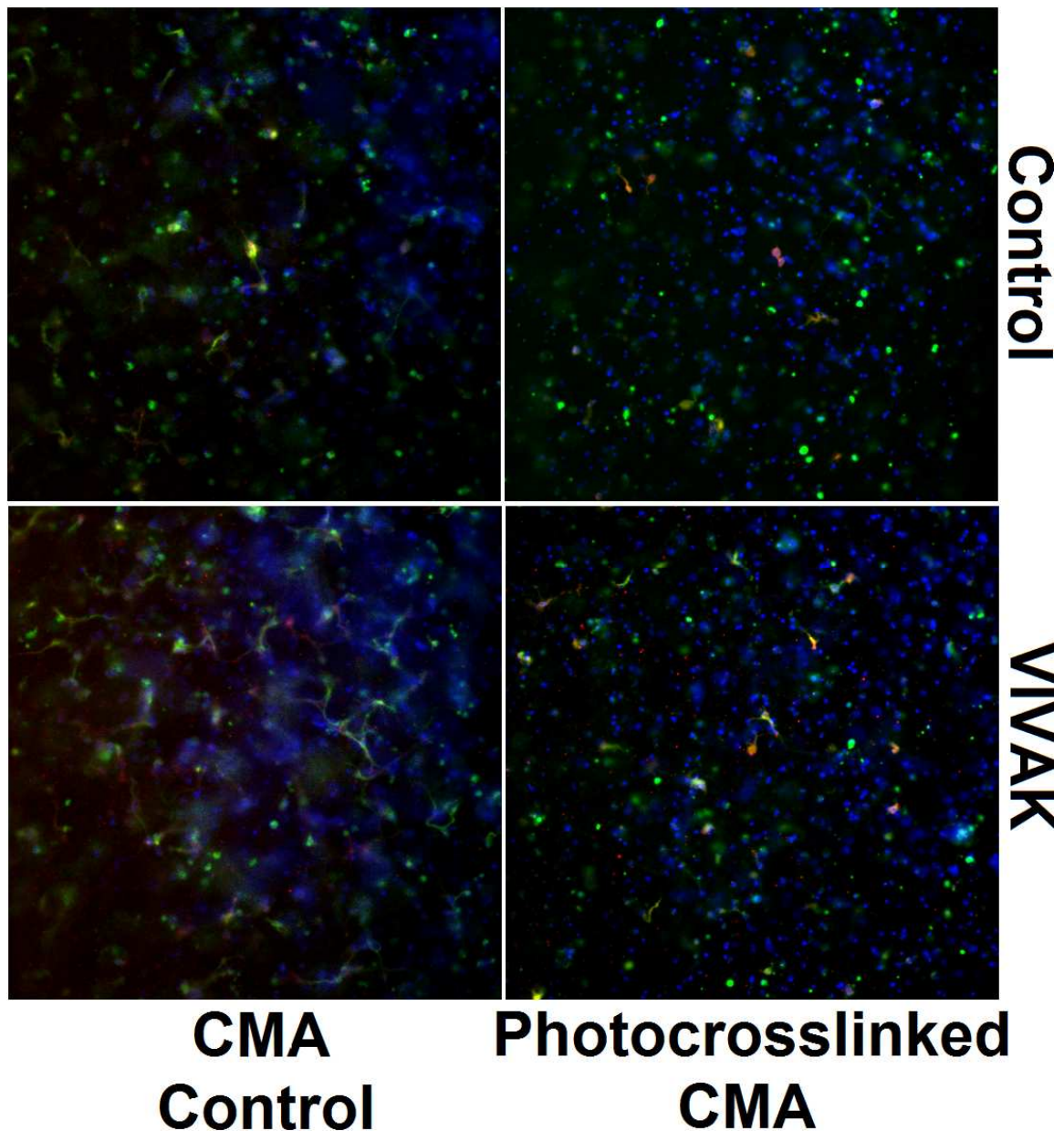


Figure 5-141: Pre-differentiated iPS-NSC in CMA \pm Photocrosslinking. Tuj1 (Green), MAP2 (Red), DAPI (Blue)

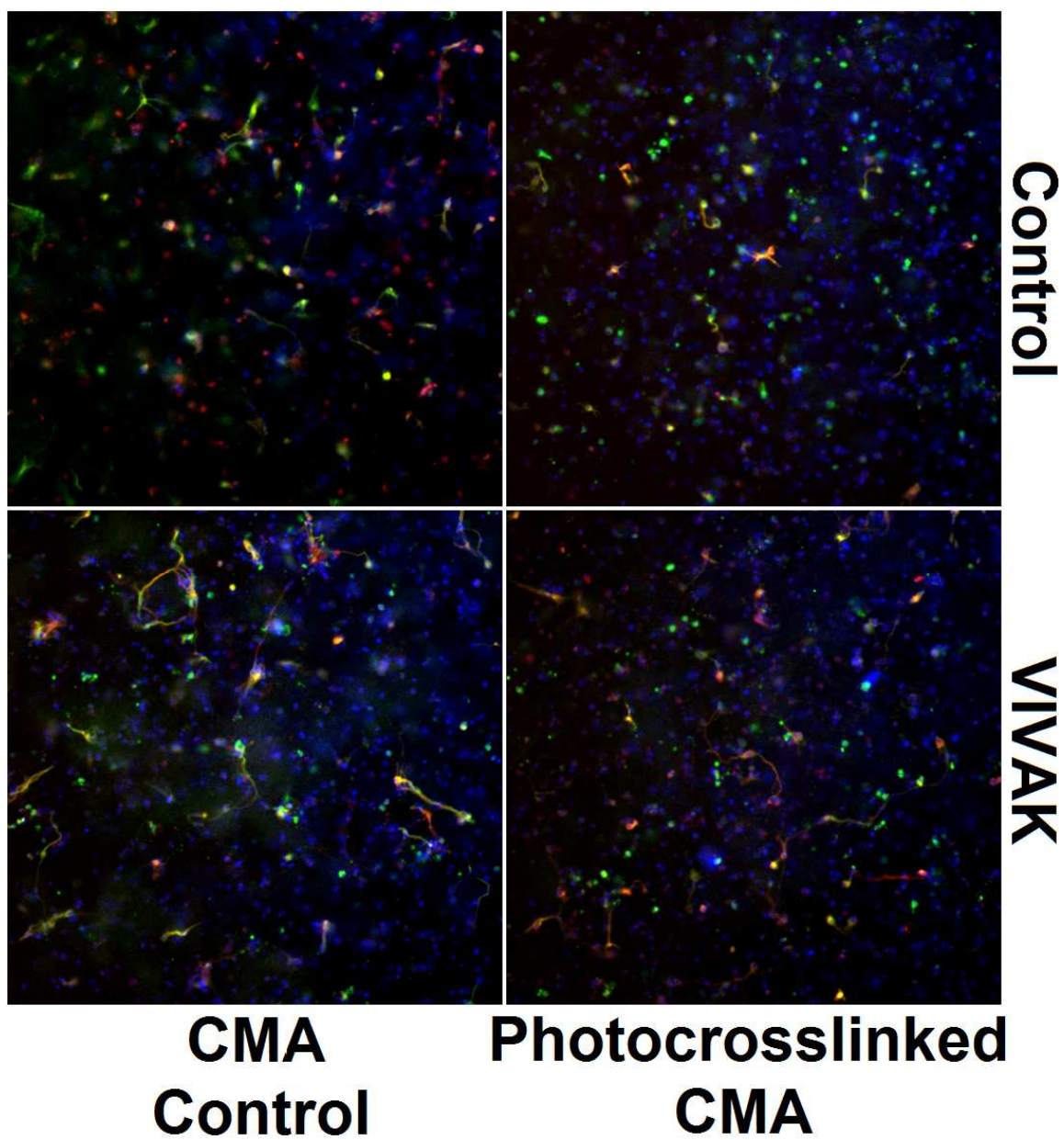


Figure 5-142: Pre-differentiated iPS-NSC in CMA \pm Photocrosslinking. Tuj1 (Green), SYN (Red), DAPI (Blue)

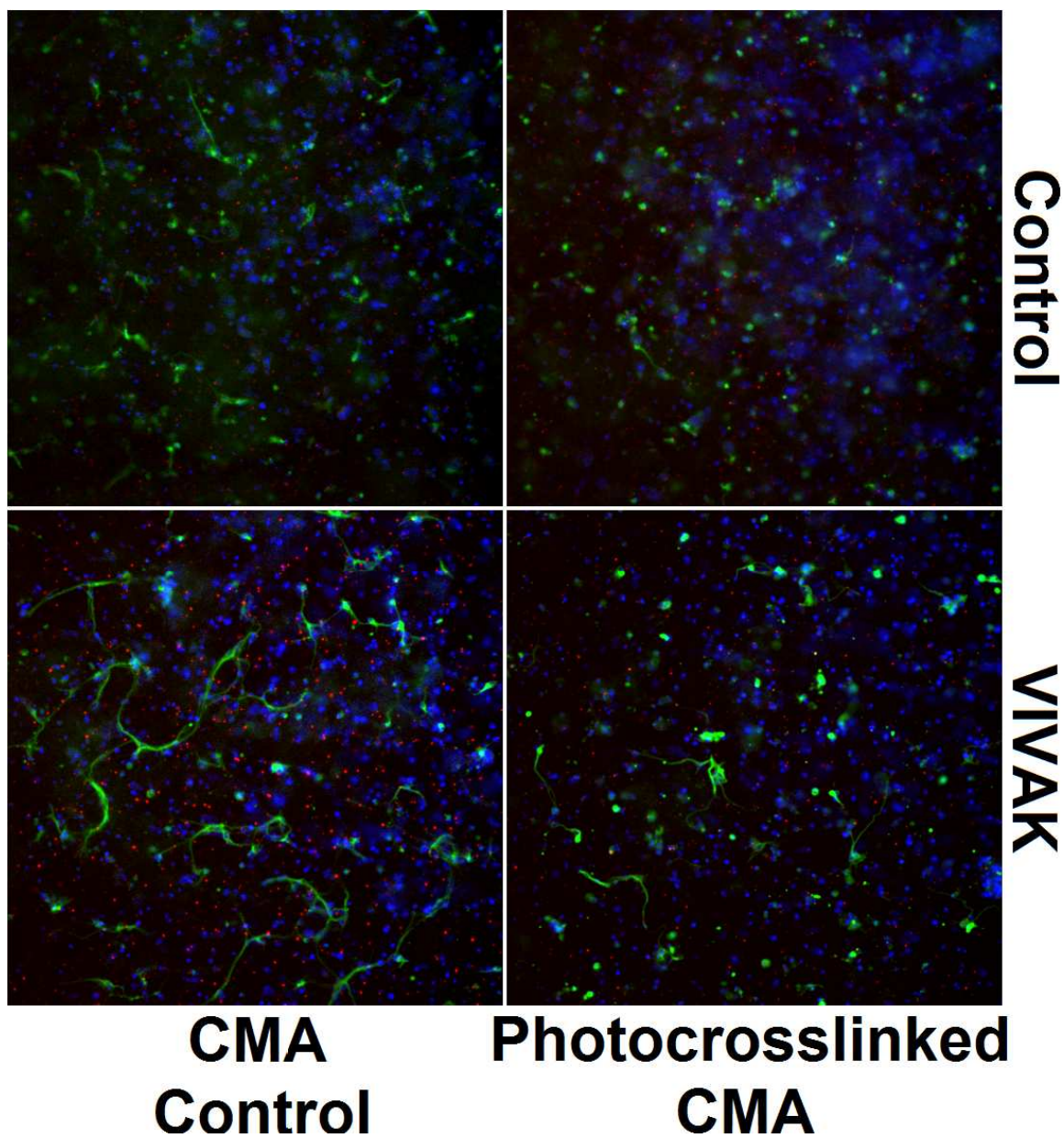


Figure 5-143: Pre-differentiated iPS-NSC in CMA \pm Photocrosslinking. Tuj1 (Green), VGLUT (Red), DAPI (Blue)

The presence of this phenomenon in both uncrosslinked and photocrosslinked conditions indicates a possible interaction of the peptide regardless of whether it has been bound to the CMA matrix via photocrosslinking. Further investigation with a simplified system such as bulk

EDC grafting compared to VIVAK in solution may provide insight into the functionality of VIVAK as a bioactive ligand and may elucidate whether it indeed has biological activity.

5.3.6 *iPS-NSC Culture on 2D Peptide-Photocrosslinked CMA Gels*

Lack of efficacy in maintaining cell viability through the inclusion of methacrylated peptide led us to step back and analyze whether peptide photografting had a noticeable effect on cellular behavior in the absence of the confounding free radical exposure. Experiments were performed by plating differentiated iPS-NSC in 2D on top of 150 μ L CMA gels previously photografted with methacrylated peptides within 48 well plates. Initially, 0.2 mg/mL concentrations of methacrylated peptide were used, with 0.05% I2959 and 180 s UV exposure used to ensure completion of photoinitiation. After washing 3X with PBS, cells were plated in NDM (4×10^5 cells/well) and cultured for 7 days, with medium changed every 2 days. Following culture cells were then fixed and stained via IHC to analyze whether morphological differences resulted from culture the various substrates. Nestin was used to assess stemness of cells, while other samples were stained with Tuj1 and either MAP2, VGLUT, SYN, or GFAP, with all images counterstained with DAPI to visualize nuclei. A significant difference was observed after examining uncrosslinked conditions, where it appeared that the cells had sufficiently contracted the gel near the center and pulled some of the gel off of the dish, which was not seen in any of the other groups. Even though iPS-NSC are not contractile cells, the sheer number of cells, exacerbated by apparent pooling of cells in the center of the well due to gel geometry, was sufficient to disrupt the gel during the 7 days in culture. As seen in Figure 5-24, overall nestin staining appeared equivalent among all groups where gel geometry was intact. Morphology of cell colonies appeared similar across all crosslinked conditions, which consisted mostly of large clusters of nuclei connected by networks of thin, axonal-looking processes, except where cells in

the uncrosslinked gels were close to the contracted border, where nuclear clusters were typically larger and had less neuronal processes. In all conditions, there were very few single cells in areas between clusters. Fasciculation of axons appeared to be random, with a spectrum of process bundle diameters and varying tortuosities.

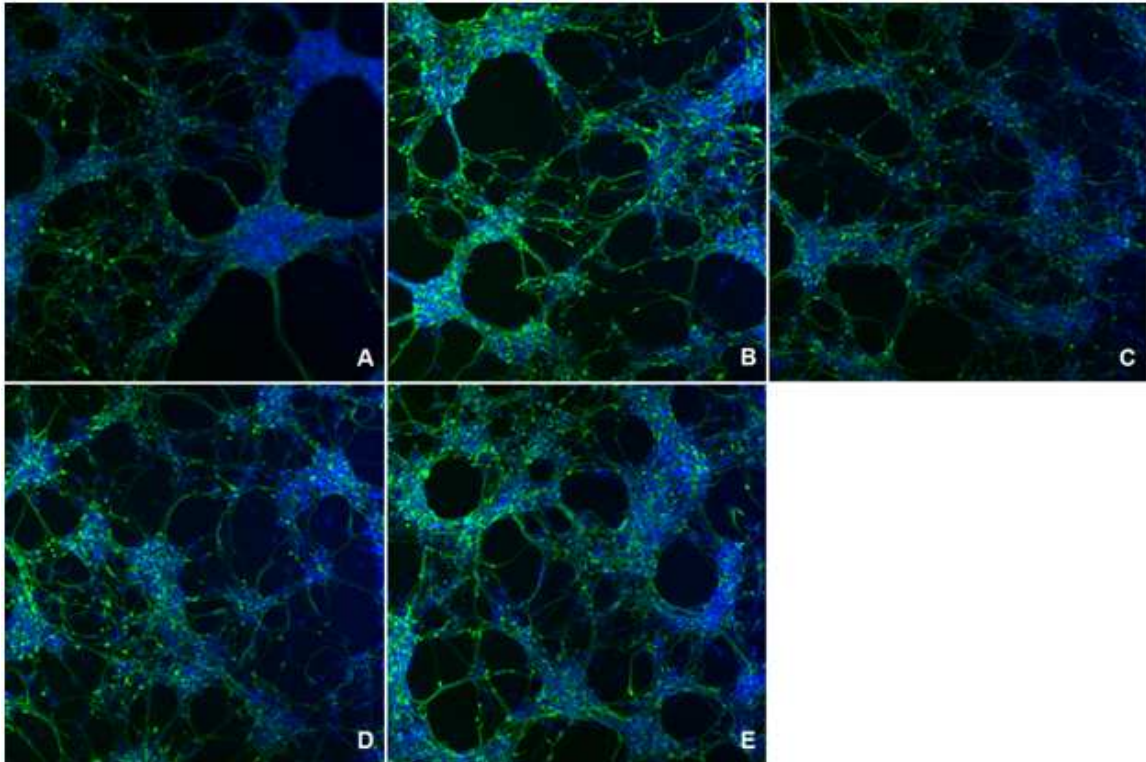


Figure 5-144: Nestin (Green) and DAPI (Blue) IHC of Differentiated iPS-NSC after 7 Days in Culture on: CMA Control (A), CMA Photocrosslinked (B), CMA + Me-G6-IKVAV (C), CMA + Me-G6-VIVAK (D), CMA + Me-G6-YIGSR (E). Images at 10X.

In Tuj1/MAP2 stained samples, Tuj1 staining intensity was similar for all crosslinked conditions, but appeared somewhat reduced in the uncrosslinked CMA gels, indicating that differentiation was suppressed slightly in that condition. In all conditions, Tuj1 staining was similar in intensity and morphology to nestin staining, indicating that both proteins were expressed simultaneously and implying that differentiation is ongoing at this stage of culture (Figure 5-25). However,

direct colocalization studies were not performed. Not surprisingly, MAP2, a more mature dendritic neuronal marker, was not measurably expressed in any condition.

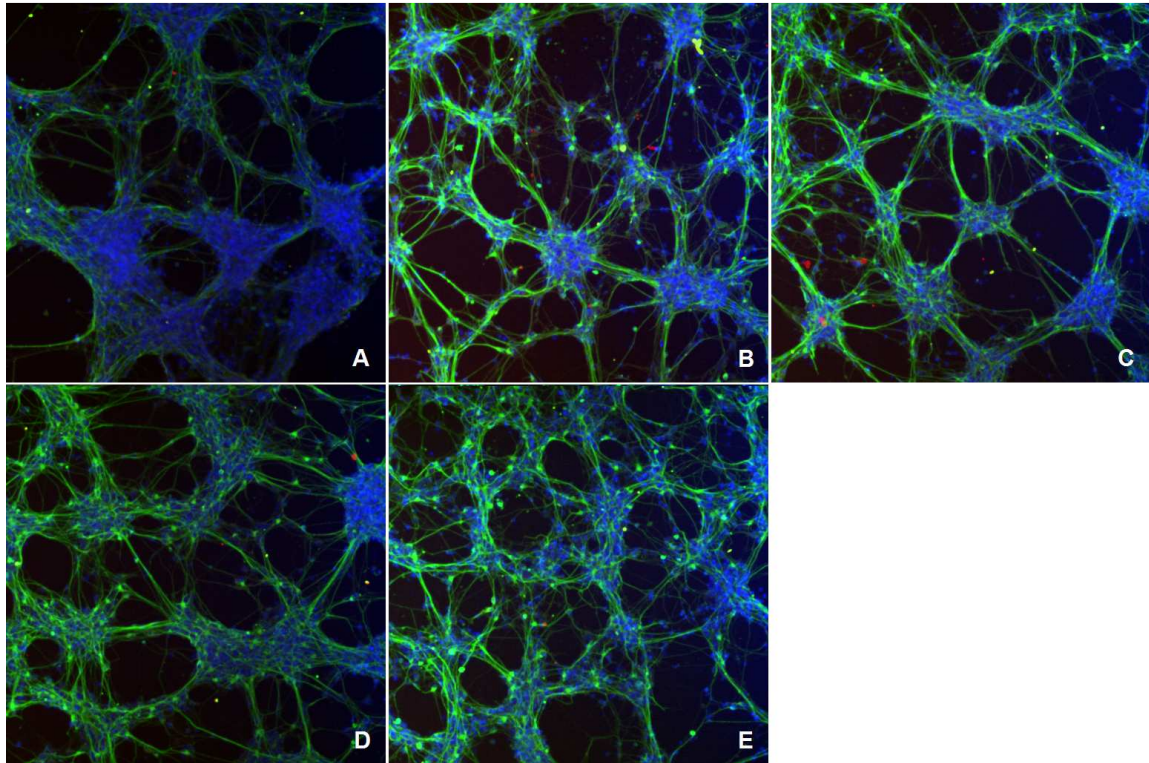


Figure 5-145: Tuj1 (Green), MAP2 (Red) and DAPI (Blue) IHC of Differentiated iPS-NSC after 7 Days in Culture on: CMA Control (A), CMA Photocrosslinked (B), CMA + Me-G6-IKVAV (C), CMA + Me-G6-VIVAK (D), CMA + Me-G6-YIGSR (E). Images at 10X.

Samples stained with Tuj1/VGLUT (Figure 5-26) displayed similar, low levels of VGLUT expression among all photocrosslinked conditions, appearing, as expected, as puncta colocalized to axonal processes and the boundaries of nuclear clusters. Soma and neurites on uncrosslinked CMA did stain for VGLUT, although expression appeared less punctuate and was more diffuse throughout all cytoplasmic regions as compared to cells on photocrosslinked substrates. Again, it appeared that iPS-NSC cultured on the disrupted CMA gels were at a less developed state of differentiation. No major differences were observed between any of the peptide conditions, indicating a lack of influence based on the presence of any photografted peptides compared to

gels crosslinked alone. As seen in Figure 5-26 A, some nuclear clusters had detached from the gel surface, although it was unclear if this was during culture or processing for immunostaining.

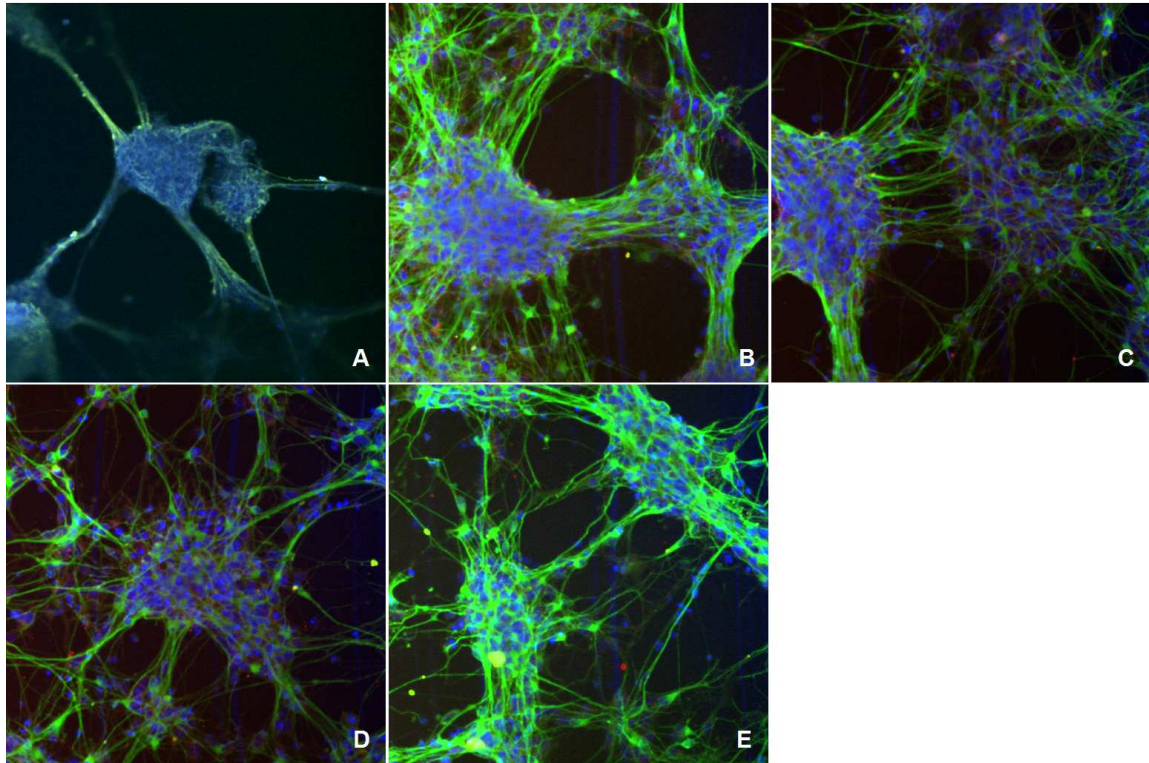


Figure 5-146: Tuj1 (Green), VGLUT (Red) and DAPI (Blue) IHC of Differentiated iPS-NSC after 7 Days in Culture on: CMA Control (A), CMA Photocrosslinked (B), CMA + Me-G6-IKVAV (C), CMA + Me-G6-VIVAK (D), CMA + Me-G6-YIGSR (E). Images at 20X.

Tuj1/SYN staining (Figure 5-27) revealed that SYN was highly expressed by iPS-NSC in every condition, largely colocalized to the nuclear clusters with some staining appearing to colocalize with axonal projections. It was unclear from qualitative morphological analysis whether prototypical synapses were formed, although the expression levels suggest that nascent neuronal connections were possibly forming. Longer differentiation periods along with electrophysiology would elucidate whether functional synapses are created in this culture

system. Again, the presence or absence of peptide was insignificant towards augmenting apparent synapse formation.

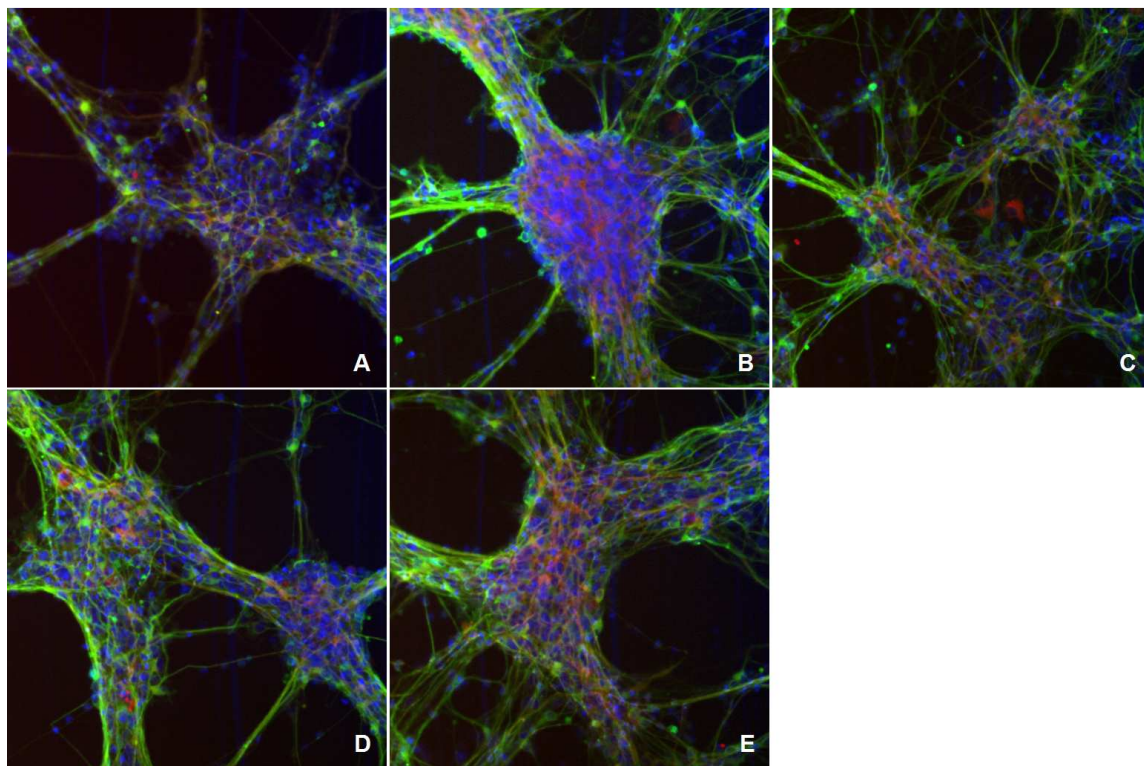


Figure 5-147: Tuj1 (Green), SYN (Red) and DAPI (Blue) IHC of Differentiated iPS-NSC after 7 Days in Culture on: CMA Control (A), CMA Photocrosslinked (B), CMA + Me-G6-IKVAV (C), CMA + Me-G6-VIVAK (D), CMA + Me-G6-YIGSR (E). Images at 20X.

GFAP expression was almost nonexistent in all conditions, indicating that culture on any of these gels did not foster preferential glial differentiation over neuronal lineages (Figure 5-28).

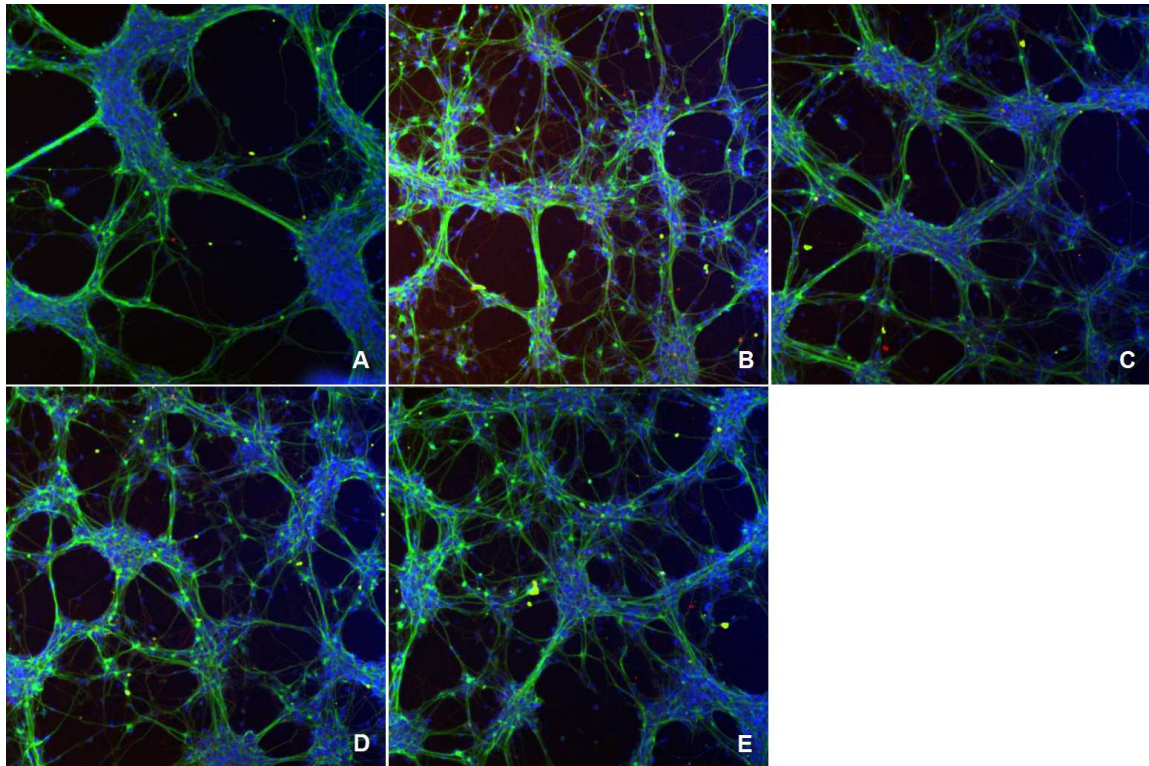


Figure 5-148: Tuj1 (Green), GFAP (Red) and DAPI (Blue) IHC of Differentiated iPS-NSC after 7 Days in Culture on: CMA Control (A), CMA Photocrosslinked (B), CMA + Me-G6-IKVAV (C), CMA + Me-G6-VIVAK (D), CMA + Me-G6-YIGSR (E). Images at 10X.

Interestingly, the morphology of iPS-NSC near the contracted edge was consistent in that nuclear clusters increased in size, presumably due to the lack of other substrate to adhere to. Due to the shape of the gels in the tall cylindrical wells, gels formed a concave shape, which funneled cells toward the center of the well during plating. In addition, the gels were thinnest at the center, resulting in a high concentration of cells on the thin center, which was then disrupted as cells adhered and migrated into clusters. It is unclear whether iPS-NSC adhered more to the uncrosslinked CMA or whether the reduced stiffness of the material compared to the other photocrosslinked gels was the main factor in the uncrosslinked CMA gels being compacted. In all staining conditions, the large nuclear clusters near the gel edge also had the lowest expression of other protein markers. As outlined in the selected images of Figure 5-29,

cells at the gel boundary cluster up and display lower expression of either nestin (Figure 5-29 A) or Tuj1 (Figure 5-29 B-C). The circumferential alignment of cells and neurites at the compacted gel edge is most striking in Figure 5-29 D, which at the low magnification of 4X shows the curved, compacted gel edge, made almost entirely of nuclei, with very little accompanying Tuj1 expression. It is unclear whether these cells have differentiated into a different lineage, as the markers stained for here reveal little about the phenotype of these boundary cells.

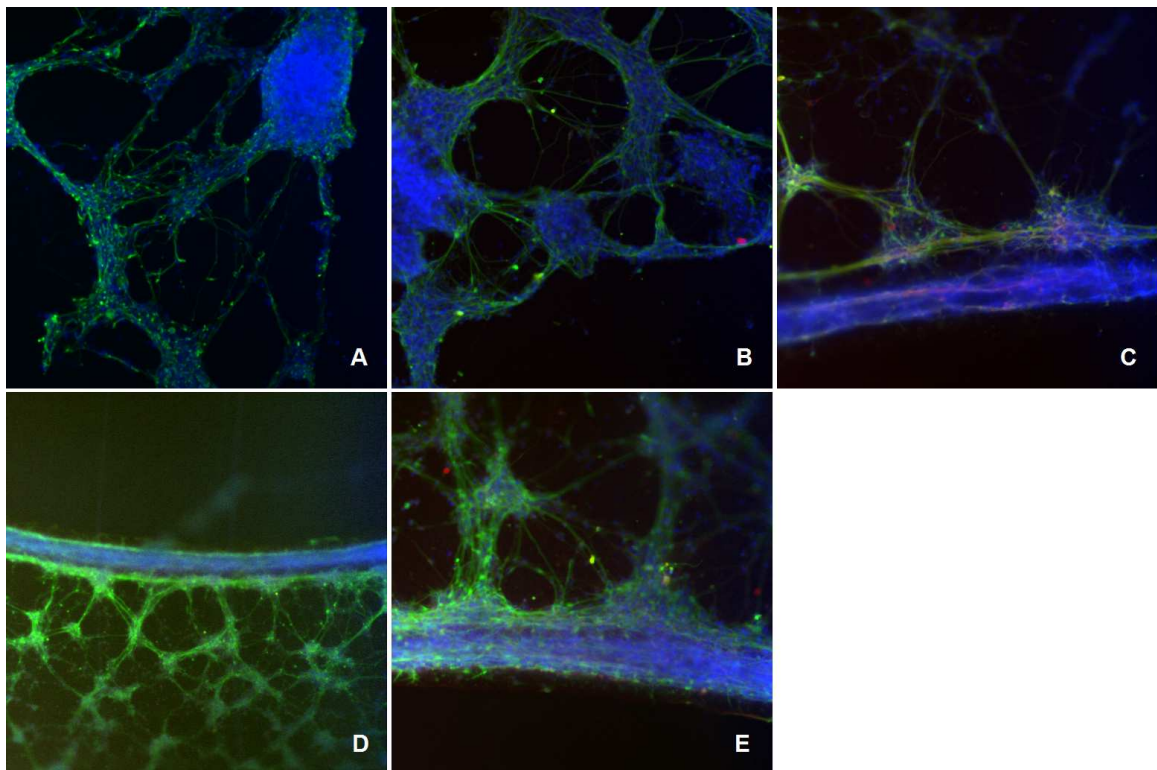


Figure 5-149: iPS-NSC near Contracted Gel Edge. Nestin/DAPI at 10X (A), Tuj1/MAP2/DAPI at 10X (B), Tuj1/SYN/DAPI at 20X (C), Tuj1/VGLUT/DAPI at 4X (D), Tuj1/GFAP/DAPI at 10x

As discussed previously, in the former 2D experimental setup, the meniscus formed by the surface tension created concave gels, resulting in non-uniform gel thickness and causing cells to pool in the center of the wells. The concomitant cellular compaction permitted by this phenomenon complicated direct comparison of iPS-NSC behavior on uncrosslinked and

photocrosslinked substrates. We repeated the experiment, this time using $\frac{1}{2}$ masked gels formed in Mat-Tek dishes similar to 3D experiments, which allowed for more uniform gel thickness. The symmetrical gels resulted in more uniform cell distribution, and in addition allowed smaller sample sizes, which enabled higher concentrations of peptide. Here we increased the peptide to 1 mg/mL as the previous experiment showed no effect with peptide at 0.2 mg/mL. Briefly, CMA \pm methacrylated peptide was plated 100 μ L each into Mat-Tek dishes, gelled, photocrosslinked, and extensively washed (2 mL/wash PBS, 4X: 5 minutes, 1 hour, 5 hours, overnight) to remove any unbound labile peptide. Differentiated iPS-NSC were plated at 4×10^6 cells/mL, 100 μ L/ gel and cultured for 7 days in NDM. Cells were then fixed and stained to analyze whether morphological differences resulted from the various substrates. Representative samples are shown in Figure 5-30, in which montages of the entire well were imaged to examine whether cell density or neurite outgrowth was effected after 7 days of culture on the substrates, of which half of each was exposed to UV (left half of well) while the right half was masked from photocrosslinking. As typified in these montages, there was no discernible difference in the distribution, orientation, or colony morphology with respect to photocrosslinking or peptide inclusion. Insets on the right margin of Figure 5-30 show magnified samples of colony morphology, which was identical among and within each condition. While cell distribution was more uniform in this experiment due to the symmetry of the gel geometry, there was still some difficulty ensuring cell suspension was spread evenly near the edges of the gels due to surface tension effects, resulting in some sparse populations. While this appears more severe some images in Figure 58, this was seen to a similar degree in all conditions. Overall, differentiating iPS-NSC were able to adhere to the surface of CMA gels and form extensive networks of fasciculated axonal-like projections. The large, rapid colony formation indicates that these cells prefer cell-cell adhesion compared to matrix attachment, and the presence of photografted

laminin peptides at 1 mg/mL was not shown to be effective towards modulation of neuronal adhesion or neurite outgrowth, although peptide aggregation likely reduced the availability of peptide presentation as a functional ligand.

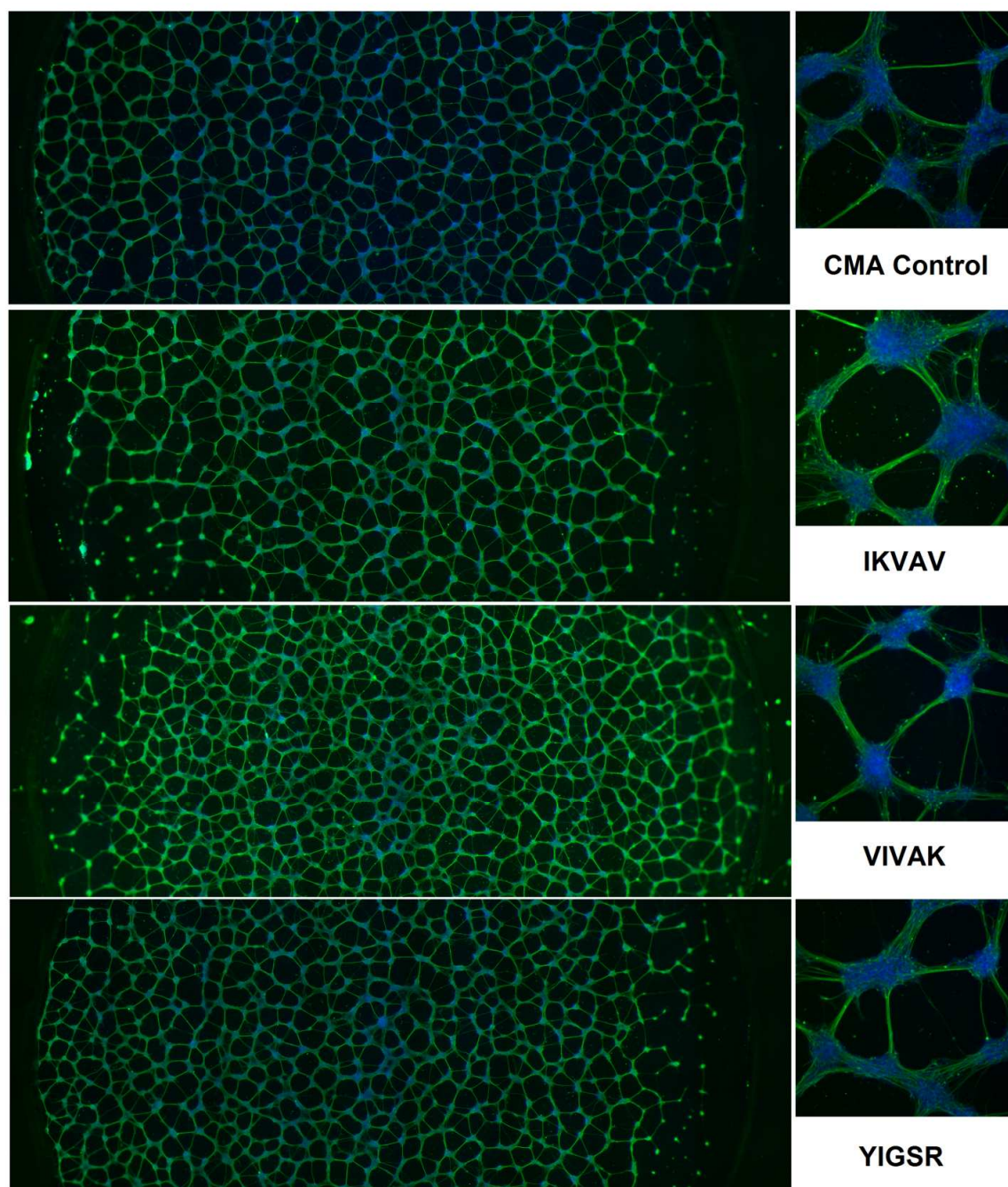


Figure 5-150: Montaged Images of CMA gels 1/2 Photocrosslinked with Methacrylated Peptide. Green is Tuj1, Blue is DAPI. Montages taken at 4X, Inset (Right) Taken at 10X

5.3.7 DRG Outgrowth in 3D CMA Gels Photocrosslinked with Methacrylated Laminin Peptide

Intact chicken DRG were encapsulated similarly to the 3D iPS-NSC experiments, in an effort to determine if peptide photografting could be used to augment neurite outgrowth. DRG have previously shown to tolerate photocrosslinking well, so here we investigated their use with CMA and methacrylated laminin peptides at 1mg/mL, photocrosslinked with 0.025% I2959 and 180 s of UV exposure. Control gels with photocrosslinking only were used to compare peptide effect. Following 5 days in culture with complete medium supplemented with NGF, gels were fixed and stained for neurofilament-M. Again, peptide aggregation was noticed in all groups, and IKVAV condition again interfered with the secondary antibody, and so was excluded from analysis. Morphologically, DRG neurite outgrowth appeared the same in all conditions. Representative samples of DRG can be seen in Figure 5-31.

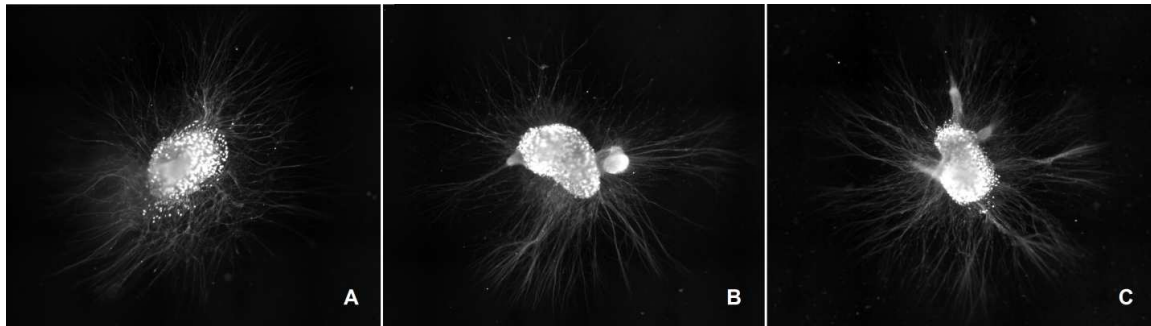


Figure 5-151: DRG stained with NF-M in CMA Control (A), CMA + Me-G6+YIGSR (B), CMA + Me-G6-VIVAK. Montaged Images, 4X.

Seven DRG in each condition were cultured, and neurite outgrowth was quantified using ImageJ. Montaged images were contrast enhanced, and neurite outgrowth area was manually obtained by tracing a line from the tip of each neurite to its closest neighbor around the entire DRG perimeter. The resultant enclosed area was measured and considered the neurite outgrowth penumbra. Area was averaged among each condition and compared statistically with one-way

ANOVA. We found no significant difference in the average outgrowth area between any conditions. The results of the quantification are presented in Figure 5-32.

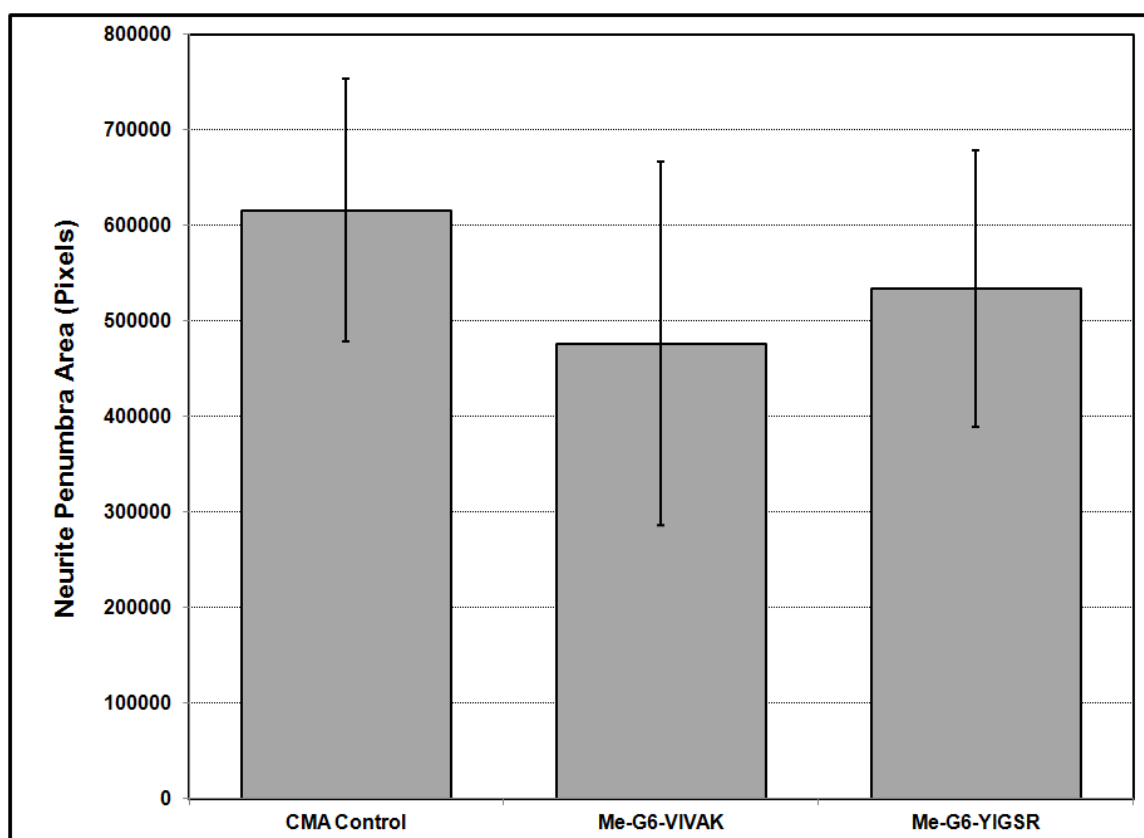


Figure 5-152: Quantification of neurite outgrowth from DRG in CMA Photocrosslinked \pm Methacrylated Peptide. Area Reported as Average Pixel Area \pm SD

While conventional wisdom, published results, and charge calculations intimated that the G6-spaced methacrylated peptides should be water soluble, our empirical data proved otherwise. As peptide solubility and aggregation were a major limitation to the investigation of efficacy towards modifying scaffold biochemistry, we attempted to improve solubility based on peptide design using a hydrophilic spacer to replace the G6. Additionally, a cell type with better scalability was desired to reduce cell culture costs, with a focus on clinical regenerative applications critical to future experimental design.

5.3.8 *Cellular Response to CMA Photografting with PSA-mimetic Peptide*

A new strategy, based on findings by other members of our laboratory that a PSA mimetic peptide could be used to augment Schwann cell proliferation and process extension, focused on modulating Schwann cell behavior via photografting. A new set of peptides were synthesized, PSA mimetic peptide (PP) and a scrambled peptide control (SP). Again, N-termini were methacrylated, but rather than spacing peptides with the 6-glycine sequence, a hydrophilic miniPEG was included that we hypothesized would allow higher concentrations of peptide to be water soluble, and limit aggregation that we presumed to be caused by the less hydrophilic glycine groups upon transition from DMSO to aqueous phase.

Schwann cells were provided through a collaborative effort with UBC and iCORD, who kindly donated skin derived precursor (SKP) derived Schwann cells (SKP-SC). SKP-SC are a clinically relevant source of glial cells that originate from neural crest-related progenitor cells harvested from dermal tissue sources and have immense potential for regenerating injured nervous system tissue through a number of mechanisms [105,106]. Additionally, adult spinal cord progenitor cells (aSCP) were evaluated for interaction with CMA modified mechanically and with PSA peptide mimics. These cells represent a possible mechanism for innate repair of SCI, and guided orientation of spinal cord glial cells is a promising strategy for permitting axonal growth into the lesion cavity as well as guiding regenerating axons to proper downstream targets. Lastly, DRG were also evaluated for interaction with PSA peptides, as previous work by Masand et al. showed that PSA mimetic peptide, when covalently bound to collagen gels, is a powerful cue for increasing neurite outgrowth from sensory neuronal populations, comprising the bulk of DRG cells [85]. Furthermore, PSA-grafted collagen also improved myelination of regenerating

peripheral nerves and improved functional outcomes in a murine femoral nerve injury model [107].

One concern with the revised peptide design was the possible toxicity of the miniPEG spacer, as previous experiments showed that small molecular weight methacrylated PEG could be toxic even at minute concentrations. Thus initial testing was performed to assess the toxicity of the peptides at concentrations ranging from 0.1-1mg/mL in the absence of photoinitiator. Briefly, iPS-NSC in growth medium were plated into a 96-well plate at 15K cells/well and cultured overnight to adhere. The following day, medium with 0.1, 0.5, and 1 mg/mL Me-mPEG-PP peptide in solution in medium was added to cells for 24 H, and MTS was used to assay viability. Positive control with no peptide and a negative control containing 10% Etoh were included. Results, provided in Figure 5-33, indicated that peptide was highly toxic at 0.1% and 0.5%, but strangely had no adverse effects at a higher concentration of 1 mg/mL. A possible explanation is that at the higher concentration, peptide was either aggregating or spontaneously polymerizing in solution, rendering it non-toxic by virtue of increasing the effective molecular weight above the toxic.

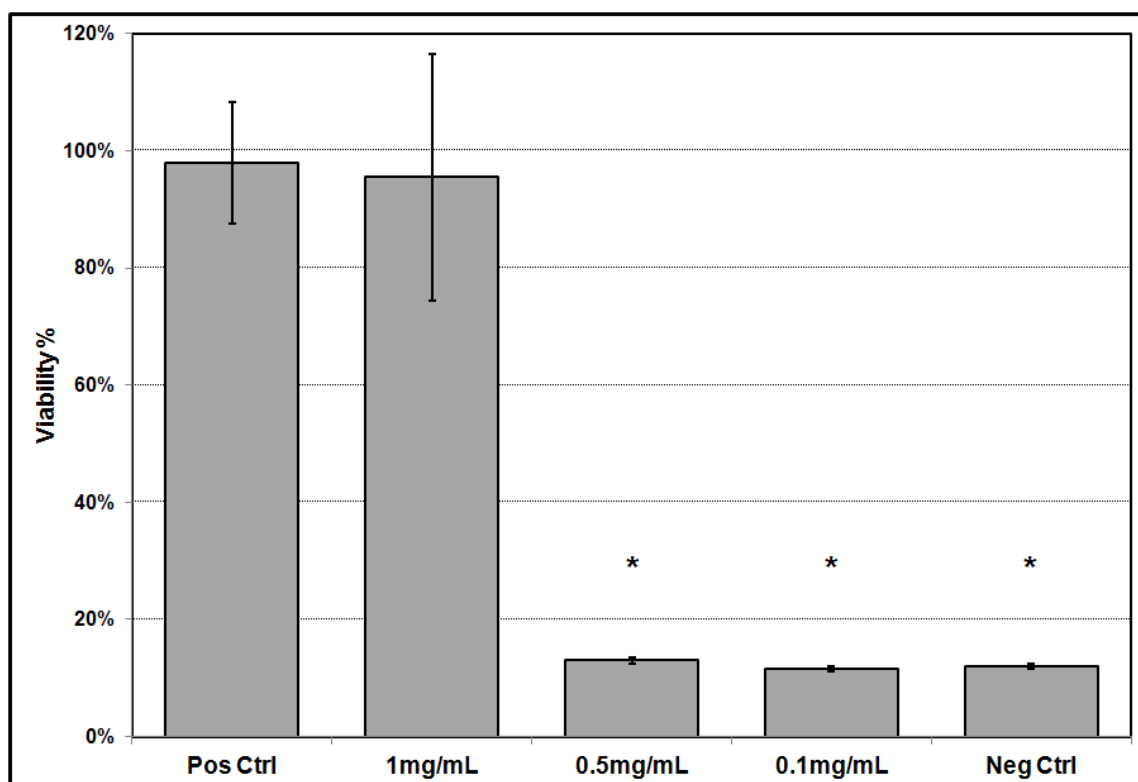


Figure 5-153: MTS Assay Results, Cytotoxic Effects of Me-mPEG-PP in Culture Medium on iPS-NSC. $p < 0.001$.

While this data was alarming, further experiments involving these peptides were performed at 1 mg/mL due to the lack of apparent toxicity. Cytotoxicity screening was performed with SKP-SC (1×10^6 cells/mL) encapsulated in CMA and photocrosslinked \pm Me-mPEG-Peptides at 1 mg/mL to evaluate whether SKP-SC would tolerate exposure to 0.025% I2959 and 2 minutes UV, and if peptide at 1 mg/mL would protect against photoinitiator toxicity. Live/Dead staining was performed after 72 H in culture following encapsulation/photocrosslinking to assess viability. Results (Figure 5-34) indicate that while SKP-SC adhered and grew in CMA gels (Figure 5-34 A), photocrosslinking, regardless of whether peptide was present, resulted in reduction of viability to near zero, not surprising given the high proliferation rate of SKP-SC.

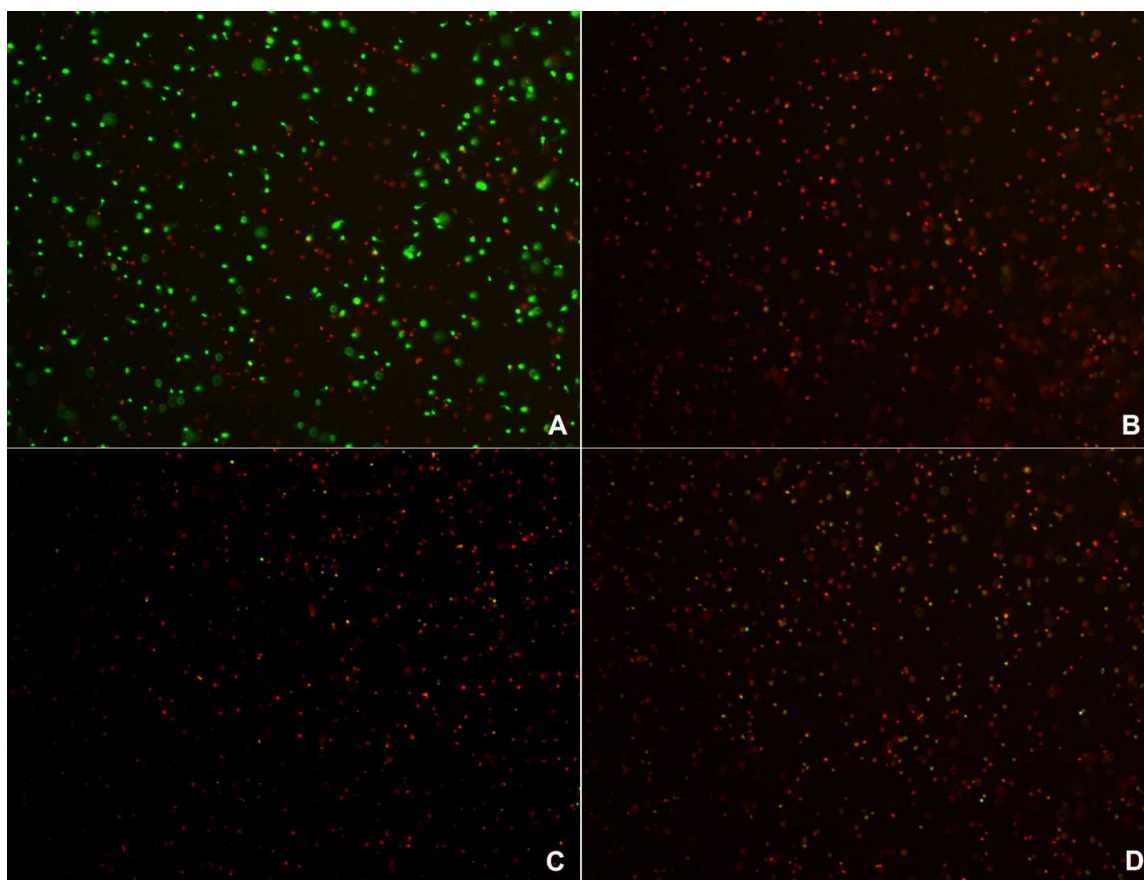


Figure 5-154: Live/Dead Stain of SKP-SC 72 H after Encapsulation in CMA (A) with Photocrosslinking (B), and Me-mPEG-P1 (C) or Me-mPEG-P2 (D)

Since SKP-SC appeared highly incompatible with the photocrosslinking process, we sought to investigate differences in cell behavior through interaction with pre-photocrosslinked CMA gels in a 2D culture system where the free radicals produced have been washed out of gels before cell seeding. Additionally, methacrylated peptides were crosslinked prior to seeding, which by virtue of washing out potentially toxic peptide beforehand allowed us to examine whether photografting these peptides resulted in modulated process morphology similar to results seen previously with bulk EDC grafting of the same sequences. Briefly, CMA gels in 48 well plates with and without photocrosslinking and methacrylated peptide (1 mg/mL) were washed thoroughly with PBS, and SKP-SC (5×10^4 cells/well) were seeded and cultured for 5 days, after which gels

were fixed and immunostained for the Schwann cell marker S100. Figure 5-35 portrays representative morphology of SKP-SC after 5 days, with DAPI included as a nuclear counterstain.

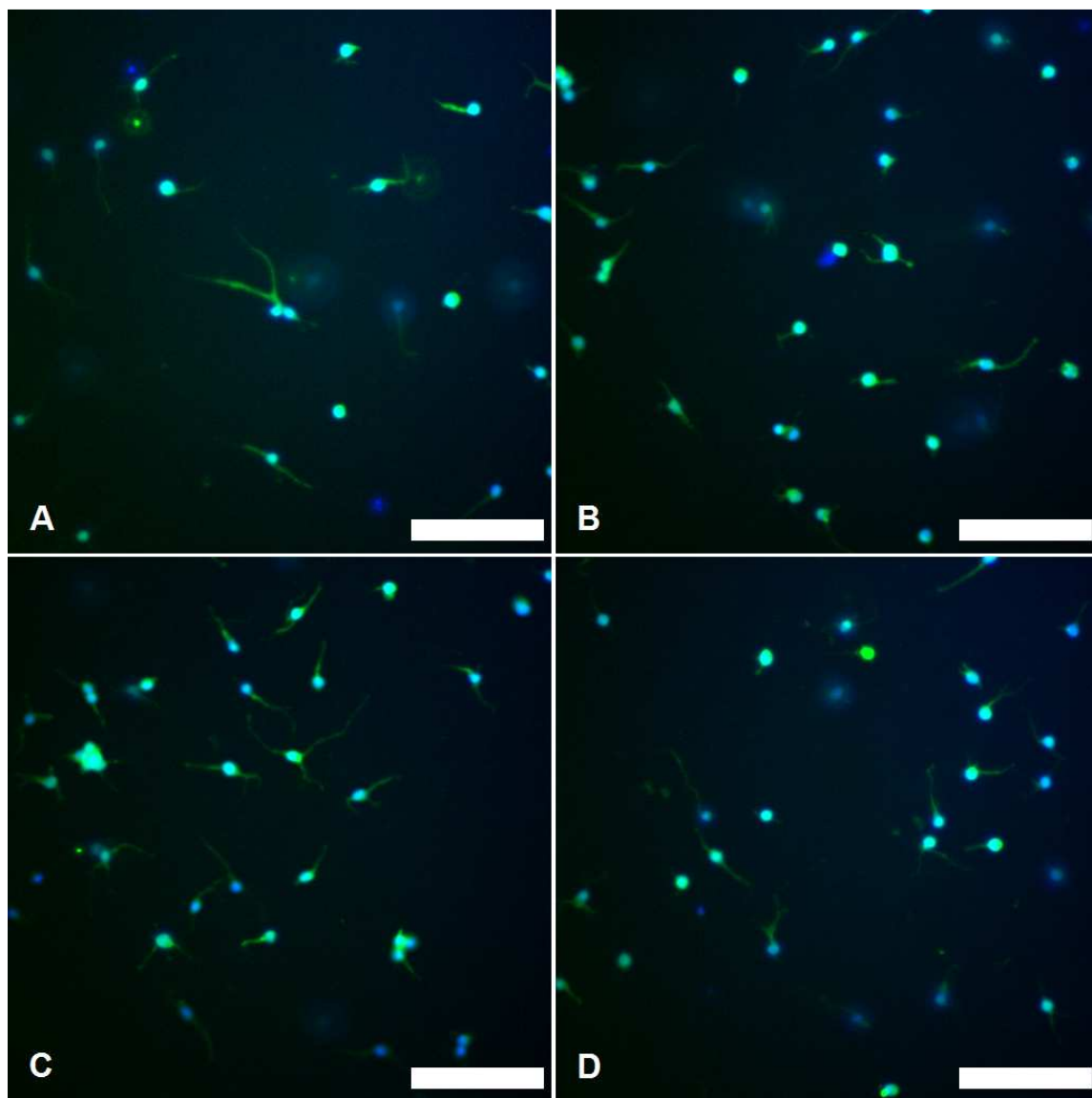


Figure 5-155: SKP-SC Cultured in 2D on CMA (A), Photocrosslinked CMA (B), and CMA Photocrosslinked with Me-mPEG-PP (C) and Me-mPEG-SP (D). Images taken at 20X, Scale Bar = 100 μ M.

Using ImageJ, we quantified several morphological features to ascertain whether photocrosslinking or peptide had a measureable effect on SKP-SC process extension. Mean cell number per image was calculated by averaging the number of DAPI positive nuclei from 4

images in each condition (Figure 5-36). After performing ANOVA combined with Tukey's *post hoc* test , we observed that the uncrosslinked CMA had significantly fewer cells per image (69.8 ± 8.3) compared to photocrosslinked CMA, CMA + PP, or CMA + SP (104.2 ± 15.9 , 93.3 ± 10.2 , 99 ± 6 , respectively). Cell number between photocrosslinked groups was not significantly different.

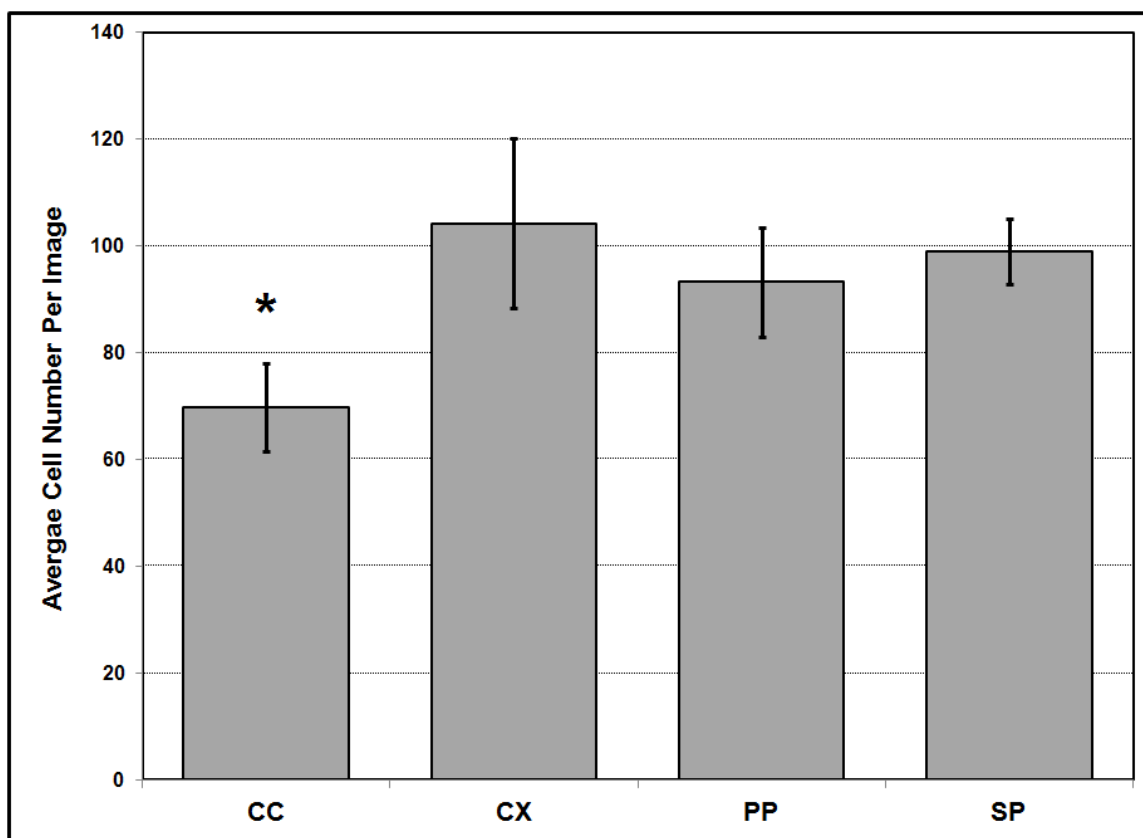


Figure 5-156: Quantification of SKP-SC Number on CMA Substrates after 5 Days in Culture. $p < 0.05$

Next, we measured the average number of primary cellular processes, normalized to cell number in each image. Primary cell processes were also measured, defined as the path length of the process from nuclear boundary to tip of furthest extended branch. Lastly, branch number was quantified by counting the number of process tips, and normalizing to primary process number as well as cell number for analysis. The results of these analyses are outlined in Figure 5-

37. Average process number per cell was not significantly different between any groups, although average process length was significantly longer in both photocrosslinked CMA and PP-photocrosslinked CMA compared to uncrosslinked CMA. Average branch number, while not significantly different between any groups, trended higher for SKP-SC cultured on PSA peptide-photocrosslinked CMA when normalized to both process and cell number. Overall, it appears that photocrosslinking CMA has a profound effect on SKP-SC interaction by increasing cellular adhesion and augmenting process extension. Furthermore, PSA mimetic peptide appeared to synergistically increase these effects, although only marginally.

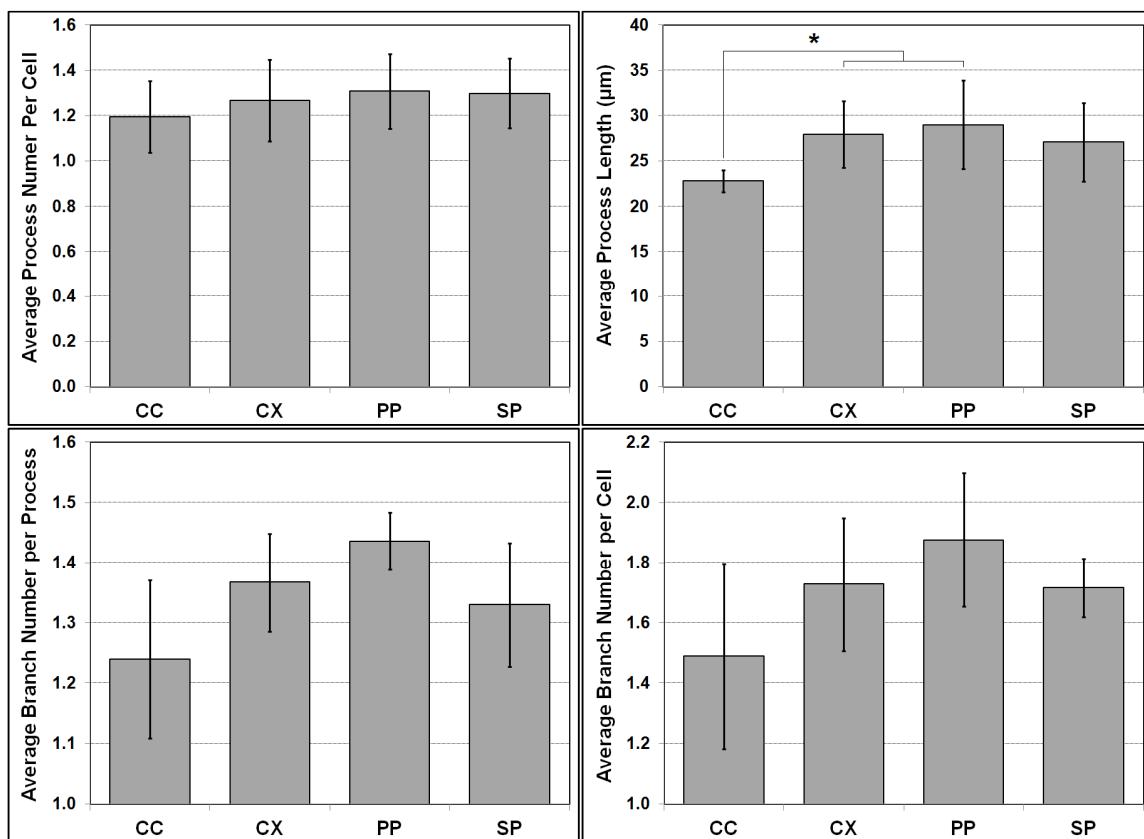


Figure 5-157: Quantification of SKP-SC Process Morphology on CMA Hydrogels (CC), Photocrosslinked CMA (CX), and CMA Photocrosslinked with 1 mg/mL Me-mPEG-PSA (PP) and Me-mPEG-Scramble (SP) Peptides. Reported as Mean \pm SD, $p < 0.05$.

We also looked at whether adult spinal cord progenitor cell (aSCP) differentiation could be performed on CMA with similar conditions, but with peptide concentrations increased to 2 mg/mL based on the marginal effect seen with SKP-SC at 1 mg/mL. Neurospheres of aSCP cultured in proliferation medium were switched to differentiation medium for 24 hours, then plated on CMA with and without photocrosslinking and methacrylated peptide. Differentiation was allowed to continue for 5 days, and then samples were fixed and stained with a panel of neural differentiation markers consisting of Nestin, Tuj1, GFAP, and NF-200. Immunostaining images were then qualitatively analyzed to determine if cell morphology or protein expression was affected with respect to matrix conditions. Analysis of images, summarized in Figure 5-38, revealed that aSCP cultured on uncrosslinked CMA gels exhibited very little process extension, with neurosphere boundaries remaining distinct. Additionally, very few cells migrated away from the neurosphere edge. Conversely, in the photocrosslinked CMA and CMA-PP gels, cellular outgrowth and migration away from the neurosphere onto the gel surface was markedly increased, with GFAP-positive cellular processes particularly more numerous and elongated on the CMA-PP gels. CMA gels photografted with SP appeared to be less permissive for aSCP outgrowth than the other crosslinked conditions, with neurosphere morphology more similar to uncrosslinked CMA. Overall, protein expression levels were similar among all groups, indicating that gel composition is more instructive for cellular orientation than differentiation lineage guidance. These data indicate that photocrosslinking and PP functionalization help to facilitate aSCP outgrowth into CMA gels, although variability in neurosphere size, shape, and distribution on gel surfaces made quantification of outgrowth difficult. Furthermore, the wide array of protein markers expressed concurrently indicate that differentiation at this timepoint is quite nascent, and longer culture periods are needed to draw any meaningful conclusion of substrate properties on aSCP differentiation.

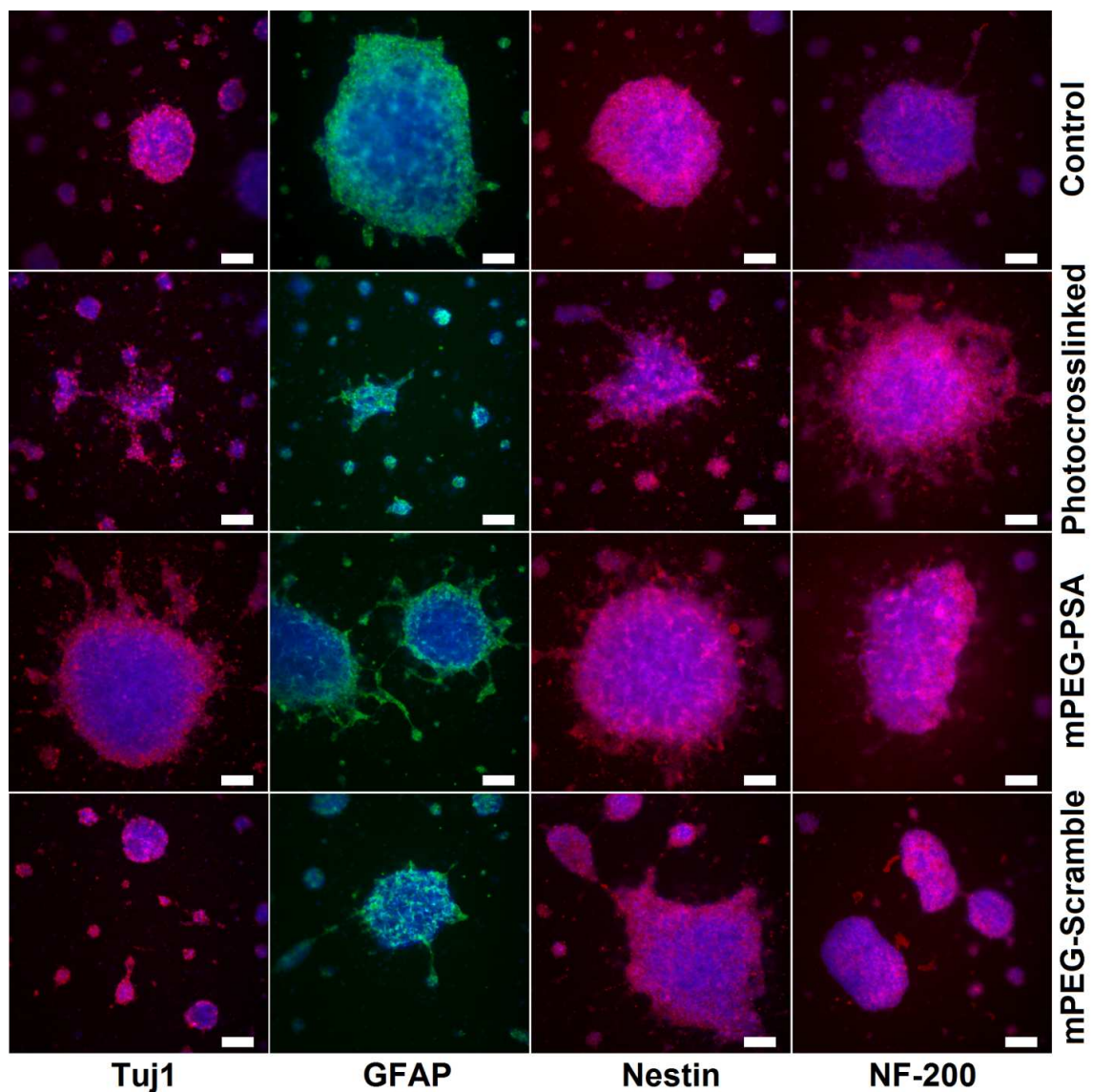


Figure 5-158: Immunostained Differentiating aSCP on CMA Gels \pm Photocrosslinking \pm PSA and Scramble Photografted Peptide at 2 mg/mL. Scale Bar = 100 μ M.

Peptide concentration was further increased to 4 mg/mL, as previous results were promising although measurable effects were subtle. However, as peptide is solvated at 10X the final concentration due to constraints for mixing CMA stock and precursor, this required stock peptide solutions of 40 mg/mL, which resulted in a number of problematic issues. First, it was unclear whether this concentration is beyond the solubility of these peptides, as visual inspection of stock peptide during dissolution revealed that some precipitate remained after

similar time periods with lower concentrations that appeared to completely dissolve all lyophilized peptide. Additionally, viscosity of peptide at this concentration was noticeably higher than previously seen, which made transfer of reagents difficult and resulted in some peptide lost to container and pipette tip adhesion. Lastly, and most troubling, after eventually going into solution with extended incubation in a heated water bath, it appeared that peptide in PP and to a worse degree SC stock solutions began to aggregate to a substantial degree, forming a viscous gel even before mixing with other CMA precursor reagents. As such, the effect concentration of labile peptide was unknown, and almost certainly different between PP and SC CMA gels, making comparison of effects on cells difficult to interpret. Even so, we plated SKP-SC and aSCP onto the resultant gels in a similar fashion to the previous experiments, and allowed them to culture. Additionally, PDL/Laminin on TCP was included as a control to compare CMA gel to standard 2D substrates. Cells were cultured for 3 days and fixed and immunostained for salient markers to assess morphological differences. Figure 5-39 shows the results with SKP-SC. Here, given the issues observed with peptide aggregation, only cursory qualitative analysis was performed. Briefly, all SKP-SC cell number and process extension on CMA conditions appeared comparable to previous data, with PP appearing to be more conducive to SKP-SC process extension than SC photografted and CMA control gels. However, process extension appeared less branched overall for all conditions, possibly due to the shorter culture period. Process extension in all CMA conditions was considerably lower than PDL/Laminin, indicating that SKP-SC preferred the PDL/Laminin to CMA based materials, although the flattened morphology of the SKP-SC in that condition was somewhat uncharacteristic for these cells, and over-confluence in the PDL/Laminin condition may have influenced this atypical morphology. Interestingly, proliferation on all CMA conditions appeared reduced compared to PDL/Laminin, which may be a useful attribute for tissue engineering where exponential proliferation may be undesirable.

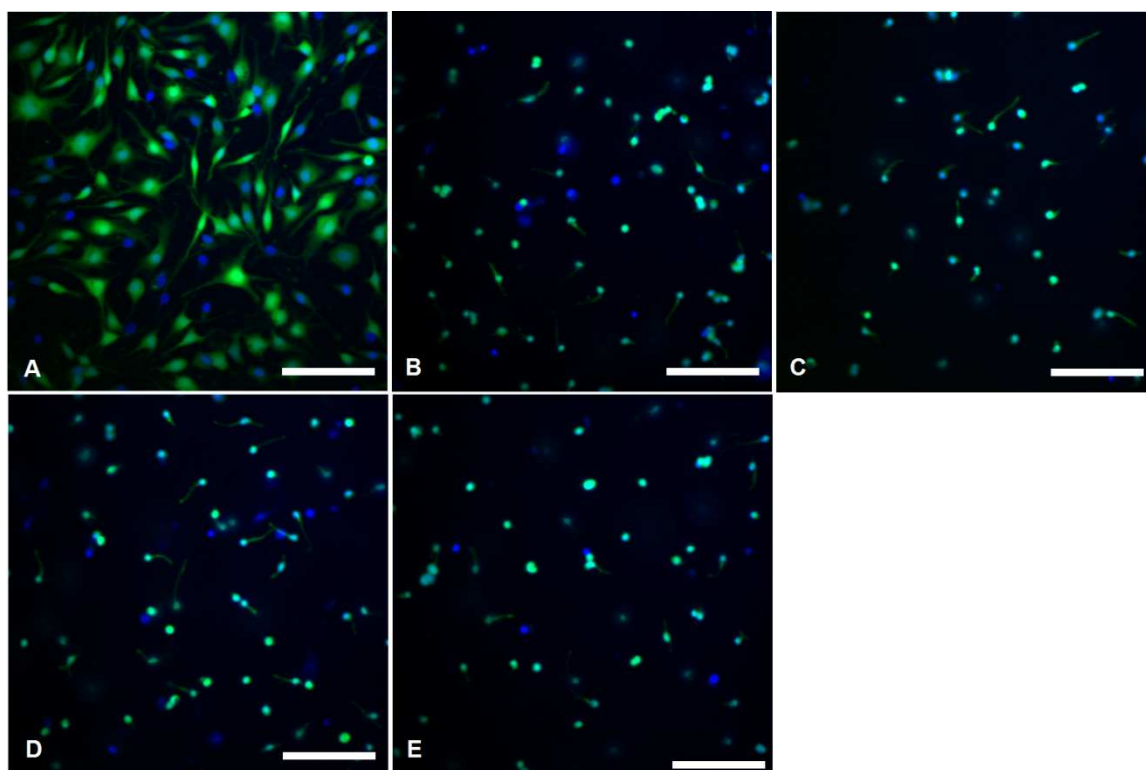


Figure 5-159: 2D Culture of SKP-SC on TCP with PDL/Laminin (A), CMA (B), Photocrosslinked CMA (C), CMA + PP (D) and CMA + SC (E). Green is S100, Blue is DAPI. Images taken at 20X Magnification. Scale Bar = 100 μm

Similar results were obtained from parallel experiments with aSCP. On TCP coated with PDL/Laminin, differentiating neurospheres self-dissociated, and a monolayer of GFAP positive, glial-like cells spread across that substrate, extending numerous processes. aSCP in all CMA groups were consistent in remaining in tightly formed neurospheres with few cells migrating out onto the hydrogel surface. Although a large fraction of the neurospheres themselves adhered to the substrate throughout the culture process, it was observed that during medium changes that a significant number of neurospheres were in suspension and were aspirated out of culture. Thus, in this set of experiments, the increased concentration of peptide appeared to have a less potent effect than at 1 mg/mL, presumably due to peptide aggregation. Representative images of aSCP morphology are displayed in Figure 5-40.

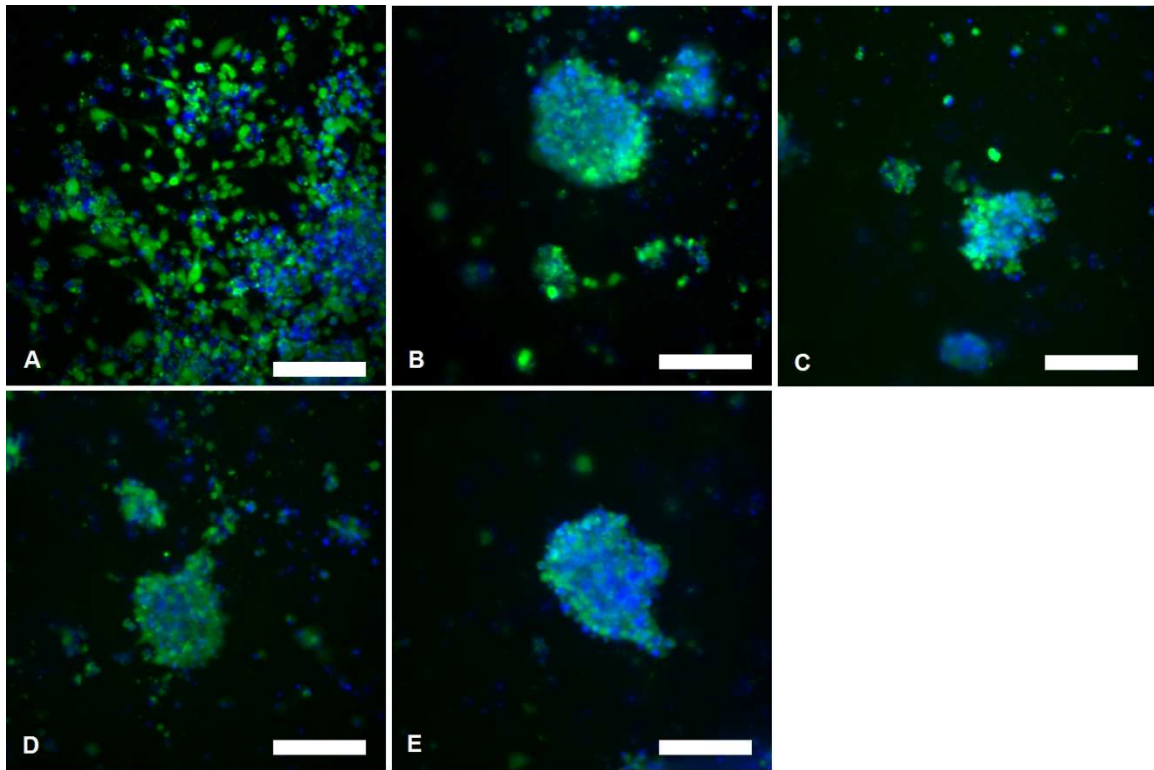


Figure 5-160: 2D Culture of aSCP on TCP with PDL/Laminin (A), CMA (B), Photocrosslinked CMA (C), CMA + PP (D) and CMA + SC (E). Green is GFAP, Blue is DAPI. Images taken at 20X Magnification. Scale Bar = 100 μ m

Encapsulated DRG in CMA gels containing 2 mg/mL PP and SP peptides were photocrosslinked with standard procedures and cultured for 3 days in complete medium to investigate whether this concentration of PSA peptide would increase neurite outgrowth in a similar fashion to EDC grafted PSA-collagen previously described and published. DRG in CMA hydrogels \pm photocrosslinking \pm PP and SP were fixed and stained for neurofilament-200. End-to-end distance of neurite extension from the portion of the DRG not extending from the severed root was measured from DRG soma to neurite tip. Data from four DRG per condition were averaged and compared, and one-way ANOVA was performed with Tukey's post hoc test to determine if photocrosslinking or peptide presence had a significant effect. As per this analysis, summarized in Figure 5-41, there was no significant difference in average neurite outgrowth between any of the conditions. Figure 5-42 displays representative images of neurofilament-200 and DAPI

stained DRG in each condition, which shows robust neurite outgrowth across all groups. Thus, we concluded that photografting PP and SC at these concentrations had no measurable effect on neurite outgrowth.

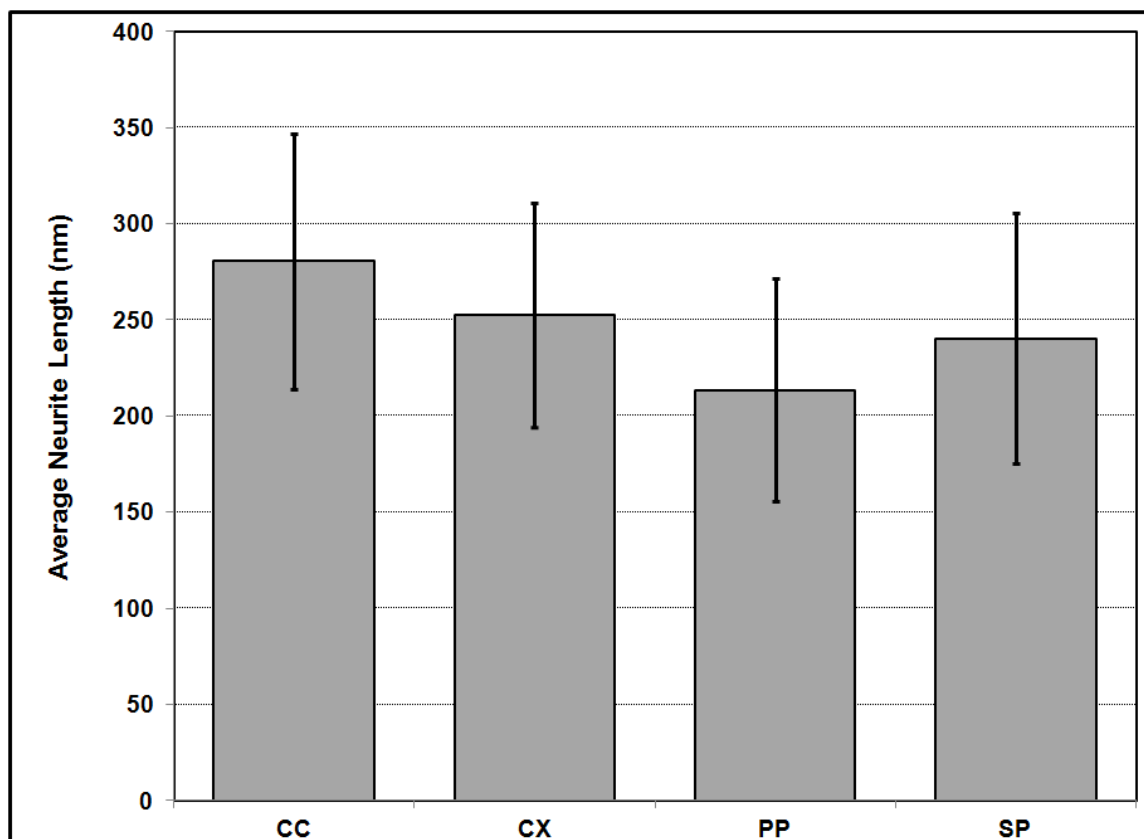


Figure 5-161: Neurite Outgrowth from CMA-encapsulated DRG \pm Photocrosslinking with PP and SC. Bars are mean neurite length \pm SD.

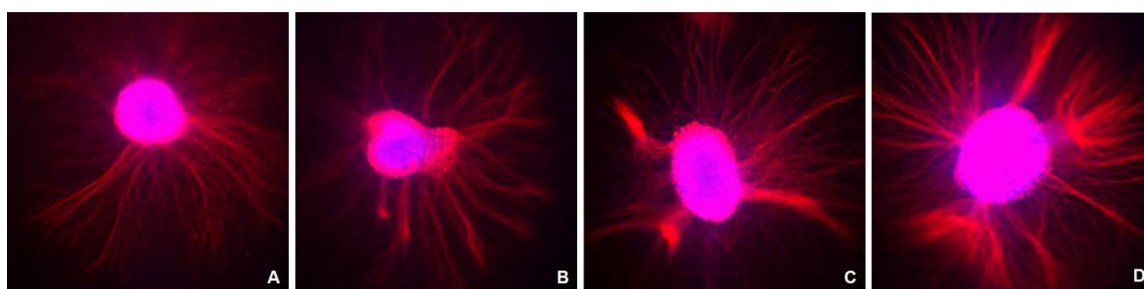


Figure 5-162: Neurofilament-200 (Red) and DAPI (Blue) Images of DRG Cultures in CMA (A), Photocrosslinked CMA (B), and CMA Photocrosslinked with Me-mPEG-PSA (C) and Me-mPEG-Scramble (D)

Lastly, we wanted to determine if patterning peptide at 4 mg/mL could be used to orient aSCP growth when cells were encapsulated at 1×10^7 cells/mL. After 24 H in differentiation medium to reduce proliferation rates, aSCP were dissociated from neurospheres with 0.25% trypsin/EDTA and encapsulated in 100 μ l CMA gels in Mat-Tek dishes. Masks with alternating 100 μ m stripes were placed between the cover-glass bottoms of the Mat-Tek dishes and UV light was applied for 2 minutes in the presence of 0.025% I2959. Following photocrosslinking, gels were washed 3X with differentiation medium and cultured for 72 H, after which Live/Dead staining was used to ascertain whether cell cytotoxicity was observed in a patterned manor, and if potential crosslinking of peptides in the pattern provided guidance to differentiating aSCP outgrowth. Here, peptides were put in solution at 37°C and then quickly cooled to prevent spontaneous gelation before admixing into CMA/cell solutions. No aggregation was observed in peptides prior to incorporation to CMA solution, although viscosity of peptide stock resulted in some lost material during reagent transfer. After analysis of Live/Dead stain, it was evident that PSA peptide was highly toxic, as the majority of cells in that condition were dead regardless of photocrosslinking. Photocrosslinking had no apparent adverse effects on the cells in the CMA alone gels, as calcein staining was equivalent for both uncrosslinked and crosslinked samples. However, while SP had no initial toxicity, cells crosslinked in the presence of that peptide were significantly reduced in viability. It was noted that no specific orientation was produced via masking of the gels. Results can be seen in Figure 5-43.

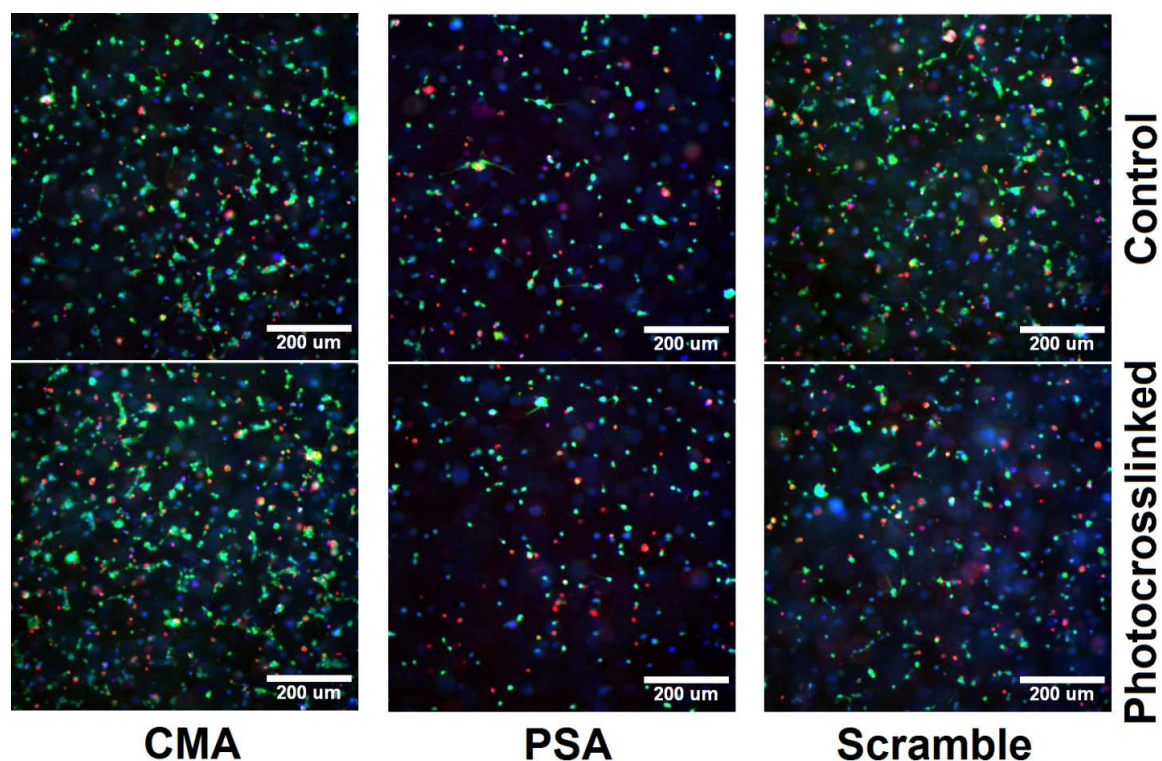


Figure 5-163: Live/Dead Staining of Dissociated, Differentiating aSCP in 3D in CMA \pm Photocrosslinking with Me-mPEG-Peptide at 4mg/mL using a Striped mask.

5.3.9 Visualization of Photopatterning

To investigate the spatial limitations of photopatterning, we attempted to incorporate reactive fluorophores into the photocrosslinking reaction process to determine patterning resolution as well as quantify photografting efficiency. Several fluorescent molecules were tested, with varying degrees of success towards visualizing photocrosslink patterns. Nile Blue Acrylamide (NBA), fluorescein-o-acrylate (FoA), methacrylate-TRITC (MeT), FITC-conjugated methacrylated peptide, DAPI-conjugated methacrylated DNA, and FITC-avidin conjugated to biotin-PEG1K-thiol were tested as visualization agents. NBA, which fluoresces in water (Ex: 635 nm, Em: 674 nm) was incorporated into CMA macromer solution, and gels were $\frac{1}{2}$ masked and photocrosslinked. While some visualization of photocrosslinking was apparent (Figure 5-44 A) as increased fluorescence intensity on the UV exposed left portion of the image, the signal was extremely

weak. In addition, NBA visually precipitated out of solution upon addition to the CMA precursor solution even at concentrations that were not measurably fluorescent. Further attempts with this reagent were not continued. FoA, seen in Figure 5-44 (B and D), required adjuvant solvents (MeOH (B), DMSO (D)) to form solutions. With methanol, FoA precipitated out of solution when added to CMA solutions. However, as seen in Figure 5-44 B, masking was able to impart patterned fluorescence in the region exposed to UV, a Rutgers “R”, in this case. However, precipitation and the resultant background fluorescence made quantification of fluorescence unreliable as a mode of measuring photografting efficiency. When FoA was dissolved first in DMSO, at low concentrations there was not substantial precipitation, although standard fluorescence microscopy used for FITC visualization was unable to capture an increase in fluorescence in UV-exposed regions. Interestingly, illumination of $\frac{1}{2}$ photocrosslinked gels with a UVA-producing flashlight revealed that conjugation was present (Figure 5-44 D), although it was unclear why this was not visible under either a standard DAPI or FITC filter set. Additionally, rheometry data of CMA photocrosslinking with FoA in solution showed evidence that FoA imparted additional stiffness to gels, distinct from storage modulus increase from I2959-mediated photoinitiation, which complicated analysis of photografting efficiency due to apparent interaction of FoA and CMA beyond the expected methacrylate-acrylate binding. Me-TRITC, a commonly used fluorophore for visualizing PEGDA-based photocrosslinked hydrogels, was unusable in our application as we observed that it non-specifically bound to CMA even in the absence of I2959 or UV light, as per visualization of CMA fibrils (Figure 5-44 C). A similar phenomenon was observed with DAPI-visualized methacrylated DNA, which also bound to CMA even without photoinitiation (Figure 5-44 F). FITC-conjugated methacrylated peptide, with a PSA mimetic as the peptide sequence, actually showed up as more fluorescent in the UV-masked region of the gel (Figure 5-44 E, left side). Again, non-specific binding and/or aggregation of the

peptide appeared to be present, and UV exposure of the fluorescent gels appeared to cause rapid photobleaching, which resulted in less fluorescence than the non-photocrosslinked portion. Lastly, biotinylated PEG-thiol (BTP, PEG M_w = 1KDa) was used as an analog for peptide photografting quantification. Thiol functionalization was used instead of methacrylate/acrylate due to commercial availability. Briefly, the BTP was added to the macromer solution, $\frac{1}{2}$ photocrosslinked, and the unbound BTP was washed out of the gel. Avidin-FITC was then incubated with the gels and unbound fluorophore was washed out. However, across various concentrations of both BTP and avidin-FITC, no measurable fluorescence was detected, indicating negligible photografting efficiency with this system. Overall, we were able to show that photocrosslinking patterns could be visualized via fluorescent monomers, although we were unsuccessful in using any of the reagents tested for quantification of photografting efficiency due to non-specific binding, fluorophore precipitation, and bleaching of fluorescence tags by photoinitiation conditions.

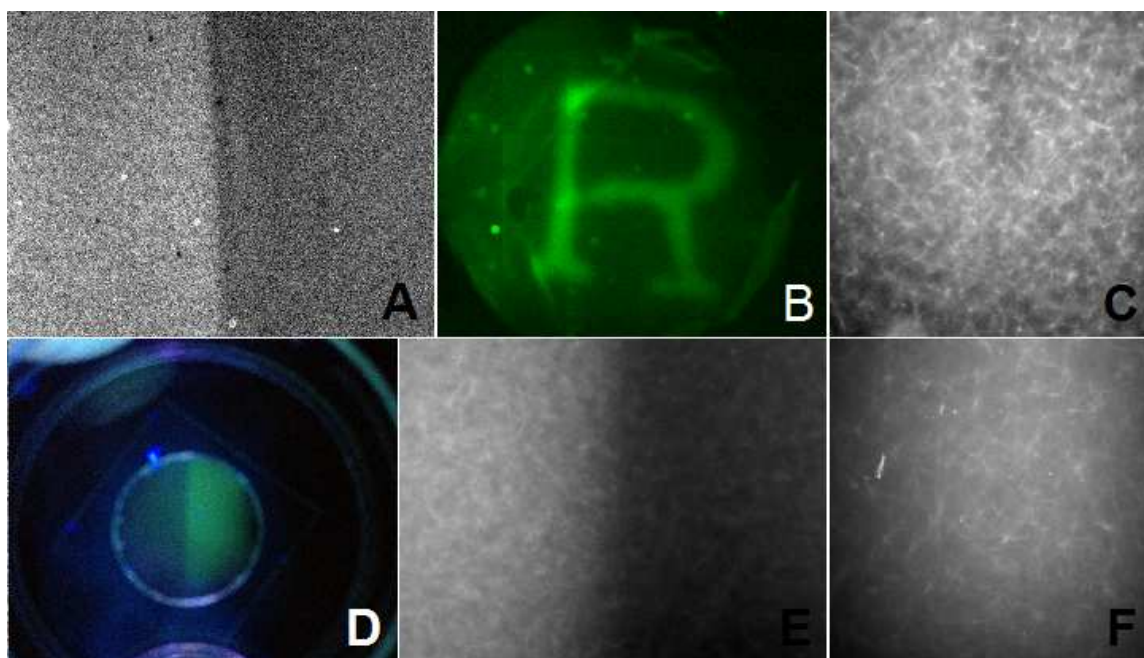


Figure 5-164: Photopatterning CMA with Various Acrylated/Methacrylated Fluorophores: Nile Blue Acrylamide (A), Fluorescein-o-Acrylate (B,D), Methacrylated DNA/DAPI (C), Methacrylate-PSA-FITC (E), Methacrylate-TRITC (F)

One concern with patterning fidelity was attenuation of UV through interaction with CMA fibrils, which may create anisotropy as a function with respect to distance from CMA gel boundary. We examined the effect of CMA gel thickness by measuring UV light intensity penetration. Gels from 0-3 mm thick were cast in PDMS wells and UV irradiance was measured with and without gels present. As outlined in Figure 5-45, UV intensity was measured to be 99% as compared to air when gel thickness was 526 μm , which was close to the thickness used for all real-time UV rheometry characterization experiments. At 1.05 mm, UV intensity was attenuated by 4%. All cell-encapsulated CMA gels in Mat-Tek dishes discussed previously were less than 1 mm thick. Light attenuation increased linearly with gel thickness, with gels measuring 2.63 mm allowing 86% of the UV light intensity.

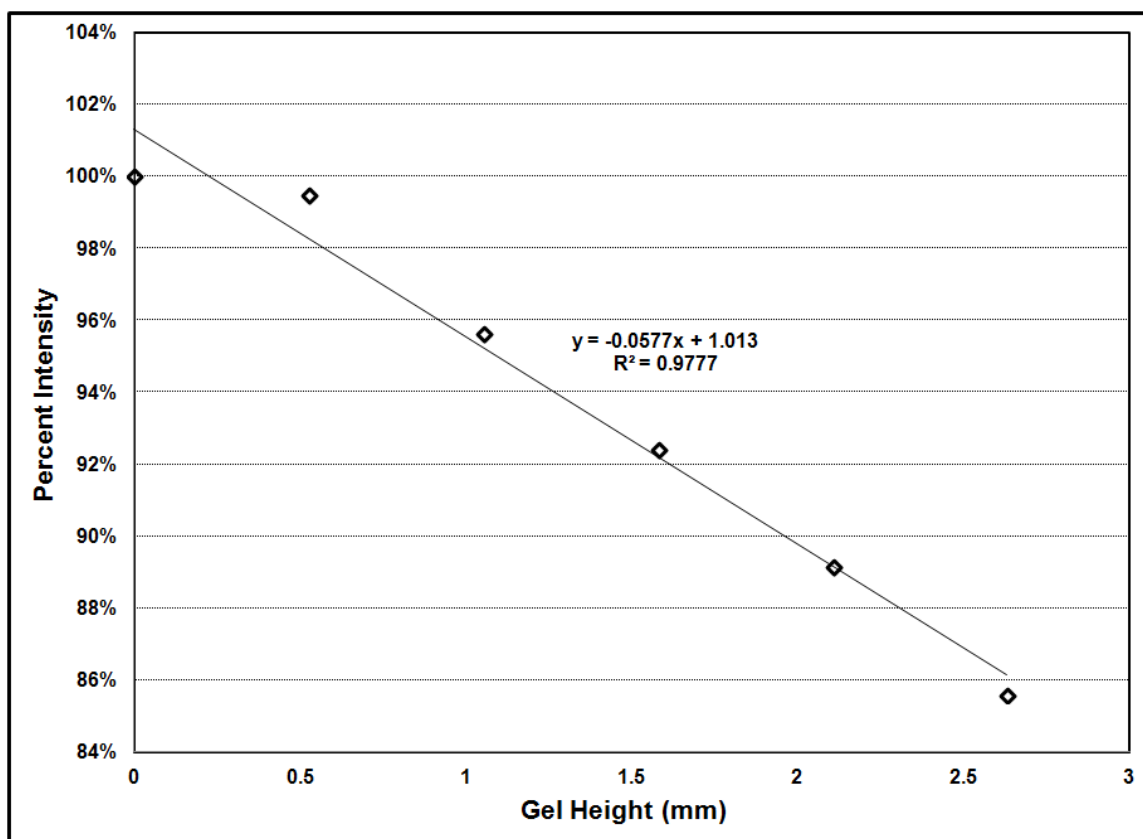


Figure 5-165: Penetration of UV light into CMA Vs Gel Height

5.4 Discussion

In order to evaluate whether CMA photocrosslinking could be used as a tool for modulating cellular behavior in the context of neural regeneration, we characterized the cytocompatibility of UVA-I2959 photoinitiation in the presence of live cells. I2959 was chosen as the photoinitiator based on its water solubility and published reports of its compatibility with mammalian cells in photocrosslinking applications [102]. Initially, I2959 was screen with multiple cell types on TCP in what we considered to be a ‘worst-case’ scenario where no photoactive material was present to act as a sink for free radicals produced upon I2959 activation. Testing was performed in this manner both to expedite testing as TCP-based assays are far simpler to execute and to remove CMA variability as a factor during CMA derivatization optimization, which was ongoing

concurrently to initial cytotoxicity screening. The rationale was that since I2959 photoinitiation was cytocompatible, cells should be able to survive its use regardless of CMA presence, and cells that screened positively in this regime would only be more compatible when encapsulated in the radical-absorbing CMA matrix. Indeed, we saw that some cells, including 3T3 fibroblasts, hMSC and RG-8 NSC, were largely tolerant of I2959 concentrations up to 0.05%, commonly reported in literature as efficient for catalyzing photopolymerization with a variety of materials [19,25,108,109]. Conversely, other cell types such as hESC, were highly susceptible to the free radical production, and were not pursued at target cells in further experiments.

Our assumption that CMA would appreciably mitigate cytotoxicity appeared to not be well-founded, as significant cytotoxicity was observed in photocrosslinked CMA-cell constructs even with modest I2959 concentrations, which was somewhat unexpected data published elsewhere using I2959 to polymerize and modify photosensitive hydrogel scaffolds. A study by Albrecht et al., using 20% PEGDA photocrosslinked with 0.1% I2959 successfully formed stable hydrogels with encapsulated 3T3 fibroblasts, and viability was not compromised [110]. In another study, Burdick et al., evaluated viability of encapsulated 3T3 fibroblasts in acrylated hyaluronic acid (AHA, 2-20% w/v), photocrosslinked with 0.05% I2959 [111]. Their results indicated that 3T3 viability was highly dependent on macromer molecular weight, indicating that significant differences in photocrosslinking toxicity may result from aspects related to photocrosslinking dynamics, which are poorly understood in CMA. One hypothesis for the overall high toxicity we observed during CMA photocrosslinking may be the relatively low per mass ratio of methacrylates on CMA compared to other photopolymers. The CMA concentration used (2-3.5 mg/mL, which equates to 0.2-0.35% of the overall mass of the hydrogel) was much lower than the aforementioned studies using PEGDA or AHA, which both have many more reactive groups per unit mass. This theory was largely validated in experiments where PEG2KDA was included at

1% w/v, which significantly improved viability compared to similar I2959 concentrations and CMA alone. Thus, the much higher concentration of reactive groups may result in a significant sink for radicals and likely is responsible for mitigating some toxicity. The fact that CMA is organized into a fibrillar network means that the methacrylate groups are confined to the fibrils, which may further decrease their overall volumetric distribution to near negligible levels. Furthermore, this non-uniform distribution may also explain why such relatively high I2959 concentration was required to achieve significant augmentation of mechanical properties as per rheological analysis discussed in previous chapters.

In our studies, some cells, such as hMSC RG-8 NSC, appeared to be more viable when exposed to I2959 photoinitiation on TCP than in CMA gels, although cell density differences between the two culture models were likely a deciding factor in the cytotoxic effects. Further evaluation of cell density in CMA gels indicated that higher cell density resulted in greatly improved post-crosslinking viability, which we conjectured was simply a stoichiometric relationship of the ratio of free radicals to cells. DRG, consisting of large tightly packed multicellular aggregates, appeared to be highly compatible with photocrosslinking in CMA gels as evidenced by robust neurite outgrowth in photocrosslinked gels. However, it is difficult to determine whether this was due to low proliferation rates of DRG neuronal cells, trophic support of associated glial cells, or simply the sheer number of cells present. Our results also mirrored published findings that proliferation rate was prognostic of I2959 compatibility, as highly proliferative cells such as L2.3 and CTX-8 exhibited significant photoinitiator toxicity even in dense neurosphere culture within CMA gels, whereas hMSC, which are less proliferative, were generally tolerant of photocrosslinking provided encapsulation density was sufficient. Additionally, hMSC are purported to have a cyto-protective role *in vivo*, mediated by the secretion of soluble factors,

which may have contributed to their robust survival of photoinitiation especially at higher cell densities [112-114].

Given the tolerance for photocrosslinking and the published correlation between substrate mechanical properties and neurogenic differentiation [46], hMSC were initially chosen as the focal cell type for evaluating *in situ* mechanical modulation via photocrosslinking CMA gels. In conjunction with real-time rheometry, we were able to optimize the UV exposure time for use with 0.025% I2959 and obtain a 5-6 fold increase in storage modulus while maintaining > 80% viability with encapsulated hMSC. This important benchmark allowed us to modulate the stiffness of the gels within a range of properties that we believed would have an effect on neurogenic differentiation, based on previously published values. Indeed, photocrosslinking appeared to have a profound effect on the morphology of hMSC encapsulated in CMA, inducing a highly branched process extension as compared to native collagen. However, comparison to uncrosslinked CMA was rendered complicated due to extensive compaction of CMA by hMSC, a surprising phenomenon that resulted in a material of dynamic material properties which was problematic given our experimental platform was designed to evaluate the effect of mechanical properties on hMSC differentiation. Furthermore, the question of whether hMSC are actually capable of differentiation into functional neuronal cells is still being debated by many researchers, and may be dependent on the source of cells. Our cells, from young adult donors, appeared to constitutively express several neuroectodermal markers, including nestin, β_{III} -Tubulin, and GFAP, even when cultured in growth medium on TCP. Evaluation of these markers in hMSC on TCP compared to in native collagen and CMA gels revealed no significant differences. In an effort to decouple hMSC compaction of CMA from stiffness, we evaluated several published methods for chemically inducing hMSC into a neuronal phenotype in the hopes that these neurally-induced (NI-hMSC) cells would be less likely to exhibit contractile

behavior. Indeed, NI-hMSC were not able to compact uncrosslinked CMA gels, exhibited down-regulated nestin expression, increased MAP2 expression, and maintained a high level of β -Tubulin expression. However, the same was true for NI-hMSC in native collagen as well as photocrosslinked hMSC. Additionally, changes observed in NI-hMSC from typical proliferation morphology to a neuronal morphology occurred in a matter of hours upon addition of neural induction medium, which raised questions about the validity of the induction and whether cytoskeletal modulation by chemical factors was mainly responsible for the neuronal-looking morphology. Indeed, over time in culture, cell morphology returned to a more typical hMSC looking appearance, and replacement with fresh induction media resulted in further transient neural morphology. Possibly, the cell source we used was inadequate for investigating neural differentiation. Thus, while we successfully developed a platform to investigate hMSC neurodifferentiation in mechanically dynamic 3D hydrogels, we decided eventually to refocus on more clinically promising cell types for neural regeneration, although application with a more appropriate cell source may be worthwhile in the future. Furthermore, other soft tissue engineering applications may be better suited to CMA-hMSC gels. The ability of hMSC to robustly compact CMA gels, and the spatial control afforded by crosslinking areas where compaction is not desirable may possibly hold promise for creating cell compacted tissue constructs with complex geometries. Additionally, the fibrillar structure of CMA results in directed compaction creating oriented microstructures, such as circumferentially aligned fibrillar bundles, which have unique biological and mechanical properties created by anisotropic scaffold remodeling. One such application, shown as a proof of concept previously, is toward engineering vertebral discs, where the native tissue geometry entails a gelatinous, amorphous gel surrounded by bundle of aligned collagen fibers to provide mechanical integrity. Using CMA-encapsulated hMSC, we were able to create a similar structure using only a 2 minute exposure

of light. Other applications for CMA include vascular engineering, a possibility investigated by undergraduates in our laboratory in which tube-like structures created by cellular compaction were then photocrosslinked afterwards to improve the mechanical properties. Finally, we evaluated hMSC and smooth muscle cell adhesion to CMA gels in comparison to native collagen to determine if the compaction phenomenon was the result of CMA derivatization significantly increasing the adhesive qualities. Our results indicated no drastic differences, leading us to the conclusion that differences in CMA gel micromechanics are the driving mechanism, possibly due to intrafibril instability as discussed in previous chapters.

Next, we evaluated CMA as a 3D substrate for culturing, differentiating, and influencing cellular behavior with an array of neuroregeneration-relevant cells including human iPS derived neural stem cells, embryonic chicken dorsal root ganglia, rat skin-derived precursor-derived Schwann cells, and rat adult spinal cord progenitor cells. Proliferating iPS-NSC were highly susceptible to I2959 associated radicals, even at cell densities as high as 1×10^7 cells/mL. However, when proliferation was inhibited by pre-differentiated into a neuronal lineage, viability was improved significantly, and cells exhibited neuronal morphology in CMA gels with and without crosslinking. However, while cellular viability was acceptable, the effect of free radical generation also greatly inhibited process extension, possibly implying that cellular health was detrimentally affected. Decoupling radical damage from mechanical cues remains a significant challenge for engineering mechanical microniches within cell-encapsulated CMA hydrogels. Thus while mechanical property modulation via photocrosslinking may be an acceptable modality for guiding cellular outgrowth through inhibition, the harmful effects of I2959 photoinitiation need to be considered as an unavoidable consequence.

Additionally, we sought to influence iPS-NSC differentiation and outgrowth through modification of the biochemical properties of CMA gels with photografted functional peptides. Functional sequences from laminin were used as model peptides as neuronal adhesion to laminin coated surfaces is a well documented characteristic, and previous work has demonstrated that micropatterned laminin can be used to guide neurite outgrowth[115]. Additionally, we believed that the increased labile methacrylate groups present in the photocrosslinking milieu would improve cell viability following photocrosslinking by reducing the excess radical pool available to attack cells. Peptide design was performed using sequences used by other members of our lab previously, as well as incorporating elements from the literature implicating increased efficacy of peptide function through the use of a flexible poly-glycine spacer, which purportedly improves cellular access to the functional sequence. Results with this peptide were problematic, primarily due to unexpectedly poor hydrophilicity of the peptide. Methacrylation may slightly reduce solubility due to replacement of the charged N-terminal amine with the neutral methacrylate, and the six-glycine spacer may also be slightly hydrophobic, but either modification alone had previously not exhibited the strong hydrophobicity we observed with all three peptides, indicating that a synergistic combination of these charge effects might be responsible for the solubility issues. As such, at high peptide concentrations, visible aggregates were observed and implied that very little labile peptide was able to photograft onto CMA. At lower concentrations, we did not see aggregates, although they may have been small enough to go unnoticed. Alternately, low concentration peptides may have been more soluble, but the effective concentration was too low to produce an effect. Interestingly, the only peptide condition that had any noticeable effect was the scrambled control, VIVAK, which has no published biological function. Possibly, the sequence order affected solubility, as the terminal amino acid, lysine, may have imparted increased hydrophilicity compared to the laminin

sequence IKVAV, which has a polar valine at the terminus. Solubility differences were observed even in DMSO stock solvation times, although peptide purity may have been a factor. It is possible that the presence of a soluble peptide, and not the sequence itself, resulted in the morphological effects observed, particularly the increased outgrowth compared to control CMA. Non-specific binding of secondary antibody to IKVAV peptide aggregates, while helping to elucidate the aggregation problem, further compromised VIVAK-IKVAV comparison biologically. Further investigation of VIVAK as a functional sequence may be warranted in the future. Experiments with DRG and the same peptides were beset by similar issues.

Overall, iPS-NSC differentiation in CMA gels showed that these gels could be used as an effective 3D tissue culture substrate with potential as a clinical tissue engineering material or as a platform for studying neurodevelopment and pathophysiology. However, in our experiments, cellular susceptibility to photoinitiator toxicity and peptide design flaws resulted in a lack of compelling data regarding guiding iPS-derived neural differentiation and outgrowth. Furthermore, the time and material costs required to expand and differentiate tens of millions of iPS-NSC per experiment became prohibitive for additional experiments. We determined that 1×10^7 iPS-NSC cells/mL was the minimum density in 3D gels to allow for viable long-term culture, as lower densities failed to thrive even in the absence of photoinitiation. While feasible, the material and reagent costs for growing such large quantities of cells became a significant detriment for rationalizing additional experiments. In addition, recent findings suggest that unexpected immunogenicity iPS cells may limit their clinical application [116].

Coinciding with the conclusion of these experiments was a collaborative research effort at the University of British Columbia, which, among other things, resulted in procurement and culture expertise with two clinically relevant cell types that were incorporated into experimental design

with the subsequence set of peptide photografting experiments. Skin-derived precursor Schwann cells have been implicated as potential target cell type for nervous system repair in both CNS and PNS injury models. In addition, collagen grafted with PSA-mimetic peptide was previously shown in our laboratory to positively modulate Schwann cell process extension, with published results by our lab and other groups indicating that PSA-peptide was useful for improving functional outcomes in peripheral nerve injury paradigms. The other cell type acquired, adult spinal cord progenitor cells, are a recently discovered population of multipotential glial precursors with exciting possibilities for spinal cord repair. Strong evidence from others in our lab working with explanted organotypic spinal cord slices indicated that spinal cord neuron regeneration could be modulated by PSA-mimetic peptide covalently bound to collagen. Additionally, published results indicate that PSA, and to a lesser degree PSA-mimetic peptide, may have a critical role in influencing the morphology of the glial scar, development of the lesion cavity, and axonal regeneration in spinal cord injury, with important implications for functional recovery [117-119].

However, peptide design again proved to be fundamentally flawed. Despite claims from Biomatik Inc., which helped us design as well as synthesize the methacrylated miniPEG spaced PSA-mimetic peptides, that miniPEG had no reported cytotoxicity, we observed that 0.1 and 0.5 mg/mL concentrations in medium resulted in severe toxicity during initial screening. Additionally, the lack of toxicity at 1 mg/mL as well as visual inspection of peptide stock solutions at higher (4 mg/mL) concentrations indicating that peptide aggregation was again a serious issue, even in the absence of photoinitiator. Likely due to the toxicity at lower concentrations and the reduction of labile peptide at higher concentrations, again we observed no rescue of photoinitiator toxicity with SKP-SC in 3D photocrosslinked CMA gels. Additionally, while DRG tolerance of photoinitiation allowed evaluation of photografting within 3D gels, no

significant benefit in neurite outgrowth was observed from inclusion of functional or scrambled control peptide, and within the samples analyzed, it appeared that the methacrylated, minPEG spaced PSA-mimetic peptide may have decreased neurite outgrowth, possibly due to aforementioned toxicity.

To test if PSA-peptide could be used to modulate cellular behavior, a 2D culture system was employed where both photocrosslinking and peptide toxicity were mitigated by modifying gels prior to introduction of cells, with I2959 radicals and toxic, labile peptide washed out beforehand. Here, we observed a significant effect on cellular morphology when comparing photocrosslinked gels to uncrosslinked CMA controls, which we interpreted as indication that stiffness modulation was primarily responsible. Indeed, previously published results from Georges et al., indicated that glial cells preferentially extend processes on stiffer substrates, which agrees with both mechanical and biological data in our studies[29]. Photocrosslinking of CMA gels may provide a valuable tool for instructive glial cell outgrowth, with applications for nervous tissue repair and fundamental research as spatially tunable hydrogel scaffolds. Peptide photografting results, while statistically insignificant, nevertheless implied that a marginal effect was observed morphologically in both SKP-SC and aSCP in promoting augmented cellular outgrowth. We attribute the lack of measurable effect via photografting compared to EDC-grafted PSA-collagen to the assumption that the majority of the peptide was likely aggregated and thus unavailable for I2959 coupled bonding to CMA groups. Further development and design of photolabile peptides, however, is required to investigate utility of this modality of biochemical modification, which will require significant resources. Future collaboration, both for improved peptide design as well as small-scale synthesis, may be necessary to for cost-effective development of effective next-generation peptides for use with this system. Conversely, there are concerns that peptide grafting through photocrosslinking may not be able to functionalize

fibrillized gels equivalently to bulk EDC-based grafting of soluble native collagen, as the much longer reaction times and higher degree of freedom of well mixed reaction solutions likely allow higher derivatization efficiency. However, until peptide design is improved, we can't conclude whether photografting allows functional quantities of peptide ligand to be introduced onto the CMA backbone. Given the utility of introducing functional peptides in therapeutically relevant spatial distributions, we feel that further development is worthwhile despite the significant effort that will be required.

Lastly, characterization of photocrosslinking patterning through the use of commercially available fluorescent monomers produced mixed results. A consistent issue was solubility in CMA solutions, which is more difficult than with many synthetic photopolymer systems due to the large number of process constraints implicit to collagen-based materials, such as pH, solvent incompatibility, temperature, and time. While we were successful in demonstrating that CMA gels could indeed be differentially patterned at biologically relevant scales, poor signal intensity and fluorophore bleaching made determination of photopattern fidelity and photografting efficiency data difficult to interpret. A promising mode for elucidating these parameters may reside in as well in custom peptide design. Peptide side chain chemistries provide a number of possibilities for detection and visualization that do not depend on pre-conjugated fluorescent groups, which are not optimal in our process due to UV bleaching, solubility issues, interaction with photoinitiation, and possible steric hindrance due to the typically large molecular weights and complex ring structures compared to small, linear peptide sequences. However, development of such peptides is not currently economically feasible with industrial peptide suppliers due to the high cost and relatively large minimum product quantities required by such companies, again implying that academic collaboration may be necessary to progress the state of the art.

5.5 Conclusion

We have developed a self-assembling photocrosslinkable type-I collagen biomaterial that can be combined with cells as a liquid solution and used to form stable 3D hydrogel tissue constructs upon pH neutralization and temperature increase. These gels are able to quickly polymerize, resulting in encapsulation of cells into a stable, inherently bioactive matrix suitable for culture of a variety of neuroregeneration-relevant cell types. Basal mechanical properties of these soft tissue constructs can be adjusted through changing macromer concentration to recapitulate the mechanical properties of native biological tissues. Additionally, we can quickly adjust the mechanical properties of these gels through photocrosslinking with Irgacure 2959 and long-wave UV light, allowing dynamic spatiotemporal control of the scaffold compliance within a range of physiologically relevant stiffness. Cellular response to CMA gels with and without photocrosslinking indicates suggests that photomanipulation of CMA hydrogels may provide a useful tool for creating instructive, anisotropic scaffolds with a number of desirable qualities, including inherent biocompatibility, cellular adhesion, and biodegradability. In addition, self-assembly may allow for injection into irregularly shaped injury defects where pre-formed solid scaffolds are impractical due to disruption of nearby healthy tissue.

However, one potential disadvantage of photocrosslinking as a mechanism for *in situ* scaffold manipulation is the significant effect of free-radicals resulting from photoinitiation. While the photoinitiator used in our system, I2959, has previously been used as an initiator with other published photosensitive materials with varying degrees of cytotoxicity, its use in our platform indicates that radical damage is more severe than previously reported, potentially due to fundamental characteristics of our material. Photoinitiator toxicity, as reported elsewhere, is highly dependent not only on biomaterial properties but biological parameters as well. Cell type, proliferation rate, cell density, and differentiation state all dramatically affect the outcome of

exposure to photocrosslinking conditions. In particular, hMSC are highly tolerant of photoinitiation, and can be successfully encapsulated, photocrosslinked, and cultured as soft tissue constructs with tailored mechanical properties. However, use of photocrosslinking to modulate neurogenic differentiation of hMSC was not successful; although the fundamental premise that hMSC can form functional neuroectodermal tissue is controversial and may depend on cell source.

Photoinitiator cytotoxicity was more pronounced with other cell types tested, resulting in contraindication of photocrosslinking as a mechanism for guiding differentiation and/or outgrowth of encapsulated iPS-NSC, SKP-SC, and aSCP cells. However, culture on pre-modified CMA gels with and without the inclusion of functional photolabile peptides indicated that photopatterning could be used successfully to spatiotemporally instruct cellular behavior if cells were not subjected to photoinitiation directly. Lastly, results pertaining to biochemically modulating CMA scaffolds through peptide photografting were largely hindered by peptide solubility and toxicity issue, which prevented straightforward analysis of biological efficacy. Further development of adequate peptides which addresses these issues is required, and will likely require outside collaboration.

5A Appendix: Stem Cell Cytotoxicity Screening of I2959 Photoinitiation

Stem Cell Screening of Irgacure 2959 Photoinitiator Toxicity

Initial screening of I2959 photoinitiation toxicity with NIH-3T3 plated on TCP revealed a concentration-dependent relationship of viability when UV light exposure was applied for 5 minutes followed by culture for 24 hours under standard conditions. Qualitative analysis of Live/Dead staining in Figure 5A1 indicated that I2959 toxicity readily increased from minimal cell death at 0.01% (Figure 5A1 B), to a transition concentration between 0.4% and 0.5% (Figure 5A1

C and D) where cell death was noticeably increased, to almost complete ablation of the cell population at 0.1% (Figure 5A1 F) as compared to control cells with no I2959 (Figure 5A1 A).

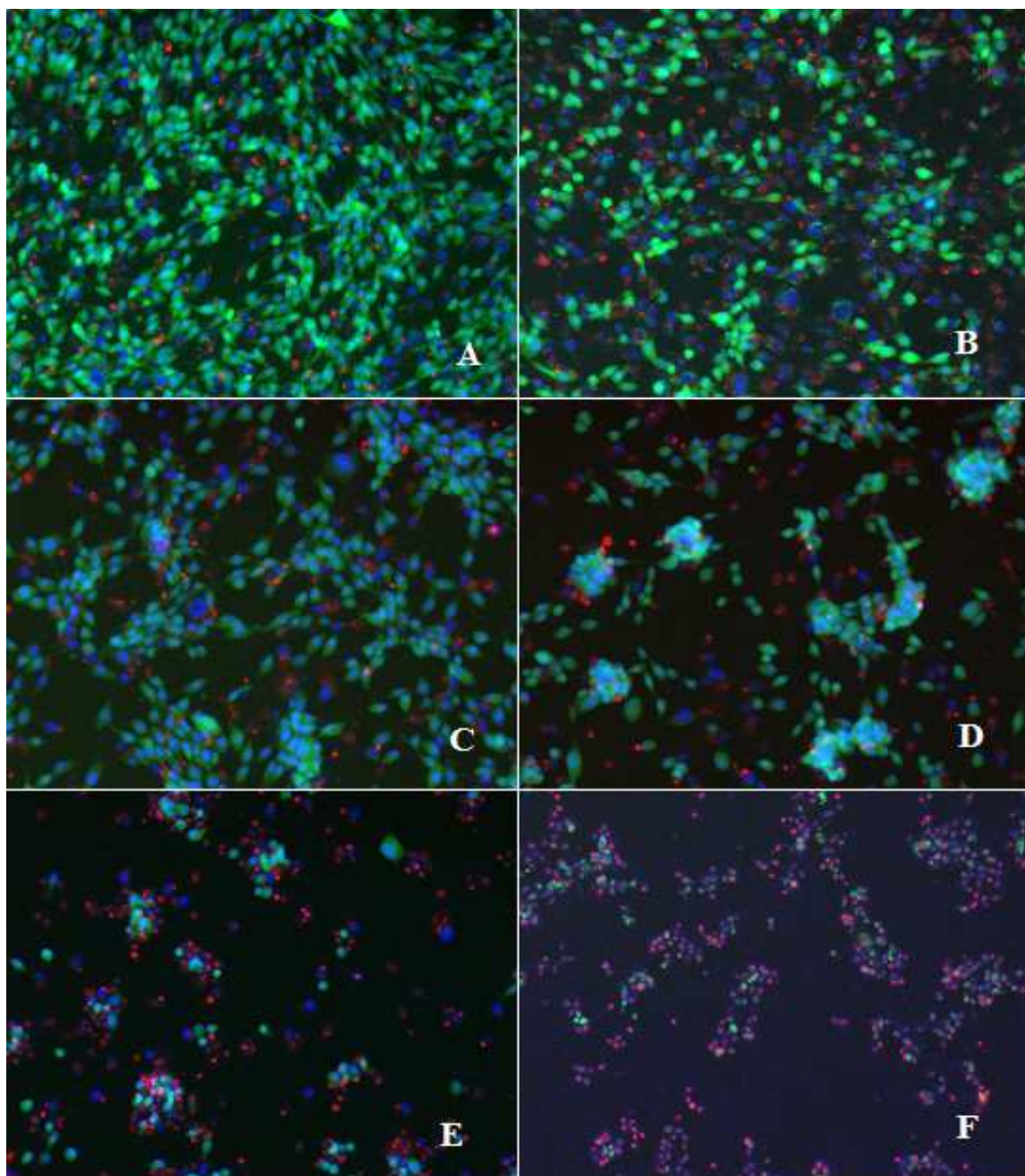


Figure 5A-1: I2959 Toxicity in NIH-3T3 24 H after Photoinitiation with 5 minutes UV light Exposure. A: Control, B: 0.01%, C: 0.02%, D: 0.04%, E: 0.05%, F: 0.1%

However, upon photoinitiation of a similar range of I2959 concentrations with hESC, it was clear that a distinct difference in cytotoxicity exists between cell types. Here, severe cytotoxicity was observed even at the lowest dose (0.0125%, Figure 5A2 C), where 90% of cells appeared dead, which increased to near 100% toxicity at the high dose (0.1%, Figure 5A2 F). UV alone was not measurably cytotoxic as compared to control cells, (Figure 5A2 B and A, respectively).

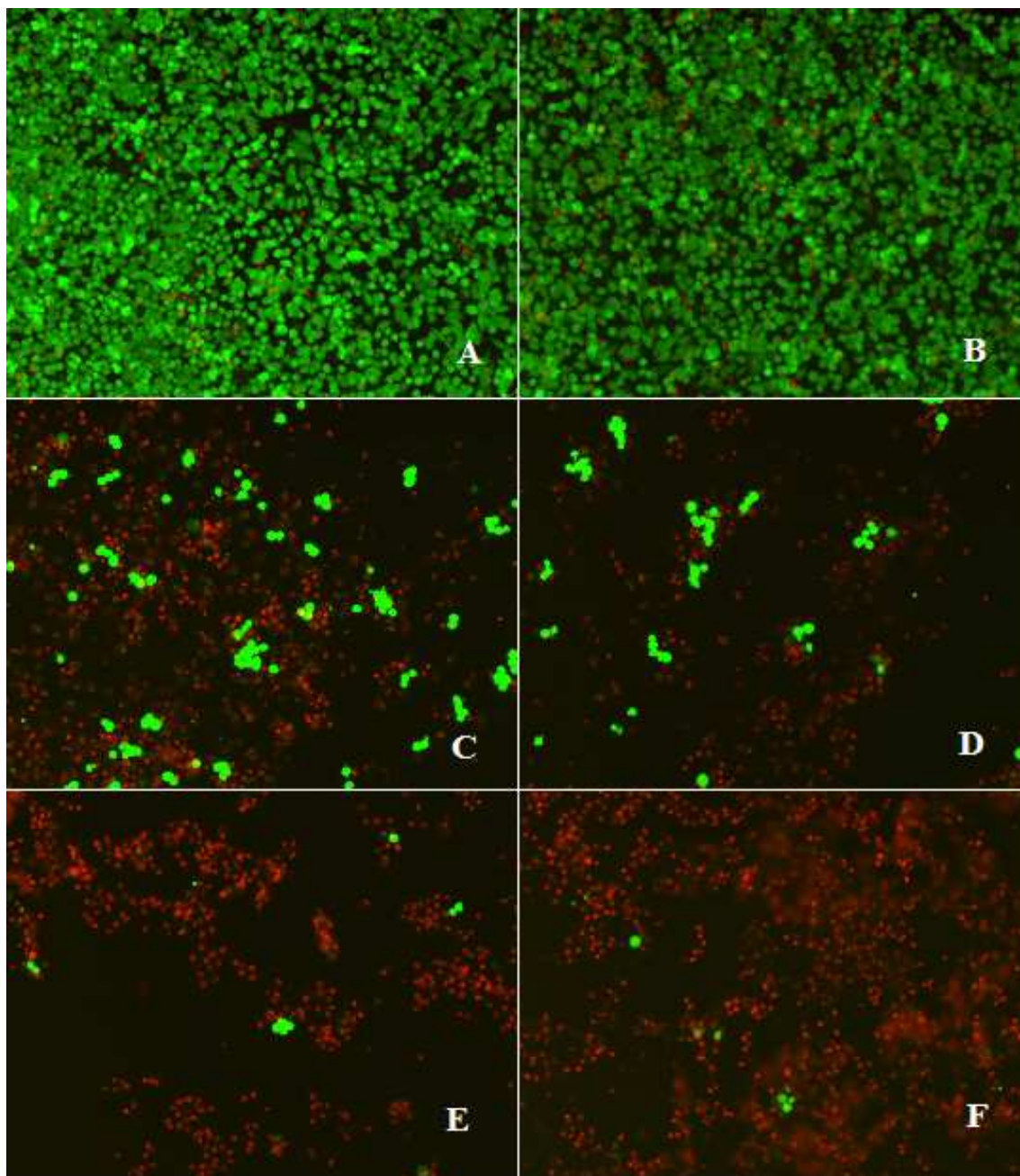


Figure 5A-2: I2959 Toxicity in hESC 24 H after Photoinitiation with UV. A: Control B: UV Ctrl C: 0.013% D: 0.025% E: 0.05% F: 0.1%

In contrast, hMSC showed remarkable resiliency to I2959 photoinitiation toxicity. Upon exposure of a monolayer of hMSC on TCP to 5 minutes UV exposure, only at the highest concentration,

0.1% (Figure 5A3 E), did I2959 exhibit significant cytotoxicity as compared to negative control (Figure 5A3 A). 10% Ethanol was included as a positive control for toxicity (Figure 5A3 F). Lower Irgacure concentrations of 0.0125%, 0.025%, and 0.05% (Figure 5A3 B, C, D) did not result in any appreciable cytotoxicity.

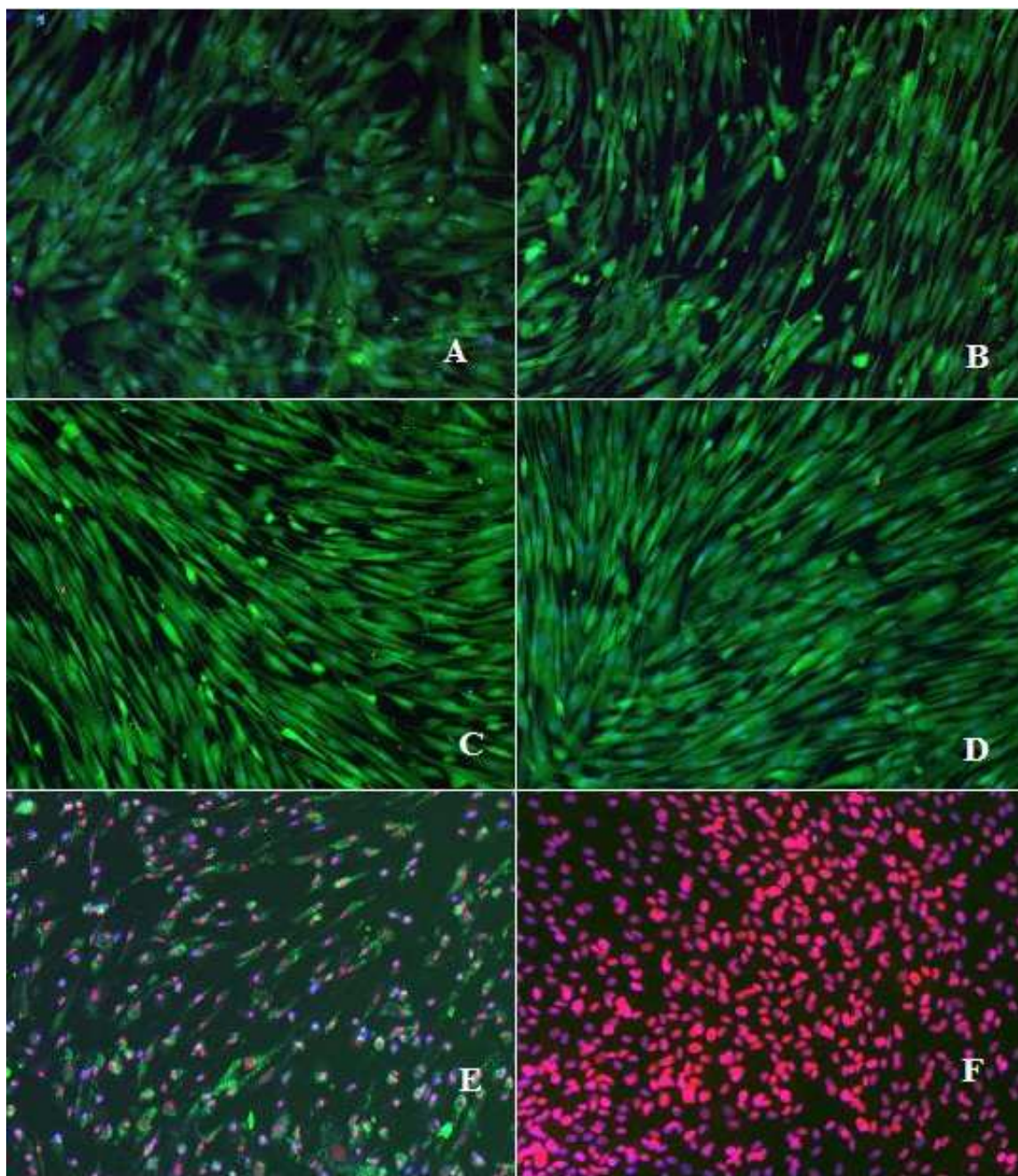


Figure 5A-3: I2959 Cytotoxicity in hMSC 24 H after Photoinitiation with UV. A: Negative Control B: 0.013% C: 0.025% D: 0.05% E: 0.1% F: Positive Control (10% Ethanol)

As hMSC will spontaneously differentiate at higher cell densities, I2959 toxicity screening was repeated at a low enough areal density to prevent contact-mediated osteoblast differentiation as determined by cellular morphology under bright field microscopy. Again, hMSC showed resiliency at up to 0.04%, although at the lower cell density the cutoff concentration appeared to be 0.05%, as significantly lower I2959 cytotoxicity was observed at 0.04% compared to 0.05% (Figure 5A4 D and E). Thus cell density appears to be a strong factor in hMSC response to Irgacure photoinitiation toxicity.

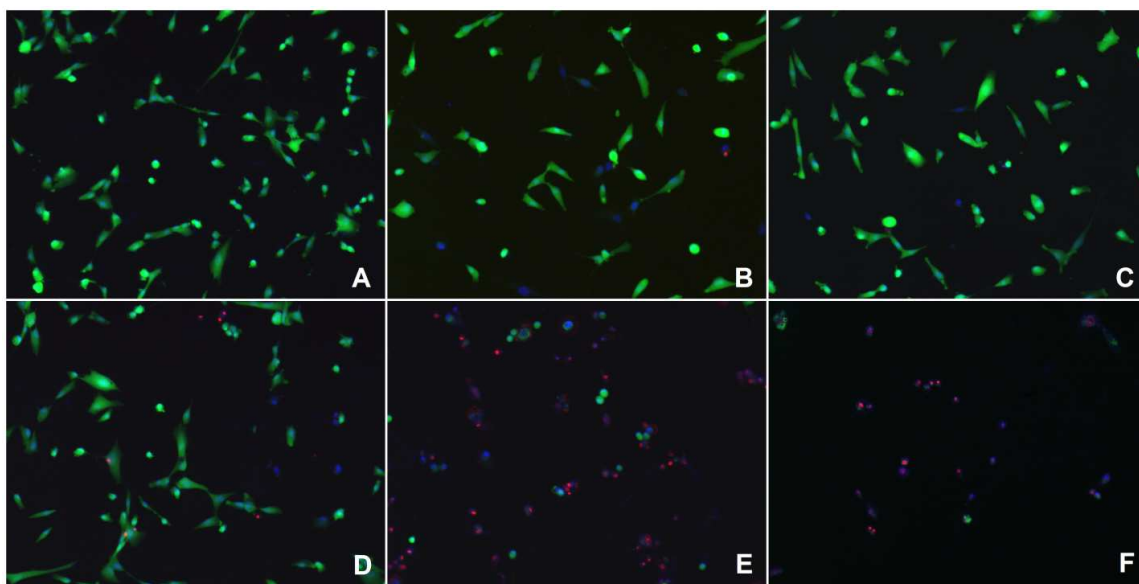


Figure 5A-4: I2959 Cytotoxicity in Sparsely Seeded hMSC 24 H after Photoinitiation with UV Light. A: Control, B: 0.01%, C: 0.02% D: 0.04%, E: 0.05%, F: 0.1%

Testing of I2959 in CMA gels in which E8 chicken DRG were embedded and photocrosslinked showed that the high density primary cells were able to withstand photoinitiation of 0.05% Irgacure with minimal toxicity as seen in Figure 5A5. Neurite outgrowth and glial cell migration appeared similar in uncrosslinked CMA (A & B) as compared to 0.05% I2959 photocrosslinked CMA gels (C & D).

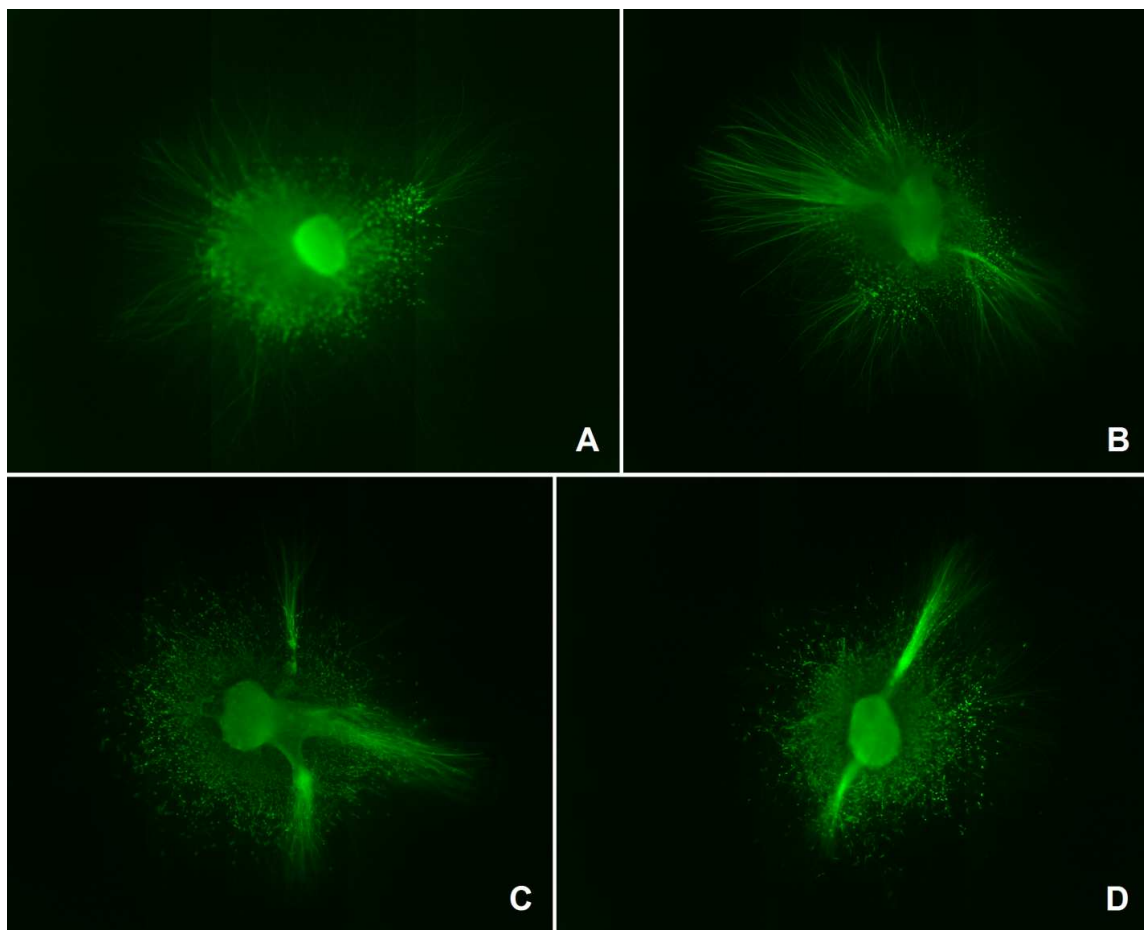


Figure 5A-5: I2959 Cytotoxicity in DRG Embedded in CMA Gels and exposed to UV photoinitiation. Control (A,B) and 0.05% I2959 Photocrosslinked (C,D)

To test whether stem cells grown in similar clusters displayed the same resiliency to photoinitiator toxicity, we used rat L2.3 glial precursor cells. L2.3 cells grow in suspension culture in neurospheres comprised of hundreds to thousands of cells and with similar cluster sizes to DRG. We encapsulated L2.3 at a high density of $\sim 840K$ /mL in native collagen and CMA. I2959 at various concentrations was included, as was PEG2KDA at 1% to act as a radical sink. As seen in the Live/Dead staining, L2.3 neurospheres were highly viable in both native collagen and CMA without photoinitiator (Figure 5A6 A,B). However, significant cytotoxicity was observed in L2.3 photocrosslinked in the presence of 0.05% I2959 (Figure 5A6 C), a stark contrast with the

results seen with DRG. At a lower concentration of photoinitiator (0.01%, Figure 5A6 D), toxicity was reduced but still present as seen by the relative lack of green calcein staining in the neurospheres. Addition of PEG2KDA served to rescue some of the cells at 0.05% I2959 (Figure 5A6 E), and at 0.01% I2959 the inclusion of PEG2KDA caused the neurospheres to look similar to the uncrosslinked controls (Figure 5A6 F). While the lack of calcein indicated non-viable cells, the lack of significant ethidium in all conditions also implies that cells are potentially in the process of dying or in a metabolically compromised state in which esterase production is reduced but cells are still alive. The MTS assay data obtained in parallel to the Live/Dead staining corroborates the latter theory. In Figure 5A7, we see that 0.05% I2959 caused a large ablation in the MTS signal, which is only partly mitigated by PEGDA. However, at 0.01% I2959, 1% PEGDA is able to completely rescue the MTS activity to control levels.

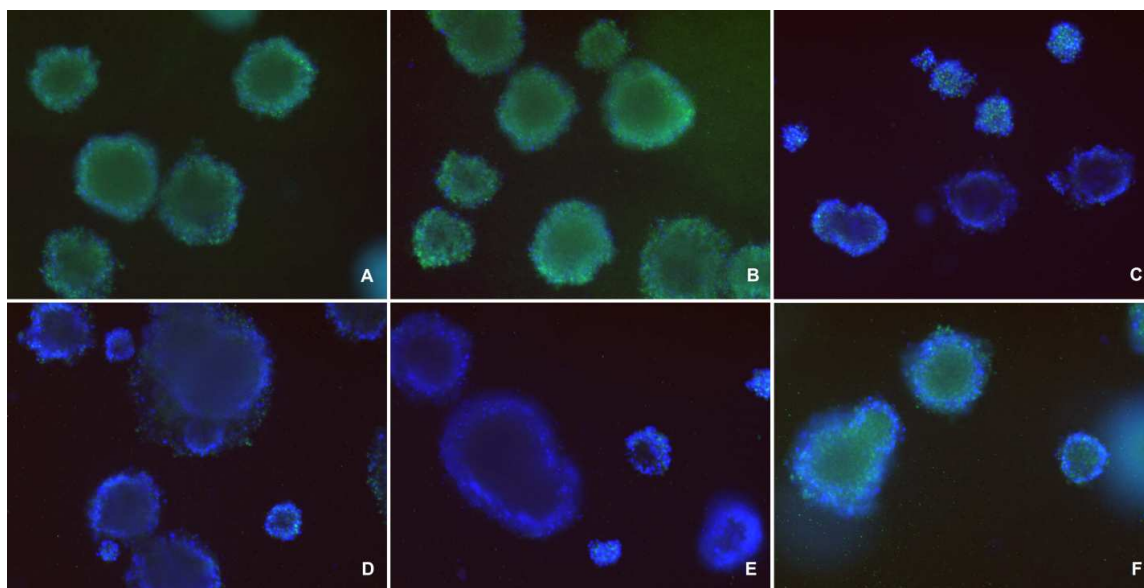


Figure 5A-6: Live/Dead Staining 48 H after I2959 Photocrosslinking of L2.3 Glial Progenitor Neurospheres in 3D Gels.
A: Native Collagen, B: CMA, C: CMA + 0.05% I2959, D: CMA + 0.01% I2959, E: CMA + 0.05% I2959 + 1% PEG2KDA, F: CMA + 0.01% I2959 + 1% PEG2KDA

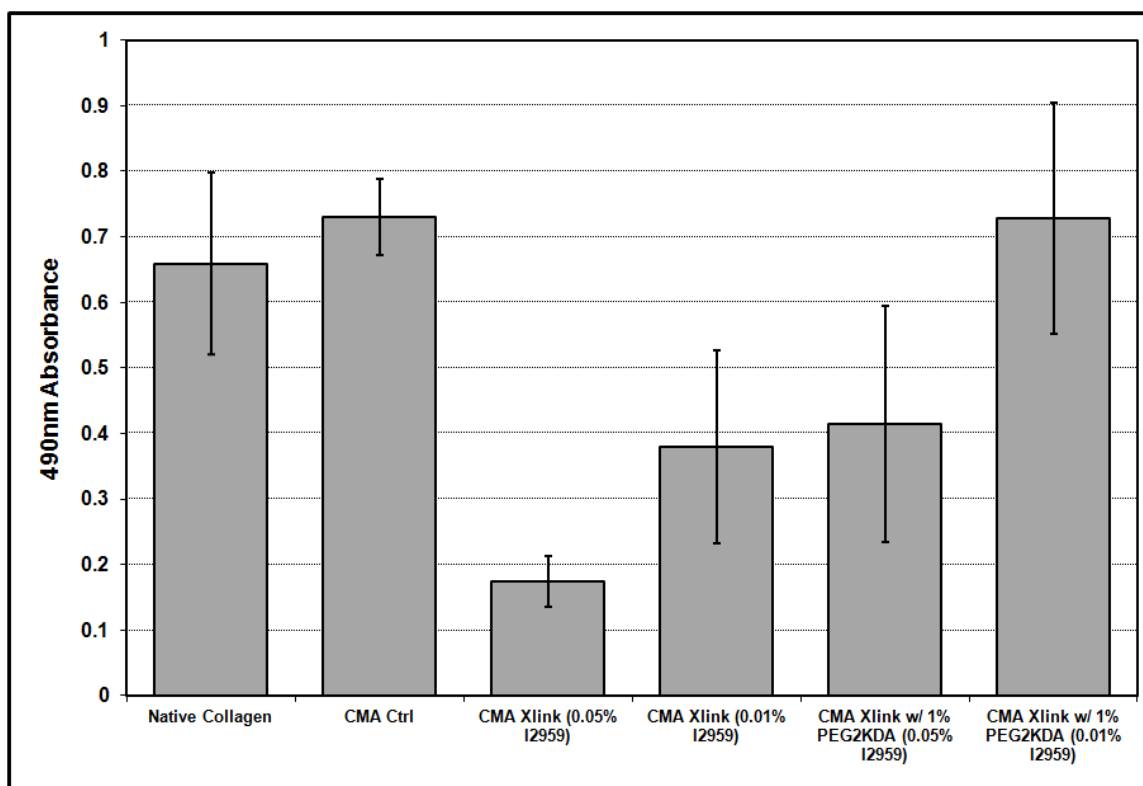


Figure 5A-7: MTS Viability Assay: High Cell Density L2.3 Glial Progenitor Neurospheres 72 H after UV-Irgacure 2959 Crosslinking \pm PEG2KDA

This experiment was repeated with a lower concentration of L2.3 cells (300K/mL). In this instance, cell number appeared to have a drastic effect on L2.3 viability following photocrosslinking. Native collagen and CMA (Figure 8 A & B) were compared to CMA gels were photocrosslinked with 0.1%, 0.05%, and 0.01% I2959 without (Figure 5A8 C-E) and with 1% PEG2KDA (Figure 5A8 F-H). The complete lack of calcein positive cells combined with extensive ethidium positive cells indicates that most L2.3 cells photocrosslinked with 0.1% or 0.05% I2959 were nonviable at the time of assay, and only a small percentage of cells with 0.01% I2959 survived. Additionally, PEG2KDA was only able to provide a marginal effect towards rescuing photoinitiator toxicity in the lowest Irgacure group of 0.01%. MTS data also indicates that there was very little difference in cell viability of L2.3 in all photocrosslinked conditions except for 0.01% I2959 with 1% PEGDA (Figure 5A9).

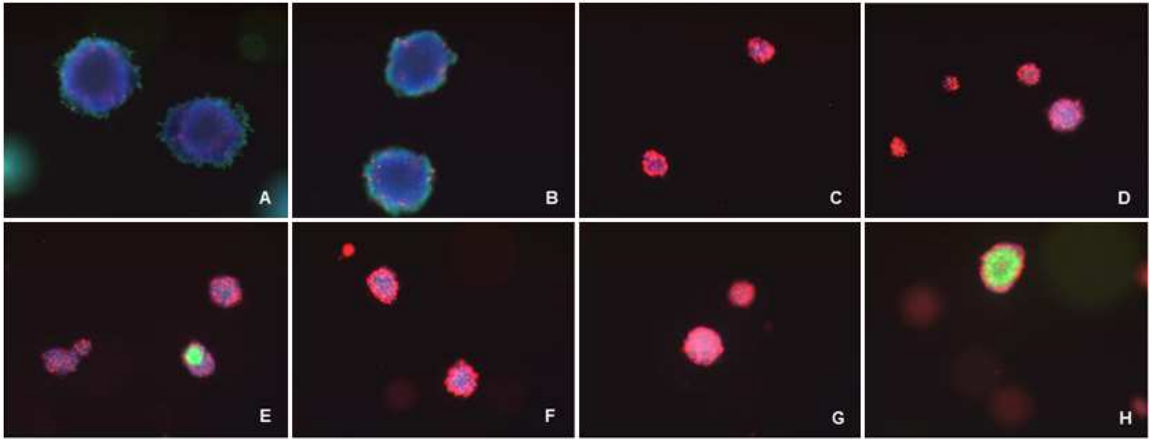


Figure 5A-8: Live/Dead Staining 48 H after I2959 Photocrosslinking of L2.3 Glial Progenitor Neurospheres in 3D Gels.
A: Native Collagen, B: CMA, C: CMA + 0.1% I2959, D: CMA + 0.05% I2959, E: CMA + 0.01% I2959, F: CMA + 0.1% I2959 + 1% PEG2KDA, G: CMA + 0.05% I2959 + 1% PEG2KDA, H: CMA + 0.01% I2959 + 1% PEG2KDA

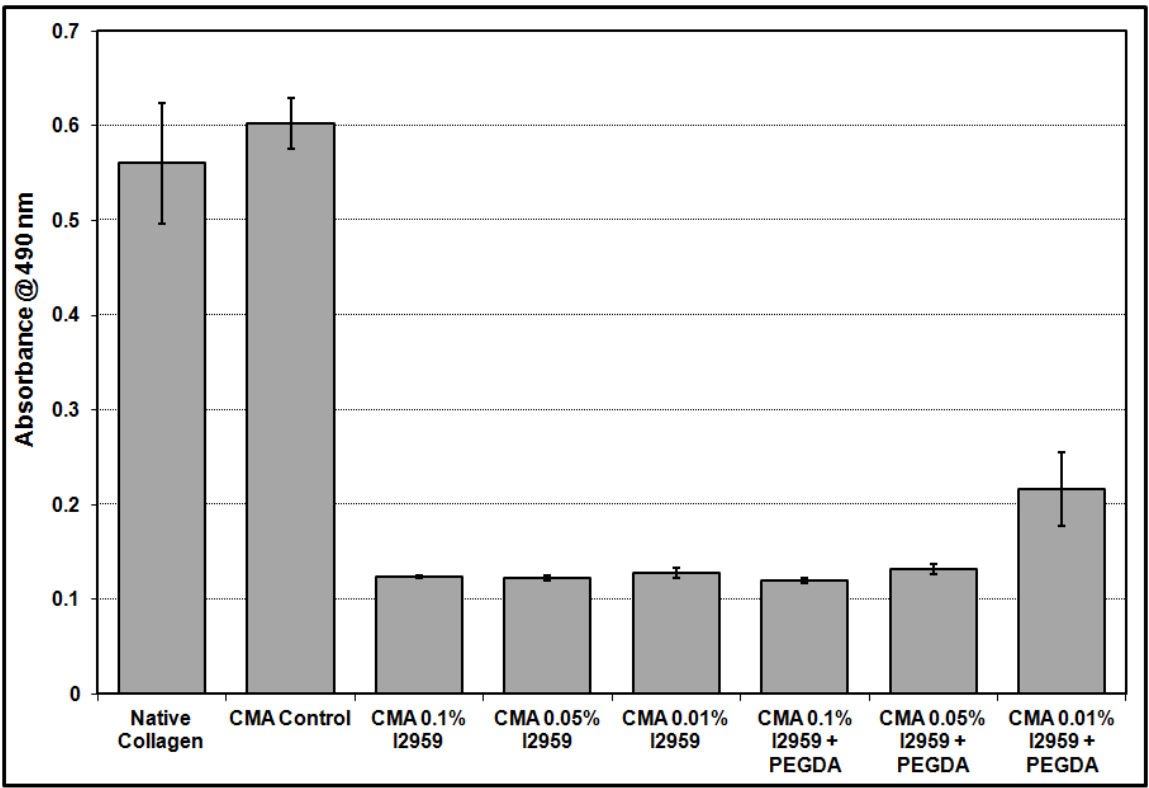


Figure 5A-9: MTS Viability Assay: Low Cell Density L2.3 Glial Progenitor Neurospheres 72 H after UV-Irgacure 2959 Crosslinking ± PEG2KDA

Human embryonic stem cell derived neural stem cells (RG-8) were also tested for compatibility with Irgacure photocrosslinking. Initial screening was performed with RG8 cells plated on TCP to determine the effect of I2959 concentration. Figure 5A10 A shows RG8 with no I2959 compared to decreasing I2959 concentrations (0.1%, 0.08%, 0.05%, 0.04%, 0.02%), where there seemed to be a dose-dependent increase in viability as per qualitative assessment (Figure 5A10 B-F). Even at the highest concentration of 0.1%, there were still some 'live' cells, although the ratio of ethidium positive cells to calcein positive cells implies that most of the RG8 cells were killed at that dose. Viability increased steadily as I2959 concentration decreased, with a strong drop-off in viability observed between 0.04% and 0.05% I2959. The lowest dose of 0.02% I2959 looked similar to controls in terms of staining and cell colony morphology. Indeed, MTS data (Figure 5A11) implies that I2959 concentrations of 0.04% and below had no measureable effect on MTS activity as compared to the control group, whereas 0.05%, 0.08%, and 0.1% caused a similar effect, apparently knocking down the metabolic activity in the RG-8 cells, although not completely ablating all activity as medium only controls were significantly lower than all cell groups.

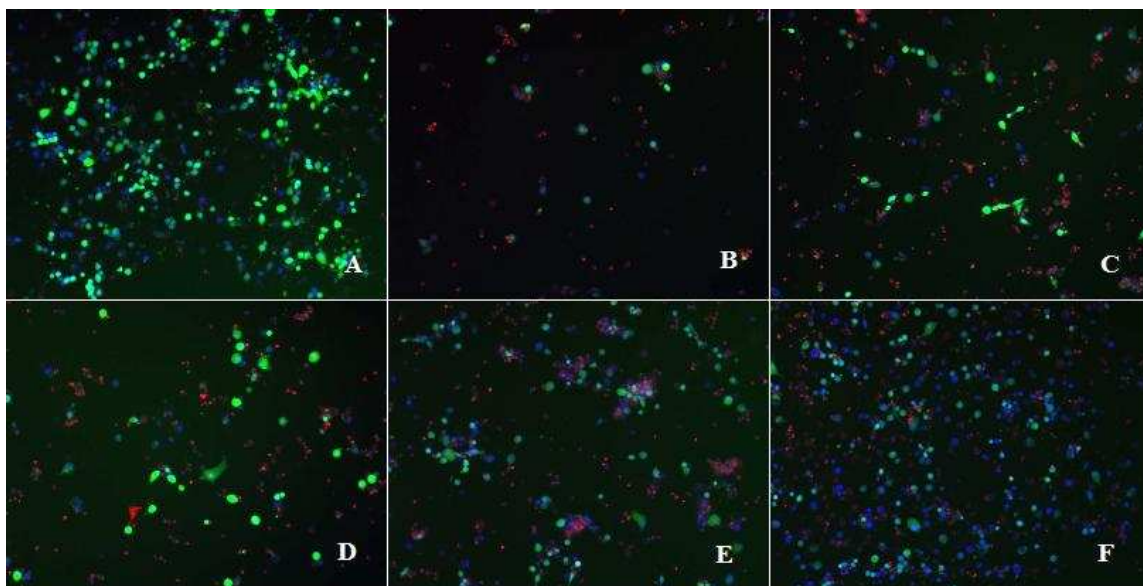


Figure 5A-10: I2959 Toxicity in hESC-derived NSC (RG8) 24 H after Photoinitiation with UV. A: Control B: 0.1% C: 0.08% D: 0.05% E: 0.04% F: 0.02%

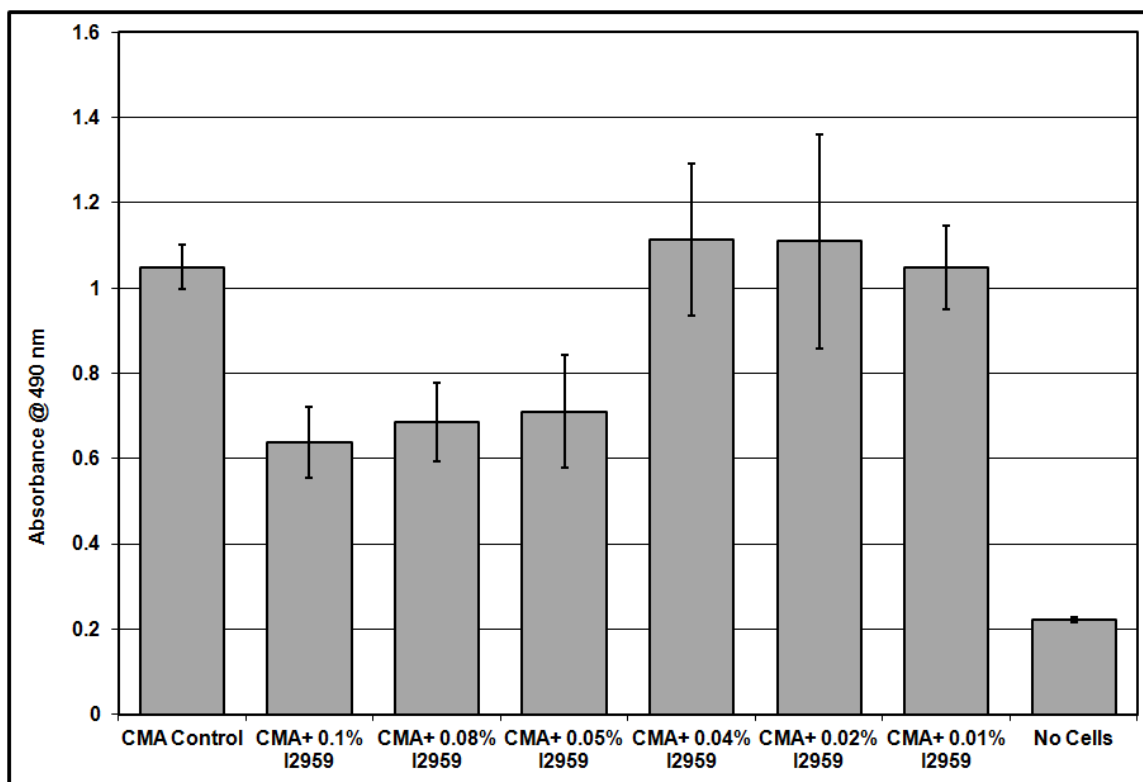


Figure 5A-11: MTS Viability Assay: I2959 Cytotoxicity in hESC-derived NSC (RG8) on TCP 24H after UV Exposure

RG-8 cells were then examined for suitability in photocrosslinked 3D CMA gels. RG8 cells were encapsulated in CMA gels at a density of 1×10^6 cells/mL then photocrosslinked with 0.1-0.01% I2959. After culture for 48 hours, RG8 were assayed for viability with Live/Dead staining and the MTS assay. Again, a decreasing dose of I2959 was accompanied by an increase in calcein positive cells, although qualitative assessment was more difficult in 3D culture (Figure 5A 12). Ethidium positive cells were seen at a higher incidence in all photocrosslinked groups compared to control. MTS data was conspicuously different, as all photocrosslinked groups produced only marginally more MTS signal than medium controls, although the 0.01% I2959 group was slightly higher than other Irgacure groups (Figure 5A 13). I2959 concentrations of 0.1-0.02% I2959 were equivalent.

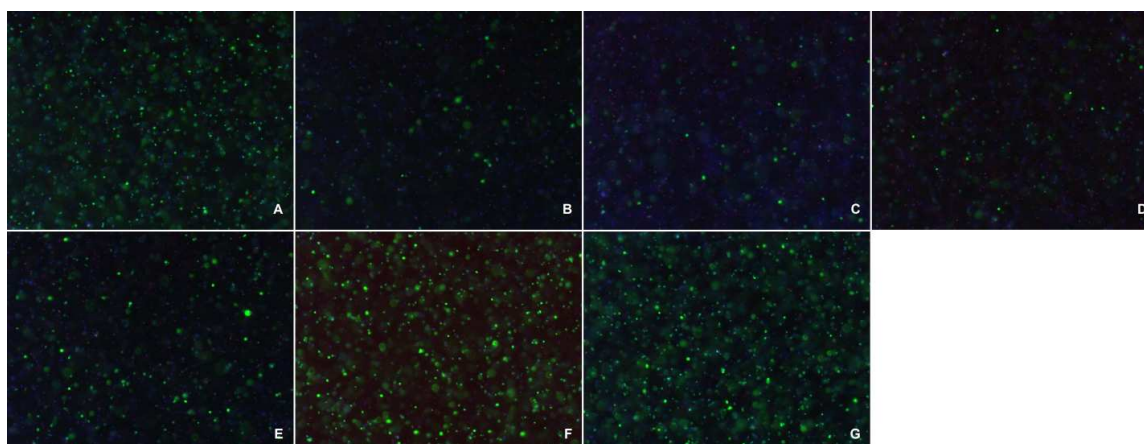


Figure 5A-12: Live/Dead Staining 48 H after UV-I2959 Photocrosslinking RG8 NSC in 3D CMA Gels. A: CMA Control B: CMA + 0.1% I2959, C: CMA + 0.08% I2959, D: CMA + 0.05% I2959, E: CMA + 0.04% I2959, F: CMA + 0.02% I2959, G: CMA + 0.01% I2959

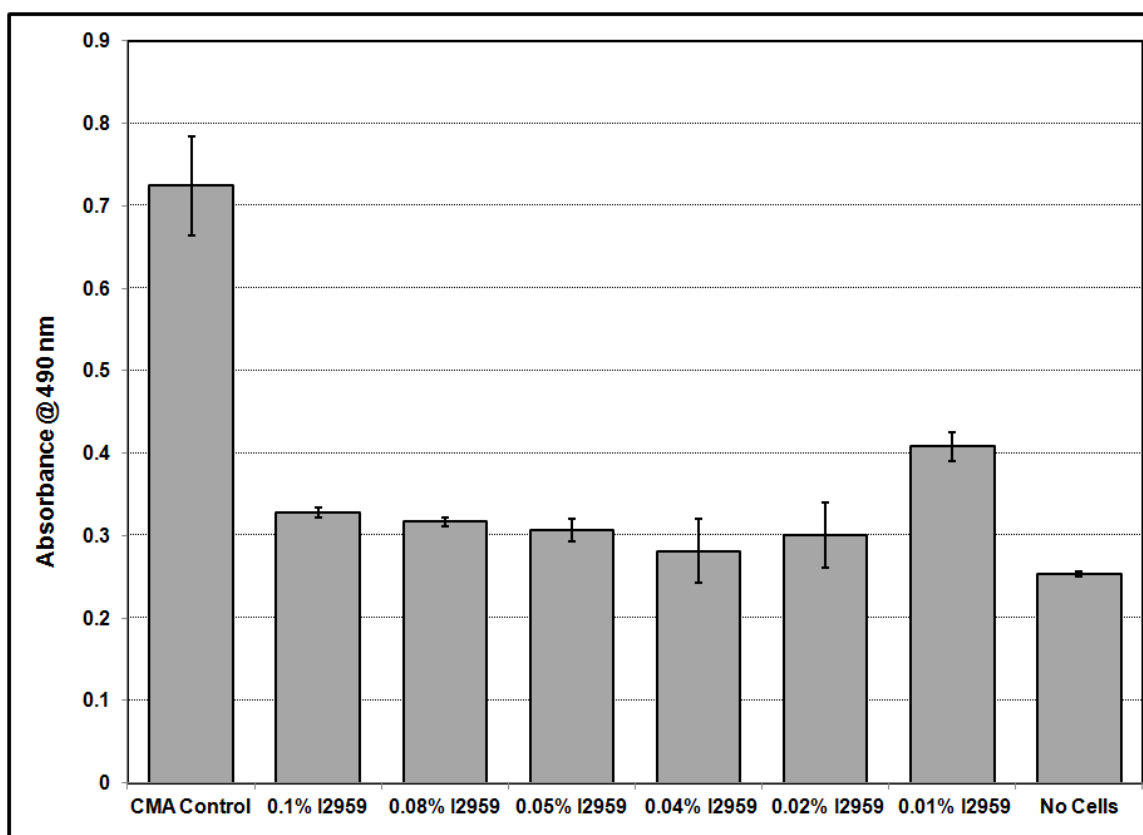


Figure 5A-13: MTS Viability Assay: I2959 Cytotoxicity in hESC-derived NSC (RG8) in CMA Gels 48 H after UV-I2959 Photocrosslinking

Yet another neural stem cell type, multipotential rat Cortex-8 NSCs (CTX8), was tested in 3D photocrosslinking conditions with various I2959 concentrations and 5 minutes of UV exposure. As evidenced by Figure 5A14 A, neurospheres dissociated into single cells were viable in CMA gels after 24 H in culture, as were cells with ethanol vehicle identical to I2959 conditions but without photoinitiator (Figure 5A14 B). However, all concentrations of Irgacure from 0.0125%-0.1% were highly toxic with complete ablation of viability observed after 24 H, indicating an extremely low tolerance to photocrosslinking with these cells in single cell suspension (Figure 5A14 C-F).

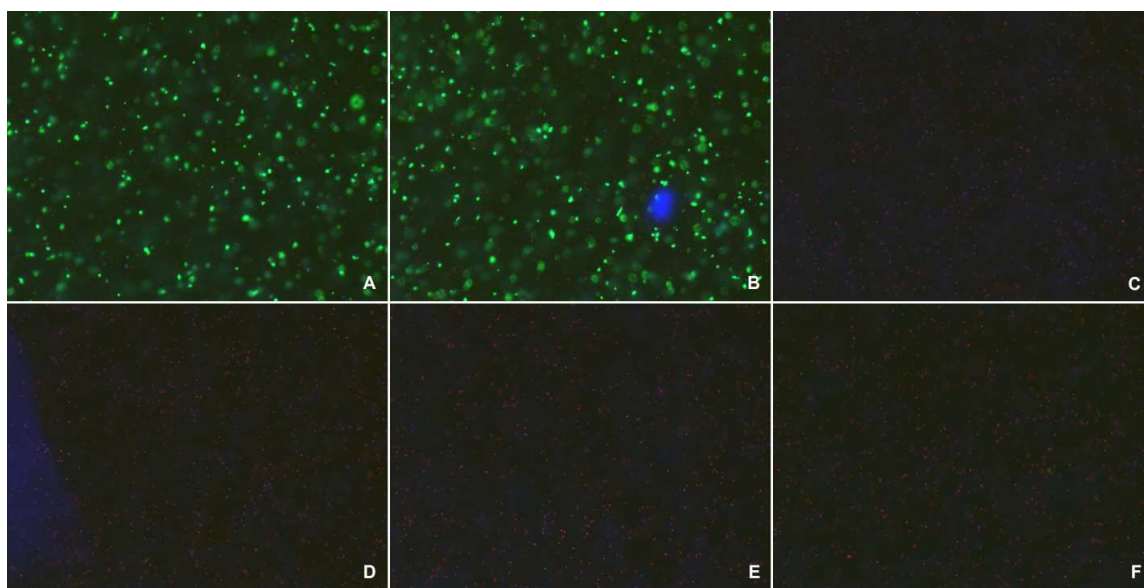


Figure 5A-14: Live/Dead Staining 24 H after UV-I2959 Photocrosslinking single cell CTX-8 in 3D CMA Gels. A: CMA Control B: CMA + Etoh Vehicle, C: CMA + 0.1% I2959, D: CMA + 0.05% I2959, E: CMA + 0.025% I2959, F: CMA + 0.0125% I2959

A separate experiment was performed to analyze whether CTX-8 cells, which are grown as neurospheres in suspension culture, would be able to withstand photoinitiation if encapsulated as intact neurospheres rather than dissociated into single cells. It was seen that even with moderate concentrations of I2959, the majority of cells in the neurosphere were non-viable as compared to control neurospheres, which appeared to be highly viable as per near-ubiquitous calcein staining (Figure 5A15 A). However, in larger neurospheres, there did appear to be a viable core at the center of the neurosphere, possibly due to shielding of cells by the shell of cells surrounding it (Figure 5A15 B & C).

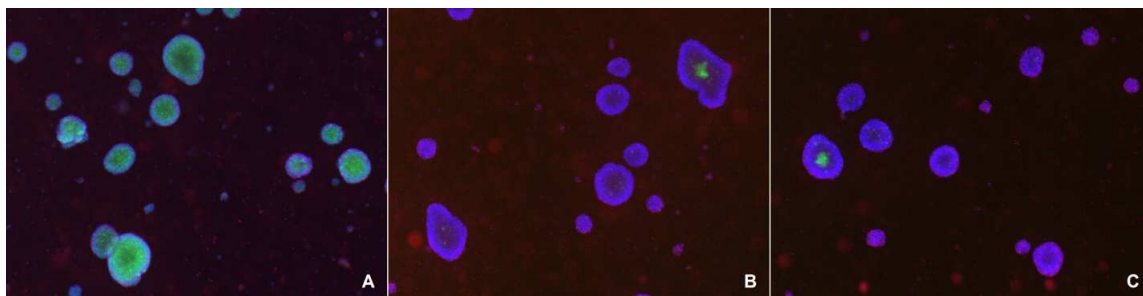


Figure 5A-15: Live/Dead Staining 24 H after UV-I2959 Photocrosslinking neurosphere CTX-8 in 3D CMA Gels. A: CMA Control B: CMA + 0.05% I2959, C: CMA + 0.025% I2959

Thus, optimization of photocrosslinking in 3D CMA gels with encapsulated hMSC was focused upon. Previous tests with hSMC in 2D indicated significant viability at mechanically active I2959 concentrations of 0.025-0.05%. However, these data were obtained using a confluent monolayer of cells. To analyze compatibility at lower cell densities in 3D CMA gels, we again varied the I2959 concentration from 0.02-0.1% and used Live/Dead staining and MTS to assay for viability after 48 H in culture. As Figure 5A16 implies, hMSC compatibility with I2959 photocrosslinking in 3D CMA gels was similar to results seen with hMSC in 2D on TCP, although more toxicity was observed in this situation overall. Again, a concentration of 0.04% I2959 seemed to represent a cutoff point for significant viability, above which the majority of cells were non-viable. Furthermore, 0.02% appeared to impart only minimal loss of viability.

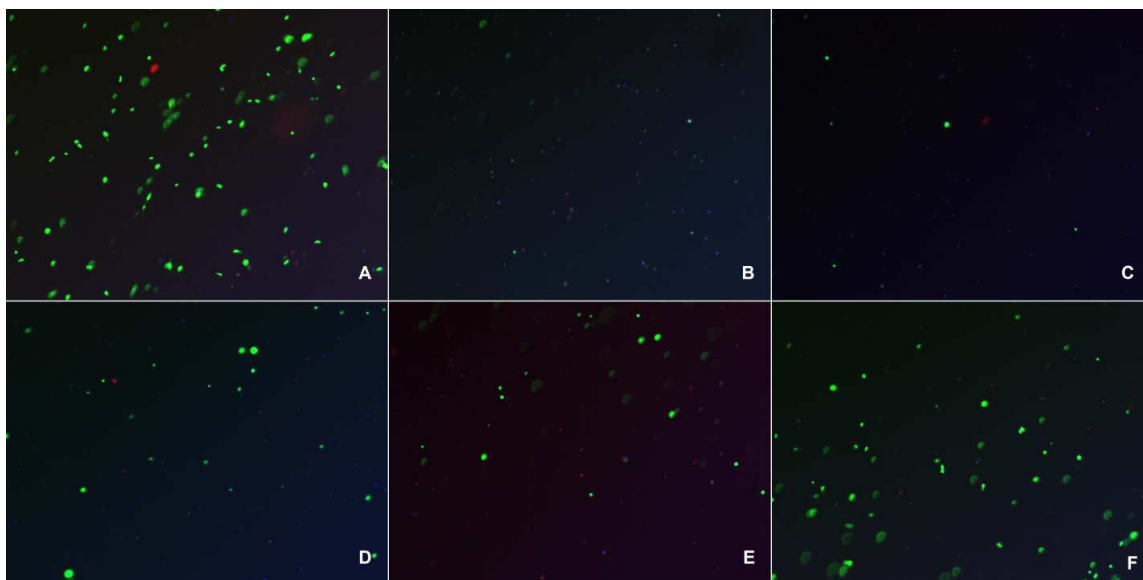


Figure 5A-16: hMSC in 3D CMA Gels 48 H after Photocrosslinking with UV-I2959. A: Control, B: CMA + 0.1% I2959, C: CMA + 0.08% I2959, D: CMA + 0.06% I2959, E: CMA + 0.04% I2959, F: CMA + 0.02% I2959

MTS viability data corroborated these results, as seen in Figure 5A17, where statistical analysis via ANOVA with Tukey's HSD test post hoc implied that at 0.02% I2959, viability ($84 \pm 7\%$) was not significantly different than control cells in CMA without I2959 or UV light ($100 \pm 11\%$), although it did appear that there was some detrimental effect. Higher concentrations of I2959 did have significant negative impact on viability, with I2959 at 0.1%, 0.08%, 0.06%, and 0.04% resulted in $-3 \pm 1\%$, $1 \pm 2\%$, $20 \pm 10\%$, and $61 \pm 12\%$ viable cells, respectively.

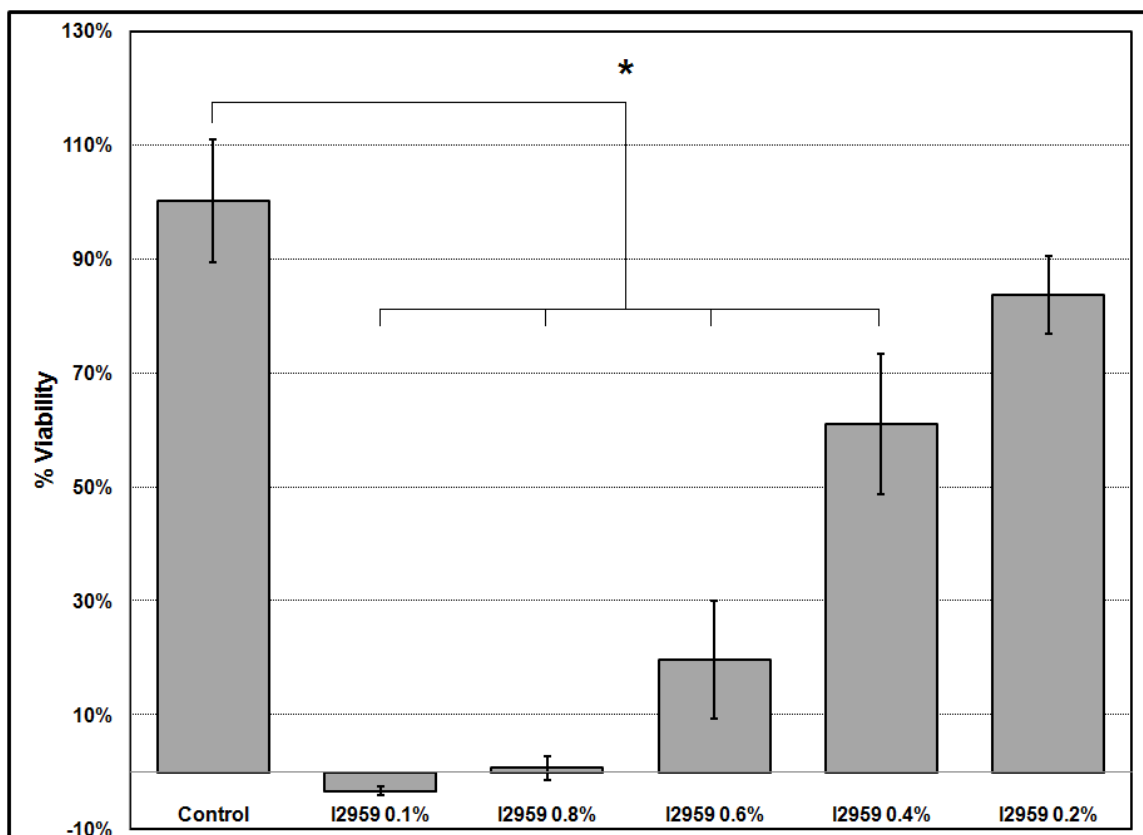


Figure 5A-17: MTS Viability Assay: hMSC in 3D CMA Gels 48 H after Photocrosslinking with UV-I2959. $p < 0.01$.

Further optimization of the photocrosslinking process resulted in a transition from ethanol to methanol as the solvent for stock I2959 solutions, as comparison of dose-response curves of ethanol and methanol implied that methanol had a less severe toxic effect at equivalent ethanol concentrations, and that at the 1% concentration there was no measureable cytotoxic effect (data not shown). Testing with hMSC at 1×10^6 cells/mL in native collagen, photoinitiated with 0.025-0.1% I2959, implied that 5 minutes of UV alone, 1% methanol vehicle, and 1% PEG2KDA had no negative effects on hMSC viability as seen with Live/Dead staining (Figure 5A18 A-D). Again, viability was drastically lower with 0.1% I2959, somewhat lower at 0.05%, and negligible at 0.025% (Figure 5A18 E-G). Additionally, inclusion of 1% PEG2KDA resulted in rescue of a measureable fraction of cells (Figure 5-18 H). Figure 5-18 I-L highlights cellular morphology at

20X magnification of Control, 0.1% I2959, 0.05% I2959, and 0.1% I2959 with 1% PEG2KDA. Notably, addition of PEG2KDA does not appear to significantly affect cell morphology compared to control cells, while noticeably reducing the number of ethidium positive cells.

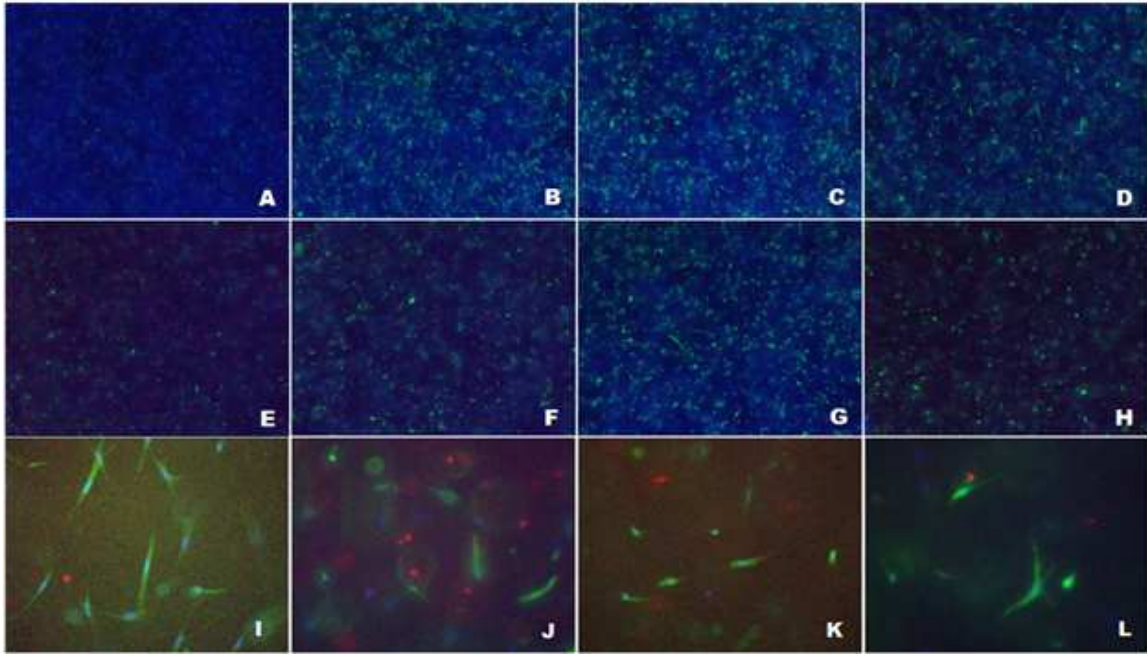


Figure 5A-18: hMSC in Native Collagen Gels 48 H after Photocrosslinking with UV-I2959. A: Control, B: UV only, C: UV + 1% MeOH, D: 1% PEG2KDA, E: 0.1% I2959, F: 0.05% I2959, G: 0.025% I2959, H: 0.1% I2959 + 1% PEG2KDA, I: 20x Control, J: 20x 0.1% I2959, K: 20x 0.05% I2959, L: 20x 0.1% I2959 + 1%PEG2KDA

Quantification of hMSC viability with the MTS assay in a parallel experiment displayed similar trends to the Live/Dead staining (Figure 5A19). MTS viability for hMSC in native collagen, native collagen with UV alone, native collagen with 1% methanol, and native collagen with 1% PEG2KDA were all comparable with no significant reduction in viability compared to control ($100\pm6\%$, $105\pm5\%$, $104\pm3\%$, $92\pm2\%$, respectively). Inclusion of photocrosslinking with 0.1% I2959, 0.05% I2959, 0.025% I2959, and 0.1% I2959 with 1% PEG2KDA resulted in viability of $32\pm4\%$, $71\pm4\%$, $95\pm8\%$, and $78\pm2\%$, respectively.

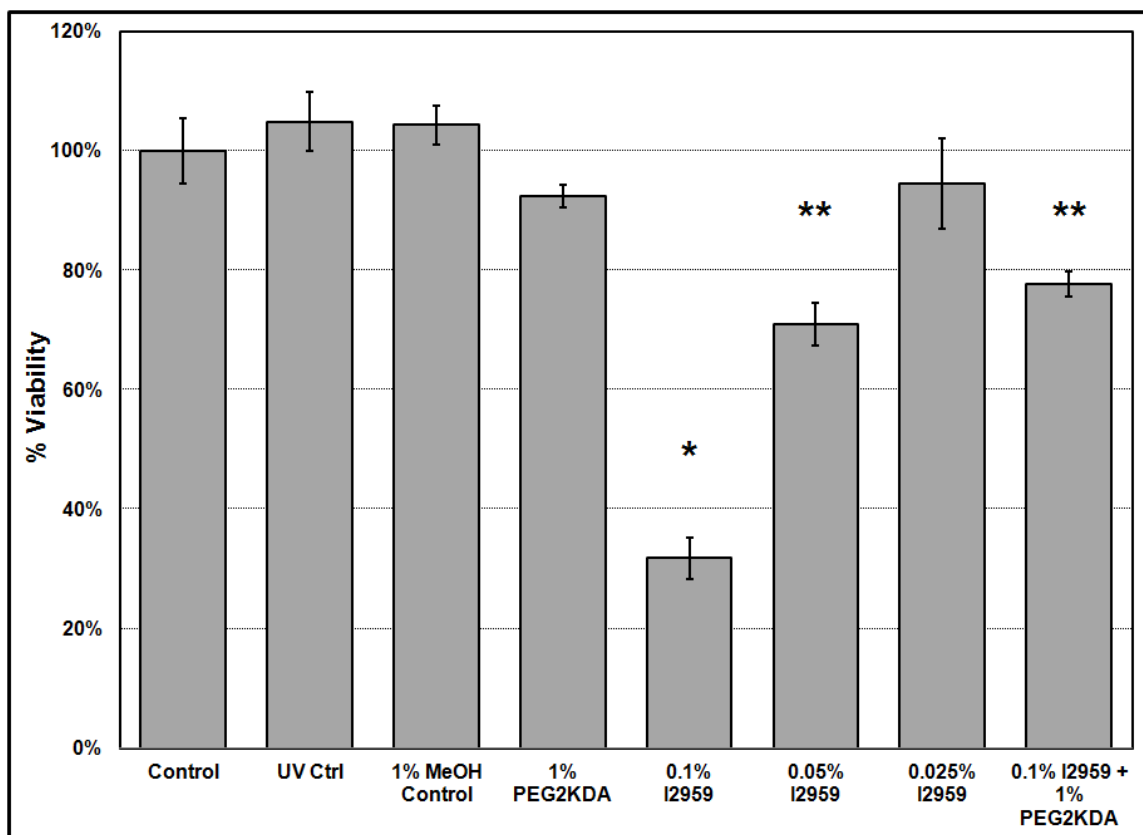


Figure 5A-19: MTS Viability Assay. hMSC in Native Collagen 48 H after Photocrosslinking with UV-I2959. $p < 0.01$.

5B Appendix: Optimization of Photocrosslinking Differentiated iPS-NSC in 3D CMA Gels

Initial screening of photocrosslinking compatibility indicated that iPS-NSC, even at high density (7.5×10^6 cells/mL) in proliferation medium were not able to survive the standard photocrosslinking in CMA (3mg/mL) with 0.025% I2959 and 90 seconds UV exposure, as indicated by the near complete lack of calcein positive staining in the photocrosslinked condition (Figure 5B1 B). Due to the requisite high areal cell density required for healthy cell culture in 2D, proportionally high density was also necessary in 3D culture. However, iPS-NSC appeared to favor cell-cell adhesion over adhesion to CMA, as seen by clustering of cells 72 hours after encapsulation in CMA gels (Figure 5B1 A).

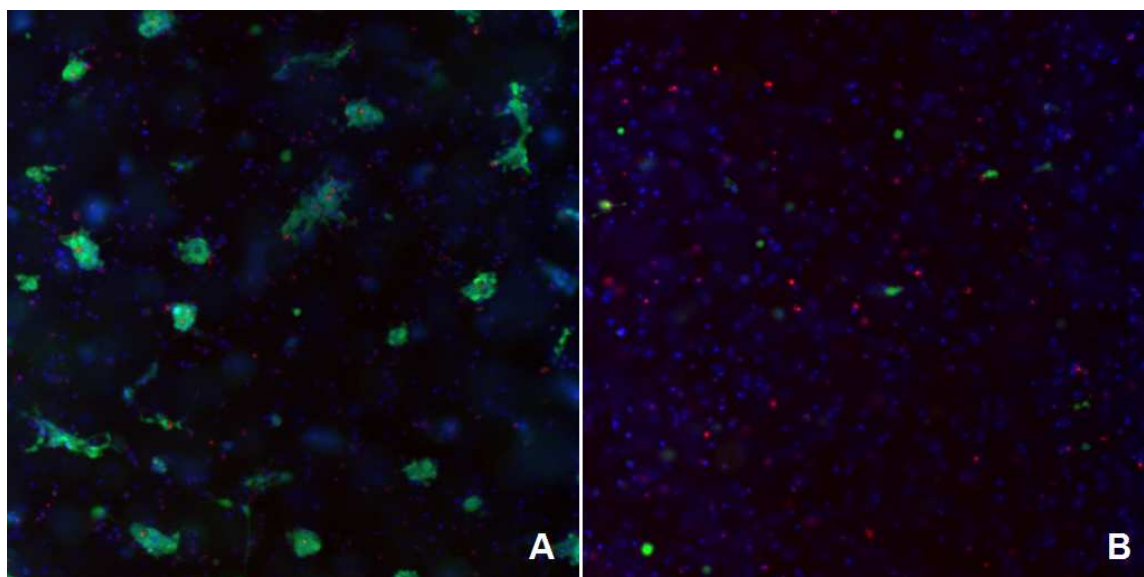


Figure 5B-1: Proliferating iPS-NSC in CMA (A) and Photocrosslinked CMA after 24 H

Previous experience with photocrosslinking CMA with various cell types as well as results published by others [102] suggested that among other factors, the proliferation rate of cells is inversely proportional to post-photocrosslinking viability, as free radicals have a more detrimental effect on actively dividing cells [120]. Additionally, as one goal of this project was to modulate neural differentiation within 3D hydrogels, we decided to induce differentiation of iPS-NSC prior to encapsulation, which would significantly reduce the average proliferation rate as cells transitioned away from the highly proliferative growth phase to a differentiated lineage. Initially, cells were induced to differentiation via withdrawal of bFGF for 24 hours, replated on PDL/Laminin-coated TCP, and medium switched to NDM for 7 days. Differentiated cells were then harvested and encapsulated in native collagen and CMA at a density of 1.8×10^6 cells/mL, and again a subset of CMA gels were subjected to standard crosslinking conditions. After 7 days, cells were assayed for viability with Live/Dead staining. As seen in Figure 5B2 A & B, overall viability of cells is quite low, evidenced by the large number of ethidium-positive dead cells as well as marginal cells that stained for neither ethidium or calcein. However, the few surviving

cells appear to display a neuronal morphology in both native collagen and CMA, indicating that at least some cells are able to adhere to the matrix and extend neurites. However, the photocrosslinked cells, while showing similar viability, did not form or extend processes to any considerable extent.

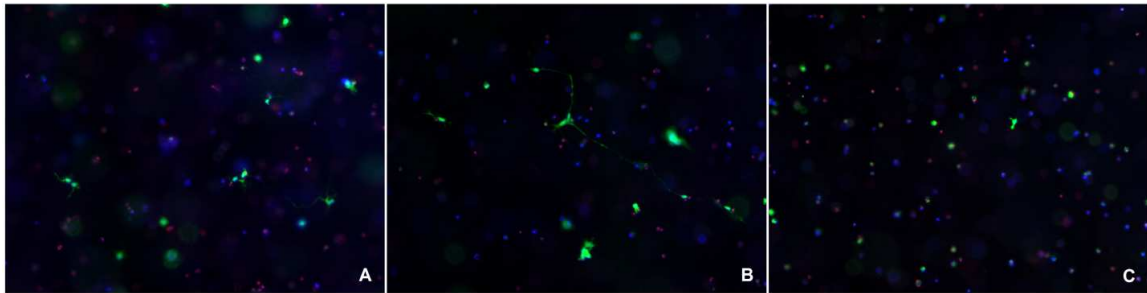


Figure 5B-2: 7 day-differentiated iPS-NSC in native collagen (A), CMA (B), and photocrosslinked CMA (C) after 7 days in culture. Images taken at 10X

To investigate the temporal development of the loss of viability in CMA compared to photocrosslinked CMA, iPS-NSC were encapsulated, this time at 1.4×10^6 cells/mL, exposed to photocrosslinking, and Live/Dead staining was used to analyze cell viability at 1, 3, and 7 days after encapsulation/photocrosslinking. Here, at 24 H after encapsulation/crosslinking, the viability is only slightly lower in the photocrosslinked condition compared to CMA controls. At 72 H, while CMA control cells are still largely viable, the majority of cells in the crosslinking condition appear dead. By 7 days, CMA control cells appeared less viable than at 72 H, whereas in photocrosslinked CMA the viability appears unchanged, indicating that the cells that survived to 72 H remained viable thereafter (Figure 5B3).

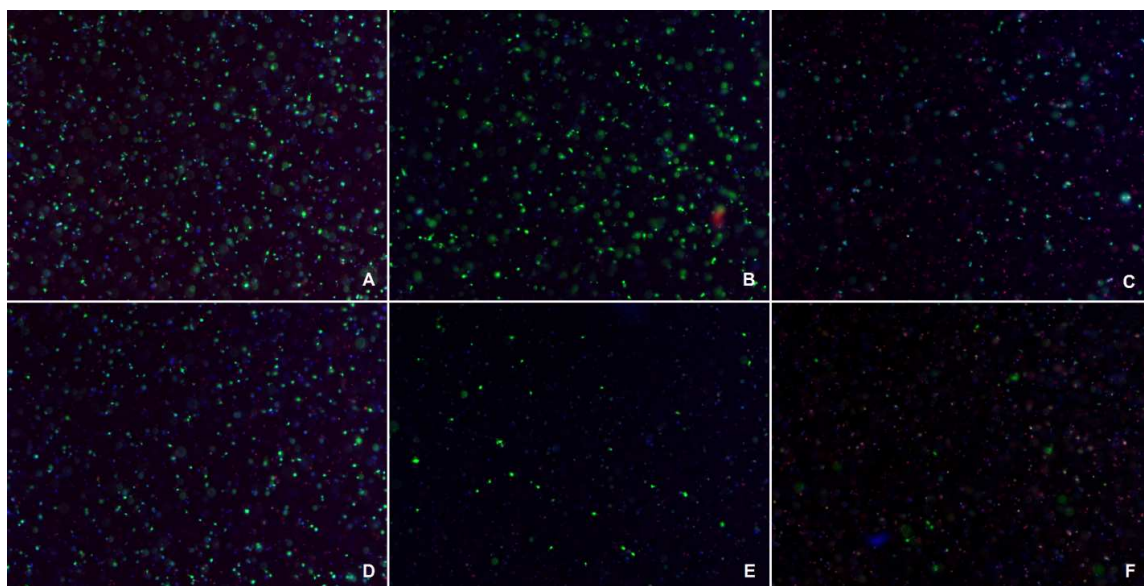


Figure 5B-3: 7 day-differentiated iPS-NSC in CMA after 1 (A), 3 (B), and 7 (C) days and photocrosslinked CMA at 1 (D), 3 (E), and 7 (F) days in culture

Although iPS-NSC undergoing differentiation inherently have a significant spontaneous cell death rate even in standard culture conditions, the unusually large number of cells in the CMA control condition that failed to thrive after 72 H indicated an apoptotic mechanism distinct from free radical generation. One possibility is that poor adhesion to the matrix may have contributed to increased apoptosis, and thus by improving cellular adhesion we could increase viability. As laminin is a required component for 2D culture of iPS-NSC (either as a major component of Matrigel or adsorbed onto TCP with PDL), we hypothesized that inclusion of laminin with the CMA might allow more uniform adhesion to the scaffold. As laminin contains a collagen binding domain, we postulated that labile laminin would associate with CMA and provide additional binding sites for the iPS-NSC. Again, iPS-NSC (2×10^6 cells/mL) were encapsulated and photocrosslinked, and medium with 1, 5 and 10 $\mu\text{g/mL}$ was added to gels once daily for 72 H, after which Live/Dead staining was used to assay viability. However, as seen in Figure 5B4, inclusion of laminin did not seem to affect cell viability or morphology in CMA \pm crosslinking.

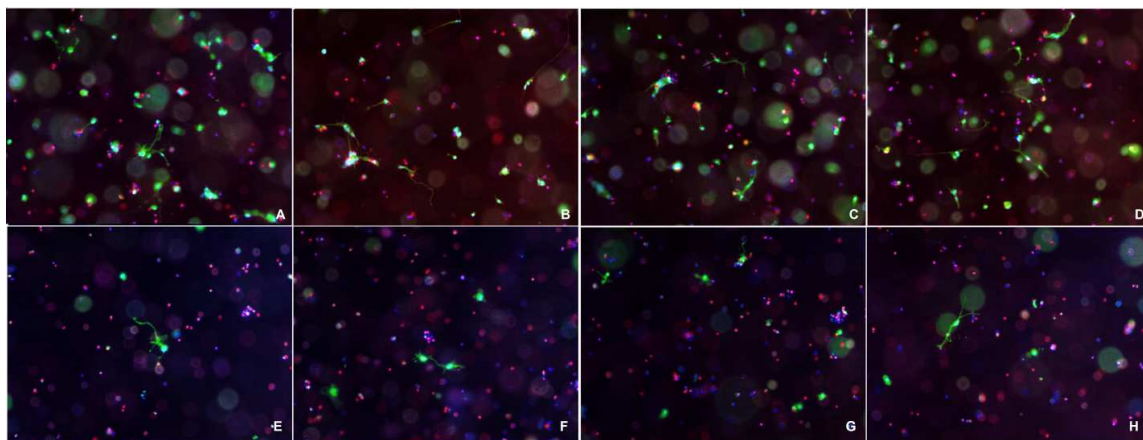


Figure 5B-4: iPS-NSC in CMA (A-D) and Photocrosslinked CMA (E-H) with 0 (A,E), 1 (B,F), 5 (C,G) and 10 (D,H) ug/mL Laminin

Another process change included addition of the rho-associated protein kinase (ROCK) inhibitor Y-27632, which has been implicated in preserving viability of hESC cells during processing [121,122] as well as promoting cellular regeneration in injured axons [123]. In particular, Y-27632 appears to protect stem cells from dissociation induced apoptosis, a possible mechanism behind the loss of viability we have observed in transitioning cells into 3D culture where cell-cell contact at similar levels to 2D culture is constrained by requiring extremely high cell densities. Y-27632 was included in the medium of iPS-NSC following encapsulation in CMA at 10 μ M, and after 72 hours a noticeable difference was observed in neurite outgrowth in the condition containing the inhibitor (Figure 5B5). Hereafter, Y-27632 was included in culture medium added to all encapsulated cells due to its beneficial effect.

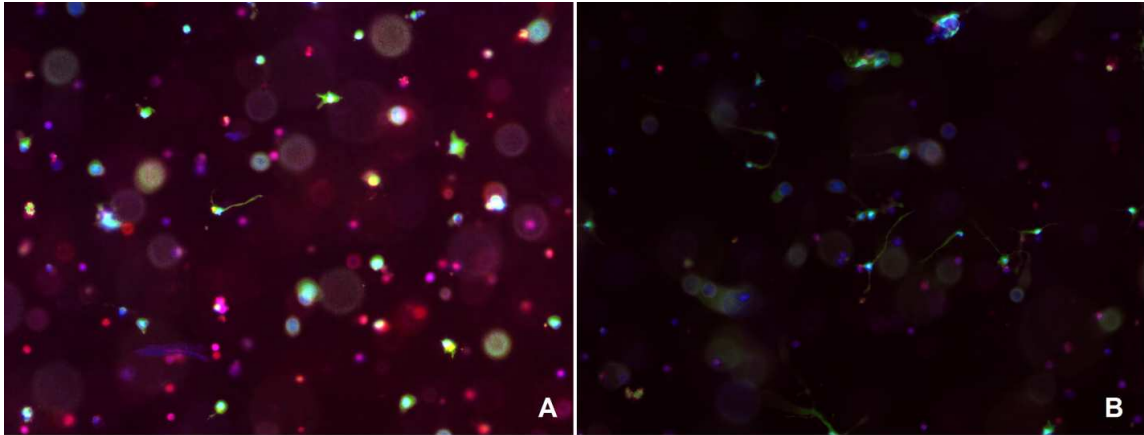


Figure 5B-5: CMA with encapsulated pre-differentiated iPS-NSC after 72 H in NDM (A) and NDM + Y-27632 (B)

While initiating differentiation of cells prior to encapsulation/crosslinking indicated that substantially more cells were able to survive the free radicals compared to proliferating cells, a major difficulty with this method was harvesting differentiating cells from PDL/Laminin coated TCP. Differentiating cell adhesion to this substrate was such that even with prolonged enzymatic treatment and manually imparted shear, a large number of cells remained bound to the flasks. Indeed, combinations of Accutase, 0.25% trypsin/EDTA, TrypLE Select (Life Technologies), and Dispase were all tested, and only trypsin or TrypLE Select (which contains trypsin) were able to remove a usable quantity of cells, and even so, close to 10 minutes of enzyme exposure combined with physically hitting flasks was required to detach cells. Not only did a large number of cells remain adhered, but the harsh treatment required to detach the others caused concern that we were inducing shear-mediated cell death, especially for differentiated cells with long, fragile processes. Instead, future differentiation was conducted on $\frac{1}{4}$ Matrigel coated flasks, which while producing slightly lower differentiation as per cell morphology analysis, and allowed a more cell-friendly Accutase-based detachment that required far less shear and yielded substantially more cells. This optimized protocol allowed evaluation of CMA modulation in the

presence of cells, including mechanical and biochemical modification via photocrosslinking. As discussed previously in Section 3.5, low concentrations of peptide had negligible effects on cellular behavior, and higher concentrations of peptide were employed to determine if previous experiments were performed with too little ligand to have a biological effect.

However, additional characterization was necessary to investigate the effects of higher concentrations of peptide on photocrosslinking kinetics and mechanics. UV rheometry was performed with similar parameters to cellular peptide photografting experiments, minus cells, to investigate the effect on storage modulus from both the DMSO needed to dissolve the peptide as well as the peptide itself. Interestingly, while there was no difference between the photocrosslinked storage modulus of the DMSO control and the peptide condition, both displayed a higher G' than the control CMA (Figure 5B6). Additionally, the DMSO self assembly was delayed compared to the peptide condition, which was delayed compared to control CMA, indicating that 1% DMSO retards self-assembly, while the presence of 0.1mg/mL peptide returns self assembly time closer to the control baseline. In any case, the UV exposure time appeared to be insufficient at 150s to completely equilibrate the photocrosslinking, as storage modulus was still increasing at 150s and didn't reach steady state until approximately 180s.

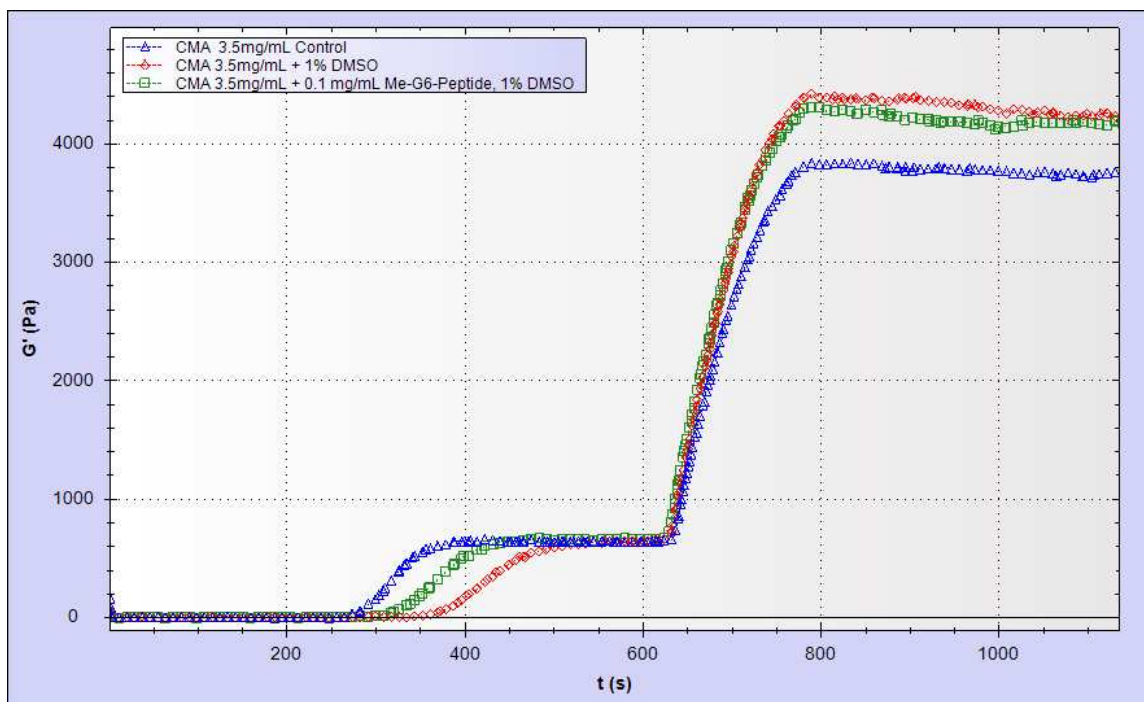


Figure 5B-6: Real-time UV rheology of CMA Control, CMA with 1% DMSO, and CMA with 0.1mg/mL Methacrylated-G6- Peptide and 1% DMSO

Given the lack of any measurable efficacy of peptide at 0.1mg/mL, increasing the concentration significantly was investigated. First, we set out to evaluate the limitations were for getting a maximal amount of soluble peptide into the CMA gels. One obvious issue was the effect of increased volumes of DMSO required to get the peptide into the macromer solution. Given the delay in self assembly seen from 1% DMSO, we looked at the effect of 2, 3, 5 and 10% DMSO on CMA self assembly kinetics. Interestingly, DMSO concentration appears to have a bimodal effect on self assembly kinetics, with gelation time increasing with addition of 1, 2, and 3% DMSO, then decreasing from 5 to 10%, where gelation time was slightly lower than control CMA. Gelation times (time at G'/G'' crossover) are plotted in Figure 5B7.

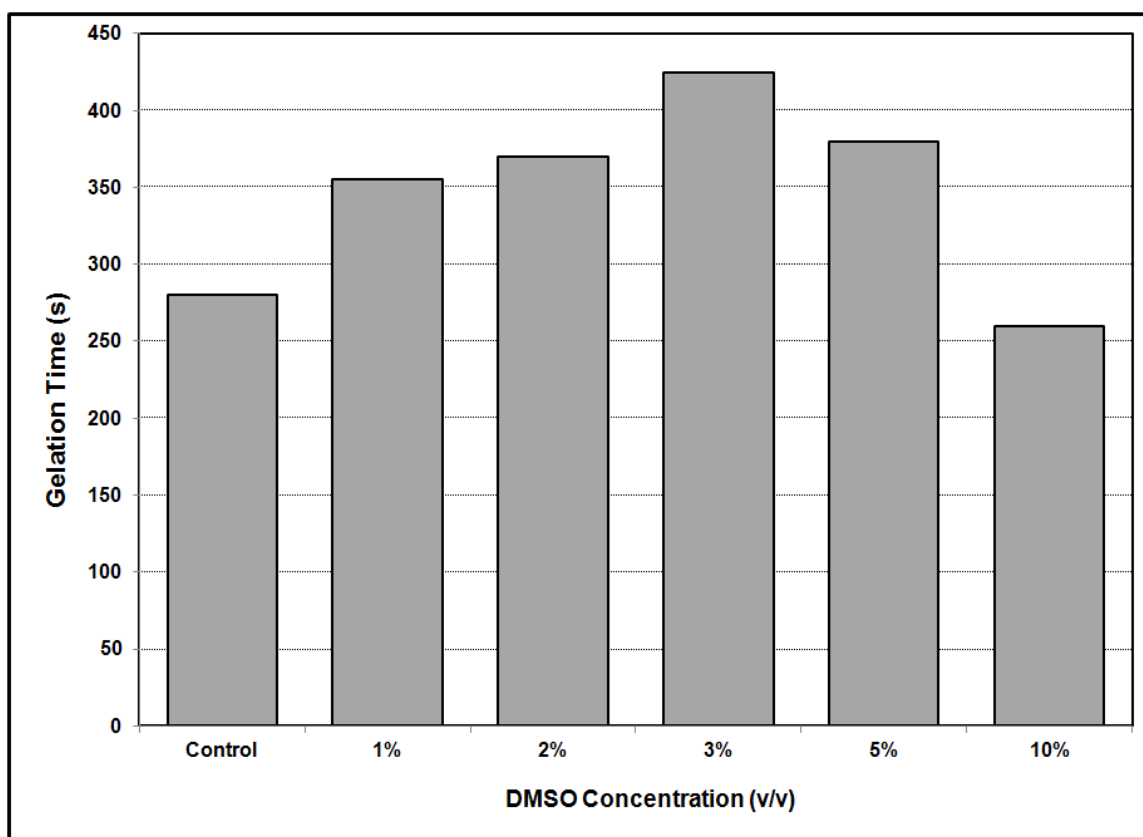


Figure 5B-7: Effect of DMSO Concentration on Gelation Time of CMA

Additionally, we wanted to characterize whether photocrosslinking occurred in the presence of cells, as the high cell density likely blocks some UV light and may potentially affect local I2959 concentration, given that cytotoxicity is derived from photoinitiator interacting with cells rather than CMA groups. To test this, CMA suspensions with methacrylate-G6-peptide and 2% DMSO, with and without iPS-NSC at 1×10^7 cells/mL, were loaded onto the UV rheometer setup and storage modulus was recorded during self assembly and photocrosslinking. Figure 5B8 suggests that while a reduction in the increase in steady state photocrosslinked storage modulus is observed when cells are present, overall, the self-assembly kinetics, self-assembled storage modulus, and the rate of photocrosslinking is unchanged. Thus, we conclude that high density

cell encapsulation is not contradictory to effective photocrosslinking, although some efficiency is lost.

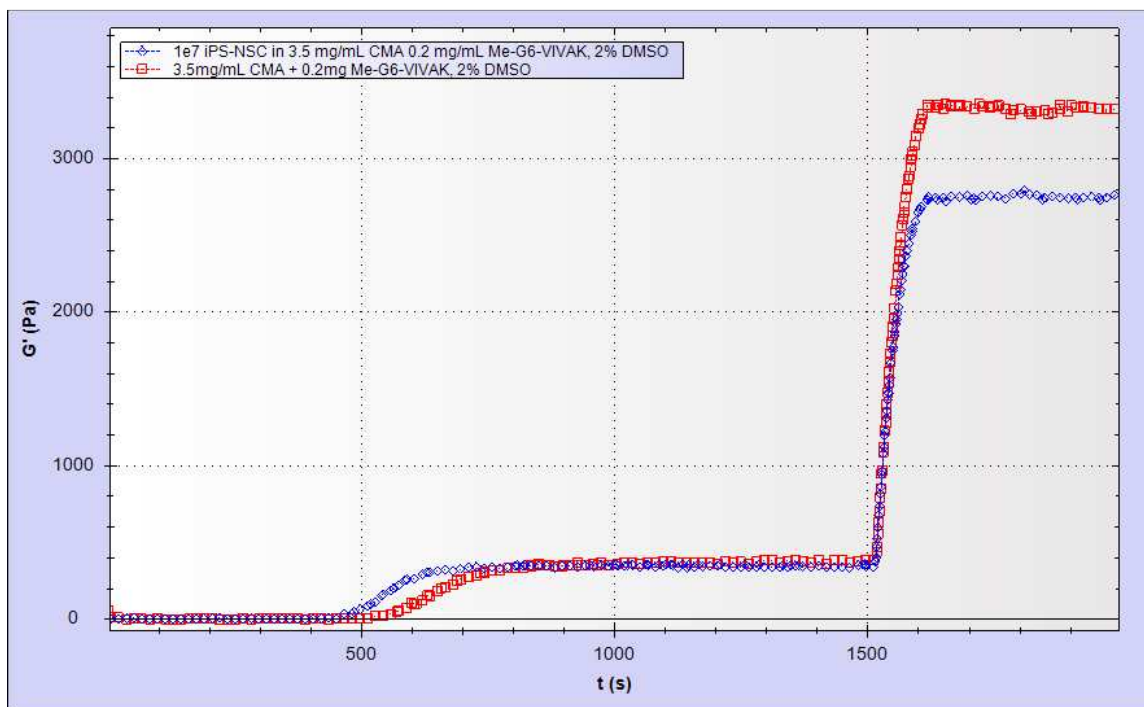


Figure 5B-8: UV photocrosslinking of CMA with and without $1e7$ cells/mL with Me-G6-Peptide an 2% DMSO

Given that even 10% DMSO did not prevent self assembly of CMA, we next asked what the effect on differentiating iPS-NSC viability would be on transient exposure to 10% DMSO. CMA gels with (1×10^7 cells/mL) differentiating iPS-NSC were encapsulated in 3.5 mg/mL CMA, gelled for 15 minutes, and photocrosslinked with 0.025% I2959 and 2 minutes UV exposure. Samples were then washed 2X with PBS and then 2X with NDM (5' each wash) and cultured for 72 H. Total time in 10% DMSO was approximately 35 minutes. Conventional wisdom being that DMSO is toxic to cells at 10%, we expected that the uncrosslinked cells would be less viable in the DMSO condition, and the photocrosslinked cells would likely be further injured by the DMSO along with free radical exposure. Surprisingly, not only did we not see a reduction in viability in

either uncrosslinked or photocrosslinked CMA, but the DMSO conditions appeared to have increased neurite outgrowth in both conditions compared to control gels, particularly in the photocrosslinked condition (Figure 5B9).

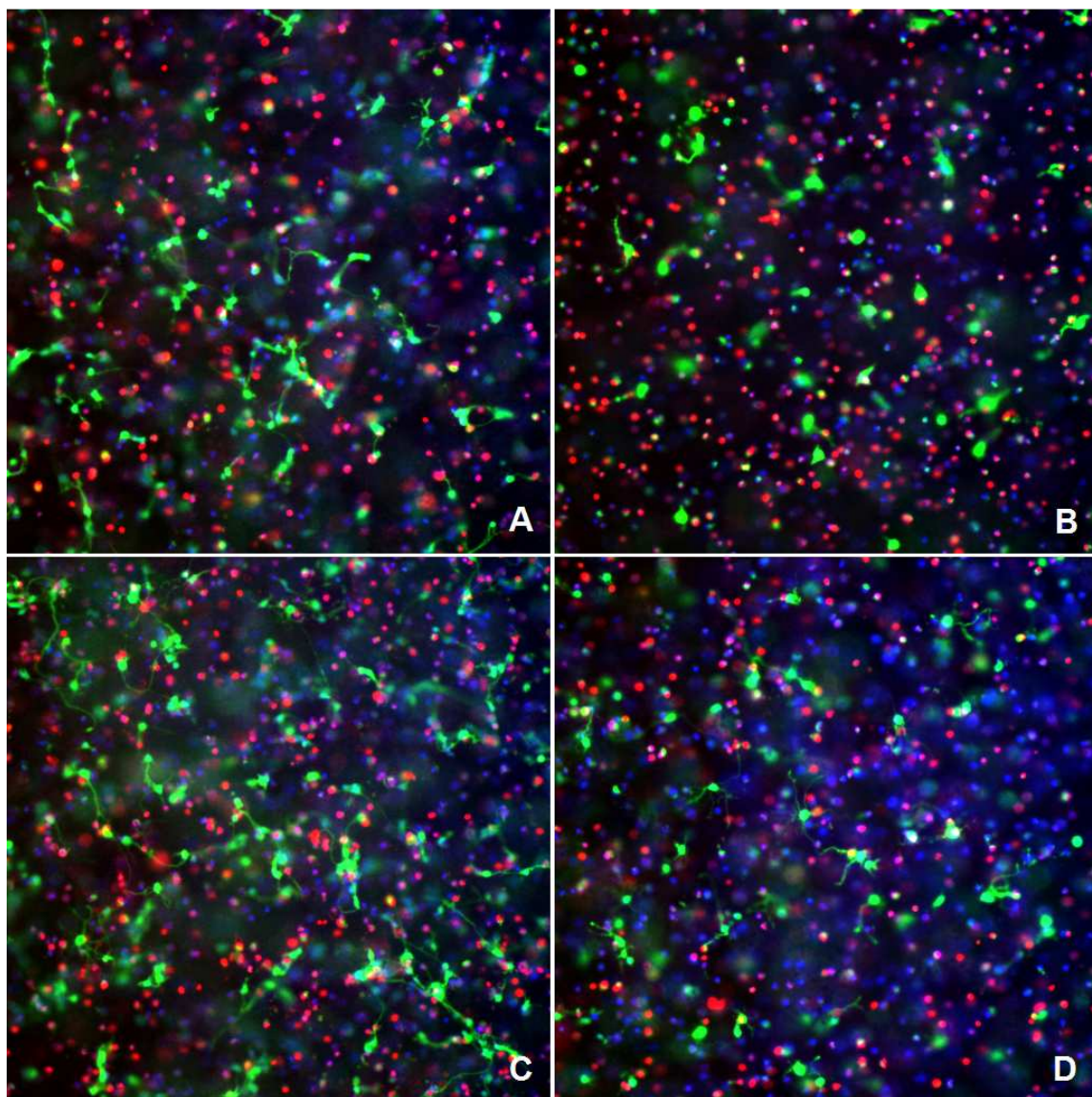


Figure 5B-9: Pre-differentiated iPS-NSC in CMA (A,B) and CMA + 10% DMSO (C,D). A & C are uncrosslinked, B & D are Photocrosslinked with 0.025% I2959 and 2 min UV.

6. Chapter 6: Computer Modeling of CMA Molecular Structure

6.1 Introduction: Collagen Structure Characterization and Modeling

Collagen structure has been extensively studied and characterized for many decades, with data obtained using X-ray diffraction techniques published as early as the 1930's [124]. Ramachandran and Kartha first described the collagen triple helix in 1954 [125], a model that was further developed by Rich and Crick [126], and is being subsequently improved as our understanding of its complex molecular structure improves. In the last few decades, our structurofunctional knowledge of fibrillar type-I collagen, the most abundant protein in mammals, has increased immensely. Through peptide sequencing, researchers have determined the complete amino acid sequences of the individual type I collagen α -chains for numerous species. These display strikingly similar sequence homology [127-131], which is presumed to be an important factor in the use of xenogeneic type I collagen as a tissue engineering scaffold in the clinic [132-134]. X-ray crystallography, NMR, and scanning and transmission electron microscopy have provided insight into the left-handed polyproline-II-like conformation [135] as well as triple helical tropocollagen structures formed by association of the α -chains, and has helped to elucidate the resultant quaternary structures formed by the association of triple helices into fibrils [136-139]. These fibrils have a characteristic D-periodicity of 670 Å caused by electrostatic and hydrophobic interactions of axially staggered residues, which serve to facilitate fibrillogenesis as well as stabilize the resultant fibrils [140,141].

Fibrillogenesis of type I collagen has also been extensively studied, resulting in an increased understanding of the role of tropocollagen structure in fibril formation dynamics and kinetics. *In vivo*, collagen fibril formation begins with the secretion of procollagen, which comprises a linear triple helical region, ~1000 residues long, bounded by non-helical C and N-terminal propeptides

[142]. Following cleavage of propeptides by appropriate C and N-proteinases, the triple helical tropocollagen macromer spontaneously self assembles into fibrils, which can grow to reach 1 cm in length and 500nm in diameter[143]. Although evidence suggests that the cleaved propeptides may affect the kinetics of fibrillogenesis [144,145], they are not necessary for the *in vitro* self-assembly of tropocollagen [146], which is an entropy-driven process governed by tropocollagen interaction with surrounding solvent [147,148]. Additionally, the effects of temperature, osmolarity, and buffer pH have been well characterized regarding their effects on fibril size and formation rates [149-151]. More recently, advanced imaging techniques have been successful in analyzing fibrillogenesis in real time [152].

However, despite intensive efforts towards understanding the relationships between collagen sequence, structure, and fibrillogenesis, significant controversy still remains regarding molecular mechanisms underlying the thermal instability and dynamics involved in collagen folding and unfolding [153-155,75]. Furthermore, the role of individual amino acid residues on overall fibril structure and stability is even less well understood given the astronomical number of possible sequences. The large size, heterogeneity, and insolubility of native collagen, in addition to its complex quaternary structure, have impeded molecular-scale investigation of the sequence-structure relationship through conventional biochemical analytical methods. A common strategy that has been adopted to circumvent the problems associated with the complexity of native collagen has been to study short, triple helical peptide sequences with similar sequence characteristics, typically based on the Gly-X-Y motif that typifies triple helical formation in type I collagen [156,157]. Using synthetic, triple helical collagen analogs with defined sequences, a number of fundamental questions have been addressed by taking advantage of the increased compatibility of these molecules with contemporary analysis methods [158]. In particular, the

role of specific amino acids on triple helix stability and fibrillogenesis dynamics has been examined using collagen mimetic peptides [159-161].

Recently, advances in computational physical chemistry technology have resulted in development of molecular models of collagen-like peptides. Additionally, a combination of experimental peptide synthesis with molecular modeling *in silico* has resulted in a powerful platform for investigating the molecular mechanisms involved in self-assembly, by allowing analysis of tertiary structure dimensions and energy states within peptides with respect to specific amino acid sequences [162]. Of particular interest is the effect of charged amino acid side-chain interactions on triple helix assembly and stability, which have been shown to contribute significantly to the thermodynamic processes governing fibrillogenesis [163]. Recently, Nanda and colleagues have developed a computational analysis paradigm utilizing explicit positive and negative design to study specificity and stability in collagen-mimetic peptide self-assembly, which aided in and rational design of novel triple helical peptides [65]. Complementary thermodynamic and structural characterization of synthetic heterotrimeric collagen mimics via CD and NMR revealed that electrostatic interactions involving lysine residues are particularly important contributors to peptide stability and molecular structure[164]. Indeed, previous studies by Persikov et al., indicated that salt-bridge formation involving lysine residues may be critical to collagen stability [165].

The role of lysine in triple helix structure and fibrillogenesis thermodynamics is especially relevant to CMA characterization, as our derivatization methodology is based on the conversion of the free amines to photosensitive methacrylamide groups. Previously discussed data indicate that a large proportion of the available amines are derivatized in our current CMA synthesis protocol. However, the differences in molecular structure and stability resulting from the

replacement of amines with methacrylates are poorly understood, and may have substantial biointerfacial implications that affect the efficacy of CMA as a dynamic tissue scaffold. During our extensive characterization of CMA, we observed a number intriguing mechanical and thermodynamic behaviors distinct from native collagen, including altered self-assembly kinetics, reduced shear moduli of CMA hydrogels, significantly different melting temperature of CMA macromers, and reversal of fibrillogenesis upon cooling. Despite a plethora of material characterization modalities, the fundamental molecular differences between native collagen and CMA responsible for these phenomena are not well understood and are difficult to resolve using conventional biochemical analytical techniques. However, simplified models of truncated collagen sequences may allow molecular scale examination of the effects of lysine-methacrylate substitution. Here, we used a modified algorithm based on the Nanda model to screen bovine type I collagen native sequences to identify segments with exceptional electrostatic interactions. We then employed a molecular dynamics simulation of all-atom model based on these sequences to examine the differences in molecular structure arising from varying degrees of methacrylamide substitution. We discuss the implications of these models towards understanding CMA structure and explaining the unique properties of CMA. Additionally, we address these results in the context of photocrosslinking, based on the simulated orientation of methacrylate moieties and how that may affect mechanical and biochemical modification.

6.2 Methods

6.2.1 Sequence-based Model

Full length sequences of native bovine type I collagen were pulled from the protein database (PDB) for $\alpha 1$ (UniProtKB/Swiss-Prot: P02453.3) and $\alpha 2$ (UniProtKB/Swiss-Prot: P02465.2) chains. From these, the triple-helical region consisting of the Gly-X-Y repeat sequence of the $\alpha 1$ and $\alpha 2$

chains (residues 109-1123 & 33-1047, respectively) were input as parent A and B chains from which our model sequence would be derived. A Matlab algorithm was used to calculate the total energy based on the electrostatic interactions of nearby charged residues (K, R, D, E) within all possible trimers (AAA, AAB, ABA, ABB, BAA, BAB, BBA, and BBB) within the canonical axially-staggered arrangement of the triple helix. Windows of 50-200 residues were analyzed sequentially along the length of both full α -chains and used to create charge-charge interaction maps of all trimers to determine sequence loci with the largest electrostatic energy density. The algorithm was then used to substitute 0-100% of the lysine residues with a neutral amino acid methacrylamide analog, and the resultant energy differences were used to determine a model triple helix sequence optimized to the energy gap for further use in an all atom molecular dynamics simulation.

6.2.2 Structure-based Model

Following the analysis of charge-charge interactions from the sequence model, 153 residue segments were selected from type I collagen for all-atom modeling, starting at residue 466 on each α -chain. Sequences were as follows, with lysine residues underlined in bold:

A (α 1):

GLPGPAGPPGEAG**K**PGEQGVPGDLGAPGPSGARGERGFPGERGVQGPPGAPPRGANGAPGNDGA**K**GD
AGAPGAPGSQGAPGLQGMPGERGAAGLPGP**K**GDRGDAGP**K**GADGAPG**K**DGVRGLTGPIGPPGPAGAPG
D**K**GEAGPSGPAGPTGAR

B (α 2):

GLPGPAGTAGEAG**K**PGERGIPGEFGLPGPAGARGERGPPGESGAAGPTGPIGSRGPSGPPGPDGN**K**GEPGV
VGAPGTAGPSGSPGLPGERGAAGIPGG**K**GE**K**GETGLRGDIGSPGRDGARGAPGAIGAPGPAGANGDRGEA
GPAGPAGPAGPR

A hi-resolution crystal structure for a 9-repeat POG sequence was obtained from the PDB. Although this sequence formed the most idealized triple helix available in the PDB, there was still variation along the length. As such, a central residue sequence for each chain was selected and then spliced together to form 153-residue chains. The selected sequences from native collagen were then threaded on to these chains to form type I $\alpha 1$ and $\alpha 2$ chains, from which we could form homo- or heterotrimers. The rotamer positions of the side chains of threaded residues were optimized with ProtCad. The structure was then minimized and equilibrated in Amber, and a dynamic simulation was run for 100ns. Simulations were performed for AAA and AAB trimers, then run again with all lysine residues replaced with leucine to simulate methacrylate derivatized CMA where lysine amines have been replaced with an uncharged side-group. An additional sequence containing a methacrylamide group, rather than the leucine substitution, was also created, with which ongoing simulations are being performed.

6.3 Results

6.3.1 Sequence-based Charge-Charge Energy Characterization

Charge-charge energetic calculation data from the Matlab algorithm using 100% lysine substitution to maximize electrostatic differences revealed that removal of lysine-related salt bridges from the total charge energy landscape caused a significant deficit along nearly the entire windowed trimer. An optimal energy trough was observed using 150 residue windowing, which also corresponded to the upper end of the simulation parameter space due to computational resource constraints. Figure 6-1 displays the total charge-charge energy of full length triple helices for each possible trimer using the 150 residue window. Overall, the energy deficit was similar for all trimers, with the most substantial continuous energy gap occurring when the window function corresponded to a starting residue between positions 400-650 of the

full sequence. To span the energetic trough with the model sequence, we concluded that starting at residue 466 resulted in the optimal electrostatic energy gap when using a 150-residue sequence with mutated lysine groups. Of particular interest was the energy trough observed in the AAB heterotrimer, as this most closely approximates the trimeric arrangement observed naturally occurring in type-I collagen.

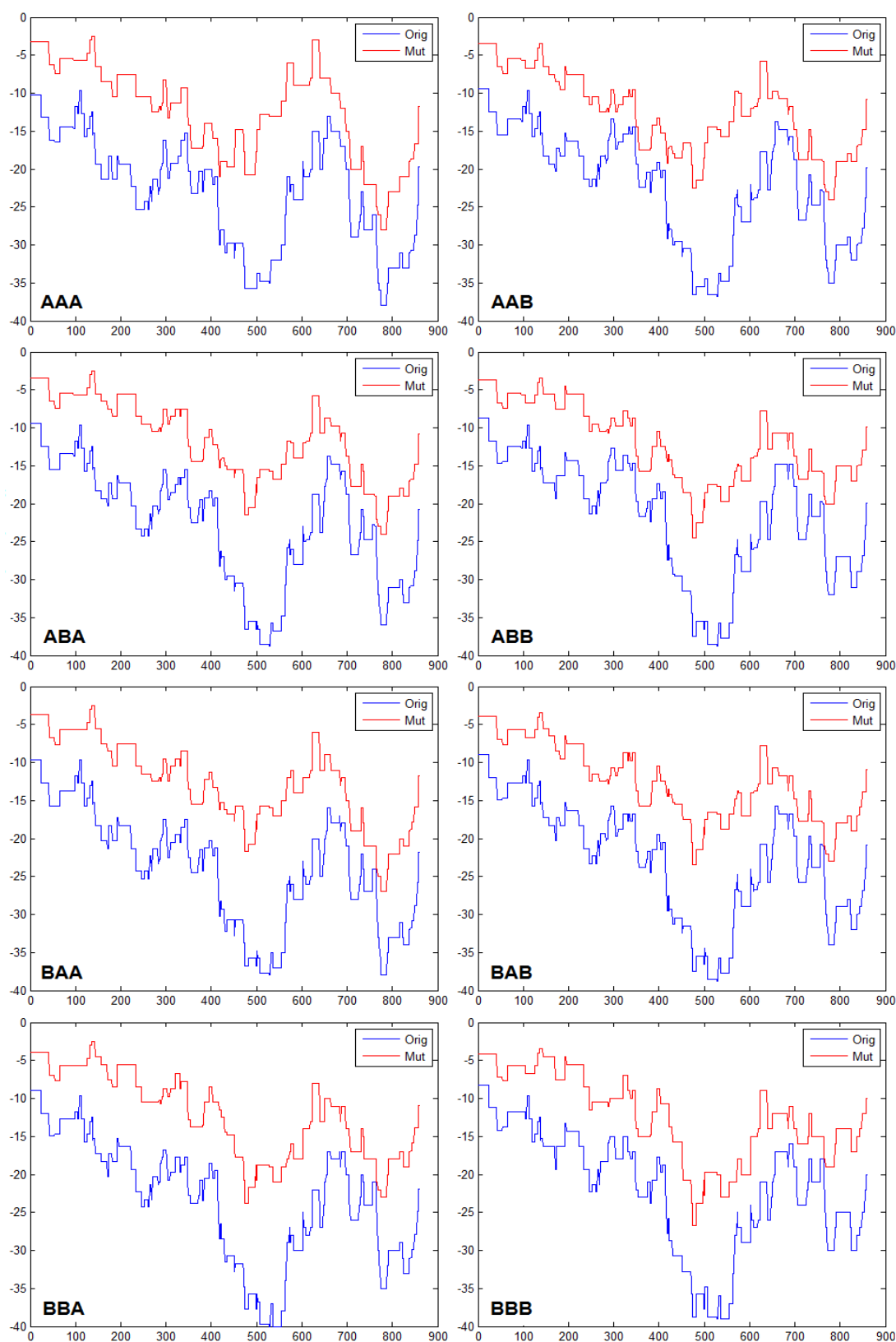


Figure 6-166: Charge-charge Energy in 153-residue Trimers, Windowed from Full-length $\alpha 1$ and $\alpha 2$ Chains. Y-axis is Charge Energy, X-axis is Starting Residue Position with respect to Full-length Sequence.

As such, further Matlab algorithm simulation of electrostatic energy was performed to analyze the energy gap between the wild-type AAB trimer and AAB with 25% of the lysine residues randomly targeted for substitution to model energy gap of CMA, where previous experimental data implied similar lysine modification. To account for error introduced by the random choosing of lysines to modify, the algorithm was repeated 50 times using the 150 residue window and the energy gap was averaged. As is evident in Figure 6-2, the energy trough is again maximized when starting residue occurred between between 400 and 650, indicating that our chosen model sequence also optimized salt-bridge energy differences with lysine derivatization efficiency similar to experimentally determined values with CMA, verifying that this model should provide relevant information.

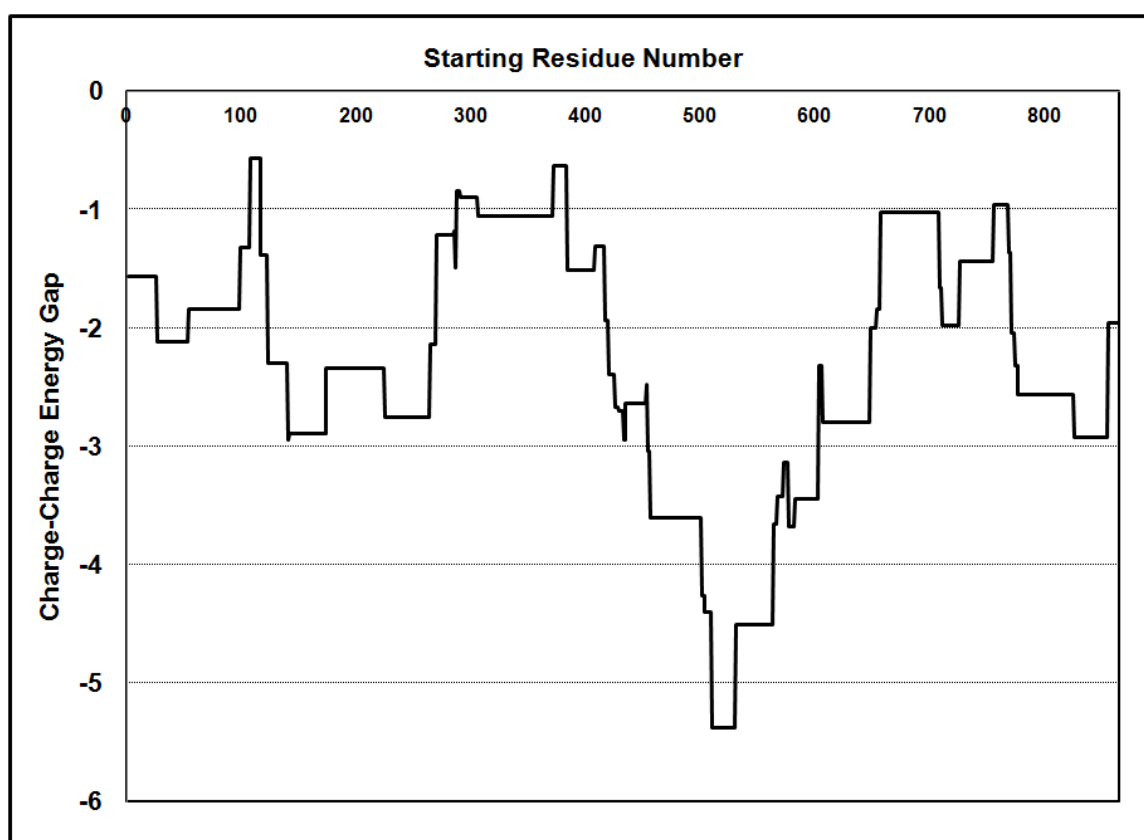


Figure 6-167: Energy Gap between Full Length Collagen AAB Heterotrimer and AAB with 25% Total Lysines Mutated to Leucines. Average of 50 Simulations Shown.

6.3.2 Structure-based Molecular Dynamics Modeling

Based on additional computational constraints concerning alignment of model triple helices, model sequence length was optimized to be 153 residues, which we culled from the full length sequences of type-I collagen α -chain residues. For the all-atom structures, triple helix models were created of the AAA homotrimer and the ABA and AAB heterotrimers, including a mutant of each whereby all lysine residues were substituted with the uncharged amino acid leucine, to allow investigation into molecular dynamics with the presence and absence of lysine-mediated salt bridges. Figure 6-3 summarizes staggered trimer sequence of AAA homotrimer and the AAB heterotrimer, with positively charged residues highlighted green and negatively charged residues highlights red. The naturally occurring placement of positively and negatively charged residues near each other results in a high probability of salt-bridge formation, which is clearly reduced in density following removal or lysine (blue boxes). However, arginine-mediated salt bridges, which are theoretically unaffected in our CMA synthesis reaction, are still able to form a significant number of salt bridges even in the absence of lysines.

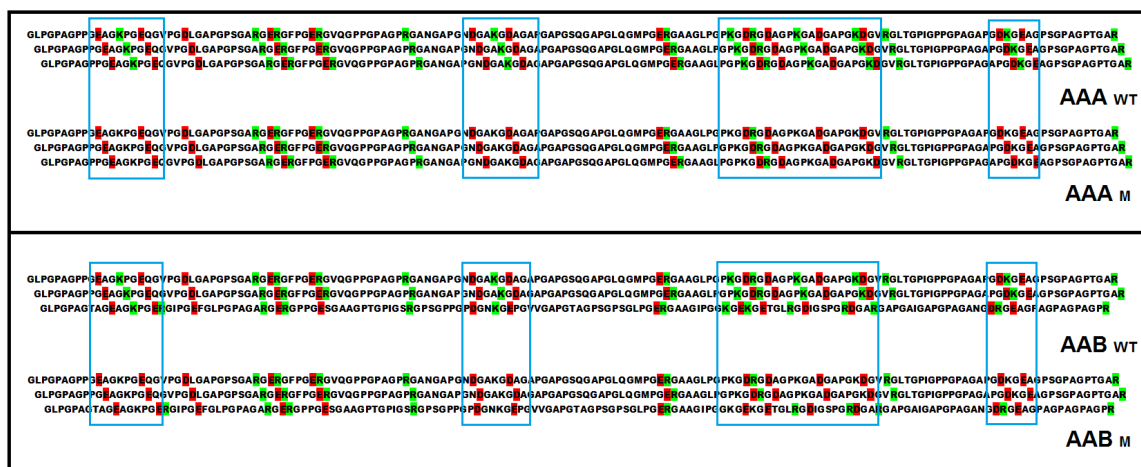


Figure 6-168: Schematic of 153 Residue AAA and AAB Trimers, Wild-type vs. 100% Lysine/Leucine Substitution Mutant. Positively Charged Residues (K,R) in Green, Negatively Charged Residues in Red (D,E). Blue Boxes Indicate Areas of Significant Salt Bridge Differences after Mutation.

Following molecular dynamics simulation for 100 ns, backbone atomic RMSD was analyzed to evaluate 'rigidity' of trimers during simulation time as a measure of molecule stability. Figure 6-4 displays backbone RMSD from $t = 0$ until equilibrium. As Figure 6-4A shows, the homotrimer AAA was initially highly unstable, but quickly settled into equilibrium as seen by the lack of RMSD fluctuation. The heterotrimers ABA, AAB and mutated AAB (Figure 6-4 B, C, & D) exhibited more unsteady behavior over longer simulation periods, indicating that the homotrimeric state may be a more rigid molecule. Lysine substitution appeared to have no significant effects towards modulating RMSD variability compared to wild type, although interestingly the mutated AAB trimer reached equilibrium more quickly than the wild-type AAB.

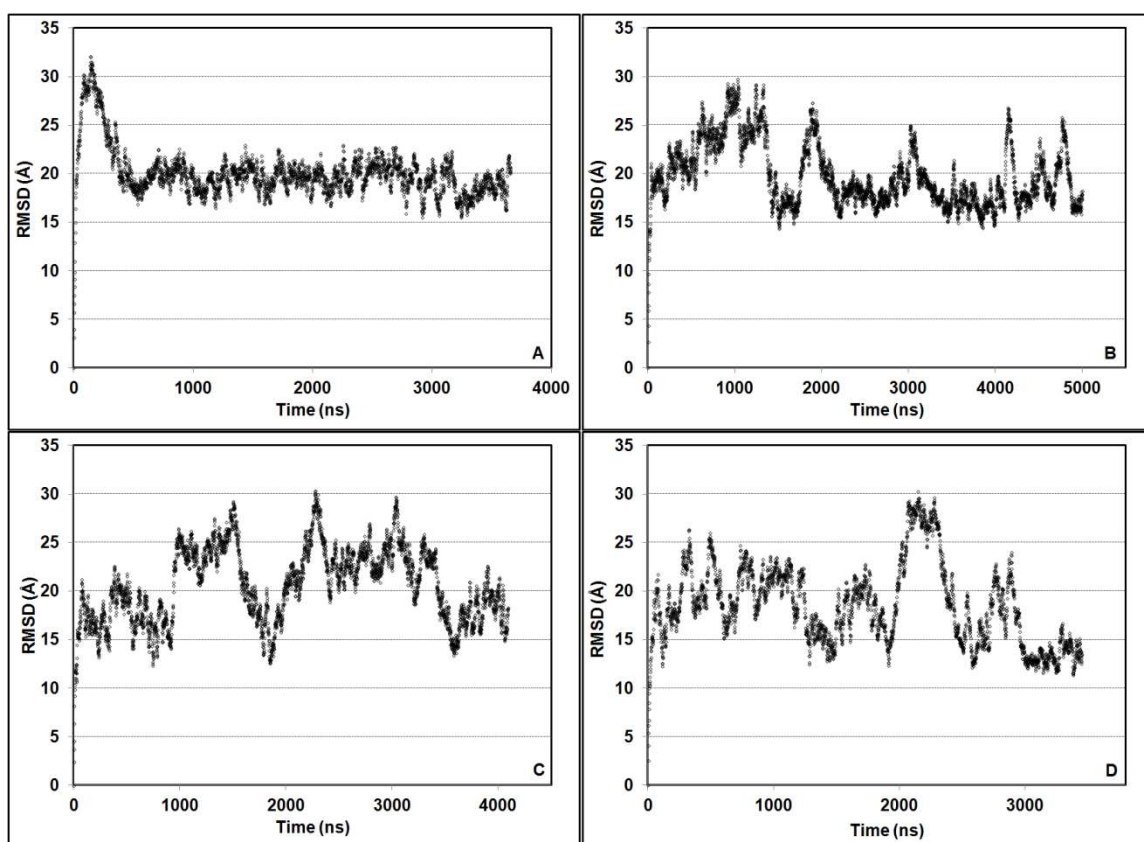


Figure 6-169: RMSD of Backbone Atoms during Molecular Dynamics Simulation. AAA_{WT} (A), ABA_{WT} (B), AAB_{WT} (C), AAB_{MUT} (D)

Additionally, the hydrogen bonding within the trimer backbone was measured during a 50 ns period post-equilibrium for AAA homotrimer and AAB heterotrimers, both wild-type and mutated. Hydrogen bond occupancy % over the duration of 50 ns was determined using 3 levels of criteria (Weak, Moderate, Strict), based on maximum bond length (3.0, 3.25, 3.5 Å) and angle (20, 30, 40°). Initial analysis of average hydrogen bond occupancy indicated that no significant differences existed between any of the trimers regardless of criteria set (Figure 6-5). Total number of hydrogen bonds was similar within each criteria set (Weak: 943, 989, 922, 977; Moderate: 548, 566, 527, 549; Strict: 194, 206, 181, 186) for AAA_{WT}, AAA_{MUT}, AAB_{WT}, and AAB_{MUT}, respectively.

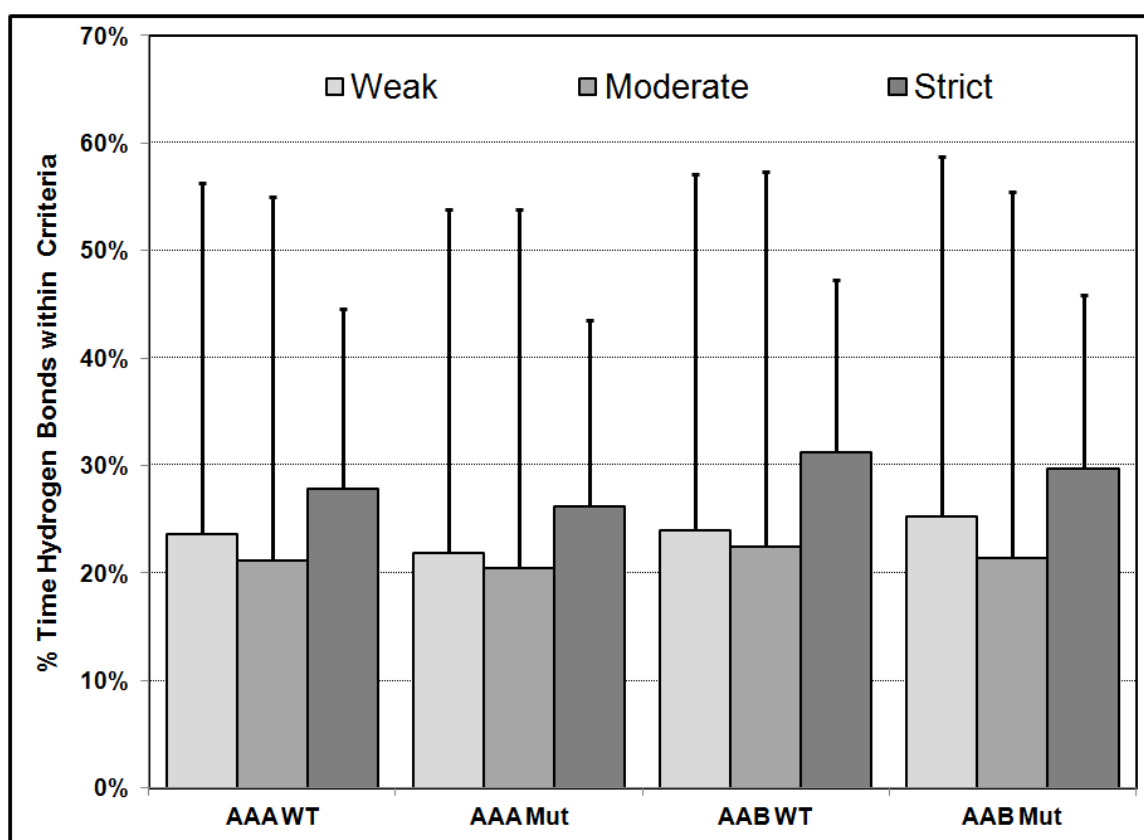


Figure 6-170: Average Backbone Hydrogen Bond Occupancy % During 50 ns Post-Equilibration Period

However, the large standard deviation of all data prompted further investigation into the distribution of bond occupancy to investigate whether significant differences existed among trimers or due to lysine substitution. Analysis was performed on the Weak criteria set to maximize the range of possible hydrogen bonds. As seen in Figure 6-6, all trimers contained a trimodal distribution of bond occupancy, with distinct separation between clusters of 70-100%, 10-70%, and 0-10%, possibly indicating the presence of three hydrogen bond formation mechanisms. Additionally, hydrogen bond occupancy in the AAB mutated trimer displays a noticeably different distribution, with the two higher % clusters appearing to have higher average occupancy times compared to the other trimers.

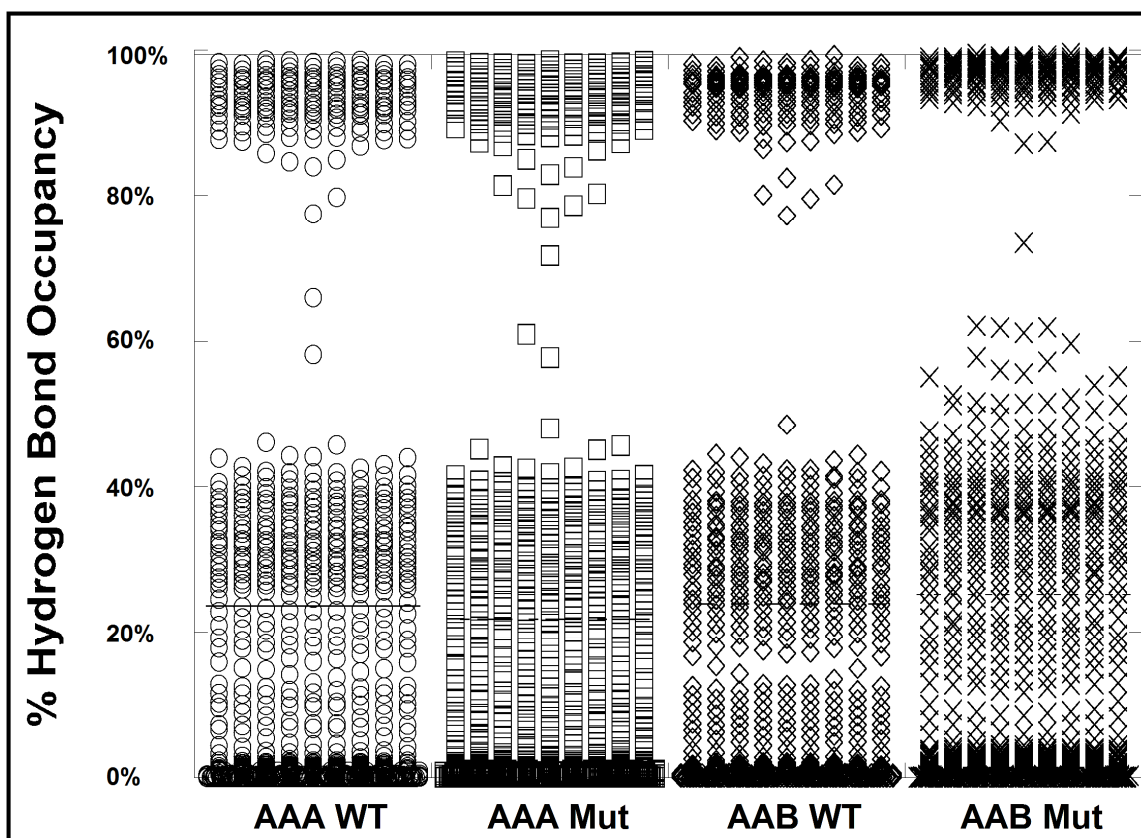


Figure 6-171: Distribution Plot of Hydrogen Bond Occupancy % within Each Trimer, Weak Criteria Set

To investigate whether significant differences existed in these clusters, we separated the datasets by parsing all hydrogen bonds into three occupancy groups: less than 10%, 10% to 70%, and greater than 70% occupancy. To ensure that data wasn't being gerrymandered between trimers, we analyzed the number of hydrogen bonds in each trimer for each cluster group and determined that bond number was not appreciably skewed by our cluster separation (Figure 6-7).

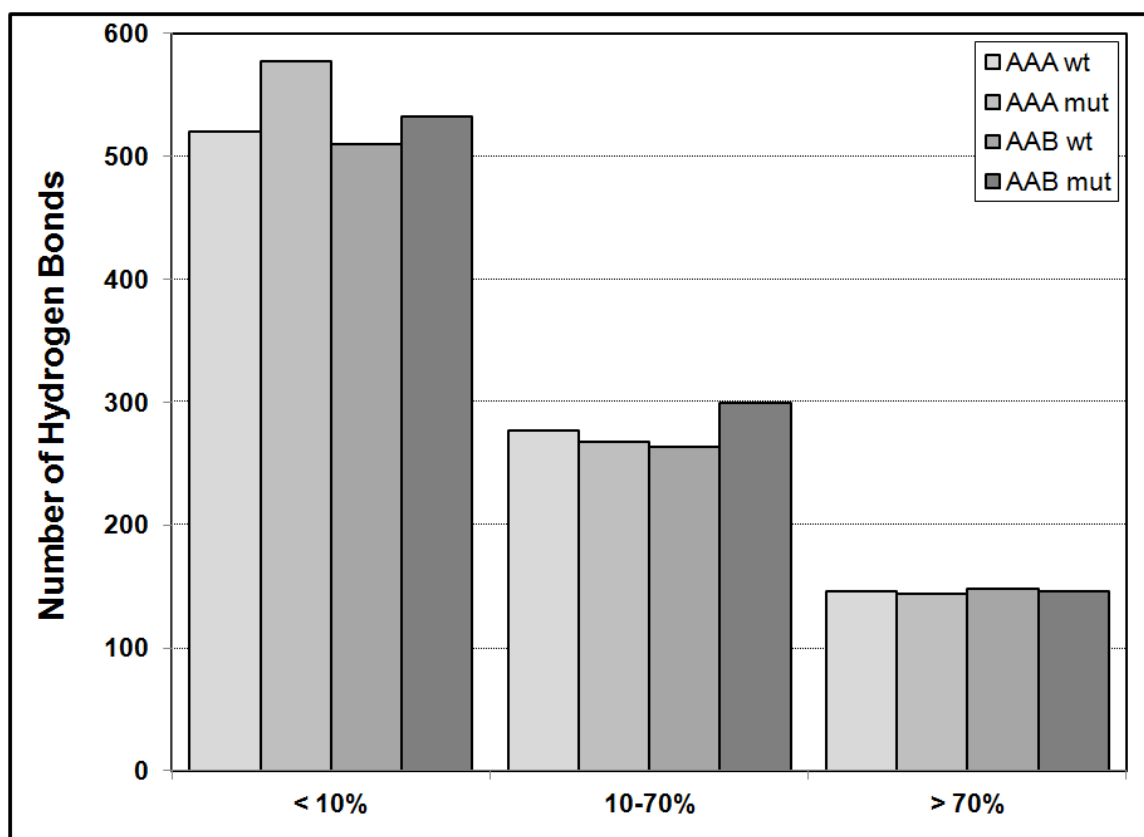


Figure 6-172: Total Number of Hydrogen Bonds within Occupancy % Clusters. Criteria: 3.5 Å & 40° Bond Angle. Filter Cutoff (X-Axis) Corresponds to Bond Occupancy % over Entire Simulation.

Comparison of hydrogen bond occupancy after cluster separation revealed that the hydrogen bonds in the upper two clusters of the AAB mutant trimer displayed significantly higher average

occupancy times, indicating a difference in the helical stability between the AAB_{Mut} and all other trimers, which were not significantly different from each other (Figure 6-8).

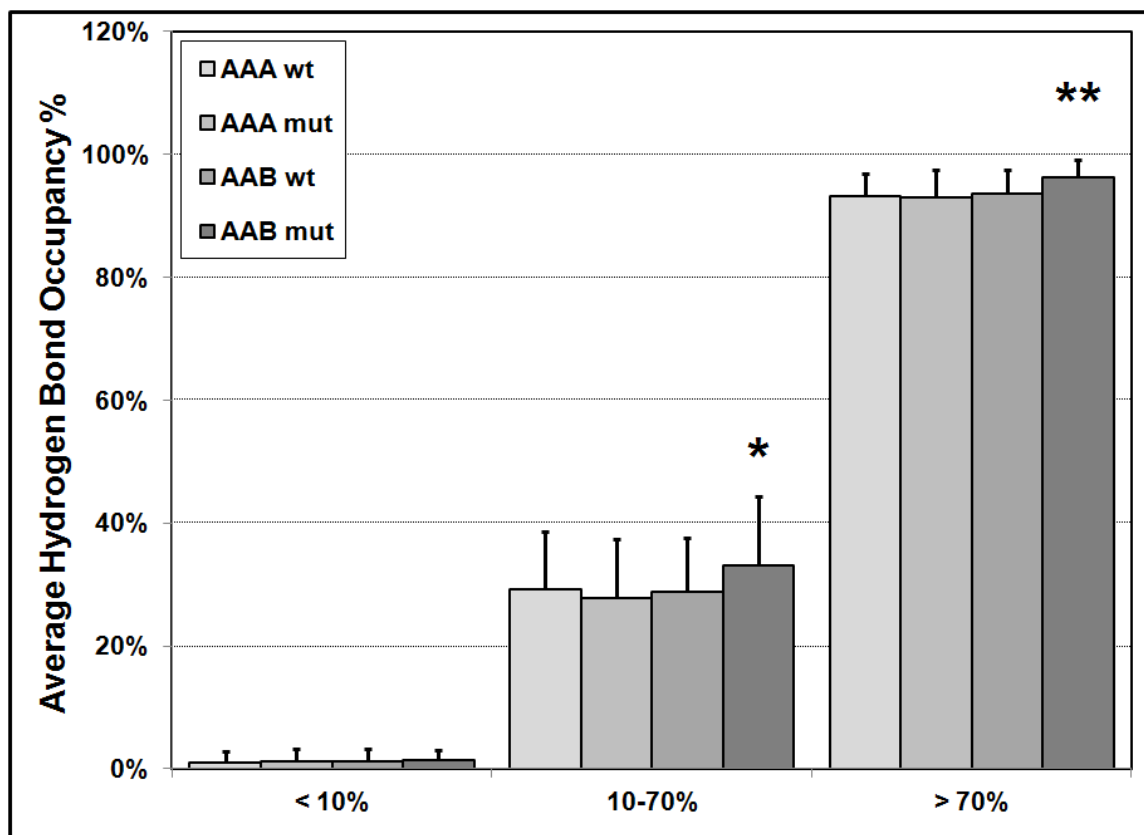


Figure 6-173: Clustered Backbone Hydrogen Bond Occupancy, 3.5 Å & 40° Bond Angle. Filter Cutoff (X-Axis) Corresponds to Bond Occupancy % over Entire Simulation. Error bars \pm SD, $p < 0.0001$.

Additionally, we quantified charge-charge interactions due to salt bridge formation between lysine, arginine, glutamate, and aspartate. A similar characterization to the hydrogen bond occupancy method was performed, with the % of time all salt bridge interactions of 6.5 Å or less recorded during the 50 ns equilibrium period. Here, we compared the occupancy time of extant salt bridges in AAA and AAB trimers compared to their respective mutant trimers with all lysines substituted. The loss of salt bridge number in the AAA homotrimer is evident in Figure 6-9, where comparison of salt bridge occupancy spikes reveals substantial regions comparatively

absent of occupancy time, indicating that loss of lysines significantly impacts the electrostatic energy landscape. Salt bridges that exist in both curves, mediated by arginine residues, display similar occupancy times, indicating that loss of lysines does not impact arginine-based interactions.

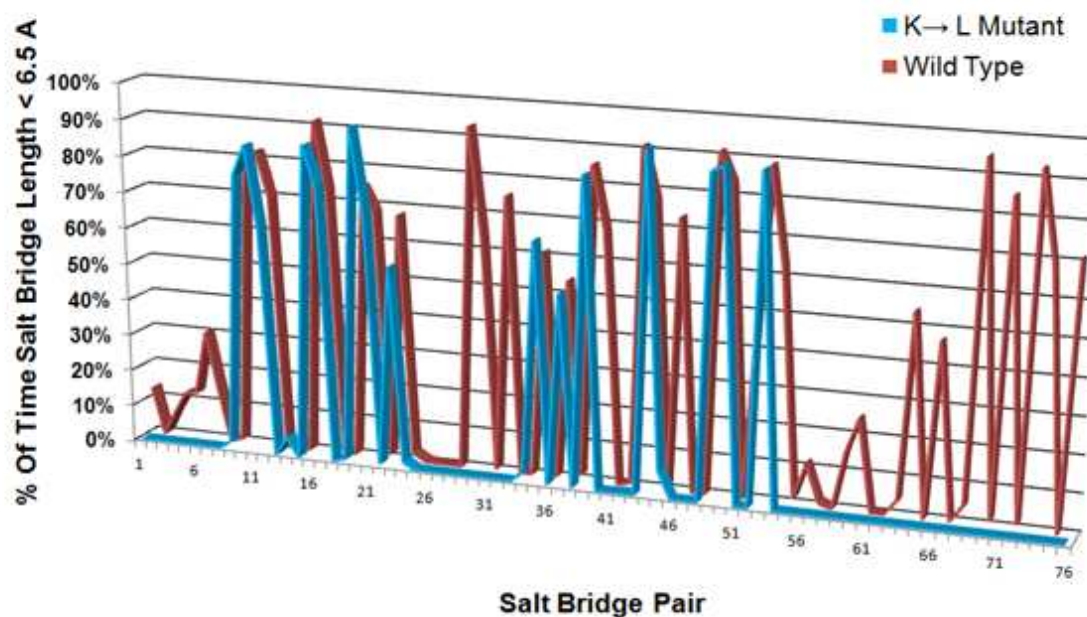


Figure 6-174: Comparison of Salt Bridge Length within 153 Residue Wild-type AAA Trimer vs. Lysine-Leucine substituted AAA Trimer during 50 ns Post-equilibration Period

Similar observations were obtained by analysis of salt bridge occupancy of AAB (Figure 6-10).

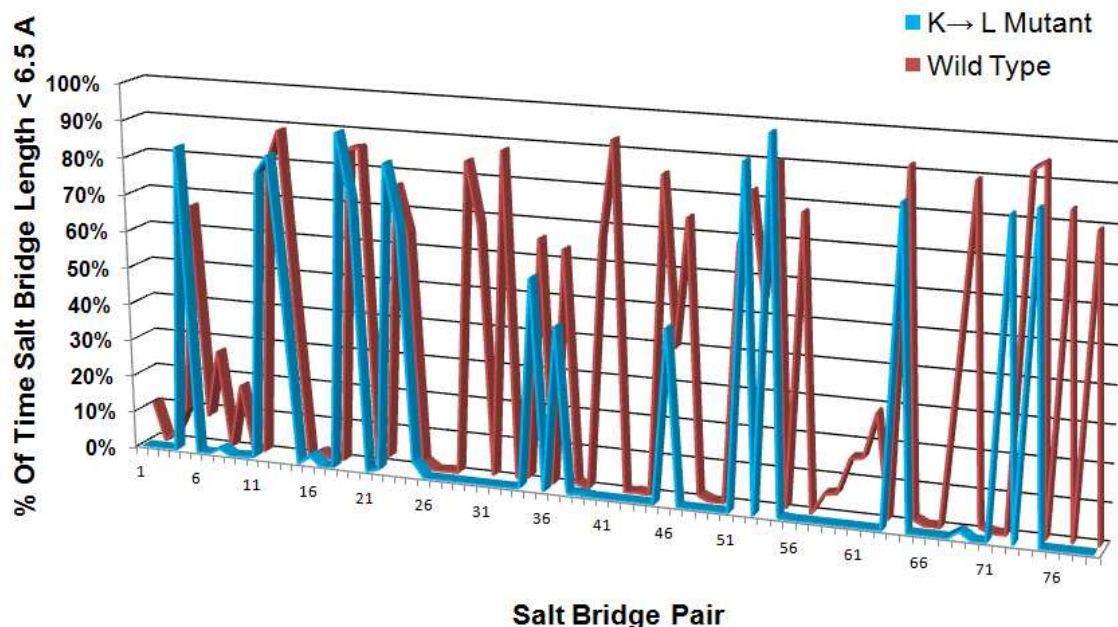


Figure 6-175: Comparison of Salt Bridge Length within 153 Residue Wild-type AAB Trimer vs. Lysine-Leucine substituted AAB Trimer during 50 ns Post-equilibration Period

Finally, while molecular dynamics simulations of the 153 residue trimers provided valuable insight regarding the effects of lysine modification on collagen stability, some concerns regarding the validity of these results exist based on the potential differences in electrostatic characteristics between the leucine residue we used as an analog to methacrylamide derivatization and methacrylamide itself. In particular, the complete lack of charge in the leucine side chain is likely different from the methacrylamide that is present on CMA, which still retains some partial charge from the amide moiety. We initially used the readily available leucine residue for simplicity of building the model, as the actual methacrylamide structure proved difficult using Amber due to the peculiar behavior of the double bond in the methacrylate vinyl. However, with help from one of the developers of Amber, Dr. David Case, we were eventually able to resolve our difficulties and successfully implemented methacrylamide substitution into the mutant chains. Images of the all-atom structure models with native lysine and the modified methacrylamide can be seen in Figures 6-11 and 6-12, respectively. Simulations using the

methacrylamide substitution are currently running, and should provide a more accurate simulation of CMA structure and dynamic stability. Indeed, preliminary data of hydrogen bond occupancy implies that the methacrylate substitution may not only allow increased helical stability compared to the leucine-substituted model, but potentially may increase helical stability beyond that of the wild-type helix. As the heat maps in Figure 6-13 suggests, the overall hydrogen bond occupancy % in AAB trimers appears to be substantially higher in the methacrylate-modified heterotrimer (AABX) as compared to the leucine-substituted heterotrimer (AAB K/L) and wild type (AAB), particularly in the 'Weak' bond criterion group. Additional analysis of longer simulation times will be necessary to determine if this phenomenon is significant, statistically and otherwise.

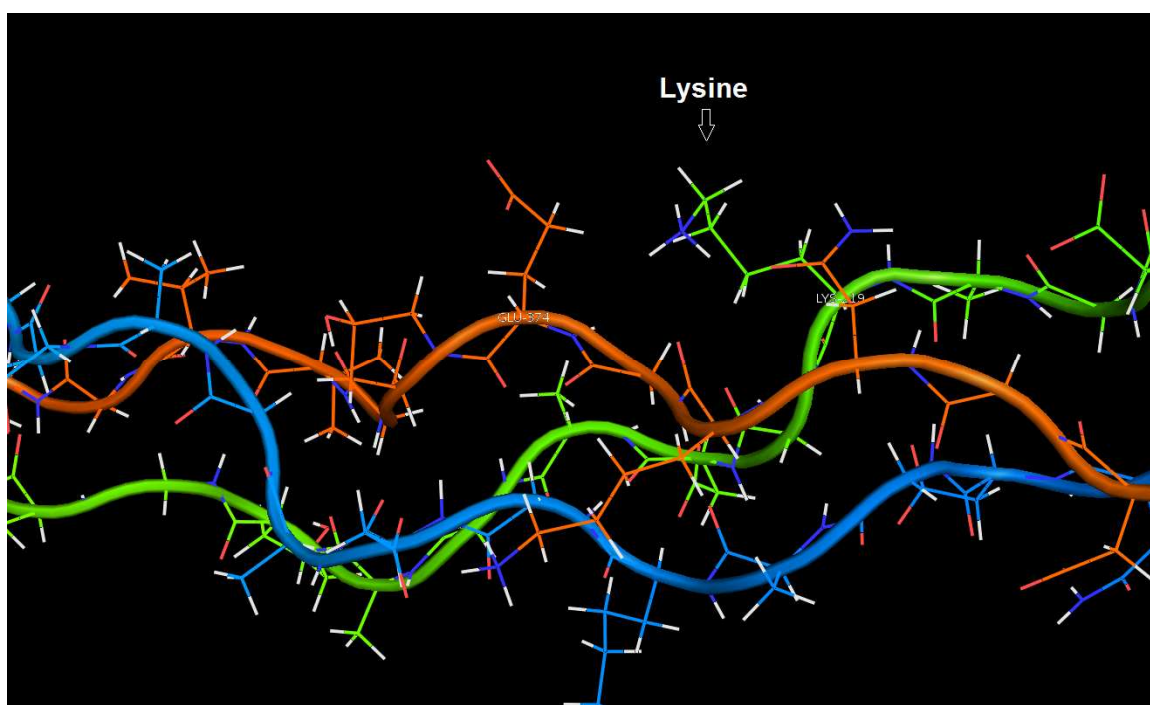


Figure 6-176: AAB trimer segment containing wild-type lysine

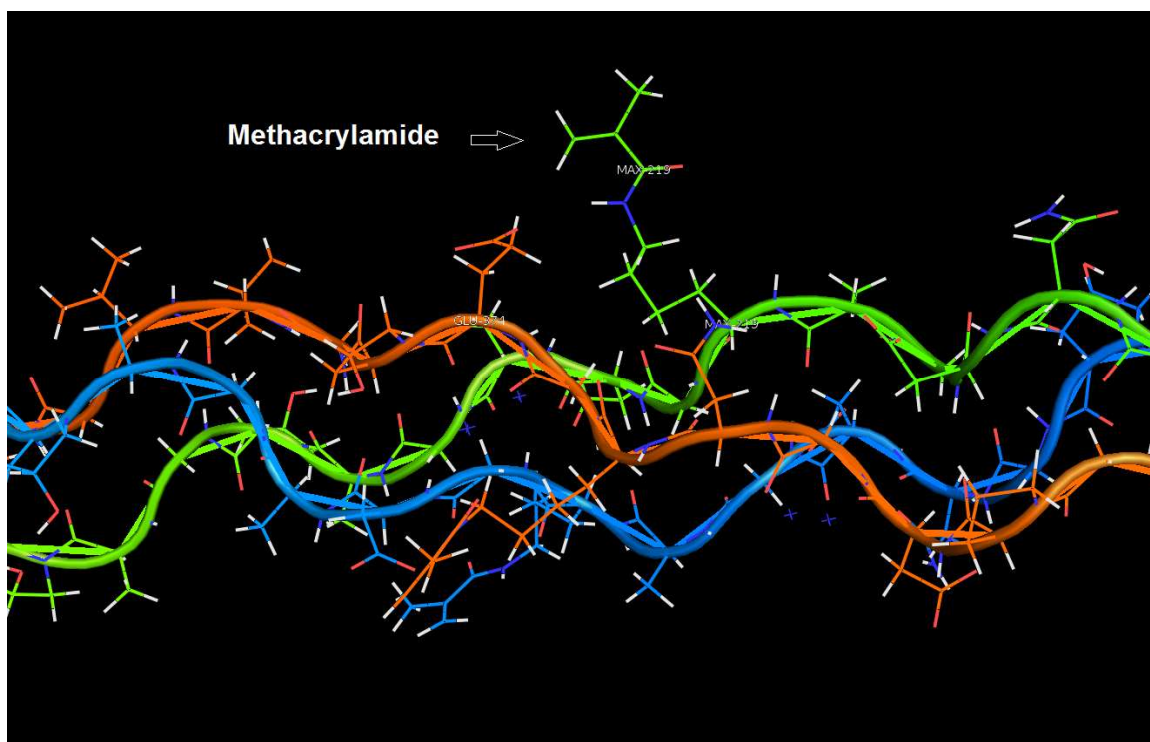


Figure 6-177: AAB trimer segment containing methacrylamide substitution

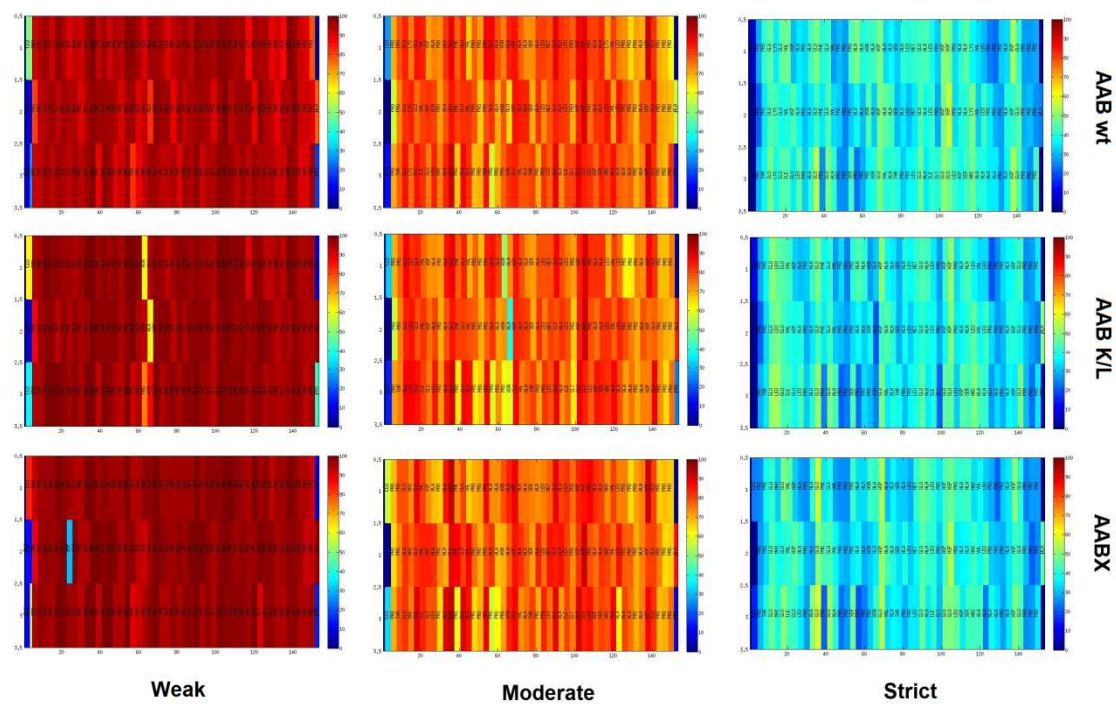


Figure 6-178: Heat Map of Backbone Hydrogen Bond Occupancy in AAB Trimers

6.4 Discussion

The goal of this computational modeling research focused on understanding how perturbations to the lysine residues targeted during CMA synthesis affect the overall stability and conformation of the triple helix. Our experimental characterization of CMA elucidated a number of fundamental differences in protein behavior that we were not able to fully understand using conventional analytical techniques due to the complexity and size inherent to natural collagen and materials derived from it. We hypothesized that we could develop a model of CMA based on recent developments with synthetic collagen-mimetic peptides that have profoundly augmented our understanding of the sequence-structure relationship of native collagen. We utilized a number of existing tools developed by the Nanda group for computational modeling of these collagen mimics, and successfully developed novel triple helical models of based on native collagen and CMA.

Sequence-based modeling was employed to determine functionally-relevant sequences of type-I collagen that could be used to analyze structural behaviors using molecular dynamics simulations. Analysis of electrostatic interactions between charged residues of the full length triple-helical segment of native bovine type I collagen using Matlab resulted in identification of several regions vulnerable to electrostatic energy disruption following substitution of charged lysines with the uncharged residue leucine. Using a discrete windowing approach, we observed several regions within the native collagen sequence that formed substantial energy troughs when comparing charge-charge energy in trimers formed from wild-type vs. lysine substituted sequences. Optimization of this energy gap resulted in determination of 153-residue sequences of the $\alpha 1$ and $\alpha 2$ chains with a high degree of sensitivity to lysine-based mutations with respect to charge-based electrostatic energetic. We showed that even modest substitution of 25% of the lysines with leucines, on par with experimental data concerning CMA derivatization,

produced a measureable energy gap in single AAB trimers formed by the mutated sequences. These data have significant implications regarding the triple helical stability of individual collagen and CMA macromers, as well as the self-assembly of those macromers into higher order fibrillar structures. Indeed, the presence of charged residues was shown to be a dominant mechanism responsible for self-assembly of a synthetic AAB heterotrimeric collagen mimetic peptide [166]. Similar studies have shown that electrostatic interactions are important for driving self-assembly kinetics and stabilizing the resultant fibrils[167]. Other experiments involving N-methylation of lysine and hydroxylysine amines on native type I collagen showed that self-assembly kinetics were retarded *in vitro*, likely due to the disruption of salt-bridge formation [73]. All of these data corroborate rheological data we have observed where CMA self assembly was markedly slower than native collagen, and we can conclude with some certainty that methacrylation of collagen amines results in disruption in salt-bridge formation, and may also explain the reduced storage modulus of CMA hydrogels. The reduction in salt bridge stabilization in CMA fibrillar networks may also be responsible for some of the biological consequences we observed, such as the substantial difference in hMSC compaction of CMA gels compared to native collagen. However, the complex effects of salt-bridge interactions within higher-order fibrillar structures are still poorly understood.

The 153-residue chains determined from the sequence-based modeling were then used to further probe the effects of lysine substitution with a structure-based model using molecular dynamics simulations. We imported these optimized sequences into an all-atom model that allowed us to investigate the ramifications of lysine modification on triple helical stability, interhelical hydrogen bond dynamics, and salt bridge formation in a variety of trimer organizations. RMSD was used to characterize the kinetics of equilibration as well as post-equilibrium molecular 'rigidity'. Interestingly, we found that the homotrimer AAA was

significantly more rigid than any of the heterotrimers examined. While this may not be directly relevant to understanding CMA behavior (AAB trimers did not exhibit similar traits), it is an interesting result in the context of understanding the role of heterogeneity in natural collagens, in which the balance of stability and specificity in triple helical associating proteins is driven by a biological requirement for a certain degree of instability [168,75]. Additionally, we concluded that lysine modification did not affect the molecular rigidity in the AAB trimer, which may have implications for explaining the ability of CMA macromers to form morphologically similar fibrillar networks despite the difference in charge characteristics. However, RMSD data did not provide any especially useful insight into why CMA thermodynamics are so drastically different than native collagen.

More intriguing to our understanding of fundamental CMA molecular structure differences was the backbone hydrogen bond characterization. These data suggest several important components regarding the stability of the triple helix in these simulations. It appears that that three distinct regimes of hydrogen bonding occurred during the post-equilibration period of the simulation, visible as clustered occupancy percentages. This which agrees with recently published results by Fallas et al., in which charged groups may participate in hydrogen bonding through ionic hydrogen bonding with residues of opposite charge, hydrogen bonding with a polar peptidic atom, or via a water-mediated bridge [169]. In our results, transient, low level hydrogen bonding, possibly mediated by nearby water molecules, was not significantly different across any trimer conditions. However, we observed a significant difference in the distribution of hydrogen bond occupancy times in the two higher occupancy percentage clusters when comparing the AAB mutant to its wild type counterpoint as well as both AAA trimers. Somewhat counterintuitively, the lack of positively charged lysines had the effect of increasing the occupancy times in the two high occupancy clusters in the AAB mutant trimer. This result

highlights the complexity in the network of molecular forces that govern collagen stability, and underscore our current lack of complete understanding regarding the interaction of charged residues, not only in salt bridge formation but with nearby uncharged residues as well. Potentially, the lack of charge-charge interactions allows the formation of other more stable hydrogen bonds. Indeed, previous results have shown that in some cases, introduction of charged groups may have a destabilizing effect [159]. Other results produced in similar molecular dynamics simulations imply that charged side groups interact dynamically with nearby water, thus producing a disruptive effect on other hydrogen bonds in the vicinity [170]. Furthermore, these results were obtained with the leucine substitution, and simulations currently running employing the methacrylamide mutation may provide further insight into how modulation of lysine charge affects the overall state of hydrogen bonding.

Analysis of salt bridge formation further validated our original hypothesis that lysine substitution would result in reduction in salt bridge formation, as we indeed observed that mutated trimers formed significantly fewer salt bridges, as expected. One interesting result seems to be that the lack of lysine-mediated salt bridges had no synergistic effect on arginine-mediated salt bridge stability, which is somewhat surprising given that both lysine and arginine are oriented near oppositely charged residues. Again, results with the methacrylamide mutation may help to elucidate whether CMA derivatization necessarily prevents salt bridge formation, or if the remaining partial charge is adequate for initiating ionic hydrogen bonds. Additionally, other implications of improving this model in conjunction with rheological assessment of fibrillar mechanics may have more far reaching impact beyond correlating CMA structure to function. For instance, understanding how alteration of salt bridge formation affects both macromer rigidity as well as fibril strength may lead to improved understanding in genetic diseases affecting collagen triple helix stability such as osteogenesis imperfecta [171-173].

6.5 Conclusion

We employed sequence and structure based computational modeling of native type I collagen and a modified CMA analog to investigate the molecular basis of intriguing thermodynamic behaviors observed during CMA characterization and experimental application. We have developed a novel, energetically optimized triple helical model based on native type I collagen that we have shown is useful in analyzing the molecular dynamics of trimeric molecules with modified amino acid side chain chemistries. Overall, we gained an appreciation for the significance of lysine-based electrostatic contributions to the stability of the triple helix, and the loss of stability through CMA derivatization is likely responsible for many of the thermodynamic behaviors observed in CMA, such as delayed fibrillogenesis and cold-induced disassembly. This computational model paradigm holds promise for analyzing molecular structural characteristics of collagen based materials that are not easily evaluated with existing experimental techniques. However, additional development with the structure-based model is needed before definitive conclusions can be inferred. Continual development, including currently ongoing simulations with methacrylamide substitution, may result in improved understanding of CMA structure-based behavioral phenomena as well as the fundamental role of charged amino acids in native collagen triple helical stability.

7. Concluding Discussion and Future Directions

We successfully developed a type-I collagen based hydrogel material, collagen methacrylamide, which we showed could be mechanically tuned through the application of light within a range of stiffness relevant to myriad soft-tissue engineering applications. The impetus for this development was based on previous work in our laboratory by Sundararaghavan et al. and Monteiro et al., in which type I collagen gels were modified mechanically and biochemically for use as instructive scaffolds in neuroregeneration applications. Their pioneering results implied that stiffness gradients and the presence of functional ligands could be used to influence neurite outgrowth and ectodermal differentiation, both of which hold promise as potential strategies for repairing injured CNS tissue and improving functional outcomes. However, the fundamental limitation of their approaches, namely the lack of spatial control over these parameters in a clinically relevant manner, posed severe limitations for translation into useful therapies in people. To this end, we aimed to incorporate their approaches into a platform by which light could be used to achieve the desired material properties, the rationale for an optical-based mechanism being that minimal disruption of spared tissue in CNS injuries is of paramount importance.

Initially, we sought to leverage existing photocrosslinking techniques, as our laboratory's field of expertise resides primarily in biomechanics rather than biochemistry. However, extensive evaluation of existing methodologies for photocrosslinking fibrillar collagen resulted in a determination that the state of the art was insufficient for our needs. We desired significant mechanical changes, produced quickly, while preserving the majority of the material characteristics inherent to type I collagen that formed the basis for its selection as the base material. We evaluated flavin mononucleotide and UVA as a direct collagen crosslinking

photoinitiator system, which has previously shown utility for corneal crosslinking [56], as well as published methods for derivatizing collagen with methacrylic anhydride to allow radical polymerization of pendant vinyl groups. In the former case, we determined that the range of stiffness provided by FMN and UV were insufficient for our applications, where the most substantial modification of fibrillar gels was limited to crosslinking macromers prior to self-assembly, and that FMN photoinitiation was highly toxic to encapsulated cells, all of which resulted in evaluation of more appropriate methods for imparting photocrosslinks into collagen gels. Collagen methacrylamide has been derivatized from native collagen previously, and we sought to employ these methods into our strategies based on published results. However, again we found limitations in these techniques, mainly that the derivatization reaction required conditions not compatible with the sufficient preservation of the collagen triple helix. Despite numerous attempts, the conclusion we reached implied that a different method for derivatizing collagen under gentler conditions was necessary for collagen methacrylamide to be a useful material for our research goals.

By employing EDC and sulfoNHS crosslinking of methacrylic acid, we developed a process for derivatizing CMA while maintaining its ability to self-assemble, and we showed that it formed fibrillar gels morphologically similar to native collagen, could be degraded enzymatically, retained characteristic triple helical structure, and provided a stable, biofunctional scaffold suitable for culturing multiple cell types. Through a laborious optimization process, we developed a platform based on CMA for spatiotemporally modulating the material properties within a self-assembling hydrogel, which we believe holds promise for a wide array of soft-tissue engineering applications. However, our initial rationale for development of this material was centered on creating instructive scaffolds for CNS injury repair, which became the focus of our biological application experiments.

Characterization of the material properties elucidated the capabilities of CMA photocrosslinking; characterization of its biological compatibility uncovered its limitations. A large portion of the developmental rationale rested on the assumption that Irgacure/UV crosslinking could be used to modify CMA in the presence of cells with acceptable negative side effects, based on numerous published studies that supported this assumption. Our results were quite different. Given the structure of CMA, the distribution of methacrylate groups, and likely a litany of other factors as yet unknown, the concentration of photoinitiator required for achieving the desired material modification was also high enough to significantly impact cells encapsulated prior to the photoinitiation. In some cases, complete ablation of viability was observed, in others, only minimal detriment. While the I2959 concentrations we determined were necessary for CMA photocrosslinking are similar to those used without apparent toxicity in other platforms, the unique distribution of reactive groups within CMA was often inadequate for reacting with radicals, leaving them free to wreak havoc on cells instead.

Despite this drawback, some cell types were able to tolerate photocrosslinking quite well, with hMSC appearing to suffer minimally even under maximal crosslinking conditions. In light of this, along with recently published literature that showed hMSC capable of neural differentiation dictated by substrate mechanics, we investigated whether CMA could be used to direct neural differentiation in a spatially controlled manner using photocrosslinking. Again, limitations of CMA hampered our application with this platform. While hMSC could be grown in CMA gels with and without crosslinking, and showed neurogenic potential, differences in CMA fibrillar structure previously believed to be insignificant were observed to have profound effects on hMSC behavior, with dramatic cellular compaction occurring overnight in CMA gels without crosslinking. While fibrillar diameter and macromer structure were observed to be indistinguishable by our biochemical analysis with SEM, DLS, and CD, the molecular differences

between CMA and native collagen proved to have significant biological consequences. As such, the dynamic nature of the material properties in gel undergoing compaction largely obviated any further application of CMA as a platform for studying hMSC neural induction. Additionally, concerns regarding the functionality of hMSC-derived neural cells by ourselves and others, led to alternate strategies for utilizing CMA as a neuroregenerative matrix. However, hMSC compacted gels may be useful in other soft-tissue engineering applications such as vascular tissue repair, tendon replacement, and vertebral disc regeneration. In particular, the ability to constrain gel compaction spatially may prove extremely useful for designing oriented, anisotropic tissue equivalents.

In a separate regime of photonicallly induced material modification, we hypothesized that CMA gels could be used as a 3D 'canvas', upon which we could paint a biofunctionally instructive mural. Recent work in our lab by Dr. Shirley Masand implied that collagen grafted with functional peptide mimics could be used to not only augment neurite outgrowth in a peripheral nerve guidance conduit, but that specificity in the regenerating axons could be targeted as well, a result with important implications for downstream targeting and functional recovery. These phenomena, coupled with the spatial control of CMA photocrosslinking, led us to investigate whether photografting of functional methacrylated peptides could be used to directionally guide neurite outgrowth, potentially providing a robust axonal targeting mechanism. In addition, the increased concentration of reactive groups on these peptides was hypothesized to improve cellular viability outcomes following photoinitiator-produced radical exposure. However, a number of unforeseen complications with this approach caused serious limitations to its implementation and evaluation of efficacy. Foremost among them, peptide design flaws resulted in solubility issues and aggregation of peptide within CMA solutions. The presence of photosensitive methacrylate groups, along with spacer sequences intended to maximize peptide

presentation to cells, combined to prevent significant coupling efficiency in the photografting paradigm. Additionally, peptide synthesis costs and long product turnaround times created significant logistical difficulties that we were unable to overcome in the scope allowed by this thesis work. While promising results indicated that this approach may be feasible in the future, significant improvements in future peptide design and access to collaborative efforts with peptide synthesis experts will be necessary for development of this technique into a functional modality. Overall, we were successful in demonstrating that CMA gels are useful substrates for neural stem and progenitor cell culture and differentiation, as well as showing utility in encouraging directed cellular behaviors with clinically relevant populations such as Schwann cells. Further development with these platforms may provide useful culture systems for regenerative medicine as well as fundamental investigation into the mechanisms of disease progression in pathological conditions.

Additionally, CMA exhibited a number of intriguing behaviors not observed in its native collagen counterpart, particularly the ability of CMA to reversibly disassemble at temperatures below 10 C°. One application that may be exploited from this quality resides in the use of CMA gels as a novel culture substrate, where temperature alone could be used to harvest sensitive differentiated cell populations without the use of enzymatic cleavage, a major impediment to transplantation of therapeutically relevant cells. Furthermore, the ability to spatially constrain specific populations through focal application of crosslinking provides an avenue for creating complex multicellular coculture systems in physiologically relevant geometries utilizing only light and temperature. The molecular basis for this 'cold-melting' phenomenon is still poorly understood, but evidence provided through our investigation with computational models of CMA model peptides using sequence based energetic analysis and structure based molecular dynamics simulations indicate that the partial shielding of charged groups on collagen residue

side chains following CMA derivatization may be responsible for the altered thermodynamic behavior. Indeed, complementary experimental results using circular dichroism to analyze protein structure indicate that significant differences exist in triple helix stability, with substantial alteration to the formation of resultant higher order fibrillar structures. Ongoing development of both molecular dynamics modeling and CD analysis experiments will hopefully elucidate the precise mechanisms driving this behavior, and may allow us to capitalize on the use of CMA as a dynamic scaffold. Lastly, this *in silico* approach may also provide insight into our current understanding of native collagen structural stability and self-assembly, with implications for augmenting our ability to design new materials as well as address pathological conditions resulting from mutations in the genes responsible for producing native collagen, such as osteogenesis imperfecta.

Bibliography

1. Nicodemus GD, Bryant SJ (2008) Cell encapsulation in biodegradable hydrogels for tissue engineering applications. *Tissue Eng Part B-Rev* 14 (2):149-165
2. Cen L, Liu W, Cui L, Zhang WJ, Cao YL (2008) Collagen tissue engineering: Development of novel biomaterials and applications. *Pediatric Research* 63 (5):492-496
3. Lin YK, Liu DC (2006) Comparison of physical–chemical properties of type I collagen from different species. *Food Chemistry* 99 (2):244-251. doi:10.1016/j.foodchem.2005.06.053
4. Shoulders MD, Raines RT (2009) Collagen Structure and Stability. *Annual Review of Biochemistry* 78 (1):929-958. doi:doi:10.1146/annurev.biochem.77.032207.120833
5. Bhattacharjee A, Bansal M (2005) Collagen Structure: The Madras Triple Helix and the Current Scenario. *IUBMB Life* 57 (3):161-172. doi:10.1080/15216540500090710
6. Kadler KE, Holmes DF, Trotter JA, Chapman JA (1996) Collagen fibril formation. *Biochem J* 316 (Pt 1):1-11
7. Persikov AV, Ramshaw JA, Kirkpatrick A, Brodsky B (2005) Electrostatic interactions involving lysine make major contributions to collagen triple-helix stability. *Biochemistry* 44 (5):1414-1422. doi:10.1021/bi048216r
8. Siegel RC, Pinnell SR, Martin GR (1970) Cross-linking of collagen and elastin. Properties of lysyl oxidase. *Biochemistry* 9 (23):4486-4492. doi:10.1021/bi00825a004
9. Friess W (1998) Collagen – biomaterial for drug delivery. *European Journal of Pharmaceutics and Biopharmaceutics* 45 (2):113-136. doi:10.1016/s0939-6411(98)00017-4
10. Cheung DT, Perelman N, Ko EC, Nimni ME (1985) Mechanism of Crosslinking of Proteins by Glutaraldehyde .3. Reaction with Collagen in Tissues. *Connective Tissue Research* 13 (2):109-115
11. Yang L, Van der Werf KO, Fitie CFC, Bennink ML, Dijkstra PJ, Feijen J (2008) Mechanical properties of native and cross-linked type I collagen fibrils. *Biophysical Journal* 94 (6):2204-2211. doi:10.1529/biophysj.107.111013
12. Badylak SF, Freytes DO, Gilbert TW (2009) Extracellular matrix as a biological scaffold material: Structure and function. *Acta Biomater* 5 (1):1-13
13. Goissis G, Junior EM, Marcantonio JAC, Lia RCC, Cancian DCJ, de Carvalho M (1999) Biocompatibility studies of anionic collagen membranes with different degree of glutaraldehyde cross-linking. *Biomaterials* 20 (1):27-34
14. Sundararaghavan HG, Monteiro GA, Lapin NA, Chabal YJ, Miksan JR, Shreiber DI (2008) Genipin-induced changes in collagen gels: Correlation of mechanical properties to fluorescence. *Journal of Biomedical Materials Research Part A* 87A (2):308-320. doi:10.1002/jbm.a.31715
15. Orban JM, Wilson LB, Kofroth JA, El-Kurdi MS, Maul TM, Vorp DA (2004) Crosslinking of collagen gels by transglutaminase. *Journal of Biomedical Materials Research Part A* 68A (4):756-762. doi:10.1002/jbm.a.20110
16. Weadock KS, Miller EJ, Bellincampi LD, Zawadsky JP, Dunn MG (1995) Physical cross-linking of collagen fibers - comparison of ultraviolet radiation and dehydrothermal treatment. *Journal of Biomedical Materials Research* 29 (11):1373-1379
17. Ibusuki S, Halbesma GJ, Randolph MA, Redmond RW, Kochevar IE, Gill TJ (2007) Photochemically cross-linked collagen gels as three-dimensional scaffolds for tissue engineering. *Tissue Eng* 13 (8):1995-2001. doi:DOI 10.1089/ten.2006.0153
18. Poshusta AK, Anseth KS (2001) Photopolymerized biomaterials for application in the temporomandibular joint. *Cells Tissues Organs* 169 (3):272-278
19. Gonen-Wadmany M, Oss-Ronen L, Seliktar D (2007) Protein-polymer conjugates for forming photopolymerizable biomimetic hydrogels for tissue engineering. *Biomaterials* 28 (26):3876-3886. doi:10.1016/j.biomaterials.2007.05.005

20. Brinkman WT, Nagapudi K, Thomas BS, Chaikof EL (2003) Photo-cross-linking of type I collagen gels in the presence of smooth muscle cells: Mechanical properties, cell viability, and function. *Biomacromolecules* 4 (4):890-895. doi:10.1021/Bm0257412
21. Hoffman AS Hydrogels for biomedical applications. *Advanced Drug Delivery Reviews* (0). doi:10.1016/j.addr.2012.09.010
22. Bryant SJ, Bender RJ, Durand KL, Anseth KS (2004) Encapsulating Chondrocytes in degrading PEG hydrogels with high modulus: Engineering gel structural changes to facilitate cartilaginous tissue production. *Biotechnol Bioeng* 86 (7):747-755
23. Burdick JA, Anseth KS (2002) Photoencapsulation of osteoblasts in injectable RGD-modified PEG hydrogels for bone tissue engineering. *Biomaterials* 23 (22):4315-4323. doi:10.1016/S0142-9612(02)00176-X
24. Nemir S, Hayenga HN, West JL (2009) PEGDA hydrogels with patterned elasticity: Novel tools for the study of cell response to substrate rigidity. *Biotechnology and Bioengineering* 105 (3):636-644
25. Ifkovits JL, Burdick JA (2007) Review: Photopolymerizable and degradable biomaterials for tissue engineering applications. *Tissue Engineering* 13 (10):2369-2385
26. Almany L, Seliktar D (2005) Biosynthetic hydrogel scaffolds made from fibrinogen and polyethylene glycol for 3D cell cultures. *Biomaterials* 26 (15):2467-2477
27. Deng C, Li FF, Hackett JM, Chaudhry SH, Toll FN, Toye B, Hodge W, Griffith M (2009) Collagen and glycopolymer based hydrogel for potential corneal application. *Acta Biomater* 6 (1):187-194
28. Omidian H, Rocca JG, Park K (2006) Elastic, superporous hydrogel hybrids of polyacrylamide and sodium alginate. *Macromolecular Bioscience* 6 (9):703-710
29. Georges PC, Miller WJ, Meaney DF, Sawyer ES, Janmey PA (2006) Matrices with compliance comparable to that of brain tissue select neuronal over glial growth in mixed cortical cultures. *Biophysical Journal* 90 (8):3012-3018
30. Suri S, Schmidt CE (2009) Photopatterned collagen-hyaluronic acid interpenetrating polymer network hydrogels. *Acta Biomater* 5 (7):2385-2397. doi:10.1016/j.actbio.2009.05.004
31. Elisseeff J, McIntosh W, Anseth K, Riley S, Ragan P, Langer R (2000) Photoencapsulation of chondrocytes in poly(ethylene oxide)-based semi-interpenetrating networks. *Journal of Biomedical Materials Research* 51 (2):164-171
32. Brigham MD, Bick A, Lo E, Bendali A, Burdick JA, Khademhosseini A (2009) Mechanically Robust and Bioadhesive Collagen and Photocrosslinkable Hyaluronic Acid Semi-Interpenetrating Networks. *Tissue Engineering Part A* 15 (7):1645-1653. doi:10.1089/ten.tea.2008.0441
33. Piantino J, Burdick JA, Goldberg D, Langer R, Benowitz LI (2006) An injectable, biodegradable hydrogel for trophic factor delivery enhances axonal rewiring and improves performance after spinal cord injury. *Experimental Neurology* 201 (2):359-367
34. Schmidt CE, Leach JB (2003) Neural tissue engineering: Strategies for repair and regeneration. *Annual Review of Biomedical Engineering* 5:293-347. doi:10.1146/annurev.bioeng.5.011303.120731
35. Burdick JA, Ward M, Liang E, Young MJ, Langer R (2006) Stimulation of neurite outgrowth by neurotrophins delivered from degradable hydrogels. *Biomaterials* 27 (3):452-459
36. Chvatal SA, Kim YT, Bratt-Leal AM, Lee HJ, Bellamkonda RV (2008) Spatial distribution and acute anti-inflammatory effects of Methylprednisolone after sustained local delivery to the contused spinal cord. *Biomaterials* 29 (12):1967-1975
37. Comolli N, Neuhofer B, Fischer I, Lowman A (2009) In vitro analysis of PNIPAAm-PEG, a novel, injectable scaffold for spinal cord repair. *Acta Biomater* 5 (4):1046-1055

38. Lee H, McKeon RJ, Bellamkonda RV (2009) Sustained delivery of thermostabilized chABC enhances axonal sprouting and functional recovery after spinal cord injury. *Proceedings of the National Academy of Sciences*:-. doi:10.1073/pnas.0905437106
39. Ziemba KS, Chaudhry N, Rabchevsky AG, Jin Y, Smith GM (2008) Targeting axon growth from neuronal transplants along preformed guidance pathways in the adult CNS. *Journal of Neuroscience* 28 (2):340-348. doi:10.1523/jneurosci.3819-07.2008
40. Loers G, Schachner M (2007) Recognition molecules and neural repair. *J Neurochem* 101 (4):865-882. doi:10.1111/j.1471-4159.2006.04409.x
41. Zhang Y, Yeh J, Richardson PM, Bo XN (2008) Cell adhesion molecules of the immunoglobulin superfamily in axonal regeneration and neural repair. *Restorative Neurology and Neuroscience* 26 (2-3):81-96
42. Deumens R, Koopmans GC, Den Bakker CGJ, Maquet V, Blacher S, Honig WMM, Jerome R, Pirard JP, Steinbusch HWM, Joosten EAJ (2004) Alignment of glial cells stimulates directional neurite growth of cns neurons in vitro. *Neuroscience* 125 (3):591-604. doi:10.1016/j.neuroscience.2004.02.010
43. Leipzig ND, Shoichet MS (2009) The effect of substrate stiffness on adult neural stem cell behavior. *Biomaterials* 30 (36):6867-6878
44. Xu RX, Jiang XD, Guo ZY, Chen JR, Zou YX, Ke YQ, Zhang SZ, Li ZH, Cai YQ, Du M, Qin LS, Tang YP, Zeng Y (2008) Functional analysis of neuron-like cells differentiated from neural stem cells derived from bone marrow stroma cells in vitro. *Cellular and Molecular Neurobiology* 28 (4):545-558
45. Wang L-S, Chung JE, Pui-Yik Chan P, Kurisawa M (2009) Injectable biodegradable hydrogels with tunable mechanical properties for the stimulation of neurogenesis differentiation of human mesenchymal stem cells in 3D culture. *Biomaterials* 31 (6):1148-1157
46. Engler AJ, Sen S, Sweeney HL, Discher DE (2006) Matrix elasticity directs stem cell lineage specification. *Cell* 126 (4):677-689
47. Rowlands AS, George PA, Cooper-White JJ (2008) Directing osteogenic and myogenic differentiation of MSCs: interplay of stiffness and adhesive ligand presentation. *Am J Physiol-Cell Physiol* 295 (4):C1037-C1044
48. Hatami M, Mehrjardi NZ, Kiani S, Hemmesi K, Azizi H, Shahverdi A, Baharvand H (2009) Human embryonic stem cell-derived neural precursor transplants in collagen scaffolds promote recovery in injured rat spinal cord. *Cytotherapy* 11 (5):618-630
49. Watanabe K, Nakamura M, Okano H, Toyama Y (2007) Establishment of three-dimensional culture of neural stem/progenitor cells in collagen Type-1 Gel. *Restorative Neurology and Neuroscience* 25 (2):109-117
50. Wong JY, Velasco A, Rajagopalan P, Pham Q (2003) Directed Movement of Vascular Smooth Muscle Cells on Gradient-Compliant Hydrogels†. *Langmuir* 19 (5):1908-1913. doi:10.1021/la026403p
51. Burdick JA, Khademhosseini A, Langer R (2004) Fabrication of Gradient Hydrogels Using a Microfluidics/Photopolymerization Process. *Langmuir* 20 (13):5153-5156. doi:10.1021/la049298n
52. Sundararaghavan HG, Monteiro GA, Firestein BL, Shreiber DI (2009) Neurite growth in 3D collagen gels with gradients of mechanical properties. *Biotechnol Bioeng* 102 (2):632-643. doi:10.1002/bit.22074
53. Wilson DF, Erecinska M, Dutton PL (1974) Thermodynamic Relationships in Mitochondrial Oxidative Phosphorylation. *Annual Review of Biophysics and Bioengineering* 3 (1):203-230. doi:doi:10.1146/annurev.bb.03.060174.001223

54. Salomon M, Christie JM, Knieb E, Lempert U, Briggs WR (2000) Photochemical and Mutational Analysis of the FMN-Binding Domains of the Plant Blue Light Receptor, Phototropin[†]. *Biochemistry* 39 (31):9401-9410. doi:10.1021/bi000585+
55. Ahearne M, Yang Y, Then KY, Liu KK (2008) Non-destructive mechanical characterisation of UVA/riboflavin crosslinked collagen hydrogels. *Br J Ophthalmol* 92 (2):268-271. doi:bjo.2007.130104 [pii] 10.1136/bjo.2007.130104
56. Wollensak G, Spoerl E, Seiler T (2003) Riboflavin/ultraviolet-a-induced collagen crosslinking for the treatment of keratoconus. *American Journal of Ophthalmology* 135 (5):620-627. doi:10.1016/s0002-9394(02)02220-1
57. Eichler M, Lavi R, Shainberg A, Lubart R (2005) Flavins are source of visible-light-induced free radical formation in cells. *Lasers in Surgery and Medicine* 37 (4):314-319. doi:10.1002/lsm.20239
58. Menter JM, Patta AM, Sayre RM, Dowdy J, Willis I (2001) Effect of UV irradiation on type I collagen fibril formation in neutral collagen solutions. *Photodermatology, Photoimmunology & Photomedicine* 17 (3):114-120. doi:10.1034/j.1600-0781.2001.170302.x
59. Avery NC, Bailey AJ (2008) Restraining Cross-Links Responsible for the Mechanical Properties of Collagen Fibers: Natural and Artificial Collagen. In: Fratzl P (ed). Springer US, pp 81-110. doi:10.1007/978-0-387-73906-9_4
60. Dong CM, Wu XY, Caves J, Rele SS, Thomas BS, Chaikof EL (2005) Photomediated crosslinking of C6-cinnamate derivatized type I collagen. *Biomaterials* 26 (18):4041-4049. doi:10.1016/j.biomaterials.2004.10.017
61. Van Den Bulcke AI, Bogdanov B, De Rooze N, Schacht EH, Cornelissen M, Berghmans H (2000) Structural and Rheological Properties of Methacrylamide Modified Gelatin Hydrogels. *Biomacromolecules* 1 (1):31-38. doi:10.1021/bm990017d
62. Monteiro GA, Fernandes AV, Sundararaghavan HG, Shreiber DI (2009) Positively and Negatively Modulating Cell Adhesion to Type I Collagen Via Peptide Grafting. *Tissue Engineering Part A* 17 (13-14):1663-1673. doi:10.1089/ten.tea.2008.0346
63. Sundararaghavan HG, Masand SN, Shreiber DI (2011) Microfluidic Generation of Haptotactic Gradients through 3D Collagen Gels for Enhanced Neurite Growth. *Journal of Neurotrauma* 28 (11):2377-2387. doi:10.1089/neu.2010.1606
64. Sheu M-T, Huang J-C, Yeh G-C, Ho H-O (2001) Characterization of collagen gel solutions and collagen matrices for cell culture. *Biomaterials* 22 (13):1713-1719. doi:10.1016/s0142-9612(00)00315-x
65. Xu F, Zhang L, Koder RL, Nanda V (2010) De Novo Self-Assembling Collagen Heterotrimers Using Explicit Positive and Negative Design. *Biochemistry* 49 (11):2307-2316. doi:10.1021/bi902077d
66. Parmar AS, Muschol M (2009) Hydration and Hydrodynamic Interactions of Lysozyme: Effects of Chaotropic versus Kosmotropic Ions. *Biophys J* 97 (2):590-598. doi:10.1016/j.bpj.2009.04.045
67. Damink LHHO, Dijkstra PJ, vanLuyn MJA, vanWachem PB, Nieuwenhuis P, Feijen J (1996) In vitro degradation of dermal sheep collagen cross-linked using a water-soluble carbodiimide. *Biomaterials* 17 (7):679-684
68. Smith PK, Krohn RI, Hermanson GT, Mallia AK, Gartner FH, Provenzano MD, Fujimoto EK, Goeke NM, Olson BJ, Klenk DC (1985) Measurement of protein using bicinchoninic acid. *Analytical Biochemistry* 150 (1):76-85. doi:10.1016/0003-2697(85)90442-7
69. Wiechelman KJ, Braun RD, Fitzpatrick JD (1988) Investigation of the bicinchoninic acid protein assay: Identification of the groups responsible for color formation. *Analytical Biochemistry* 175 (1):231-237. doi:10.1016/0003-2697(88)90383-1

70. Steffens GCM, Yao C, Prevel P, Markowicz M, Schenck P, Noah EM, Pallua N (2004) Modulation of angiogenic potential of collagen matrices by covalent incorporation of heparin and loading with vascular endothelial growth factor. Tissue Eng 10 (9-10):1502-1509. doi:Doi 10.1089/1076327042500382
71. Shaw MT, Tuminello WH (1994) A closer look at the MWD-viscosity transform. Polymer Engineering & Science 34 (2):159-165. doi:10.1002/pen.760340213
72. Branch J (2012) Synthesis and Characterization of Collagen Methacrylamide Sponges for Use as a Biological Scaffold. Rutgers, the State University of New Jersey, Piscataway, NJ
73. Tenni R, Sonaggere M, Viola M, Bartolini B, Tira ME, Rossi A, Orsini E, Ruggeri A, Ottani V (2006) Self-aggregation of fibrillar collagens I and II involves lysine side chains. Micron 37 (7):640-647. doi:10.1016/j.micron.2006.01.011
74. Tiffany ML, Krimm S (1972) Effect of temperature on the circular dichroism spectra of polypeptides in the extended state. Biopolymers 11 (11):2309-2316. doi:10.1002/bip.1972.360111109
75. Leikina E, Merts MV, Kuznetsova N, Leikin S (2002) Type I collagen is thermally unstable at body temperature. P Natl Acad Sci USA 99 (3):1314-1318. doi:DOI 10.1073/pnas.032307099
76. Lin DC, Dimitriadis EK, Horkay F (2007) Robust strategies for automated AFM force curve analysis - I. Non-adhesive indentation of soft, inhomogeneous materials. J Biomech Eng-T Asme 129 (3):430-440. doi:Doi 10.1115/1.2720924
77. Walton RS, Brand DD, Czernuszka JT (2010) Influence of telopeptides, fibrils and crosslinking on physicochemical properties of Type I collagen films. J Mater Sci-Mater M 21 (2):451-461. doi:DOI 10.1007/s10856-009-3910-2
78. Weadock KS, Miller EJ, Keuffel EL, Dunn MG (1996) Effect of physical crosslinking methods on collagen-fiber durability in proteolytic solutions. J Biomed Mater Res 32 (2):221-226
79. Park SN, Park JC, Kim HO, Song MJ, Suh H (2002) Characterization of porous collagen/hyaluronic acid scaffold modified by 1-ethyl-3-(3-dimethylaminopropyl)carbodiimide cross-linking. Biomaterials 23 (4):1205-1212
80. Rault I, Frei V, Herbage D, AbdulMalak N, Huc A (1996) Evaluation of different chemical methods for cross-linking collagen gel, films and sponges. J Mater Sci-Mater M 7 (4):215-221
81. Elkin BS, Azeloglu EU, Costa KD, Morrison B (2007) Mechanical heterogeneity of the rat hippocampus measured by atomic force microscope indentation. J Neurotraum 24 (5):812-822. doi:DOI 10.1089/neu.2006.0169
82. Chung C, Burdick JA (2009) Influence of three-dimensional hyaluronic acid microenvironments on mesenchymal stem cell chondrogenesis. Tissue Eng Part A 15 (2):243-254.
83. Seggio AM, Narayanaswamy A, Roysam B, Thompson DM (2010) Self-aligned Schwann cell monolayers demonstrate an inherent ability to direct neurite outgrowth. J Neural Eng 7 (4). doi:Artn 046001 Doi 10.1088/1741-2560/7/4/046001
84. Alto LT, Havton LA, Conner JM, Hollis ER, Blesch A, Tuszynski MH (2009) Chemotropic guidance facilitates axonal regeneration and synapse formation after spinal cord injury. Nat Neurosci 12 (9):1106-U1108. doi:Doi 10.1038/Nn.2365
85. Masand SN, Perron IJ, Schachner M, Shreiber DI (2012) Neural cell type-specific responses to glycomimetic functionalized collagen. Biomaterials 33 (3):790-797. doi:10.1016/j.biomaterials.2011.10.013
86. Hill CE, Moon LDF, Wood PM, Bunge MB (2006) Labeled Schwann cell transplantation: Cell loss, host Schwann cell replacement, and strategies to enhance survival. Glia 53 (3):338-343. doi:10.1002/glia.20287

87. Li Y, Raisman G (1994) Schwann cells induce sprouting in motor and sensory axons in the adult rat spinal cord. *The Journal of Neuroscience* 14 (7):4050-4063
88. Pearse DD, Sanchez AR, Pereira FC, Andrade CM, Puzis R, Pressman Y, Golden K, Kitay BM, Blits B, Wood PM, Bunge MB (2007) Transplantation of Schwann cells and/or olfactory ensheathing glia into the contused spinal cord: Survival, migration, axon association, and functional recovery. *Glia* 55 (9):976-1000. doi:10.1002/glia.20490
89. Toma JG, McKenzie IA, Bagli D, Miller FD (2005) Isolation and Characterization of Multipotent Skin-Derived Precursors from Human Skin. *STEM CELLS* 23 (6):727-737. doi:10.1634/stemcells.2004-0134
90. Thompson DM, Buettner HM (2001) Schwann cell response to micropatterned laminin surfaces. *Tissue Eng* 7 (3):247-265. doi:10.1089/10763270152044125
91. Carlson AL, Florek CA, Kim JJ, Neubauer T, Moore JC, Cohen RI, Kohn J, Grumet M, Moghe PV (2012) Microfibrous substrate geometry as a critical trigger for organization, self-renewal, and differentiation of human embryonic stem cells within synthetic 3-dimensional microenvironments. *The FASEB Journal* 26 (8):3240-3251. doi:10.1096/fj.11-192732
92. Ludwig TE, Bergendahl V, Levenstein ME, Yu J, Probasco MD, Thomson JA (2006) Feeder-independent culture of human embryonic stem cells. *Nat Methods* 3 (8):637-646. doi:nmeth902 [pii] 10.1038/nmeth902
93. Li H, Babiarz J, Woodbury J, Kane-Goldsmith N, Grumet M (2004) Spatiotemporal heterogeneity of CNS radial glial cells and their transition to restricted precursors. *Developmental Biology* 271 (2):225-238. doi:10.1016/j.ydbio.2004.02.028
94. Woodbury D, Schwarz EJ, Prockop DJ, Black IB (2000) Adult rat and human bone marrow stromal cells differentiate into neurons. *Journal of Neuroscience Research* 61 (4):364-370. doi:10.1002/1097-4547(20000815)61:4<364::aid-jnr2>3.0.co;2-c
95. Lu P, Jones LL, Tuszynski MH (2005) BDNF-expressing marrow stromal cells support extensive axonal growth at sites of spinal cord injury. *Experimental Neurology* 191 (2):344-360. doi:10.1016/j.expneurol.2004.09.018
96. Hermann A, Gastl R, Liebau S, Popa MO, Fiedler J, Boehm BO, Maisel M, Lerche H, Schwarz J, Brenner R, Storch A (2004) Efficient generation of neural stem cell-like cells from adult human bone marrow stromal cells. *Journal of Cell Science* 117 (19):4411-4422. doi:10.1242/jcs.01307
97. Tao H, Rao R, Ma DDF (2005) Cytokine-induced stable neuronal differentiation of human bone marrow mesenchymal stem cells in a serum/feeder cell-free condition. *Development, Growth & Differentiation* 47 (6):423-433. doi:10.1111/j.1440-169X.2005.00810.x
98. Dezawa M, Kanno H, Hoshino M, Cho H, Matsumoto N, Itokazu Y, Tajima N, Yamada H, Sawada H, Ishikawa H, Mimura T, Kitada M, Suzuki Y, Ide C (2004) Specific induction of neuronal cells from bone marrow stromal cells and application for autologous transplantation. *The Journal of Clinical Investigation* 113 (12):1701-1710. doi:10.1172/jci20935
99. Tio M, Tan KH, Lee W, Wang TT, Udolph G (2010) Roles of db-cAMP, IBMX and RA in Aspects of Neural Differentiation of Cord Blood Derived Mesenchymal-Like Stem Cells. *PLoS One* 5 (2):e9398. doi:10.1371/journal.pone.0009398
100. Deng W, Obrocka M, Fischer I, Prockop DJ (2001) In Vitro Differentiation of Human Marrow Stromal Cells into Early Progenitors of Neural Cells by Conditions That Increase Intracellular Cyclic AMP. *Biochemical and Biophysical Research Communications* 282 (1):148-152. doi:10.1006/bbrc.2001.4570
101. Long XX, Olszewski M, Huang W, Kletzel M (2005) Neural cell differentiation in vitro from adult human bone marrow mesenchymal stem cells. *Stem Cells Dev* 14 (1):65-69. doi:DOI 10.1089/scd.2005.14.65

102. Williams CG, Malik AN, Kim TK, Manson PN, Elisseeff JH (2005) Variable cytocompatibility of six cell lines with photoinitiators used for polymerizing hydrogels and cell encapsulation. *Biomaterials* 26 (11):1211-1218. doi:DOI 10.1016/j.biomaterials.2004.04.024
103. Tranquillo RT (1999) Self-organization of tissue-equivalents: the nature and role of contact guidance. *Biochemical Society symposium* 65:27-42
104. Wang W, Itoh S, Matsuda A, Aizawa T, Demura M, Ichinose S, Shinomiya K, Tanaka J (2008) Enhanced nerve regeneration through a bilayered chitosan tube: The effect of introduction of glycine spacer into the CYIGSR sequence. *Journal of Biomedical Materials Research Part A* 85A (4):919-928. doi:10.1002/jbm.a.31522
105. McKenzie IA, Biernaskie J, Toma JG, Midha R, Miller FD (2006) Skin-derived precursors generate myelinating Schwann cells for the injured and dysmyelinated nervous system. *Journal of Neuroscience* 26 (24):6651-6660. doi:Doi 10.1523/Jneurosci.1007-06.2006
106. Biernaskie J, Sparling JS, Liu J, Shannon CP, Plemel JR, Xie Y, Miller FD, Tetzlaff W (2007) Skin-derived precursors generate myelinating Schwann cells that promote remyelination and functional recovery after contusion spinal cord injury. *Journal of Neuroscience* 27 (36):9545-9559. doi:Doi 10.1523/Jneurosci.1930-07.2007
107. Masand SN, Chen J, Perron IJ, Hammerling BC, Loers G, Schachner M, Shreiber DI (2012) The effect of glycomimetic functionalized collagen on peripheral nerve repair. *Biomaterials* 33 (33):8353-8362. doi:10.1016/j.biomaterials.2012.08.018
108. Cheung YK, Gillette BM, Zhong M, Ramcharan S, Sia SK (2007) Direct patterning of composite biocompatible microstructures using microfluidics. *Lab Chip* 7 (5):574-579. doi:Doi 10.1039/B700869d
109. Fisher JP, Dean D, Engel PS, Mikos AG (2001) Photoinitiated polymerization of biomaterials. *Ann Rev Mater Res* 31:171-181. doi:DOI 10.1146/annurev.matsci.31.1.171
110. Albrecht DR, Tsang VL, Sah RL, Bhatia SN (2005) Photo- and electropatterning of hydrogel-encapsulated living cell arrays. *Lab Chip* 5 (1):111-118. doi:Doi 10.1039/B406953f
111. Burdick JA, Chung C, Jia X, Randolph MA, Langer R (2004) Controlled Degradation and Mechanical Behavior of Photopolymerized Hyaluronic Acid Networks. *Biomacromolecules* 6 (1):386-391. doi:10.1021/bm049508a
112. Phinney DG, Prockop DJ (2007) Concise review: Mesenchymal stem/multipotent stromal cells: The state of transdifferentiation and modes of tissue repair - Current views. *STEM CELLS* 25 (11):2896-2902. doi:DOI 10.1634/stemcells.2007-0637
113. Barminko J, Kim JH, Otsuka S, Gray A, Schloss R, Grumet M, Yarmush ML (2011) Encapsulated mesenchymal stromal cells for in vivo transplantation. *Biotechnology and Bioengineering* 108 (11):2747-2758. doi:10.1002/bit.23233
114. Caplan AI, Dennis JE (2006) Mesenchymal stem cells as trophic mediators. *J Cell Biochem* 98 (5):1076-1084. doi:Doi 10.1002/Jcb.20886
115. Voyiadjis AG, Doumi M, Curcio E, Shinbrot T (2011) Fasciculation and Defasciculation of Neurite Bundles on Micropatterned Substrates. *Annals of Biomedical Engineering* 39 (1):559-569. doi:10.1007/s10439-010-0168-2
116. Zhao TB, Zhang ZN, Rong ZL, Xu Y (2011) Immunogenicity of induced pluripotent stem cells. *Nature* 474 (7350):212-U251. doi:Doi 10.1038/Nature10135
117. El Maarouf A, Petridis AK, Rutishauser U (2006) Use of polysialic acid in repair of the central nervous system. *P Natl Acad Sci USA* 103 (45):16989-16994. doi:DOI 10.1073/pnas.0608036103
118. Mehanna A, Jakovcevski I, Acar A, Xiao MF, Loers G, Rougon G, Irintchev A, Schachner M (2010) Polysialic Acid Glycomimetic Promotes Functional Recovery and Plasticity After Spinal Cord Injury in Mice. *Mol Ther* 18 (1):34-43. doi:Doi 10.1038/Mt.2009.235

119. Rutishauser U, Landmesser L (1996) Polysialic acid in the vertebrate nervous system: A promoter of plasticity in cell-cell interactions. *Trends Neurosci* 19 (10):422-427. doi:Doi 10.1016/S0166-2236(96)10041-2
120. Wood KA, Youle RJ (1994) Apoptosis and Free Radicals. *Annals of the New York Academy of Sciences* 738 (1):400-407. doi:10.1111/j.1749-6632.1994.tb21829.x
121. Emre N, Vidal JG, Elia J, O'Connor ED, Paramban RI, Hefferan MP, Navarro R, Goldberg DS, Varki NM, Marsala M, Carson CT (2010) The ROCK Inhibitor Y-27632 Improves Recovery of Human Embryonic Stem Cells after Fluorescence-Activated Cell Sorting with Multiple Cell Surface Markers. *PLoS One* 5 (8):e12148. doi:10.1371/journal.pone.0012148
122. Watanabe K, Ueno M, Kamiya D, Nishiyama A, Matsumura M, Wataya T, Takahashi JB, Nishikawa S, Nishikawa S, Muguruma K, Sasai Y (2007) A ROCK inhibitor permits survival of dissociated human embryonic stem cells. *Nat Biotechnol* 25 (6):681-686. doi:Doi 10.1038/Nbt1310
123. Sagawa H, Terasaki H, Nakamura M, Ichikawa M, Yata T, Tokita Y, Watanabe M (2007) A novel ROCK inhibitor, Y-39983, promotes regeneration of crushed axons of retinal ganglion cells into the optic nerve of adult cats. *Experimental Neurology* 205 (1):230-240. doi:DOI 10.1016/j.expneurol.2007.02.002
124. Clark GL, Parker EA, Schaad JA, Warren WJ (1935) NEW MEASUREMENTS OF PREVIOUSLY UNKNOWN LARGE INTERPLANAR SPACINGS IN NATURAL MATERIALS. *Journal of the American Chemical Society* 57 (8):1509-1509. doi:10.1021/ja01311a504
125. Ramachandran GN, Kartha G (1955) Structure of collagen. *Nature* 176 (4482):593-595
126. Rich A, Crick FHC (1961) The molecular structure of collagen. *Journal of Molecular Biology* 3 (5):483-IN484. doi:[http://dx.doi.org/10.1016/S0022-2836\(61\)80016-8](http://dx.doi.org/10.1016/S0022-2836(61)80016-8)
127. Hofmann H, Fietzek PP, Kühn K (1978) The role of polar and hydrophobic interactions for the molecular packing of type I collagen: A three-dimensional evaluation of the amino acid sequence. *Journal of Molecular Biology* 125 (2):137-165. doi:[http://dx.doi.org/10.1016/0022-2836\(78\)90342-X](http://dx.doi.org/10.1016/0022-2836(78)90342-X)
128. Fietzek P, Kühn K (1975) Information contained in the amino acid sequence of the $\alpha 1(I)$ -chain of collagen and its consequences upon the formation of the triple helix, of fibrils and crosslinks. *Mol Cell Biochem* 8 (3):141-157. doi:10.1007/bf01792765
129. Dalglish R (1997) The human type I collagen mutation database. *Nucleic Acids Res* 25 (1):181-187. doi:Doi 10.1093/Nar/25.1.181
130. Fraser RDB, Trus BL (1986) Molecular Mobility in the Gap Regions of Type-1 Collagen Fibrils. *Bioscience Rep* 6 (2):221-226. doi:Doi 10.1007/Bf01115010
131. Bornstein P, Sage H (1980) Structurally distinct collagen types. *Annu Rev Biochem* 49:957-1003. doi:10.1146/annurev.bi.49.070180.004521
132. Lynn AK, Yannas IV, Bonfield W (2004) Antigenicity and immunogenicity of collagen. *Journal of Biomedical Materials Research Part B: Applied Biomaterials* 71B (2):343-354. doi:10.1002/jbm.b.30096
133. Jeng JC, Fidler PE, Sokolich JC, Jaskille AD, Khan S, White PM, Street JHI, Light TD, Jordan MH (2007) Seven Years' Experience With Integra as a Reconstructive Tool. *Journal of Burn Care & Research* 28 (1):120-126 110.1097/BCR.1090b1013E31802CB31883F
134. Ruszczak Z (2003) Effect of collagen matrices on dermal wound healing. *Advanced Drug Delivery Reviews* 55 (12):1595-1611. doi:<http://dx.doi.org/10.1016/j.addr.2003.08.003>
135. Lam SL, Hsu VL (2003) NMR identification of left-handed polyproline type II helices. *Biopolymers* 69 (2):270-281. doi:Doi 10.1002/Bip.10354
136. Shoulders MD, Raines RT (2009) Collagen Structure and Stability. *Annu Rev Biochem* 78:929-958. doi:DOI 10.1146/annurev.biochem.77.032207.120833

137. Fratzl P, Misof K, Zizak I, Rapp G, Amenitsch H, Bernstorff S (1998) Fibrillar Structure and Mechanical Properties of Collagen. *Journal of Structural Biology* 122 (1–2):119-122. doi:<http://dx.doi.org/10.1006/jsbi.1998.3966>
138. Fraser RDB, MacRae TP, Miller A, Suzuki E (1983) Molecular conformation and packing in collagen fibrils. *Journal of Molecular Biology* 167 (2):497-521. doi:[http://dx.doi.org/10.1016/S0022-2836\(83\)80347-7](http://dx.doi.org/10.1016/S0022-2836(83)80347-7)
139. Orgel JPRO, Irving TC, Miller A, Wess TJ (2006) Microfibrillar structure of type I collagen in situ. *P Natl Acad Sci USA* 103 (24):9001-9005. doi:DOI 10.1073/pnas.0502718103
140. Hulmes DJS, Miller A, Parry DAD, Piez KA, Woodhead-Galloway J (1973) Analysis of the primary structure of collagen for the origins of molecular packing. *Journal of Molecular Biology* 79 (1):137-148. doi:[http://dx.doi.org/10.1016/0022-2836\(73\)90275-1](http://dx.doi.org/10.1016/0022-2836(73)90275-1)
141. Hofmann H, Fietzek PP, Kühn K (1980) Comparative analysis of the sequences of the three collagen chains $\alpha 1(I)$, $\alpha 2$ and $\alpha 1(III)$: Functional and genetic aspects. *Journal of Molecular Biology* 141 (3):293-314. doi:[http://dx.doi.org/10.1016/0022-2836\(80\)90182-5](http://dx.doi.org/10.1016/0022-2836(80)90182-5)
142. Kadler KE, Holmes DF, Trotter JA, Chapman JA (1996) Collagen fibril formation. *Biochem J* 316:1-11
143. Craig AS, Birtles MJ, Conway JF, Parry DAD (1989) An Estimate of the Mean Length of Collagen Fibrils in Rat Tail-Tendon as a Function of Age. *Connect Tissue Res* 19 (1):51-62. doi:DOI 10.3109/03008208909016814
144. Gelman RA, Poppke DC, Piez KA (1979) Collagen fibril formation in vitro. The role of the nonhelical terminal regions. *Journal of Biological Chemistry* 254 (22):11741-11745
145. Prockop DJ, Fertala A (1998) Inhibition of the self-assembly of collagen I into fibrils with synthetic peptides - Demonstration that assembly is driven by specific binding sites on the monomers. *Journal of Biological Chemistry* 273 (25):15598-15604. doi:DOI 10.1074/jbc.273.25.15598
146. Kuznetsova N, Leikin S (1999) Does the Triple Helical Domain of Type I Collagen Encode Molecular Recognition and Fiber Assembly while Telopeptides Serve as Catalytic Domains?: EFFECT OF PROTEOLYTIC CLEAVAGE ON FIBRILLOGENESIS AND ON COLLAGEN-COLLAGEN INTERACTION IN FIBERS. *Journal of Biological Chemistry* 274 (51):36083-36088. doi:10.1074/jbc.274.51.36083
147. Na GC, Phillips LJ, Freire EI (1989) In vitro collagen fibril assembly: thermodynamic studies. *Biochemistry* 28 (18):7153-7161. doi:10.1021/bi00444a004
148. Cooper A (1970) Thermodynamic studies of the assembly in vitro of native collagen fibrils. *Biochem J* 118 (3):355-365
149. Wood GC (1962) The heterogeneity of collagen solutions and its effect on fibril formation. *Biochem J* 84:429-435
150. Gelman RA, Williams BR, Piez KA (1979) Collagen fibril formation. Evidence for a multistep process. *Journal of Biological Chemistry* 254 (1):180-186
151. Kadler KE, Hojima Y, Prockop DJ (1988) Assembly of type I collagen fibrils de novo. Between 37 and 41 degrees C the process is limited by micro-unfolding of monomers. *Journal of Biological Chemistry* 263 (21):10517-10523
152. Bancelin S, Aime C, Coradin T, Schanne-Klein MC (2012) In situ three-dimensional monitoring of collagen fibrillogenesis using SHG microscopy. *Biomed Opt Express* 3 (6):1446-1454. doi:10.1364/BOE.3.001446 166900 [pii]
153. Tiktopulo EI, Kajava AV (1998) Denaturation of type I collagen fibrils is an endothermic process accompanied by a noticeable change in the partial heat capacity. *Biochemistry* 37 (22):8147-8152. doi:10.1021/bi980360n

bi980360n [pii]

154. Burjanadze TV (1979) Hydroxyproline content and location in relation to collagen thermal stability. *Biopolymers* 18 (4):931-938. doi:10.1002/bip.1979.360180413
155. Liu Y, Liu L, Chen M, Zhang Q (2012) Double thermal transitions of type I collagen in acidic solution. *J Biomol Struct Dyn*. doi:10.1080/07391102.2012.715042
156. Fields GB, Prockop DJ (1996) Perspectives on the synthesis and application of triple-helical, collagen-model peptides. *Peptide Science* 40 (4):345-357. doi:10.1002/(sici)1097-0282(1996)40:4<345::aid-bip1>3.0.co;2-w
157. Koide T (2005) Triple helical collagen-like peptides: Engineering and applications in matrix biology. *Connect Tissue Res* 46 (3):131-141. doi:10.1080/03008200591008518
158. Bella J, Eaton M, Brodsky B, Berman HM (1994) Crystal and molecular structure of a collagen-like peptide at 1.9 Å resolution. *Science (New York, NY)* 266 (5182):75-81
159. Persikov AV, Ramshaw JAM, Kirkpatrick A, Brodsky B (2000) Amino Acid Propensities for the Collagen Triple-Helix†. *Biochemistry* 39 (48):14960-14967. doi:10.1021/bi001560d
160. Berisio R, Vitagliano L, Mazzarella L, Zagari A (2002) Crystal structure of the collagen triple helix model [(Pro-Pro-Gly)₁₀]₃. *Protein Science* 11 (2):262-270. doi:10.1110/ps.32602
161. Persikov AV, Ramshaw JAM, Brodsky B (2005) Prediction of Collagen Stability from Amino Acid Sequence. *Journal of Biological Chemistry* 280 (19):19343-19349. doi:10.1074/jbc.M501657200
162. Nanda V, Zahid S, Xu F, Levine D (2011) Computational design of intermolecular stability and specificity in protein self-assembly. *Methods in enzymology* 487:575-593
163. Venugopal MG, Ramshaw JAM, Braswell E, Zhu D, Brodsky B (1994) Electrostatic Interactions in Collagen-like Triple-Helical Peptides. *Biochemistry* 33 (25):7948-7956. doi:10.1021/bi00191a023
164. Xu F, Zahid S, Silva T, Nanda V (2011) Computational Design of a Collagen A:B:C-Type Heterotrimer. *Journal of the American Chemical Society* 133 (39):15260-15263. doi:10.1021/Ja205597g
165. Persikov AV, Ramshaw JAM, Kirkpatrick A, Brodsky B (2005) Electrostatic Interactions Involving Lysine Make Major Contributions to Collagen Triple-Helix Stability†. *Biochemistry* 44 (5):1414-1422. doi:10.1021/bi048216r
166. Russell LE, Fallas JA, Hartgerink JD (2010) Selective Assembly of a High Stability AAB Collagen Heterotrimer. *Journal of the American Chemical Society* 132 (10):3242-3243. doi:10.1021/ja909720g
167. Gauba V, Hartgerink JD (2007) Self-Assembled Heterotrimeric Collagen Triple Helices Directed through Electrostatic Interactions. *Journal of the American Chemical Society* 129 (9):2683-2690. doi:10.1021/ja0683640
168. Fallas JA, Lee MA, Jalan AA, Hartgerink JD (2011) Rational Design of Single-Composition ABC Collagen Heterotrimers. *Journal of the American Chemical Society* 134 (3):1430-1433. doi:10.1021/ja209669u
169. Fallas JA, Dong JH, Tao YZ, Hartgerink JD (2012) Structural Insights into Charge Pair Interactions in Triple Helical Collagen-like Proteins. *Journal of Biological Chemistry* 287 (11):8039-8047. doi:10.1074/jbc.M111.296574
170. Raman SS, Vijayaraj R, Parthasarathi R, Subramanian V, Ramasami T (2008) A molecular dynamics analysis of ion pairs formed by lysine in collagen: Implication for collagen function and stability. *Journal of Molecular Structure: THEOCHEM* 851 (1-3):299-312. doi:<http://dx.doi.org/10.1016/j.theochem.2007.11.030>

171. Bächinger HP, Morris NP, Davis JM (1993) Thermal stability and folding of the collagen triple helix and the effects of mutations in osteogenesis imperfecta on the triple helix of type I collagen. American Journal of Medical Genetics 45 (2):152-162. doi:10.1002/ajmg.1320450204
172. Gautieri A, Uzel S, Vesentini S, Redaelli A, Buehler MJ (2009) Molecular and Mesoscale Mechanisms of Osteogenesis Imperfecta Disease in Collagen Fibrils. Biophys J 97 (3):857-865. doi:<http://dx.doi.org/10.1016/j.bpj.2009.04.059>
173. Yang W, Battineni ML, Brodsky B (1997) Amino Acid Sequence Environment Modulates the Disruption by Osteogenesis Imperfecta Glycine Substitutions in Collagen-like Peptides†. Biochemistry 36 (23):6930-6935. doi:10.1021/bi970051h

Curriculum Vitae

IAN D. GAUDET

Education:

Ph.D. in Biomedical Engineering from Rutgers University in New Brunswick, New Jersey (2013)

B.S. in Bioengineering (ABET) from University of California, San Diego (2003)

Employment History:

Graduate Research Fellow – Rutgers Dept. of Biomedical Engineering (September 2006 – December 2012)

Cell Process Development Engineer – Microslet (October 2004 – August 2006)

Bioprocess Engineer - Telos Pharmaceuticals (July 2003 – September 2004)

Research Associate - Vertex Pharmaceuticals (November 2001 - June 2003)

Laboratory Technician - UCSD Department of Psychiatry (March 2000 - November 2001)

Publications:

Gaudet I, Shreiber D (2012) Characterization of Methacrylated Type-I Collagen as a Dynamic, Photoactive Hydrogel. *Biointerphases* 7(1-4):1-9

Swerdlow NR, Shoemaker JM, Noh HR, Ma L, Gaudet I, Munson M, Crain S, Auerbach PP. The ventral hippocampal regulation of prepulse inhibition and its disruption by apomorphine in rats are not mediated via the fornix. *Neuroscience*. 2004;123(3):675-85.

Swerdlow NR, Platten A, Kim YK, Gaudet I, Shoemaker J, Pitcher L, Auerbach P. Sensitivity to the dopaminergic regulation of prepulse inhibition in rats: evidence for genetic, but not environmental determinants. *Pharmacol Biochem Behav*. 2001 Oct-Nov;70(2-3):219-26.

Swerdlow NR, Hanlon FM, Henning L, Kim YK, Gaudet I, Halim ND. Regulation of sensorimotor gating in rats by hippocampal NMDA: anatomical localization. *Brain Res*. 2001 Apr 20;898(2):195-203.

Patents:

PROCESS FOR THE SYNTHESIS OF METHACRYLATE-DERIVATIZED TYPE-1 COLLAGEN AND DERIVATIVES THEREOF

D Shreiber, I Gaudet - US Patent 20,120,220,691, (2012)